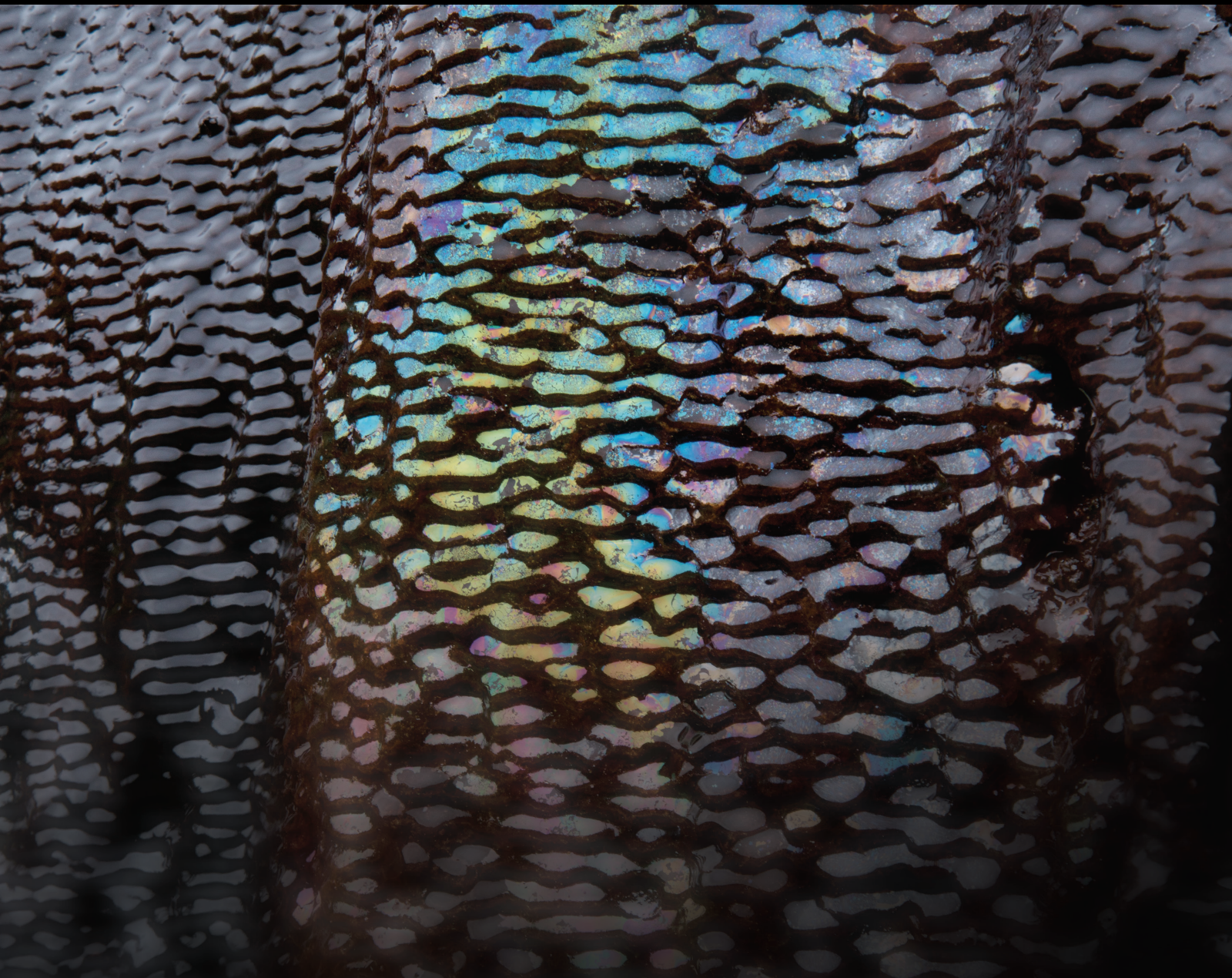


Innovative Methods in Understanding Groundwater Flow in Fractured Rock Reservoirs

Lead Guest Editor: Tanguy Robert

Guest Editors: Frédéric Nguyen and Delphine Roubinet





Innovative Methods in Understanding Groundwater Flow in Fractured Rock Reservoirs

Geofluids

Innovative Methods in Understanding Groundwater Flow in Fractured Rock Reservoirs

Lead Guest Editor: Tanguy Robert

Guest Editors: Frédéric Nguyen and Delphine
Roubinet







Copyright © 2020 Hindawi Limited. All rights reserved.

This is a special issue published in "Geofluids." All articles are open access articles distributed under the Creative Commons Attribution License, which permits unrestricted use, distribution, and reproduction in any medium, provided the original work is properly cited.



























Chief Editor

































Umberta Tinivella, Italy

Associate Editors

Paolo Fulignati , Italy
Huazhou Li , Canada
Stefano Lo Russo , Italy
Julie K. Pearce , Australia

Academic Editors


Basim Abu-Jdayil , United Arab Emirates
Hasan Alsaedi , USA
Carmine Apollaro , Italy
Baojun Bai, USA
Marino Domenico Barberio , Italy
Andrea Brogi , Italy
Shengnan Nancy Chen , Canada
Tao Chen , Germany
Jianwei Cheng , China
Paola Cianfarra , Italy
Daniele Cinti , Italy
Timothy S. Collett , USA
Nicoló Colombani , Italy
Mercè Corbella , Spain
David Cruset, Spain
Jun Dong , China
Henrik Drake , Sweden
Farhad Ehya , Iran
Lionel Esteban , Australia
Zhiqiang Fan , China
Francesco Frondini, Italy
Ilaria Fuoco, Italy
Paola Gattinoni , Italy
Amin Gholami , Iran
Michela Giustiniani, Italy
Naser Golsanami, China
Fausto Grassa , Italy
Jianyong Han , China
Chris Harris , South Africa
Liang He , China
Sampath Hewage , Sri Lanka
Jian Hou, China
Guozhong Hu , China
Lanxiao Hu , China
Francesco Italiano , Italy
Azizollah Khormali , Iran
Hailing Kong, China

Karsten Kroeger, New Zealand
Cornelius Langenbruch, USA
Peter Leary , USA
Guangquan Li , China
Qingchao Li , China
Qibin Lin , China
Marcello Liotta , Italy
Shuyang Liu , China
Yong Liu, China
Yueliang Liu , China
Constantinos Loupasakis , Greece
Shouqing Lu, China
Tian-Shou Ma, China
Judit Mádl-Szonyi, Hungary
Paolo Madonia , Italy
Fabien Magri , Germany
Micòl Mastroicco , Italy
Agnes Mazot , New Zealand
Yuan Mei , Australia
Evgeniy M. Myshakin , USA
Muhammad Tayyab Naseer, Pakistan
Michele Paternoster , Italy
Mandadige S. A. Perera, Australia
Marco Petitta , Italy
Chao-Zhong Qin, China
Qingdong Qu, Australia
Reza Rezaee , Australia
Eliahu Rosenthal , Israel
Gernot Rother, USA
Edgar Santoyo , Mexico
Mohammad Sarmadivaleh, Australia
Venkatramanan Senapathi , India
Amin Shokrollahi, Australia
Rosa Sinisi , Italy
Zhao-Jie Song , China
Ondra Sracek , Czech Republic
Andri Stefansson , Iceland
Bailu Teng , China
Tivadar M. Tóth , Hungary
Orlando Vaselli , Italy
Benfeng Wang , China
Hetang Wang , China
Wensong Wang , China
Zhiyuan Wang , China
Ruud Weijermars , Saudi Arabia

Bisheng Wu , China
Da-yang Xuan , China
Yi Xue , China
HE YONGLIANG, China
Fan Yang , China
Zhenyuan Yin , China
Sohrab Zendeboudi, Canada
Zhixiong Zeng , Hong Kong
Yuanyuan Zha , China
Keni Zhang, China
Mingjie Zhang , China
Rongqing Zhang, China
Xianwei Zhang , China
Ye Zhang , USA
Zetian Zhang , China
Ling-Li Zhou , Ireland
Yingfang Zhou , United Kingdom
Daoyi Zhu , China
Quanle Zou, China
Martina Zucchi, Italy




Contents

Methodology for Hydrogeochemical Sampling to Characterise Groundwaters in Crystalline Bedrock: Developments Made within the Swedish Radwaste Programme

Ann-Chatrin Nilsson, María J. Gimeno , Eva-Lena Tullborg, John Smellie, Stig Jönsson, Ignasi Puigdomenech, and Cecilia Berg


Review Article (13 pages), Article ID 8740492, Volume 2020 (2020)

Effect of Natural Fractures on Stress Evolution of Unconventional Reservoirs Using a Finite Element Method and a Fracture Continuum Method

Qiang Wang , Yongquan Hu , and Jinzhou Zhao 

Research Article (16 pages), Article ID 1481960, Volume 2019 (2019)

A Fractal Model for Characterizing Hydraulic Properties of Fractured Rock Mass under Mining Influence

Xiaoli Liu , Tao Liang, Sijing Wang, and Kumar Nawnit



Research Article (17 pages), Article ID 8391803, Volume 2019 (2019)

The Role of In Situ Stress in Organizing Flow Pathways in Natural Fracture Networks at the Percolation Threshold

Chuanyin Jiang, Xiaoguang Wang , Zhixue Sun, and Qinghua Lei





Research Article (14 pages), Article ID 3138972, Volume 2019 (2019)

How Do Secondary Minerals in Granite Help Distinguish Paleo- from Present-Day Permeable Fracture Zones? Joint Interpretation of SWIR Spectroscopy and Geophysical Logs in the Geothermal Wells of Northern Alsace

Carole Glaas , Jeanne Vidal , Patricia Patrier, Jean-François Girard, Daniel Beaufort, Sabine Petit, and Albert Genter






Research Article (20 pages), Article ID 8231816, Volume 2019 (2019)

Applying Rare Earth Elements, Uranium, and $^{87}\text{Sr}/^{86}\text{Sr}$ to Disentangle Structurally Forced Confluence of Regional Groundwater Resources: The Case of the Lower Yarmouk Gorge

Christian Siebert , Peter Möller, Fabien Magri , Eyal Shalev , Eliahu Rosenthal , Marwan Al-Raggad, and Tino Rödiger

Research Article (21 pages), Article ID 6727681, Volume 2019 (2019)

Experimental Investigation on Nonlinear Flow Anisotropy Behavior in Fracture Media

Chun Zhu , Xiaoding Xu , Xiuting Wang, Feng Xiong , Zhigang Tao , Yun Lin , and Jing Chen

Research Article (9 pages), Article ID 5874849, Volume 2019 (2019)


Evolution Model of Seepage Characteristics in the Process of Water Inrush in Faults

Jianli Shao , Fei Zhou , and Wenbin Sun 

Research Article (14 pages), Article ID 4926768, Volume 2019 (2019)

Review Article

Methodology for Hydrogeochemical Sampling to Characterise Groundwaters in Crystalline Bedrock: Developments Made within the Swedish Radwaste Programme

Ann-Chatrin Nilsson,¹ María J. Gimeno ,² Eva-Lena Tullborg,³ John Smellie,⁴ Stig Jönsson,⁵ Ignasi Puigdomenech,⁶ and Cecilia Berg⁷

¹Geosigma AB, Granitvägen 45, SE-183 63 Täby, Sweden

²Earth Sciences Department, Sciences Faculty, University of Zaragoza, Pedro Cerbuna, 12, E-50009 Zaragoza, Spain

³Terralogica AB, Östra Annekärrsvägen 17, SE-443 72 Gråbo, Sweden

⁴Conterra AB, Fridhemsgatan 66B, SE-112 46 Stockholm, Sweden

⁵Geosigma AB, Enstigen 10, SE-740 20 Vänge, Sweden

⁶Swedish Nuclear Fuel and Waste Management Co. (SKB), Box 3091, SE-169 03 Solna, Sweden

⁷Swedish Nuclear Fuel and Waste Management Co. (SKB), Vega Site Office, Stora Asphällan 4, SE-742 94 Östhammar, Sweden

Correspondence should be addressed to María J. Gimeno; mjgimeno@unizar.es

Received 9 May 2019; Revised 2 January 2020; Accepted 22 February 2020; Published 3 August 2020

Guest Editor: Delphine Roubinet

Copyright © 2020 Ann-Chatrin Nilsson et al. This is an open access article distributed under the Creative Commons Attribution License, which permits unrestricted use, distribution, and reproduction in any medium, provided the original work is properly cited.

The search by SKB (Swedish Nuclear Fuel and Waste Management Co.) for a site to locate the deep geological repository for spent nuclear fuel in Sweden has involved geoscientific investigations at several locations since the 1970s. The objectives were to characterise geologically a bedrock volume as well as its hydrogeology and hydrochemistry. To acquire high-quality hydrogeochemical data, a complete system for groundwater sampling and analysis, as well as for interpretation strategies, has been developed through a continuous process of modification and refinement. Since the largest part of the Swedish bedrock is composed of granitoids, the site investigations had to adapt to the special difficulties of fractured crystalline rocks. This paper discusses the problems with groundwater sampling that are specific to fractured crystalline rocks and describes the solutions adopted and methods developed by SKB since the early 2000s during the site investigations. The methodology described in this paper for the characterisation of deep groundwaters in crystalline rocks is not only applicable in the context of radioactive waste disposal but also useful when sampling groundwaters for any purpose in such rocks. Sampling of groundwaters in fractured rocks at depth, often down to approximately 1,000 m, involves special challenges since the natural conditions of the groundwater are easily disturbed, especially by the initial drilling, but also by every subsequent activity performed in the borehole, including the actual groundwater sampling. The sampling strategy presented in this paper shows that planning of the sampling preferably starts already when the drilling procedure is decided. Each following step is described in detail and includes tracing the drilling fluid, selecting the best borehole sections to sample, procedures for the actual sampling, and selection of analytical protocol; all this with the goal of taking representative samples. Although the evaluation of the sampling uncertainties is not a straightforward procedure, an adequate categorisation routine has been established to classify groundwater samples regarding sample quality, representativeness, and suitability for further interpretations and modelling.

1. Introduction

The need for reliable groundwater sampling procedures has been recognised for years. The United States Geological Sur-

vey was one of the first institutions to publish rigorous sampling and analytical protocols and procedures [1–3]. Since then, and together with the United States Environmental Protection Agency, more detailed manuals of sampling

procedures, devices, techniques, etc. in different host rocks have been reported in various publications by these two organisations [4–15]. Along similar lines, other countries such as Australia and South Africa have recently published guidelines for groundwater sampling [16–20]. Nevertheless, the hydrogeochemical characterisation of groundwaters remains a challenging task [21–23].

In crystalline rocks, where groundwater flow is dependent on the fracture systems, the heterogeneous hydrogeological conditions imposed by the fractures and fracture zones result in a very inhomogeneous distribution of groundwater compositions. Therefore, in these environments, in addition to the usual groundwater sampling problems, it is necessary to monitor simultaneously the hydraulic pressure during sampling, in order to establish unambiguously that the groundwater sample represents the fractures intersecting the sealed-off borehole section [9]. In this way, the samples from boreholes drilled into intact rock will represent undisturbed conditions while sampling in boreholes close to a tunnel should give information on the disturbed system (often influenced by drawdown and/or artificial mixing).

In Sweden and Finland, deep geological disposal of spent nuclear fuel is being planned in fractured rock at approximately 400 to 500 m depth [24–28]. The planning for this type of repositories requires the characterisation of groundwaters in sparsely fractured rocks to depths down to ~1,000 m [29]. The aim of this paper is to provide insights in the difficulties of groundwater characterisation for such systems, and the solutions adopted within the site characterisation program conducted by the Swedish Nuclear Fuel and Waste Management Co. (SKB). The present paper therefore fills in the gap between technically detailed reports from SKB (available at <http://www.skb.com/publications>) and the peer-reviewed publications in the open literature, which concentrate on interpretation and modelling aspects, for example, [30–43]. This paper also is aimed at providing an overall picture of those aspects of geoscientific site investigations that have implications on the quality and the performance of the hydrogeochemical studies in fractured crystalline bedrocks, e.g., drilling technique and execution and investigation sequence.

One must emphasise that the techniques described here-with are the result of large efforts during a relatively long period of time (since the middle of the 1970s) by several organisations dedicated to the disposal of radioactive wastes around the globe. It is not the purpose of this paper to provide a detailed historical account of the developments in the field of groundwater characterisation in fractured rocks; however, the interested reader may find a short account in the Supplementary Material 1.

2. Investigations in Boreholes: Effects on the Representativity of Groundwater Samples

2.1. The Sequence of Borehole Drilling and Investigations. Investigations in deep groundwater systems imply borehole drilling followed by logging and sampling activities which, in fractured crystalline rocks, normally result in the mixing of groundwaters from different depths. As a consequence,

this can cause a variety of physical processes and chemical reactions that impact the representativity of the water samples.

To avoid disturbances in the system and to obtain as much useful information as possible, drilling and borehole investigations have to be carefully planned to follow a systematic sequence of proven strategies. A close cooperation among different disciplines is also needed during the planning and execution of the field work (and subsequent interpretations). A general investigation sequence is shown in Figure 1.

2.2. The Drilling. Drilling is one of the most important activities within the scope of site investigations for a deep repository, and its performance is of particular importance in order to achieve high-quality groundwater samples and representative measurements from the boreholes. The boreholes can be either percussion drilled or core drilled.

Percussion drilling is the faster and cheaper technique used to supplement and increase the number of sampling locations as well as to provide boreholes with diameters between 200 and 250 mm. The technique is restricted to relatively short boreholes in the range of 50 to 300 m. No flushing water is used for the drilling, and no drill cores are obtained since the rock is crushed.

Core drilling is used for deeper boreholes down to around 1,000 m depth or when information from a drill core is required for specific studies like mapping and sampling of fractures, of rock types, and of fracture infills. In the case of the site investigations performed by SKB, flushing water without recirculation is used to cool the drill bit and no-drill mud or lubricants are used to avoid unnecessary contamination. After the late 1980s, most core boreholes drilled by SKB from the ground surface are of the so-called telescopic type: the first 100 m correspond to a wider percussion-drilled borehole, followed by a core-drilled hole with a smaller diameter (76–77 mm). This technique was developed specifically for hydrochemical investigations. It allows efficient gas-lift pumping from the upper percussion-drilled part of the borehole during and after core drilling. This pumping decreases the amount of flushing water and of drilling debris which, otherwise, would be forced into conductive bedrock fractures by the high pressure prevailing during drilling. This type of borehole also allows the installation of standpipes to facilitate groundwater head measurements and sampling during the following long-term hydrochemical monitoring phase (Section 3.3).

In the case of boreholes drilled from tunnels, the conventional core or percussion drilling techniques are used. The telescopic design is not necessary since there is no need for standpipes or pumping during groundwater sampling. The water from the borehole is discharged during drilling and sampling due to the difference between the pressure in the bedrock and the atmospheric pressure in the tunnel.

Different equipment and investigation methods are in general required for the different borehole types, and they will be indicated in the corresponding sections of this paper. The most extensive hydrochemical investigations are performed in telescopic core boreholes, and their drilling protocol includes the following:

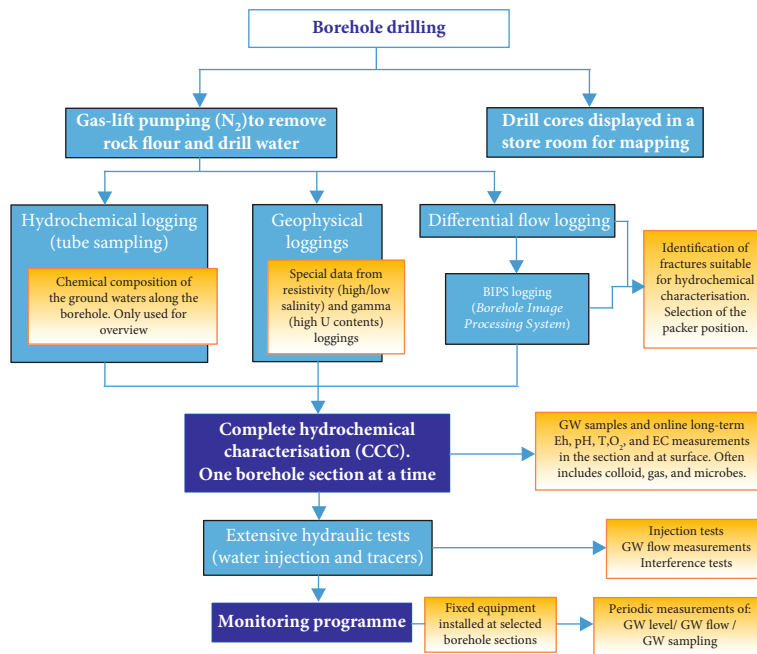


FIGURE 1: Schematic overview of a general investigation sequence in a telescopic core-drilled borehole designed for chemical characterisation. The most important hydrochemical sampling methods (Complete Chemical Characterisation, i.e., CCC, and monitoring) are shown in boxes with a darker blue colour and text in bold. GW: groundwaters; Eh: redox potential; T: temperature; EC: electrical conductivity. A more detailed description can be found in Supplementary Material 2.

- (i) The flushing water is spiked with a tracer (e.g., sodium fluorescein), and it is discharged as return water (i.e., a mixture of flushing water, formation groundwater, and drill cuttings) by gas-lift pumping during drilling. Due to contamination risks, the selection of the flushing water source and the possible impact of the flushing water on the groundwater composition are important issues that are discussed in more detail in Supplementary Material 2.
- (ii) The downhole drilling equipment and the flushing water system require a strict routine of cleanliness (more details can be found in Supplementary Material 2).
- (iii) The percussion drilled part of a telescopic borehole is cased, and the gap between the borehole wall rock and the casing is grouted with cement to prevent groundwater inflow from the upper part to the lower core-drilled borehole part during drilling.
- (iv) Grooves are milled into the borehole wall at certain intervals for length calibration to ensure reliable depth readings.
- (v) The use of a triple tube system is indispensable for preserving the fracture infillings (in the extracted drill cores) whose study, among other things, will facilitate the correlation of transmissive fractures with the flow log and the BIPS (Borehole Image Processing System, cf. Section 2.3.2).

2.3. Sampling Conditions: When, Where, and How

2.3.1. When to Sample. The time delay between drilling and chemical sampling is an important factor affecting the representativity of groundwater samples. Sampling close in time to the completion of the borehole may result in groundwater samples still impacted from the drilling, i.e., flushing water and groundwaters from different depths, introduced by the pressure impact during drilling. However, the problem could be even more serious if a borehole is kept open for some time without packers installed between the different hydraulically conductive fractures. In an inflow area, large volumes of shallow water are likely to intrude from fractures in the upper part of the borehole down to greater depths and mix with deeper groundwaters, and microbial activity and sulfide production could be promoted [44, 45], which drastically decreases the representativity of the groundwater samples.

For similar reasons, groundwater sampling should be avoided when activities such as drilling or hydraulic tests are ongoing in the vicinity of the borehole.

2.3.2. Where to Sample: Selection of the Borehole Sections. The main criteria for the selection of the borehole sections are (1) presence of one or more fractures with a suitable hydraulic transmissivity, (2) appropriate borehole wall conditions (less fractured rock) that allow isolation of the section by inflatable packers, and (3) favourable distribution of the water yielding fractures in the isolated borehole section to facilitate the removal of water in the section prior to sampling (Figure 2).

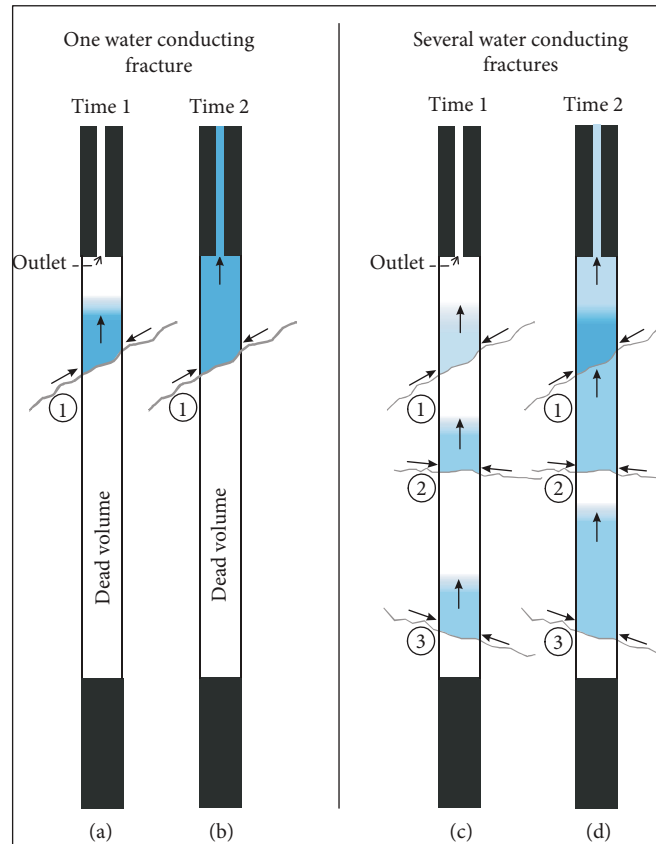


FIGURE 2: Schematic drawing of two different situations of the water yielding fractures in an isolated borehole section (modified from [49]). The blue colour intensity illustrates the amount of formation groundwater in the borehole section during pumping. The presence of a single water-bearing fracture in the upper part of the borehole section, close to the outlet of the section (fracture ^① in (a) and (b), on the left part of the figure), is a favourable situation since the rest of the water volume beneath the fracture will stay trapped, regardless of the removed amount of water from the borehole section (i.e., the lower part of the isolated section is a dead volume). Figure (a) illustrates the moment shortly after pumping starts (time 1) when the water from the only fracture has not reached the outlet yet. Figure (b) shows that after a while (time 2) all the water leaving the section is formation groundwater. If there are several fractures in the section ((c) and (d) in the right part of the figure), the section water between the fractures will contribute to the sample until the formation groundwater from the deepest fracture reaches the outlet: shortly after pump starts (c), no formation water has reached the outlet yet; after a certain time (time 2 in (d)), formation groundwater from fracture ^① has reached the outlet and formation groundwater from fracture ^② has passed fracture ^①; however, formation groundwater from fracture ^③ has not yet reached fracture ^② and the section water between fractures ^② and ^③ will still contribute to the sample. In this last case, the water volume that should be extracted prior to collecting a representative sample of the isolated borehole section may become unrealistically long.

The selection of water yielding fractures and the isolation of the borehole sections are based on the information provided by the flow logging [46, 47] and the BIPS [48]. In core-drilled boreholes, the differential flow logging method is especially useful. This method gives better information on the location of the water yielding fractures than other methods, and it also helps to estimate the groundwater volumes to be extracted prior to sampling. The BIPS logging is helpful to locate suitable packer positions and to identify each water-yielding fracture.

Borehole sections including fractures with moderate hydraulic transmissivities (around $10^{-7} - 10^{-8} \text{ m}^2 \text{ s}^{-1}$) or isolated borehole sections close to the bottom of the borehole are preferred from a practical point of view. In both cases, the amount of flushing water and/or water from other parts of the borehole, intruded into the fractures

during drilling, will be less either because of the low transmissivity or because the drill bit has stayed a shorter time in the lower part of the borehole. This lower amount of drilling fluid in the fractures will shorten the time needed for purging prior to sampling. Hydraulic transmissivities lower than $10^{-8} \text{ m}^2 \text{ s}^{-1}$ require special equipment and sampling methods, cf. Section 3.2.

Once the water yielding fracture(s) have been selected, the next important step is to optimise the position of the packers: (1) in order to decrease the required volume of water (Figure 2) to be exchanged prior to sampling and (2) to obtain a fully isolated borehole section without short circuits between the section and the borehole water above and/or below the section. The latter can be checked by observing the pressure responses in other parts of the borehole during pumping.

2.3.3. *How to Create Adequate Sampling Conditions.* Essential for the sampling procedure is (1) the evaluation of the contribution of flushing water from the drilling, (2) the adequate exchange of water from the borehole sections prior to sampling, and (3) the check of pressure responses in other parts of the borehole (or other boreholes in the vicinity) to exclude short-circuiting effects. Well-documented sampling conditions considering these aspects are important to facilitate the data evaluation during later stages of the site investigation.

The discharge of water prior to sampling is necessary to remove (1) the drilling debris and the remains of flushing water from the drilling and (2) the water initially present in the borehole section (section water). With respect to the flushing water, the calculation of its contribution requires a good homogeneous mixing of the tracer dye in the drilling fluid and frequent analyses of the tracer. The limit for the flushing water content for the best quality data in the SKB site investigations has been set to 2%; however, up to 10% may be considered acceptable if the groundwater data for such samples are used with care. The main problem associated with this task is the often long time needed to reach low enough flushing water content in the samples. With respect to the section water, its removal is needed to exchange the initial mixture of waters present in the borehole section. This water mixture may originate from different fractures at varying depths along the borehole, and in the case of monitored sections, the water may be affected by the stagnant conditions of the isolated section (e.g., microbial activity and corrosion, Section 3.3). The general recommendation to remove approximately five volumes of the sampled section [50] may be valid in the case of porous media but not for crystalline bedrock where the required purged volume is often larger. Individual discharge volumes for each section are calculated using plug flow estimations. These calculations consider the number of water yielding fractures, their hydraulic transmissivity, and their location in the isolated borehole section (Figure 2), and at least two plug flow volumes are discharged to compensate for the unknown contribution from laminar flow.

Finally, three ways to secure adequate sampling conditions are (1) checking the absence of pressure responses in other parts of the sampled borehole or adjacent boreholes, (2) estimation of the sampling-day hydraulic transmissivity (based on flow rate and pressure measurement during sampling) which can be compared with the hydraulic transmissivity values obtained from differential flow logging, and (3) collection of sample series of minimum three samples (if possible) to check their hydrochemical behaviour with time.

3. The Hydrogeochemical Sampling Methods

3.1. *Available Methods.* The hydrogeochemical investigations conducted by SKB involve groundwater sampling and measurements and analyses of different parameters (chemical and isotopic composition, electrical conductivity, Eh and pH, colloids, dissolved gas, and microbes). Some special topics such as matrix pore water, fracture mineralogy, microbes and gases, and new methods for detailed studies on isotopic

zoning in minerals, that require other types of sampling and treatment, have been described thoroughly elsewhere [30–41]. Archive samples are collected for back-up in case of failures or possible later need of additional analyses/constituents. Different groundwater sampling methods have been used for different purposes as summarised below.

- (i) Hydrochemical logging (tube sampling) with the purpose of obtaining the composition of the groundwater present along the borehole. A tube consisting of connected 50 m long tube sections is used for the sampling, and each 50 m section constitutes one sample. This type of sampling provides only an approximate characterisation of the depth dependency of the geochemical characteristics of the groundwaters.
- (ii) Comprehensive groundwater characterisation (also known as *Complete Chemical Characterisation*, CCC) is the premium type of sampling carried out on carefully selected transmissive structures in core boreholes based on flow and core logging (Section 2.3.2). A special sampling unit can be combined with parts of the equipment for CCC for the sampling of low transmissive fractures ($T < 10^{-8} \text{ m}^2 \text{ s}^{-1}$; Section 3.2).
- (iii) Long-term hydrochemical monitoring in core and percussion boreholes to study the evolution of the groundwater composition over time (several years; Section 3.3).

The data obtained with the tube sampling method are mainly used for initial discussion and to allow the comparison with the hydrochemical data obtained later. Even not being suitable for modelling purposes, these data may be useful for the understanding of the borehole hydraulic conditions and its evolution with time. The last two methods, including the special equipment used for sampling of low transmissive fractures, are described in more detail below.

3.2. *The CCC Sampling Method.* Among all the sampling methods used by SKB, the Complete Chemical Characterisation (CCC), developed during the 1980s [51, 52] and further improved during the first decade of the 21st century [53], involves the most extensive sampling schemes and the most advanced equipment (Figure 3). The method is almost exclusively used in core boreholes where more information on structural geology and on hydrogeology is available compared to the percussion boreholes. The equipment can be used in boreholes from the ground surface (preferably telescopic boreholes) or from vertical and subvertical boreholes in tunnels. It comprises an integrated system for (1) sealing off a borehole section by inflatable packers and pumping of groundwater from the section, (2) sampling of pumped groundwater as well as sampling *in situ* (downhole in the section) to obtain groundwater samples at maintained pressure, and (3) online long-term measurements (weeks to months) of the chemical and

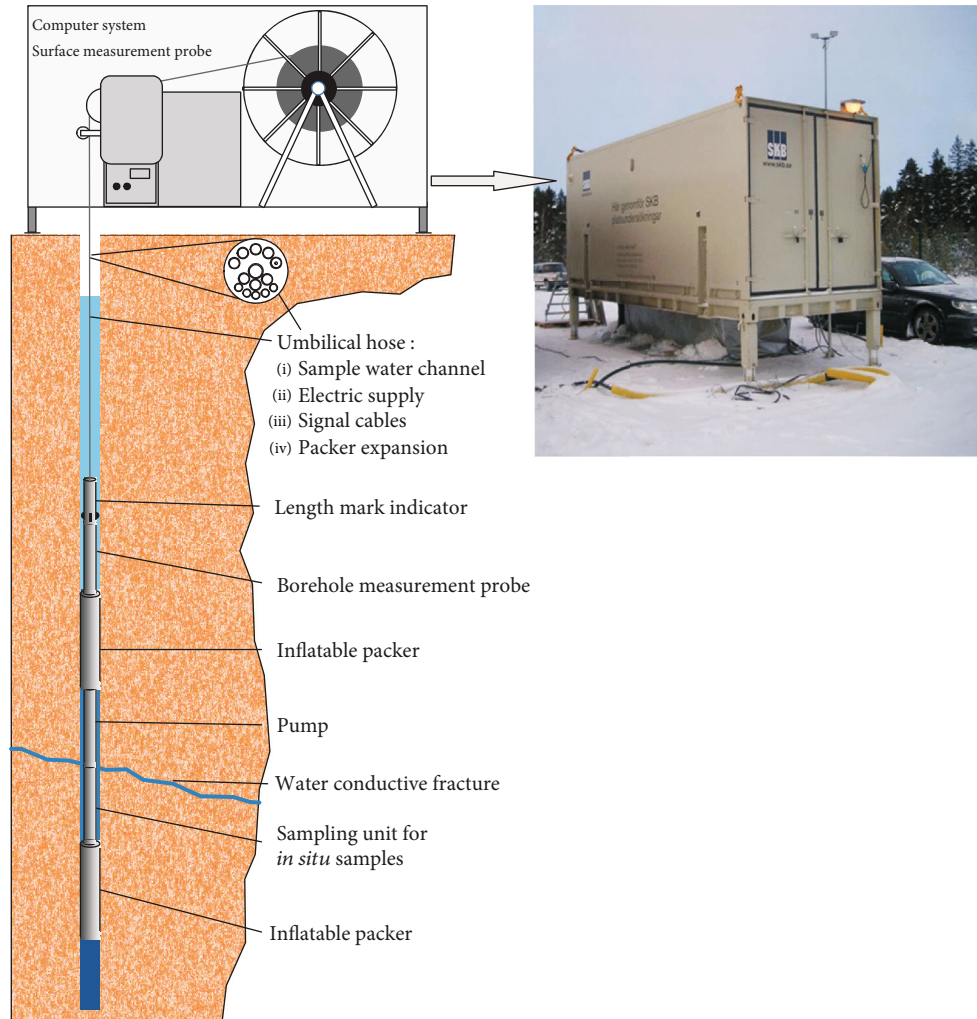


FIGURE 3: Outline of the integrated system comprising a carriage/container with downhole equipment (umbilical hose, inflatable packers, pump, downhole measurement probe, and downhole sampling unit) and facilities for lowering and raising this equipment. This system is placed over the borehole (see photo), and the container's indoor temperature is adjusted to maintain the temperature of the groundwater in the section to be investigated.

physicochemical parameters Eh (redox potential), pH, dissolved O_2 , EC (electrical conductivity), and T (groundwater temperature), both at the surface and at depth downhole (measurement probe in Figure 3).

The CCC sampling campaigns usually start as soon as the preceding logging activities (Figure 1) are finished which may take one or two months after the completion of drilling. The lengths of the packed-off borehole sections are often around seven meters, but they can also be shorter (from 0.5 m) or longer (up to approximately 15 m). The CCC investigations are performed in one borehole section at a time. Initially, the downhole equipment is internally rinsed and filled with deaerated and deionised water before use. The outside of the equipment and the hose is cleaned/wiped using 70% ethanol (being careful not to introduce it to the borehole since it may promote microbial activity) while being lowered into the borehole. Despite this cleaning, sterile equipment cannot be expected, and foreign microbes may anyhow be introduced into the borehole.

Finally, all surfaces in contact with the water sample are composed of either polyamide or high-quality stainless steel, and lubricants (Teflon spray or Vaseline) are used sparsely on O-rings in valves and other connections.

The water is pumped to the ground surface through the downhole equipment and then through the polyamide tube housed in the umbilical hose (Figure 3). The first sample in the series is collected when the groundwater from the section reaches the surface. This sample is important to understand the conditions in the borehole section (considering, for example, sulfide or organic carbon concentrations) before exchanging the section water to obtain representative groundwater samples from the bedrock formation (Sections 2.3.2 and 2.3.3). Experience shows that pumping flow rates of around 100 to 250 mL/minute are preferred to avoid unnecessary particle release and to optimise the function of the *in situ* flow-through cell in the borehole section. If the water yield is low, care has to be taken to avoid that the drawdown creates any leakage between the isolated section

being sampled and the rest of the borehole (the already mentioned pressure measurements in the borehole section and above it will help to control this; Section 2.3.2).

Online regular logging of pH, Eh, dissolved oxygen, electrical conductivity, and groundwater temperature starts as soon as the packers are inflated, and the pumping has started. Once the water is at the surface, sample portions are collected regularly for analysis during pumping (usually for a period of three weeks or until stable Eh readings are obtained).

The sample series of groundwater collected by the CCC method are of the best possible quality and include the most complete set of analyses as well as supporting information. Moreover, the series allow verification of stable conditions and identification and exclusion of single outliers. At the end of the pumping period, *in situ* samples (maximum four samples), maintaining the pressure from the borehole section, are enclosed in their containers and then lifted to the ground surface together with the rest of the equipment. These samples are used for gas analyses, as well as microbial and colloid determinations.

A variation of the CCC method was developed in order to sample low transmissive fractures ($T < 10^{-8} \text{ m}^2 \text{ s}^{-1}$). These fractures are important since they are likely to contain groundwaters representative of those associated with the bedrock volumes where the spent nuclear fuel repository will be located in the future.

The special sampling unit for low transmissive fractures, to be used with the umbilical hose of the CCC equipment, consists of (a) inflatable packers delimiting a borehole section of a fixed length of one metre (instead of adjustable length of up to 15 m); (b) a dummy, whose surface is coated with Teflon, that is mounted in between the packers to reduce the water volume in the section to 0.3 L (absent in the standard sampling unit); and (c) a single sample container (1.2 L) connected to the sampling section but placed above the upper packer, outside the section. The water is sucked into the evacuated sample container. The filling of water is recorded by a pressure sensor. Once the sampling is finished, the equipment is raised to the ground surface and the water is portioned into bottles and sent for analysis.

3.3. Monitoring. The main aim of the hydrogeochemical monitoring is to create a long time series of data to study the evolution of the composition of the groundwaters with time. Apart from obtaining base-line data covering the normal variations, monitoring is essential to study the impacts of the construction and operation of a facility at a later stage.

After completion of the general investigation activities in a borehole (Figure 1), packer equipment is installed to allow continuous pressure measurements (up to ten sections) as well as regular flow measurements and groundwater sampling (up to two sections). Besides packers, boreholes drilled from the ground surface also require standpipes in the upper part of the borehole that are connected to each section at depth (Figure 4). Only telescopic and percussion boreholes allow these standpipe installations due to the required diameter. In addition to the possibility of long-term evaluation of the pressure and the major groundwater chemistry (and environmental iso-

topes, $\delta^2\text{H}$, ^3H , and $\delta^{18}\text{O}$), the packer system prevents undesired short-circuiting effects that would occur if boreholes were kept open.

Tunnel boreholes are also monitored. The design of the equipment in these boreholes is basically similar although there are no standpipes since no pumping is needed to discharge the groundwater due to the hydrostatic pressure.

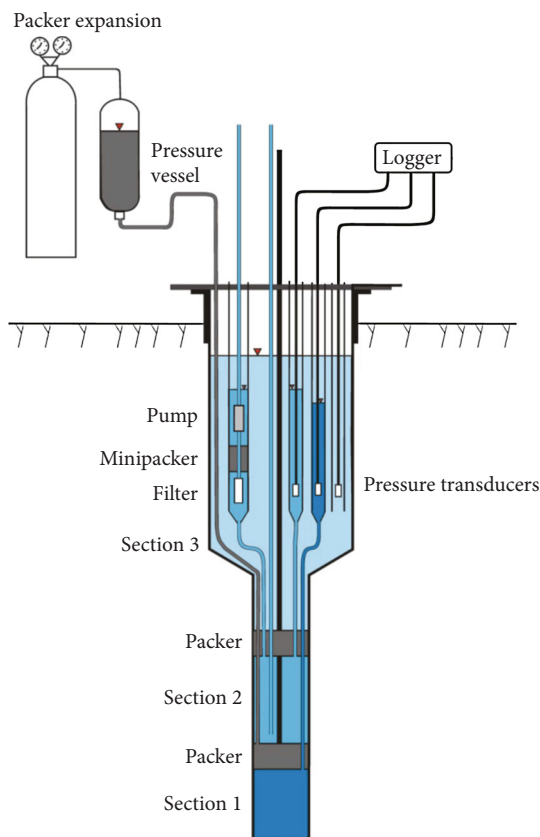
Hydrochemical monitoring includes the collection of sample series (minimum of three samples) during continuous pumping/discharge at each sampling occasion. As indicated above (Section 2.3.3), individual plug flow volumes are calculated for the monitored sections to estimate the volume of water needed to be discharged. This is particularly important in this case since the long contact time between the water isolated in the section and the installed borehole equipment may promote contamination, microbial activity, sulfide production, and corrosion. All this may have consequences on pH, organic carbon content, and trace- and redox-sensitive elements. Other sources of contamination are the biological remains (biofilm, pollen, insects, etc.) that are introduced into the standpipes between sampling occasions. With time, these contaminants will reach the isolated sections. Finally, the lowering and raising of equipment in the standpipes create pressure differences and water movements that may propagate down to the connected borehole section and promote contamination. Taking all these conditions into consideration, the recommendation is to omit (or consider with caution) the analysis of the monitoring data for the more sensitive geochemical parameters/constituents.

Besides the impact on sensitive constituents, monitored boreholes from the surface are also unsuitable for Eh measurements as the equipment cannot be lowered into the borehole due to the fixed packer system. Additionally, the system with standpipes does not allow completely oxygen-free operation (Figure 4).

4. Analyses and Measurements

4.1. Groundwater Chemical Components and Isotopes. Analytical programmes are designed to provide information/data for different purposes: (1) to describe the distribution, age, and geochemical evolution of groundwaters of different origins in the bedrock, (2) to complement the hydrogeological information in order to characterise the flow paths of the water and validate the hydrogeological models and *vice versa*, and (3) to evaluate some of the safety indicators in the repository performance assessment (pH, Eh, colloids, organic compounds, microbes, nitrogen compounds, sulfide, sulfate, inorganic carbon, phosphate, and total salinity).

The analytical protocol for groundwater analyses has included the same basic components and parameters since the beginning of the 1980s: major constituents, nutrient salts, and other anions of lower concentrations, DOC and TOC (dissolved and total organic carbon concentrations, respectively), trace metals, and stable and radioactive isotopes [54]. The list of isotopes in the early days contained $\delta^2\text{H}$, $\delta^{18}\text{O}$, ^3H , ^{14}C (percent modern carbon, pMC), and $\delta^{13}\text{C}$ on inorganic carbon, and a few have been added more recently, especially during the site investigations in Forsmark and



(a)



(b)

FIGURE 4: (a) Installed equipment for pressure, groundwater sampling, and groundwater flow monitoring in a telescopic borehole. A maximum of 10 pressure sections can be installed in a telescopic borehole, of which generally two are equipped for water sampling and circulation of tracers during flow measurements. These circulation sections are connected to three tubes. Two of them connect the section to the two standpipes for pressure measurements and groundwater sampling (the wider pipe), respectively, in the uppermost part of the borehole. The third tube leads all the way to the ground surface for the circulation experiments. (b) Lowering of a pump connected to a minipacker (for isolating the standpipe from the atmosphere) and a $50\ \mu\text{m}$ filter (polyamide) into a large diameter standpipe. To collect samples, pumping is conducted in the closed standpipe (cf. (a)); when the pressure decreases, groundwater from the connected borehole section is sucked into the standpipe and pumped to the ground surface. Modified from [48].

Laxemar ($^{10}\text{B}/^{11}\text{B}$, $^{87}\text{Sr}/^{86}\text{Sr}$, $\delta^{37}\text{Cl}$, $\delta^{34}\text{S}$, ^{36}Cl , and ^{14}C (pMC) and $\delta^{13}\text{C}$ on organic carbon). This list of analyses reflects the full protocol, but it is only used for some of the collected samples depending on the nature of the boreholes, types of samples, and/or the aims of the investigation.

Different sample classes are established to define the parameters to be included in the analytical protocol as well as the adequate sampling procedures and sample treatments. The lowest classes include basic measurements and analyses (pH, electrical conductivity, chloride, and alkalinity). An intermediate class includes the main chemical components and some of the isotopes. Sampling according to the highest classes demands trained personnel and specialised equipment since these classes comprise, in addition, components that need online filtering and/or special conservation/treatment of the water sample (trace elements, redox-sensitive components, and additional isotopes).

Analyses that need to be conducted soon after sampling (Fe^{2+} , Fe-tot , NH_4 , HCO_3^- , and lab-pH) are conducted onsite. In addition, Cl^- , EC, HS^- , and ion chromatographic (IC) determinations of SO_4^{2-} , Br^- , and F^- are generally per-

formed by SKB but not necessarily at the investigation site. Besides IC, the analyses performed by SKB laboratories are conducted by spectrophotometric, titrimetric, and potentiometric methods (additional methods, such as ICP, are conducted in external laboratories; see Supplementary Material 1; Table SM3-1). Most analyses and sample treatments (filtration, conservation, storage, etc.) follow standards from the Swedish Standards Institute (SIS) and from the Comité Européen de Normalisation (EN) or from the US Environmental Protection Agency (USEPA), but in some exceptional cases, suitable standards are missing (e.g., Fe^{2+}). Calculation of measurement uncertainties is made according to the EUR-ACHEM/CITAC guide [55].

4.2. Measurements of Eh and pH In Situ and at Ground Surface. Reliable and plausible Eh measurements at the very negative range observed for deep groundwaters [30] require optimal conditions from several aspects. For example, the smallest diffusion of oxygen into the measurement system will have a significant impact on the results. Furthermore, the most useful pH measurements for hydrogeochemical

modelling are those performed with maintained *in situ* (downhole) pressure and temperature. The CCC method (see Section 3.2) offers the best possibilities to meet these demands in telescopic core-drilled boreholes. However, a simplified equipment can also be used in tunnel boreholes. In this case, a flow-through cell is used, preferably located as close as possible to the opening of the borehole (to avoid oxygen diffusion through tubing, valves, and connections) and kept either at a pressure similar to the borehole section pressure or at atmospheric pressure, depending on the equipment.

The CCC method includes simultaneous measurements of Eh and pH at depth as well as in a flow-through cell at the ground surface. Three different redox electrodes (platinum, gold, and glassy carbon) measure Eh, and one or two glass electrodes are used for pH at each location (borehole and surface flow-through cells, respectively). Agreeing measurements by the different types of redox electrodes indicate stable conditions and reliable values. The logging continues until the parameters stabilise [30], and for Eh, this may take up to four weeks depending on the time needed to remove the very small amounts of oxygen initially present in the equipment.

The reference electrode for the Eh and pH measurements is of the Ag/AgCl, double junction type. The downhole reference electrodes and the glass (pH) electrodes are specially designed by SKB to stand high pressures by allowing compression of the electrolyte volume. The electrodes used at the surface are all commercially available. The electrical ground in the probes is galvanically isolated from earth.

With respect to the pH measurements, apart from those performed in the field together with the Eh, pH is also measured in the laboratory at 25°C (batch). The possibility of comparing different measurements to evaluate reliability has been proven to be important.

5. Data Quality Evaluation

5.1. Data Quality Control Sequence. The chemical data (analytical results and measured values) from different sources are checked in several steps before they are used in interpretations and modelling work.

- (1) First screening at the investigation site is important since it is conducted close in time to the sampling and analyses and by personnel familiar with the sampling and analytical performance. This screening involves charge balance calculations, simple consistency checks (Section 5.2), and judgments based on experience and previous results. In the case of questionable data, there is still the possibility of repeating analyses at this stage.
- (2) A further check is performed when the data are entered into SKB's geoscientific database, mainly to confirm correct entries by signing the quality check for each sample record. Further control is added by plotting large amounts of data in x - y scatter plots to check for trends and outliers.
- (3) Finally, when the dataset is delivered for hydrochemical interpretation and modelling, the quality of

the data is assessed with respect to sample representativity. At this stage, more information is available (a larger dataset, complete isotope data, hydrogeological and geological interpretations, etc.) allowing representativity assessments based on an integrated hydrochemical, geological, and hydrogeological approach (Section 5.3).

5.2. Consistency Checks. Some basic consistency checks are performed prior to inserting the data in the database. The usual checks are described below:

- (i) Comparison of the measured electrical conductivity (EC) with the concentration of the dominating dissolved ion (chloride in most of the Fennoscandian groundwaters) in order to discover outliers. Since the dominating ion contributes the most to the electrical conductivity, the comparison should result in a close to a straight line in the relevant salinity range for the considered deep groundwaters [56–58].
- (ii) Charge imbalance calculations provide verification of reliable major components. The acceptable range is set to $\pm 5\%$; however, in the case of dilute waters ($\text{Cl} < 50 \text{ mg/L}$), a range of $\pm 10\%$ is tolerable. Charge imbalances outside these limits often require repeated analyses or repeated sampling.
- (iii) Comparison between the values obtained by different analytical methods. In the analytical routine followed by SKB, this applies to iron, sulfate, and uranium (the element and the U-238 activity) which are all routinely determined by two methods that are based on different principles.
- (iv) Bromide concentrations are plotted versus corresponding chloride contents to give a rough check of the plausibility of the bromide concentrations. Some correlation is usually found for the entire dataset also in the case of groundwaters with different origins (marine and nonmarine).

5.3. Categorisation of Samples according to Quality. The quality and representativity of groundwater data may be influenced by different factors, for example, contamination from drilling, different sampling methods, the hydraulic conditions in the borehole at the sampling occasion, and the analytical performance. After some initial strategies developed for groundwater data evaluation during the 1980s and 1990s (see the Supplementary Material 1), a more refined approach for quality categorisation was developed during the site characterisation of the Forsmark and Laxemar sites [54, 59, 60]. This was further developed during the more recent site characterisation for the extension of the SFR (the repository for low- and intermediate-level short-lived radioactive wastes) and the Äspö Underground Laboratory data evaluation [57, 61].

The objective of the categorisation is to assess the data quality by grading the set of data corresponding to a sampling occasion from 1 to 5 according to several quality

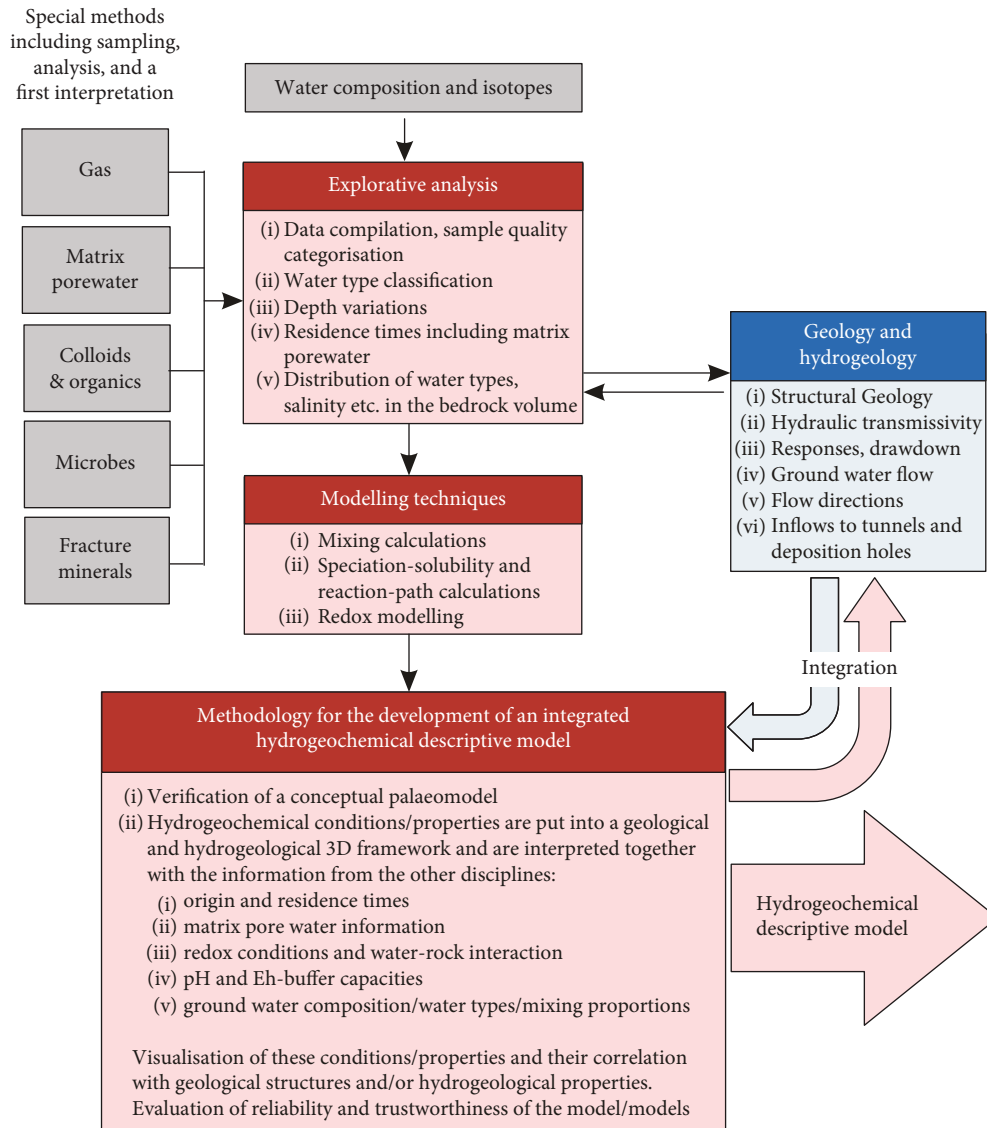


FIGURE 5: Schematic overview of the interpretation and modelling procedure to produce an integrated hydrogeochemical site model/description. Grey frames are used for hydrogeochemical input data. Blue colour indicates geological and hydrogeological methods and data flows, and red boxes indicate descriptive hydrogeochemical interpretation methods, generally performed with specific software.

criteria. Of these (1) is the highest quality, while quality (5) is not considered acceptable for modelling purposes (see Supplementary Material 3; Table SM3-2). The criteria include, for example, the flushing water content, the borehole section length, the hydraulic responses in other borehole sections or in other boreholes during sampling, and the possible concentration trends in sample time series.

The major reasons for performing this categorisation are to facilitate future interpretation and modelling work by providing well-structured data tables representing quality categorised data and also to guide users on how to select data for their purposes. Additionally, this evaluation is very useful to identify samples unsuitable for general modelling purposes (affected by experimental conditions, grouting, etc.). The first step for the categorisation needs to be a general overview of the dataset to establish the best categorisation criteria.

Once the data have been evaluated and categorised, they are ready to be used in the hydrogeochemical interpretation and modelling. The main objective is to use an integrated framework like the one shown in Figure 5 to produce a total conceptual hydrogeochemical model of the site (see some examples in [57, 62–65]).

6. Conclusions

The methodology developed by SKB for the characterisation of deep groundwaters in crystalline rocks has been based on forty years of experience and of collaboration with other international agencies and research institutions. This paper describes advances and improvements applicable to groundwater sampling, for any purpose, in crystalline rocks. The text also identifies the questions to be considered during data

interpretation for the hydrogeochemical characterisation of a crystalline bedrock system.

The sampling protocol emphasises the collection of hydrogeochemical data that accurately represent *in situ* conditions, minimising disturbances as much as possible and following quality assurance guidelines. However, it is important to keep in mind that no single method or procedure is universally applicable to all groundwater systems or to all types of groundwater sampling programmes. Therefore, the selection of appropriate sampling processes and equipment is vital to the success of any groundwater investigation. The same is applicable to the categorisation and quality assurance protocols, which are also site specific. The success of any site characterisation programme relies on a robust and comprehensive sampling protocol, coupled with proven analytical schemes, careful documentation, and the performance of quality assurance procedures.

Some general points/measures of importance in order to obtain representative groundwater samples of the best possible quality are as follows:

- (i) Planning of the hydrochemical investigations at an early stage, i.e., hydrochemical demands need to be considered already when preparing for the drilling of the boreholes.
- (ii) A thoughtful selection of borehole sections based on flow logging and BIPS data as well as specific hydrogeological evaluations to facilitate adequate sampling.
- (iii) Online measurements of Eh and pH, preferably *in situ* in the borehole section.
- (iv) Collection of sample time series to ensure hydrochemical stability.
- (v) Adequate data evaluation and quality check. Quality categorisation of data to provide guidance on their use for different purposes.

Finally, one of the most relevant issues to consider is the importance and usefulness of close cooperation and integration of hydrogeochemistry with other geoscientific disciplines, such as structural geology, hydrogeology, and geomicrobiology. This collaboration should start already during the planning and execution of the field work (and subsequent interpretations) in order to optimise the quality and the amount of information. The combination of different types of knowledge from all the geoscientific disciplines, ranging from field and laboratory studies to interpretation and modelling work, is the only way to obtain a final coherent and integrated understanding of the system.

Conflicts of Interest

The authors declare that they have no conflicts of interest.

Acknowledgments

This work has been conducted with the support of the Swedish Nuclear Fuel and Waste Management Company (SKB),

Stockholm. The experiences and ideas of the SKB personnel and consultants involved in the field and laboratory work at Forsmark and Äspö during the many years of investigations, in combination with talented technical solutions by contracted workshops (Maskinteknik AB in Oskarshamn and Geosigma Geoteknik AB in Uppsala), have resulted in the well-established methods and equipment of today. This research was fully financed by the Swedish Nuclear Fuel and Waste Management Co. (SKB), a company in charge of the safe disposal of the Swedish spent nuclear fuel and other radioactive wastes in deep geologic repositories. It is in SKB's interest to demonstrate the use of scientifically sound methods during site characterisations.

Supplementary Materials

There is one file with supplementary information associated with this article. Inside that file, 3 supplementary sections are included: Supplementary Material 1 gives a summary of the background on the development of this type of methodology worldwide in the context of radioactive waste disposal. Supplementary Material 2 describes in detail some additional issues related to the drilling and after drilling procedures, especially about the flushing water. Finally, Supplementary Material 3 includes two tables with detailed information on some methodological aspects related to Sections 4.1 and 5.3. Table SM3-1 lists the analytical protocol followed for the groundwaters, including the detection limits and the measurement uncertainties, and Table SM3-2 displays an example of cornerstone criteria that were found to be relevant independently of the type of dataset. (*Supplementary Materials*)

References

- [1] W. W. Wood, "Guidelines for collection and field analysis of groundwater samples for selected unstable constituents," *U.S. Geological Survey Techniques for Water Resources Investigations, Book 1, Chapter D-2*, 1976.
- [2] US Geological Survey, *National Handbook of Recommended Methods for Water-Data Acquisition*. USGS Office of Water Data Coordination, Reston, Virginia, 1977.
- [3] J. D. Hem, *Study and interpretation of the chemical characteristics of natural water*, Geological Survey Water-Supply Paper 2254, U.S., 1985.
- [4] M. J. Barcelona, J. P. Gibb, J. A. Hellfrich, and E. E. Garske, *Practical guide for ground-water sampling*, Environmental Protection Agency, EPA/600/2-85/104, U.S., 1985.
- [5] R. W. Gillham, M. J. L. Robin, J. F. Barker, and J. A. Cherry, *Groundwater monitoring and sample bias*. Department of Earth Sciences University of Waterloo, Prepared for Environmental Affairs Department, American Petroleum Institute, API Pub. 4367, June, Waterloo, Ontario, 1983.
- [6] M. T. Koterba, F. D. Wilde, and W. W. Lapham, *Ground-water data-collection protocols and procedures for the National Water-Quality Assessment Program—collection and documentation of water-quality samples and related data*, Geological Survey Open-File Report 95-399, U.S., 1995.
- [7] K. F. Pohlmann, C. Rosal, and B. Beldsoe, *Sample handling and analysis*. EPA Groundwater Sampling EPA/600/R-94/205, 94-98, 1993.

- [8] R. W. Puls and M. J. Barcelona, *Low-flow (minimal draw-down) ground-water sampling procedures*, Environmental Protection Agency, Ground Water Issue Report, EPA/540/S-95/504, U.S., 1996.
- [9] A. M. Shapiro, "Cautions and suggestions for geochemical sampling in fractured rock," *Groundwater Monitoring & Remediation*, vol. 22, no. 3, pp. 151–164, 2002.
- [10] US Environmental Protection Agency, *Subsurface Characterization and Monitoring Techniques: A Desk Reference Guide: Volume I: Solids and Ground Water Appendices A and B; EPA/625/R-93/003a*, 1993.
- [11] US Environmental Protection Agency, "Compendium of ERT groundwater sampling procedures," in *Report EPA/540/P-91/007, January 1991*, US Environmental Protection Agency, Washington DC, 1999.
- [12] US Geological Survey, *Characterizing ground-water chemistry and hydraulic properties of fracture-rock aquifers using the multifunction bedrock-aquifer transportable testing tool (BAT3). USGS Fact Sheet FS-075-01, August 2001*, 2001.
- [13] US Geological Survey, *National Field Manual for the Collection of Water-Quality Data*, Geological Survey Techniques of Water-Resources Investigations, book 9, chaps. A1–A9, U.S., 2005, January 2005, <http://pubs.water.usgs.gov/twri9A/>.
- [14] D. Yeskis and B. Zavala, *Ground-water sampling guidelines for Superfund and RCRA project managers*, Environmental Protection Agency, EPA 542-S-02-001, U.S., 2002.
- [15] D. Johnston, *Regulatory Monitoring and Testing Groundwater Sampling*, Draft EPA Guidelines, Environment Protection Authority, 2006.
- [16] J. M. C. Weaver, "Groundwater sampling: a comprehensive guide for sampling methods," in *Report TT 54/92*, Water Research Commission, Pretoria, 1992.
- [17] J. M. C. Weaver, L. Cave, and A. S. Talma, *Groundwater sampling. A comprehensive guide for sampling methods*, WRC Report No. TT 303/07, South Africa, 2007.
- [18] Murray-Darling Basin Commission, *Murray-Darling basin groundwater quality sampling guidelines, Technical Report No. 3, MDBC Groundwater Working Group, Commonwealth of Australia*, 1997.
- [19] Standards Australia, *AS/NZS 5667.1:1998 water quality—sampling—guidance on the design of sampling programs, sampling techniques and the preservation and handling of samples, standards Australia, New South Wales*, 1998.
- [20] V. E. P. Authority, *Groundwater Sampling Guidelines, Publication Number 669, (EPA Victoria), Melbourne*, 2000.
- [21] J. D. Pennino, "There's no such thing as a representative ground water sample," *Groundwater Monitoring & Remediation*, vol. 8, no. 3, pp. 4–9, 1988.
- [22] M. J. Barcelona, "Uncertainties in ground water chemistry and sampling procedures," in *Chemical Modeling of Aqueous Systems II*, D. C. Melchior and R. L. Bassett, Eds., pp. 311–320, American Chemical Society, Washington, D.C., 1990.
- [23] M. J. Barcelona, M. D. Varljen, R. W. Puls, and D. Kaminski, "Ground water purging and sampling methods: History vs. hysteria," *Groundwater Monitoring & Remediation*, vol. 25, no. 1, pp. 52–62, 2005.
- [24] P. Wikberg, K. Ahlbom, and O. Olsson, "Site investigations of potential repository sites in Sweden," in *Scientific Basis for Nuclear Waste Management XXVII*, V. M. Oversby and L. O. Werme, Eds., pp. 9–14, Materials Research Society (MRS), Warrendale, PA, 2004.
- [25] A. Ström, J. Andersson, K. Skagius, and A. Winberg, "Site descriptive modelling during characterization for a geological repository for nuclear waste in Sweden," *Applied Geochemistry*, vol. 23, no. 7, pp. 1747–1760, 2008.
- [26] N. Marcos, P. Hellä, M. Snellman et al., *The role of the geosphere in POSIVA's safety case. Stability and Buffering Capacity of the Geosphere for Long-term Isolation of Radioactive Waste: Application to Crystalline Rock. Workshop Proceedings Manchester, United Kingdom, 13-15 November 2007*, OECD Nuclear Energy Agency (NEA), Paris, France, 2009.
- [27] B. Pastina, J. Lehtikoinen, and I. Puigdomenech, "Safety case approach for a KBS-3 type repository in crystalline rock," *Proc. NEA-IGSC Workshop on cementitious materials in safety cases for geological repositories for radioactive waste: role, evolution and interactions*, OECD, Nuclear Energy Agency; NEA/RWM/R(2012)3, pp. 165–170, 2012.
- [28] J. Andersson, K. Skagius, A. Winberg, T. Lindborg, and A. Ström, "Site-descriptive modelling for a final repository for spent nuclear fuel in Sweden," *Environmental Earth Sciences*, vol. 69, no. 3, pp. 1045–1060, 2013.
- [29] J. A. T. Smellie, M. Laaksoharju, and P. Wikberg, "Äspö, SE Sweden: a natural groundwater flow model derived from hydrogeochemical observations," *Journal of Hydrology*, vol. 172, no. 1-4, pp. 147–169, 1995.
- [30] L. F. Auqué, M. J. Gimeno, J. Gómez, and A.-C. Nilsson, "Potentiometrically measured Eh in groundwaters from the Scandinavian shield," *Applied Geochemistry*, vol. 23, no. 7, pp. 1820–1833, 2008.
- [31] H. N. Waber and J. A. T. Smellie, "Characterisation of pore-water in crystalline rocks," *Applied Geochemistry*, vol. 23, pp. 1836–1861, 2008.
- [32] H. N. Waber, T. Gimmi, and J. A. T. Smellie, "Reconstruction of palaeoinfiltration during the Holocene using porewater data (Laxemar, Sweden)," *Geochimica et Cosmochimica Acta*, vol. 94, pp. 109–127, 2012.
- [33] L. Hallbeck and K. Pedersen, "Characterization of microbial processes in deep aquifers of the Fennoscandian shield," *Applied Geochemistry*, vol. 23, no. 7, pp. 1796–1819, 2008.
- [34] L. Hallbeck and K. Pedersen, "Culture-dependent comparison of microbial diversity in deep granitic groundwater from two sites considered for a Swedish final repository of spent nuclear fuel," *FEMS Microbiology Ecology*, vol. 81, no. 1, pp. 66–77, 2012.
- [35] H. Drake and E.-L. Tullborg, "Paleohydrogeological events recorded by stable isotopes, fluid inclusions and trace elements in fracture minerals in crystalline rock, Simpevarp area, SE Sweden," *Applied Geochemistry*, vol. 24, no. 4, pp. 715–732, 2009.
- [36] H. Drake, E.-L. Tullborg, J. Hogmalm, and M. Åström, "Trace metal distribution and isotope variations in low-temperature calcite and groundwater in granitoid fractures down to 1 km depth," *Geochimica et Cosmochimica Acta*, vol. 84, pp. 217–238, 2012.
- [37] H. Drake, M. Åström, E.-L. Tullborg, M. J. Whitehouse, and A. E. Fallick, "Variability of sulphur isotope ratios in pyrite and dissolved sulphate in granitoid fractures down to 1 km depth - evidence for widespread activity of sulphur reducing bacteria," *Geochimica et Cosmochimica Acta*, vol. 102, pp. 143–161, 2013.
- [38] B. Sandström and E.-L. Tullborg, "Episodic fluid migration in the Fennoscandian shield recorded by stable isotopes, rare earth elements and fluid inclusions in fracture minerals at

- Forsmark, Sweden,” *Chemical Geology*, vol. 266, no. 3-4, pp. 126–142, 2009.
- [39] B. Sandström, E.-L. Tullborg, J. Smellie, A. B. MacKenzie, and J. Suksi, *Fracture mineralogy of the Forsmark site. SDM-Site Forsmark. SKB Report R-08-102*, Svensk Kärnbränslehantering AB, Stockholm, Sweden, 2008.
- [40] E.-L. Tullborg, H. Drake, and B. Sandstrom, “Palaeohydrogeology: a methodology based on fracture mineral studies,” *Applied Geochemistry*, vol. 23, no. 7, pp. 1881–1897, 2008.
- [41] A.-C. Nilsson, K. Pedersen, B. Hallbeck, J. Johansson, and E.-L. Tullborg, *Development and testing of gas samplers in tunnel environments*, SKB R-16-16, Svensk Kärnbränslehantering AB, Stockholm, Sweden, 2017.
- [42] M. J. Gimeno, L. F. Auqué, P. Acero, and J. Gómez, “Hydrogeochemical characterisation and modelling of groundwaters in a potential geological repository for spent nuclear fuel in crystalline rocks (Laxemar, Sweden),” *Applied Geochemistry*, vol. 45, pp. 50–71, 2014.
- [43] J. B. Gómez, M. J. Gimeno, L. F. Auqué, and P. Acero, “Characterisation and modelling of mixing processes in groundwaters of a potential geological repository for nuclear wastes in crystalline rocks of Sweden,” *Science of The Total Environment*, vol. 468-469, pp. 791–803, 2014.
- [44] H. Drake, L. Hallbeck, K. Pedersen et al., *Investigation of sulphide production in core-drilled boreholes in Äspö Hard Rock Laboratory. Boreholes KA3110A, KA3385A and KA3105A*, SKB TR-13-12, Svensk Kärnbränslehantering AB, Stockholm, Sweden, 2014.
- [45] P. Wersin, P. Alt-Epping, P. Pitkänen et al., “Sulphide fluxes and concentrations in the spent nuclear fuel repository at Olkiluoto,” in *Posiva report 2014-01*, Posiva Oy, Eurajoki, Finland, 2014.
- [46] J. Komulainen, “Posiva flow log (PFL), tool for detection of groundwater flows in bedrock,” in *13th International Mine Water Association Congress – Mine Water & Circular Economy*, C. Wolkersdorfer, L. Sartz, M. Sillanpää, and A. Häkkinen, Eds., pp. 556–563, Lappeenranta University of Technology (LUT) Scientific and Expertise Publications, Lappeenranta, Finland, 2017.
- [47] J. J. Komulainen, T. Vaitinen, P. Picken, and E. Heikkinen, “Hydrogeological bedrock characterisation based on Posiva flow log measurement data,” in *11th ICARD/IMWA/MWD Conference 2018*, C. Wolkersdorfer, L. Sartz, A. Weber, J. Burgess, and G. Tremblay, Eds., pp. 654–659, International Mine Water Association, Denver, Colorado, 2018.
- [48] M. Stigsson, “Orientation uncertainty of structures measured in cored boreholes: methodology and case study of Swedish crystalline rock,” *Rock Mechanics and Rock Engineering*, vol. 49, no. 11, pp. 4273–4284, 2016.
- [49] A.-C. Nilsson, C. Berg, J. Harrström et al., “Hydrochemical monitoring of groundwaters and surface waters. Results from water sampling in the Forsmark area, January-December 2009,” *Forsmark site investigation. SKB P-10-40*, p. 224, 2010.
- [50] L. A. Richards, D. Magnone, B. E. van Dongen, C. J. Ballentine, and D. A. Polya, “Use of lithium tracers to quantify drilling fluid contamination for groundwater monitoring in Southeast Asia,” *Applied Geochemistry*, vol. 63, pp. 190–202, 2015.
- [51] F. Karlsson and P. Wikberg, “Some highlights on the isotope geochemistry studies within the Swedish research program on radioactive waste disposal,” *Applied Geochemistry*, vol. 2, no. 1, pp. 25–31, 1987.
- [52] P. Wikberg, “The natural chemical background conditions in crystalline rocks,” in *Scientific Basis for Nuclear Waste Management XI*, M. J. Apted and R. E. Westerman, Eds., pp. 373–382, Materials Research Society (MRS), Pittsburgh, Pennsylvania, 1988.
- [53] A. Bergelin, A. Lindquist, K. Nilsson, P. Wacker, and A.-C. Nilsson, “Hydrochemical characterisation in borehole KFM08D,” *Results from two investigated borehole sections at 669.7-676.8 m and 828.4-835.5 m. Forsmark site investigation. SKB P-07-190*, p. 107, 2007.
- [54] A.-C. Nilsson, “Laxemar site investigation: quality of hydrochemical analyses (DF version 2.3),” in *Background complementary hydrogeochemical studies. SKB Report R-08-111*, B. Kalinowski, Ed., Svensk Kärnbränslehantering AB, Stockholm, Sweden, 2009.
- [55] A.-C. Nilsson, “Forsmark site investigation: analytical uncertainties,” in *Background complementary hydrogeochemical studies. SKB Report R-08-87*, B. Kalinowski, Ed., Svensk Kärnbränslehantering AB, Stockholm, Sweden, 2008.
- [56] R. B. McCleskey, D. K. Nordstrom, J. N. Ryan, and J. W. Ball, “A new method of calculating electrical conductivity with applications to natural waters,” *Geochimica et Cosmochimica Acta*, vol. 77, pp. 369–382, 2012.
- [57] A.-C. Nilsson, M. Gimeno, E.-L. Tullborg, F. Mathurin, and J. Smellie, “Hydrogeochemical data report,” in *Site descriptive modelling Äspö SDM. SKB R-13-26*, Svensk Kärnbränslehantering AB, Stockholm, Sweden, 2013.
- [58] F. Visconti, J. M. De Paz, and J. L. Rubio, “An empirical equation to calculate soil solution electrical conductivity at 25 °C from major ion concentrations,” *European Journal of Soil Science*, vol. 61, no. 6, pp. 980–993, 2010.
- [59] J. Smellie, E.-L. Tullborg, A.-C. Nilsson et al., “Explorative analysis of major components and isotopes,” in *SDM-Site Forsmark. SKB Report R-08-84*, Svensk Kärnbränslehantering AB, Stockholm, Sweden, 2008.
- [60] J. Smellie and E.-L. Tullborg, “Quality assurance and categorisation of groundwater samples from the Laxemar-Simpevarp area,” in *Background complementary hydrogeochemical studies. SKB Report R-08-111*, B. Kalinowski, Ed., Svensk Kärnbränslehantering AB, Stockholm, Sweden, 2009.
- [61] A.-C. Nilsson, E.-L. Tullborg, J. Smellie et al., “SFR site investigation,” in *Bedrock Hydrogeochemistry. SKB R-11-06*, Svensk Kärnbränslehantering AB, Stockholm, Sweden, 2011.
- [62] M. Laaksoharju, J. Smellie, E.-L. Tullborg et al., “Bedrock hydrogeochemistry, Forsmark,” in *Site descriptive modelling. SDM-Site Forsmark. SKB Report R-08-47*, Svensk Kärnbränslehantering AB, Stockholm, Sweden, 2008.
- [63] M. Laaksoharju, J. Smellie, E.-L. Tullborg et al., “Hydrogeochemical evaluation and modelling performed within the Swedish site investigation programme,” *Applied Geochemistry*, vol. 23, no. 7, pp. 1761–1795, 2008.
- [64] M. Laaksoharju, J. Smellie, E.-L. Tullborg et al., “Bedrock hydrogeochemistry Laxemar,” in *Site descriptive model, SDM-Site Laxemar. SKB Report R-08-93*, Svensk Kärnbränslehantering AB, Stockholm, Sweden, 2009.
- [65] J. Öhman, N. Bockgård, and S. Follin, “Bedrock hydrogeology,” in *Site Investigation SFR. SKB Report R-11-03*, Svensk Kärnbränslehantering AB, Stockholm, Sweden, 2012.

Research Article

Effect of Natural Fractures on Stress Evolution of Unconventional Reservoirs Using a Finite Element Method and a Fracture Continuum Method

Qiang Wang , Yongquan Hu , and Jinzhou Zhao 

State Key Laboratory of Oil-Gas Reservoir Geology & Exploitation, Southwest Petroleum University, Chengdu 610500, China

Correspondence should be addressed to Jinzhou Zhao; 201811000142@stu.swpu.edu.cn

Received 23 May 2019; Revised 16 November 2019; Accepted 25 November 2019; Published 27 December 2019

Guest Editor: Frédéric Nguyen

Copyright © 2019 Qiang Wang et al. This is an open access article distributed under the Creative Commons Attribution License, which permits unrestricted use, distribution, and reproduction in any medium, provided the original work is properly cited.

Refracturing, temporary plugging, and infilling well design play an important role in the development of reservoirs. The prediction of stress distribution can provide the basic guiding theory for the design and implementation of these techniques. In this paper, a fully-coupled three-dimensional production model based on the finite element method (FEM) and fracture continuum method (FCM) for naturally fractured reservoirs is presented to study the effects of fluid consumption on the reservoir stress. Furthermore, the effects of natural fractures on the stress re-distribution and stress re-orientation are also studied. The model also considers the influence of natural fractures on the permeability, and the effect of the effective stress on natural fracture openings, pore-elastic deformation, and fluid consumption. An analytical solution model and Eclipse were used for the comparison, which verifies the accuracy of the model results. Based on two cases of one cluster of fractures and three clusters of non-planar fractures, the research results revealed that natural fractures have a significant influence on the surrounding drainage, stress distribution, and stress re-orientation during the development. Under the influence of natural fractures, the production of the fluid along the direction of natural fractures is significantly easier, and it is highly probably that the insufficient consumption area is perpendicular to the direction of natural fractures. Compared with the conventional model, the stress distribution in the proposed model is deflected to a certain extent under the flow mode dominated by natural fractures, which is significantly prominent in the non-planar fracture model. Due to the effect of natural cracks, the absolute values of the stress, displacement, and stress difference in this model are relatively larger than those in the conventional model. Moreover, the re-orientation angles of the maximum principal stress are significantly different. After considering the natural cracks, there was an increase in the change in re-orientation and the re-orientation range. The research findings reported in this paper can be used to predict the initiation, extension, and steering process of temporary plugging fracturing fractures and refracturing fractures in fractured reservoirs.

1. Introduction

In oil and gas exploitation, the pore pressure in reservoirs gradually decreases in accordance with the development. At this point, the pore pressure gradient due to the heterogeneity of the reservoir pore pressure distribution induces a change in the initial reservoir stress distribution [1]. In conventional reservoir research, the reservoir is generally considered as a porous medium elastomer. When evaluating the coupling law between fluid flow and geological stress in the porous elastic model, the fluid flow is generally considered to occur in three main directions. However, the fluid flow is

due to the pressure gradient. For reservoirs such as shale, wherein natural fractures develop and dominate the reservoir fluid flow, the fluid flow is mainly along the direction of natural fractures. In this flow mode, the conventional permeability representation cannot accurately describe the flow of fluid. Therefore, the relationship between the natural fracture permeability and permeability tensor [2], the relationship between the permeability and fracture width [3], and the relationship between the effective stress and natural fracture width were established [4]. The permeability tensor can then be used to describe the flow of the fluid in other directions, and the variation in the width of the natural fracture can be

used to describe the permeability evolution during production. Hence, a three-dimensional fluid-solid coupling mathematical model in porous media was developed as an equivalent simulator for the analysis and evaluation of the stress evolution and stress steering in fractured reservoirs during depletion.

Several studies have been conducted on the fluid-solid coupling in porous media; however, the effect of natural fractures on the reservoir stress was considered in a few of these studies. The study on the coupling between fluid and geomechanics in porous media can be divided into two parts. The first aspect is the coupling of fluid and geomechanics during injection [5–10]. The other aspect is the coupling of the fluid and geological stress in the depletion [11–13]. The change in the reservoir stress due to the fluid loss during hydraulic fracturing is the result of the coupling between the flow and geomechanics, which is a process that occurs within a short-time period. Ghassemi et al. established a three-dimensional fluid-solid coupling model for hydraulic fracturing and then solved the model using the finite element and displacement discontinuity methods. The distribution of the pore pressure and stress in the vicinity of the hydrofractures was obtained, and the failure of the rocks in the vicinity of the hydrofractures was analyzed using the Mohr-Coulomb failure criterion [14]. Salimzadeh et al. proposed a fully coupled three-dimensional (3D) finite element model for the hydraulic fracturing of permeable rocks and then evaluated the applicable range of classical analytic solutions in the limit case using this model [15]. Gao and Ghassemi established a pore elastic model in the process of full 3D heterogeneous hydraulic fracturing using the coupling method of fluid flow and geomechanics and then solved it using the finite element method. The induced stress distribution and steering around hydraulic fractures in heterogeneous reservoirs were confirmed as functions of time and space [16].

In addition to changes in the reservoir stress during fluid injection, changes were observed when the reservoir was depleted. Oil and gas production is a significantly long-term reservoir consumption process [17–19]. Gupta et al. evaluated the influence of production consumption and completion migration on the reservoir stress, and the findings of the study indicated that the stress is more easily diverted under low-stress difference conditions. Moreover, the fracture characteristics, pressure exhaustion, and interwell interference have a significant influence on the infill well design and refracturing design in the latter stages [20]. Using a state-of-the-art coupled symmetric Galerkin boundary-element method (SGBEM) and the finite element method (FEM) model, Rousel and Sharma simulated the influence of prior production from the offset wells on the propagation direction of fractures initiated in an infill horizontal well. A stress reorientation zone was observed near the offset well after several years of production, which exhibited a significant influence on the fracture extension in the infill well [11]. Safari and Ghassemi proposed a numerical evaluation model for the changes in stress due to the depletion of the infill wells and then analyzed the bending of hydraulic fractures in the disturbed stress field and the connectivity of the hydraulic fractures between wells [21]. The failure effect and critical parameters that determine

the fracture bending were systematically evaluated [21, 22]. The results revealed that the depletion perturbed the stress tensor of the stratum around the fractured horizontal well. The perturbation stress field is related to stress/formation anisotropy, fluid fluidity, pore pressure, bottom hole working pressure, and Biot's constant. Sangnimnuan et al. evaluated the influence of the hydrofracture morphology on the stress evolution in the production process using the embedded discrete fracture method (EDFM) and the finite volume method (FVM) [1]. The study revealed that the fracture morphology has a significant influence on the stress distribution, surrounding drainage, and stress reorientation. Moreover, with a decrease in the stress difference, the steering is easier to achieve. The propagation path and radius of curvature of the hydrofractures can be predicted using the fracture propagation model combined with the varying stress field. In this paper, reservoir simulation was integrated with rock geomechanics to predict the well poststimulation productivities [23]. Several numerical and field studies have been presented to study the impact of the reservoir depletion on the pore pressure and the stress variation in the infill well zones [24]. Rezaei et al. presented refracturing analysis using a 2D poroelastic plain strain displacement discontinuity model built on the work of Zhang, Ghassemi and Zhang, and Chun [25–28]. Kumar and Ghassemi presented a geomechanical perspective to better understand the problem of “frac-hits” in horizontal well refracturing and to design solutions for it using geomechanics analysis and modeling [13]. The numerical analysis was based on a fully coupled 3D model “GeoFrac3D” with the capabilities to simulate multistage fracturing of multiple horizontal wells.

However, for reservoirs with natural fractures, the evolution of the reservoir-induced stress is influenced by the pressure consumption, hydrofracture morphology, and natural fractures, among others. Moreover, the influence of natural fractures is significant. Most researchers know that natural fractures have a significant impact on production during oil and gas production. However, when natural fractures and fluid-solid coupling are considered at the same time, the treatment of natural fractures becomes a difficult task. In summary, no research was found on the effect of the natural fracture heterogeneity on the induced stress in reservoir production. This paper summarizes and presents the results of the analysis conducted on the effect of natural fractures on the stress and stress diversion under the condition of plane fractures and nonplane fractures. This study was a combination and expansion of the fluid flow/geomechanics coupling theory and natural fracture heterogeneity in the pore elastic model. Compared with previous studies, our model is closer to the actual geological situation of the reservoir, so the results are more reliable and accurate. The research findings reported in this paper can be used to predict the initiation, extension, and steering process of temporary plugging fracturing fractures and refracturing fractures in fractured reservoirs.

2. Mathematic Model

2.1. Natural Fracture Continuum Method. In naturally fractured reservoirs such as shale and tight sandstone, the

permeability of the reservoir matrix is significantly small and it is difficult to extract the fluid based only on the matrix [23, 29]. In engineering, multicluster fracturing is generally employed in horizontal wells to activate reservoirs with natural fractures. The natural fractures then become the main channel of the oil and gas production and then dominate the flow mode of the reservoir fluid. Given that the permeability of natural fractures is significantly greater than that of the matrix, the contribution of the matrix permeability to fluid flow is neglected in this model and only the influence of natural fractures is considered [29]. The distribution angle of natural fractures developed in shale reservoirs is typically consistent, i.e., the inclination angle and approximation angle are generally distributed within a certain range of the main direction [30]. Therefore, it was assumed that the approximation angle and inclination angle of all-natural fractures in the model are consistent. In this model, the fracture continuum method proposed by McKenna and Reeves is used to describe the characteristics of natural fractures. The permeability of the element grid is characterized by the natural fracture inclination angle, approximation angle, opening angle, and fracture spacing [31]. The advantage of this method is that the natural fracture grid cannot be processed separately, and the results were obtained under the condition that the element is sufficiently small to meet the precision requirements [3, 32]. Based on previous research [3], the natural fracture permeability was dispersed to the continuous unit. The permeability tensor of natural fractures defines the permeability for each grid cell in the model domain. For one fracture set, the permeability tensor can be expressed as follows:

$$\mathbf{k} = k_{\text{nf}} \begin{bmatrix} (n_2)^2 + (n_3)^2 & -n_1 n_2 & -n_3 n_1 \\ -n_1 n_2 & (n_2)^2 + (n_3)^2 & -n_2 n_3 \\ -n_3 n_1 & -n_2 n_3 & (n_2)^2 + (n_3)^2 \end{bmatrix}, \quad (1)$$

where \mathbf{k} is the permeability tensor; n_1 , n_2 , and n_3 are the units normal to the fracture plane in the x , y , and z directions, respectively; and k_{nf} is the permeability of the natural fracture. Moreover, n_1 , n_2 , and n_3 can be expressed as follows:

$$\begin{aligned} n_1 &= \cos\left(\zeta \frac{\pi}{180}\right) \sin\left(\xi \frac{\pi}{180}\right), \\ n_2 &= \cos\left(\zeta \frac{\pi}{180}\right) \cos\left(\xi \frac{\pi}{180}\right), \\ n_3 &= -\sin\left(\zeta \frac{\pi}{180}\right), \end{aligned} \quad (2)$$

where $\zeta = 90^\circ - \text{dip}$ and $\xi = \text{strike} - 90^\circ$. Using Equations (1) and (2), the permeability tensor can be used to represent the heterogeneity caused by natural fractures. This heterogeneity is determined by the opening, spacing, inclination, and approach angle of natural fractures. In the model, the fluid-solid coupling of the depletion is considered and the stress distribution of the reservoir changes with respect to time, thus leading to changes in the natural fracture permeability. The

natural fracture permeability is mainly determined by the fracture opening as follows [3]:

$$k_{\text{nf}} = \frac{\delta^3}{12d}, \quad (3)$$

where δ is the reduction of the fracture aperture (fracture closure) and d is the fracture spacing.

To accurately describe the natural fracture permeability as a function of time, a coupling model of the natural fracture opening and effective stress was introduced. Bandis et al. evaluated the crack opening and effective normal stress and then proposed a semi-logarithmic relationship [33]:

$$\log \sigma_n = \omega + \chi \delta, \quad (4)$$

where σ_n is the normal stress on the crack surface and ω and χ represent the constants in the semilog fracture closure/stress relationship.

The effective normal stress that acts on the crack surface can be expressed as follows:

$$\sigma'_n = \frac{1}{2} (\sigma'_H + \sigma'_h) + \frac{1}{2} (\sigma'_H - \sigma'_h) \cos 2\theta, \quad (5)$$

where θ is the angle between the normal to the fracture and the σ_H direction and σ'_H and σ'_h , respectively, represent the maximum effective principal stress and the minimum effective principal stress, MPa.

By combining Equations (4) and (5), the following was obtained [4]:

$$\delta = \frac{1}{\chi} \log \left(\frac{n+1}{2n} + \frac{n-1}{2n} \cos 2\theta \right) + \frac{\log \sigma'_H}{\chi} - \frac{\omega}{\chi}, \quad (6)$$

where n is the effective stress ratio, which can be expressed as $n = \sigma'_H / \sigma'_h$.

2.2. Mechanism of Fluid-Solid Coupling Mechanics

2.2.1. Principle of Effective Stress.

Rock is a porous medium composed of a solid skeleton and pores. In addition, there are fluids (oil, gas, and water) stored in the pores of the skeleton. The fluid in the rock can bear or transfer pressure, which is defined as the pore pressure. Moreover, the stress transmitted through the contact surface between the rock particles is the effective stress. The Biot effective stress can be expressed as follows [34, 35]:

$$\sigma'_{ij} = \sigma_{ij} + \alpha \delta_{ij} p_f, \quad (7)$$

where σ'_{ij} is the effective stress, σ_{ij} is the total stress, δ_{ij} is the Kronecker symbol, and α represents the Biot constant, which can be defined as follows [36]:

$$\alpha = 1 - \frac{K_v}{K_s}, \quad (8)$$

where K_v and K_s represent the volume compression modulus of the rock and the compression modulus of the solid particles, respectively. Moreover, α is typically close to 1; thus, $\alpha = 1$ was used.

2.2.2. Stress Balance Equation. The theory of saturated-unsaturated seepage evaluates the movement of two or more fluids through pores. This study addressed the flow of a single-phase fluid in a porous medium. Based on the principle of virtual work, it can be known that at a certain moment, the virtual work of the rock mass of a unit is equal to the virtual work generated by the force that acts on the unit (physical force and surface force); thus,

$$\int_V \delta \varepsilon^T d\sigma dV - \int_V \delta u^T df dV - \int_S \delta u^T dF ds = 0, \quad (9)$$

where F is the surface force, f is the body force, and $\delta \varepsilon$ and δu are the virtual strain and virtual displacement, respectively.

The constitutive relationship expressed in an incremental form is

$$d\sigma' = D_{ep}(d\varepsilon - d\varepsilon_l), \quad (10)$$

where D_{ep} is the elastoplastic matrix and $d\varepsilon_l$ is the particle compression due to the pore fluid pressure, which only deforms in the positive direction without shear direction. The specific expression is as follows:

$$d\varepsilon_l = -m \frac{dp_f}{3K_s}, \quad (11)$$

where $m = [1, 1, 1, 0, 0, 0]^T$.

Formula (7) can be expressed as follows:

$$\sigma' = \sigma + \alpha m p_f. \quad (12)$$

For $\alpha = 1$, the combination of Formula (12) and the sum Formula (9) can be expressed as follows:

$$\begin{aligned} \int_V \delta \varepsilon^T D_{ep} \left(d\varepsilon + m \frac{dp_f}{3K_s} \right) dV - \int_V \delta \varepsilon^T m dp_f dV \\ - \int_V \delta u^T df dV - \int_S \delta u^T dF dV = 0. \end{aligned} \quad (13)$$

Given that the seepage continuity equation contains a time-related term, to couple the stress with the seepage, the time derivative of the virtual work Equation (13) is required. The specific expression is as follows:

$$\begin{aligned} \int_V \delta \varepsilon^T D_{ep} \left(\frac{\partial \varepsilon}{\partial t} + m \frac{1}{3K_s} \frac{\partial p_f}{\partial t} \right) dV - \int_V \delta \varepsilon^T m \frac{\partial p_f}{\partial t} dV \\ - \int_V \delta \varepsilon^T m \frac{\partial p_f}{\partial t} dV - \int_S \delta u^T \frac{\partial F}{\partial t} dS = 0. \end{aligned} \quad (14)$$

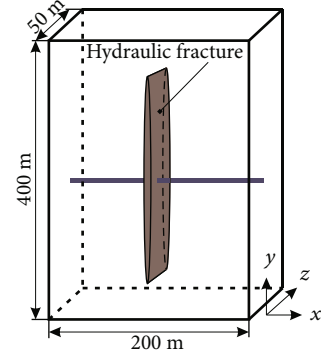


FIGURE 1: Single-phase solution validation model.

2.2.3. Continuity Equation. By combining Darcy's law with the conservation of fluid mass, a matrix flow model can be established to characterize the flow of porous media. The amount of fluid that flows into this volume in time dt should be equal to the increase in its internal water storage. Through derivation, the continuity equation of seepage flow can be obtained as follows:

$$\left(\phi c_f + \frac{\alpha - \phi}{K_s} \right) \frac{\partial p_f}{\partial t} + \alpha \frac{\partial \varepsilon}{\partial t} - \nabla \cdot \left[\frac{\mathbf{k}}{\mu_f} (\nabla p_f + \rho_f g) \right] = 0, \quad (15)$$

where g is the acceleration vector of gravity, c_f is the compressibility of the fluid, and ϕ is the matrix porosity.

In the process of oil and gas development, hydraulic fracturing is generally used to generate hydrofractures to increase the productive drainage area. As shown in the Figure 1, a hydrofracture was located at the y - z section. Hence, the continuity equation can be expressed as follows:

$$\left(\phi c_f + \frac{\alpha - \phi}{K_s} \right) \frac{\partial p_f}{\partial t} + \alpha \frac{\partial \varepsilon}{\partial t} - \nabla \cdot \left[\frac{k}{\mu_f} (\nabla p_f + \rho_f g) \right] + q_r = 0, \quad (16)$$

where q_r represents the interchange term between the fracture and matrix.

3. Model Calculation and Validation

3.1. Finite Element Dispersion. The shape function can be defined as follows:

$$\begin{cases} u = N_u \bar{u}, \\ \varepsilon = B \bar{u}, \\ p_f = N_p \bar{p}_f, \end{cases} \quad (17)$$

where B and N_u represent the shape function of the displacement, N_p is the shape function of pore pressure, \bar{u} is the nodal displacement, and \bar{p}_w is the pore pressure of the element node.

By substituting Equation (17) into Equation (15), the solid phase finite element formula can be obtained after simplification, as follows:

$$K \frac{d\bar{u}}{dt} + C \frac{d\bar{p}_w}{dt} = \frac{df}{dt}, \quad (18)$$

where

$$\begin{aligned} K &= \int_V B^T D_{ep} B dV, \\ C &= \int_V B^T \frac{D_{ep} m}{3K_s} N_p dV - \int_V B^T m N_p dV, \\ df &= \int_V N_u^T df dV + \int_S N_u^T dt dS. \end{aligned} \quad (19)$$

In the analysis of the seepage field, there are two types of boundary conditions. The first is the flow boundary condition, and the second is the pore pressure boundary condition. The flow boundary conditions can be expressed as follows:

$$q_r = \frac{k}{\mu_f} \frac{\partial p_f}{\partial \mathbf{n}_c}, \quad (20)$$

where \mathbf{n}_c is the normal unit of the flow boundary. This boundary condition can be used as the outer boundary condition. When there are production fractures in the reservoir after fracturing, the flow boundary condition can also be considered as the internal boundary condition or fracture boundary condition.

The pore pressure boundary conditions can be expressed as follows:

$$p_f = p_{fb}, \quad (21)$$

where p_{fb} is the pore pressure value at the known boundary.

The Galerkin method can be used, which can be expressed as follows:

$$\int_V a^T \bar{A} dV + \int_S b^T \bar{B} dS = 0, \quad (22)$$

where a and b are arbitrary functions, \bar{A} is the governing equation, and \bar{B} is the continuity equation through the boundary.

By substituting Equation (15) as \bar{A} , Equation (20) as \bar{B} , and the formal function expression (17) into Equation (22) and by setting $a = -b$, after the simplification, the following can be obtained:

$$E \frac{d\bar{u}}{dt} + F \bar{p}_w + G \frac{d\bar{p}_w}{dt} = \hat{f}, \quad (23)$$

TABLE 1: Primary parameters of calculation.

Parameter	Value	Unit
Young's modulus	35.5	GPa
Poisson's ratio	0.2	—
Biot coefficient	1	—
Initial porosity	0.25	—
Fluid compressibility	8×10^{-4}	MPa ⁻¹
Fluid viscosity	1.1	MPa s
The principal stress in x -direction	50	MPa
The principal stress in y -direction	54	MPa
The principal stress in z -direction	57	MPa
The initial pore pressure	30	MPa
The initial opening of natural fracture	0.2	mm
Average natural fracture spacing	20	m
Natural fracture dip	80	°
Natural fracture strike	40	°
Well radius	0.0762	m

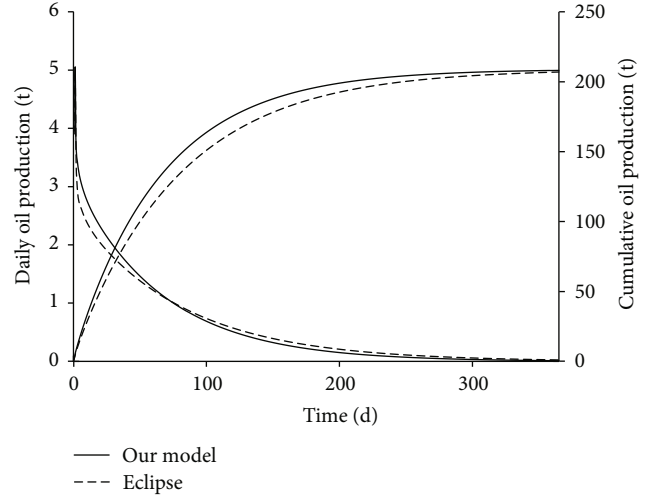


FIGURE 2: Flow rate comparison between the proposed model and Eclipse for one year of production.

where

$$\begin{aligned} E &= \int_V N_p^T \alpha B dV, \\ F &= \int_V (\nabla N_p)^T \frac{k}{\mu_f} \nabla N_p dV, \\ G &= \int_V N_p^T \left(\phi c_f + \frac{\alpha - \phi}{K_s} \right) N_p dV, \\ \hat{f} &= \int_S N_p^T q_r dS - \int_V (\nabla N_p)^T \frac{k}{\mu_f} \rho_f g dV. \end{aligned} \quad (24)$$

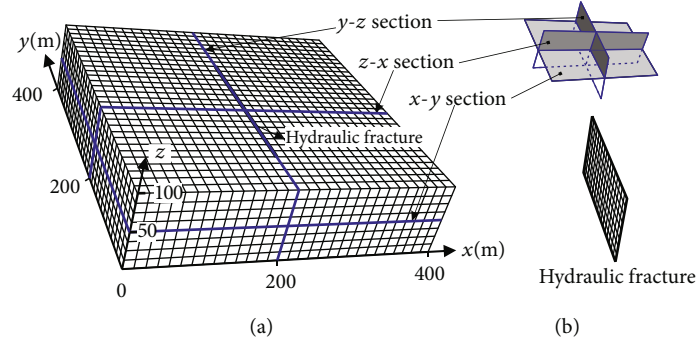


FIGURE 3: A schematic diagram of the 3D physical model.

By combining Equation (18) with Equation (23), the geomechanic-seepage coupling equation can be expressed as follows:

$$\begin{bmatrix} K & C \\ E & G \end{bmatrix} \frac{d}{dt} \begin{Bmatrix} \bar{u} \\ \bar{p}_w \end{Bmatrix} + \begin{bmatrix} 0 & 0 \\ 0 & F \end{bmatrix} \begin{Bmatrix} \bar{u} \\ \bar{p}_w \end{Bmatrix} = \begin{Bmatrix} \frac{df}{dt} \\ \hat{f} \end{Bmatrix}. \quad (25)$$

3.2. Model Validation

3.2.1. Single-Phase Flow Solver. To verify the oil-water flow model, a single fracture seepage model was established (as shown in Figure 1) and the same model was established by Eclipse software for a simulation comparison. The permeability, porosity, and reservoir thickness of the model were 5 md, 0.1, and 50 m, respectively. The boundary of the model was closed; thus, the reserves in the model were constant. The other main parameters were the same as those shown in Table 1. In the proposed model, the flow model was established without considering natural fractures. Fluid-solid coupling is not considered in Eclipse software. The daily output and cumulative oil production after one year of production were obtained by adopting the method of constant pressure production, as shown in Figure 2. The results of the model were approximately consistent with those of Eclipse. Due to the different factors considered by the models, the change process was slightly different. Therefore, the model in this paper demonstrated a high accuracy.

4. Case Studies

4.1. Basic Parameters. As discussed in this section, a three-dimensional reservoir physical model was established to evaluate the influence of anisotropy due to natural fractures on the reservoir stress during the oil and gas development. To fully demonstrate the significant influence of natural fractures on the generation of induced stress, a model was established that does not consider the influence of k_{xz} , k_{yz} , and k_{xy} . However, the influence of the permeability in the main direction was considered for comparison. As shown in Figure 3, the length, width, and height of the model were 400 m, 400 m, and 100 m, respectively, and the hydraulic fracture

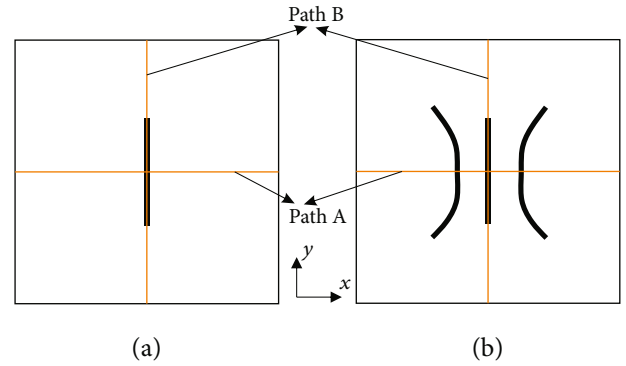


FIGURE 4: A schematic diagram of the hydrofracture layout ((a) presents the planar single fracture, and (b) presents the nonplanar multiple fractures).

was located at the cross section of the y - z -axis. The domain was discretized to 50 four-node cells in the x - and y -directions and 20 four-node cells in the z -direction. For the treatment of the reservoir boundary, the nodes on the left and right surfaces of the model were free to move along the x -axis and not the y -axis. All the nodes at the top and bottom outer surfaces were free to move along the y -axis and not the x -axis. Only the vertical displacement of all the nodes on the outer surface of the top and bottom could be achieved. Moreover, the six boundaries were nonflow boundaries, i.e., the pore pressure in the reservoir was continuously reduced in the process of production. In all the calculations below, the downhole flow velocity was calculated using the Peaceman equation [37]. The other parameters in the calculation are shown in Table 1. Figures 4(a) and 4(b) present the locations of the single fractures and three clusters of nonplanar fractures, respectively.

4.2. Single Fracture Study. Based on the model and physical parameters established in Section 4.1, in this section, the focus is on the influence of natural fractures on the stress distribution and steering in the production process of a single fracture in the y - z section. To fully reflect the effect of natural fractures on the stress, a conventional model was established without considering the effect of natural fractures, for

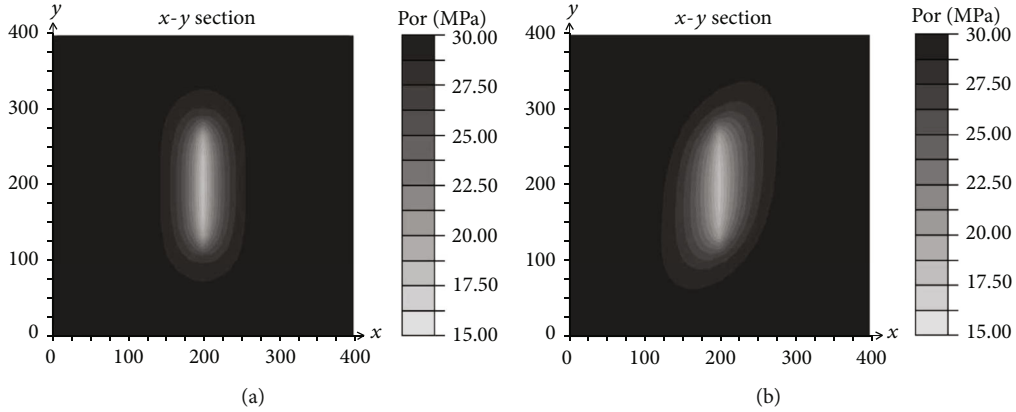


FIGURE 5: Panels (a) and (b), respectively, represent the pore pressure distribution without the influence of the natural fractures and the pore pressure under the influence of the natural fractures.

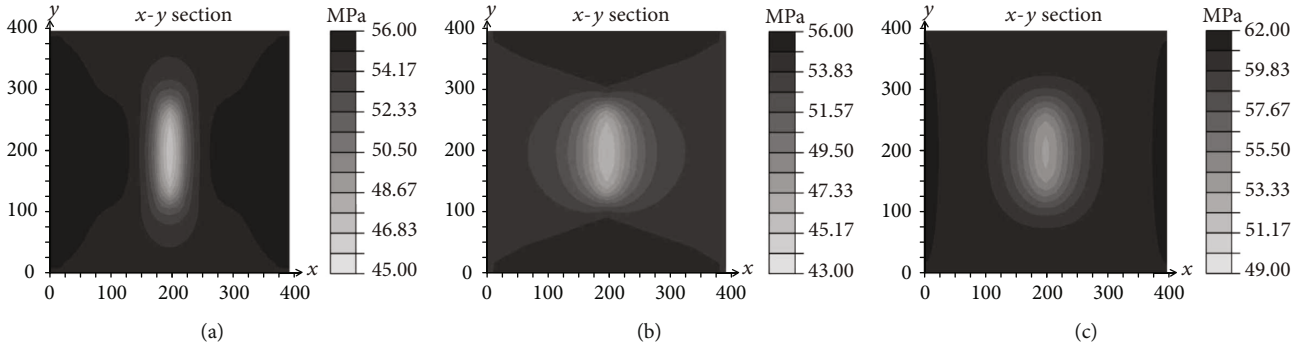


FIGURE 6: (a), (b), and (c) present the principal stress in the x -direction, y -direction, and z -direction without considering the influence of the permeability tensor of natural fractures.

comparison. Compared with the boundary conditions in the model, the calculated parameters were consistent with the proposed model.

During the production, the pore pressure decreases continuously due to the continuous fluid extraction and the pressure is the lowest near the fracture. Figure 5 compares the distribution of the reservoir pore pressure after 5 years of production with and without considering the influence of natural fractures. As can be seen from the figure, due to the influence of natural fractures, there was a change in the fluid flow pattern. Compared with the conventional model, the pore pressure dissipation area was greater and it was easier to reduce the pore pressure along the direction of natural fractures for the formation of a clockwise deflecting pressure drop funnel. Therefore, under the natural fracture distribution condition, the fluid in the upper right and lower left corners could be easily extracted, whereas the fluid in the upper left and lower right corners could not be easily extracted. This can serve as an essential guide to the design of infill wells.

According to the principle of effective stress, the reservoir stress changes under the influence of the constant dissipation of the pore pressure. For the conventional model, the distribution of the stress σ_{xx} , σ_{yy} , and σ_{zz} in the reservoir after 5 years of production is shown in Figures 6(a), 6(b), and 6(c). Due to fluid consumption, the reservoir stress distribution

exhibited a high complexity. Moreover, there was a decrease in σ_{xx} near the crack as a result of the pressure dissipation, whereas σ_{xx} increased on the left and right parts of the domain to support the pressure depletion in the x -direction. In addition, there was a decrease in σ_{yy} near the crack as a result of the pressure dissipation, whereas σ_{yy} increased at the top and bottom parts of the domain to support the pressure depletion in the y -direction. Moreover, σ_{zz} mainly exhibited a decrease in stress in the central region of the domain. Considering the influence of natural fractures on the stress evolution, the results are shown in Figures 7(a), 7(b), and 7(c). Compared with the conventional model, the stress distribution of the proposed model is similar to that of the conventional model. However, considering the influence of tensors, the pressure dissipation of the proposed model was more rapid and the changes in stress were greater. The most significant difference is that the distributions of σ_{xx} , σ_{yy} , and σ_{zz} exhibited a degree of deflection. The stress distribution deflection was found to be significantly different from the stress distribution near the fractures in the conventional model, and this difference has a significant influence on the fracture initiation direction and fracture extension of refracturing. As can be seen in Figures 8(a) and 8(b), the distribution of the shear stress on the x - y section exhibited a clockwise deflection when compared with the conventional

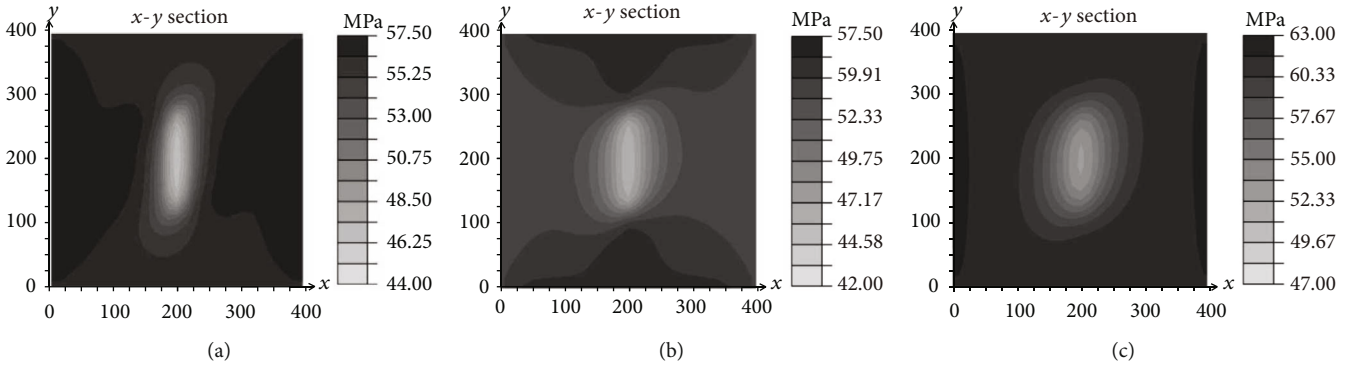


FIGURE 7: (a), (b), and (c) present the principal stress in the x -direction, y -direction, and z -direction considering the influence of the permeability tensor of natural fractures.

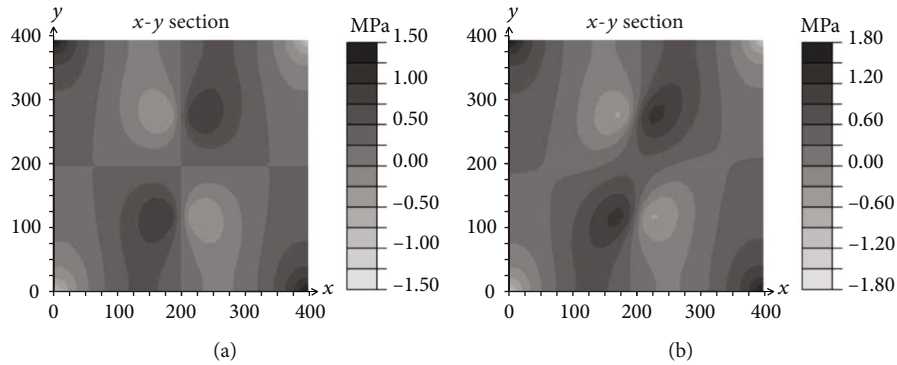


FIGURE 8: (a) and (b) present the induced shear stress in the x - y section with and without considering natural fractures, respectively.

model, due to the influence of natural fractures. From a comparison between Figures 9(c) and 9(d) and Figures 9(a) and 9(b), the distribution of the displacement was found to be deflected to a certain extent under the influence of natural fractures. Figures 10(a) and 10(b) present the displacement profiles on Paths A and B, respectively. In all the figures, the solid lines represent the proposed model and the dotted lines represent the conventional model. The displacement trend of the two models was similar. The main difference was that there was a more significant change in the absolute value of the displacement after the influence of natural fractures was considered.

Figures 11(a), 11(b), and 11(c) present the σ_{xx} , σ_{yy} , and σ_{zx} stress distributions of the proposed model and conventional model after 5 years of production on the z - x section, respectively. As can be seen from the figure, the stress distribution of the conventional model exhibited a symmetrical distribution. Compared with the conventional model, the overall trend of the stress distribution in the proposed model was in good agreement. However, the stress distribution was symmetrically distributed under the influence of natural fractures, and there was a relative increase in the variation range of the stress value.

Significant attention has been directed toward the reservoir stress evolution and surrounding drainage in the process of fluid recovery, given their significance for the latter refrac-

turing and completion of infill wells. The change in the direction of the horizontal principal stress direction has a significant influence on the design of refracturing. Due to the heterogeneity of the permeability and natural fractures, the heterogeneity consumption of the pore pressure may result in stress reorientation and changes in the direction of the horizontal maximum principal stress. As can be seen from Figures 12(a) and 12(b), a region with a stress difference less than 0 was observed near the fracture after one year of production. In addition, the stress in this region was reversed. It can also be found that the time when the stress difference changes the most is not the 20 years with the longest production life but the 10th year. This is because with an increase in the production life, most of the fluid in the easily flowing region was produced, whereas the fluid in the previously relatively noneasily flowing region was gradually produced. Therefore, there was a decrease in the difference between the pore pressures in the regions, which led to a decrease in the stress differences and an increase in the influence range. Figures 12(c) and 12(d) present the shear stress profiles on Paths A and B. Compared with the conventional model, the shear stress absolute value of the proposed model is influenced more significantly by natural cracks.

Refracturing is one of the most effective methods for latter reservoir development. The distribution of the reservoir stress after the production and the direction of the horizontal

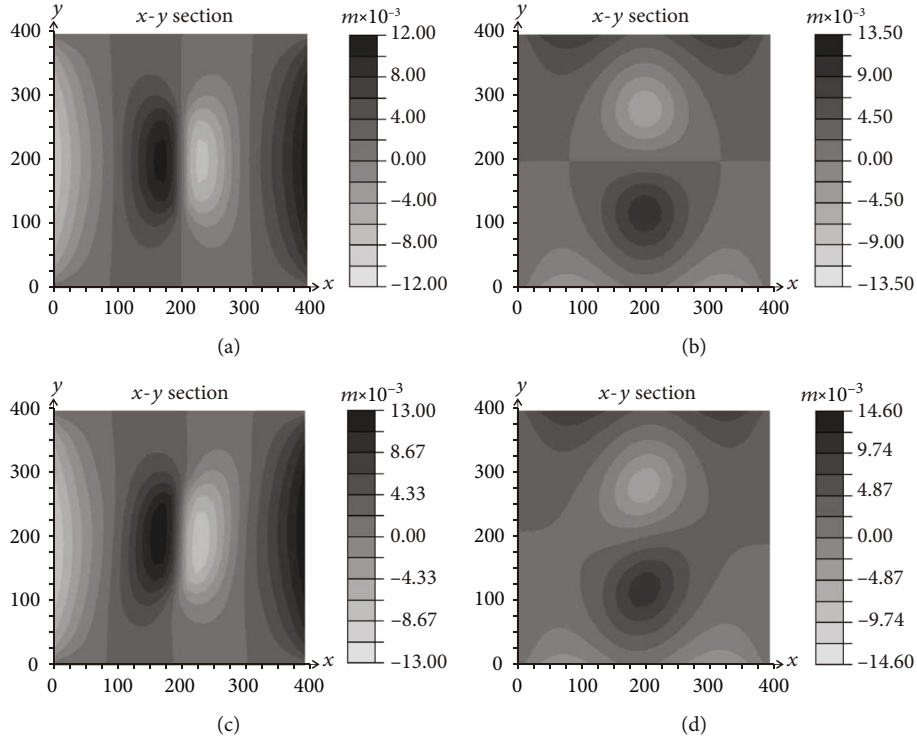


FIGURE 9: (a) and (b) present u_x and u_y on the x - y section without considering natural fractures, respectively, and (c) and (d) present u_x and u_y on the x - y section considering natural fractures, respectively.

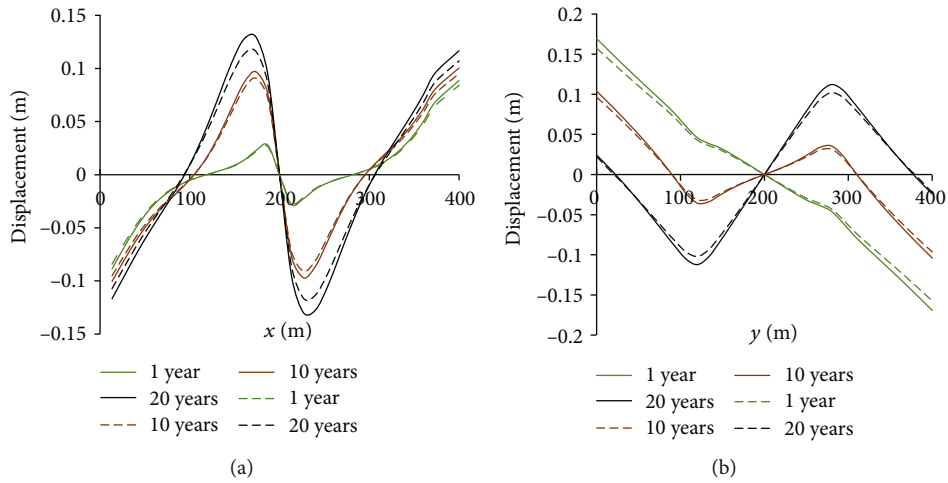


FIGURE 10: (a) and (b) present the displacement profiles on Paths A and B.

maximum principal stress are two critical factors that determine the fracture pressure, fracture initiation direction, and fracture extension trajectory of refracturing. The stress evolution in the production process was previously analyzed. For the solution of the change in reorientation of the maximum horizontal principal stress ($\sigma_{H \max}$) on the x - y section, the action of the vertical principal stress (σ_{zz}) was neglected; thus, the original direction of the maximum horizontal principal stress is shown in Figure 13(a). After 5 and 10 years of production, there was a significant change in the direction

of $\sigma_{H \max}$. In the conventional model, the change area of the principal stress direction was in the shape of a vertical ellipse, whereas the change area of the $\sigma_{H \max}$ direction in the proposed model was in the shape of an inclined ellipse. The degree of inclination is related to the location of natural fractures. The area with the largest reorientation change of $\sigma_{H \max}$ was near the hydrofracture. Compared with the conventional model, the change in reorientation of $\sigma_{H \max}$ in the proposed model was influenced more significantly by natural fractures ($\theta'_1 > \theta_1$, $\theta'_2 > \theta_2$). In the conventional

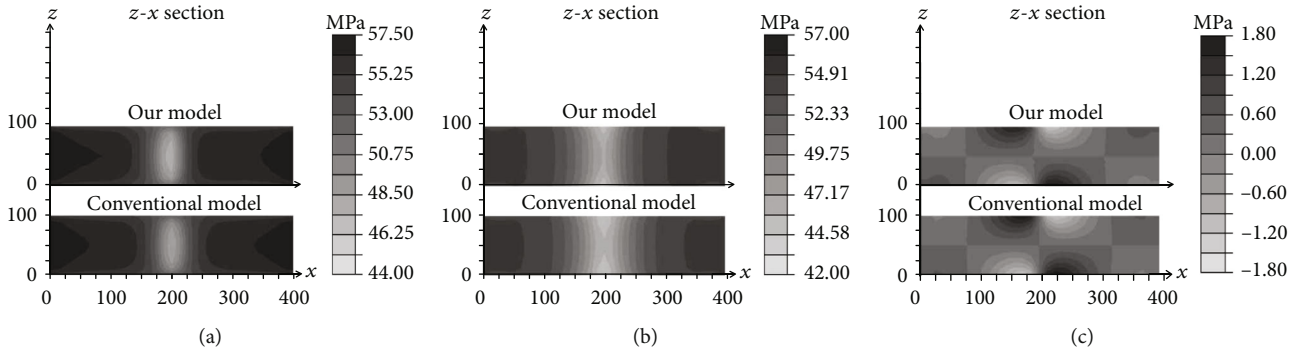


FIGURE 11: (a), (b), and (c) present the comparison of the principal stress along the x -direction, y -direction, and the induced shear stress on the z - x section, respectively.

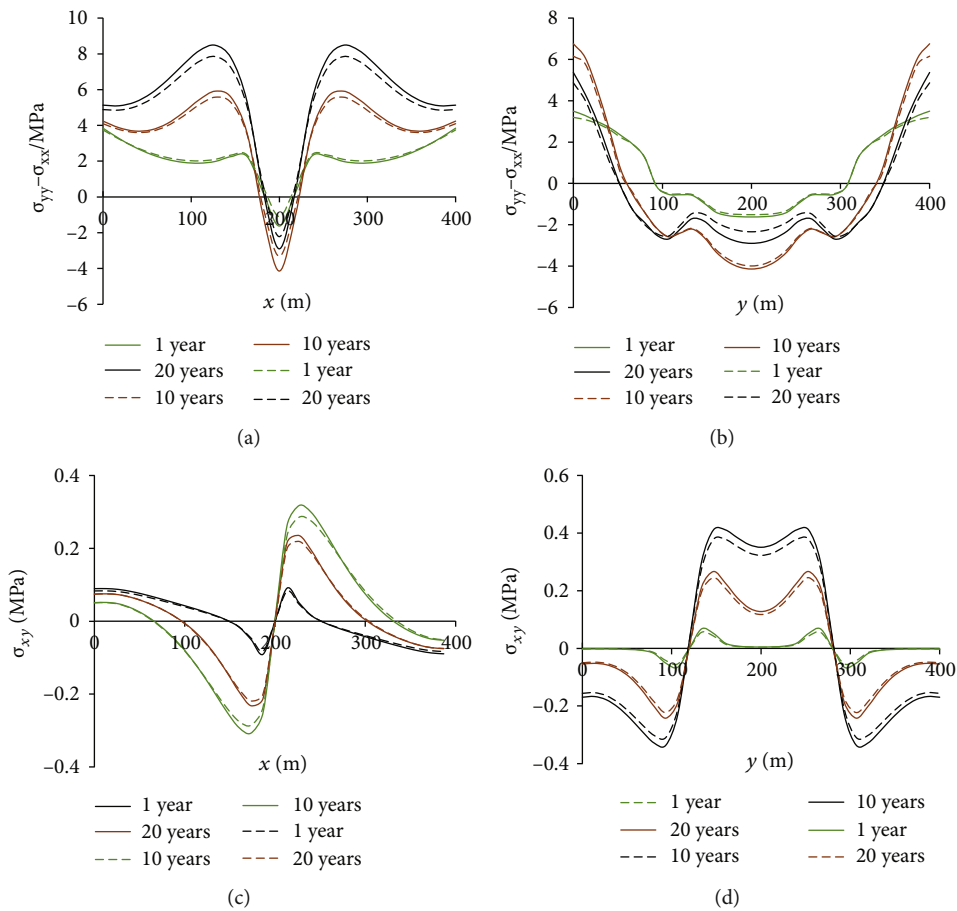


FIGURE 12: (a) and (b) are present the stress difference profiles on Paths A and B of different production years, and (c) and (d) present the shear stress profiles on Paths A and B of different production years.

model, the change in reorientation of $\sigma_{H \max}$ was 90° (Figure 14(a)); however, the change in reorientation of $\sigma_{H \max}$ in the proposed model was 110° under the influence of natural cracks (Figure 14(b)). Similar to the change in the stress difference, the change in the reorientation was the largest at the 10th year, not the 20th year. Moreover, the range of the reorientation areas is proportional to production time.

4.3. Nonplanar Multifracture Study. In the actual segmented multicluster fracturing process, there is stress interference between the fractures when multiple fractures are simultaneously extended, which leads to the case wherein the middle fractures are restrained and the fractures on both sides are extended in a nonplanar manner. Hence, the displacement discontinuity method was used to simulate the extended trajectories of three clusters of hydrofractures with spacings of

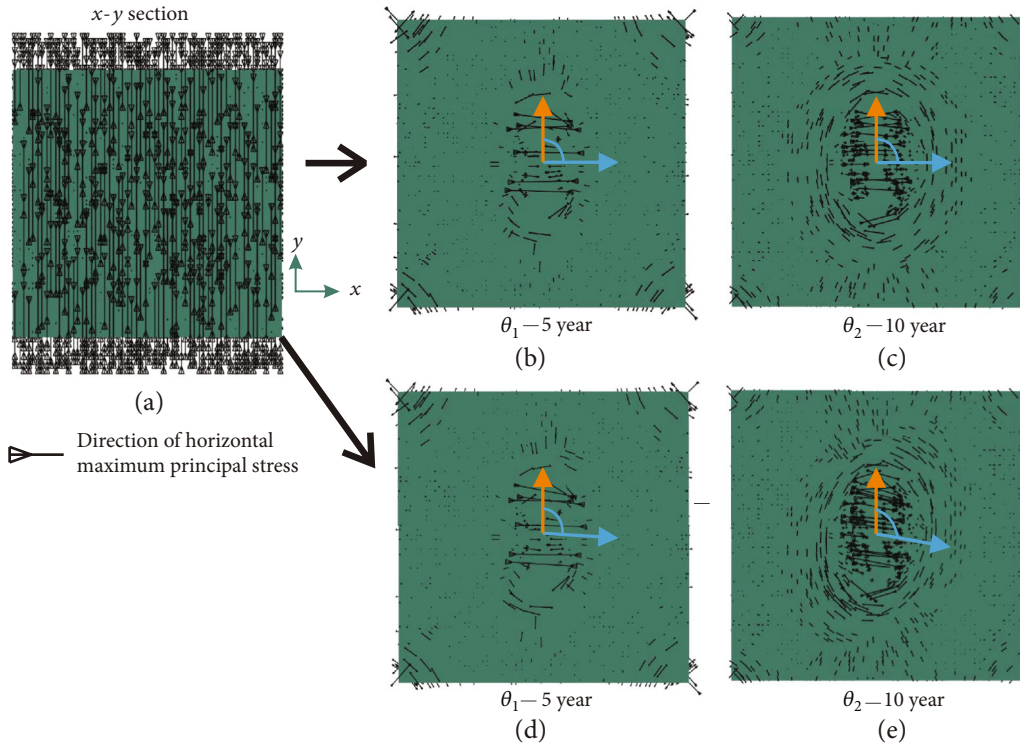


FIGURE 13: (a) presents the direction of the maximum principal stress on the x-y section in the initial state. (b) and (c) present the direction of the maximum horizontal principal stress after 5 years and 10 years of production without considering natural fractures. (d) and (e) present the direction of the maximum horizontal principal stress after 5 years and 10 years of production considering the influence of natural fractures.

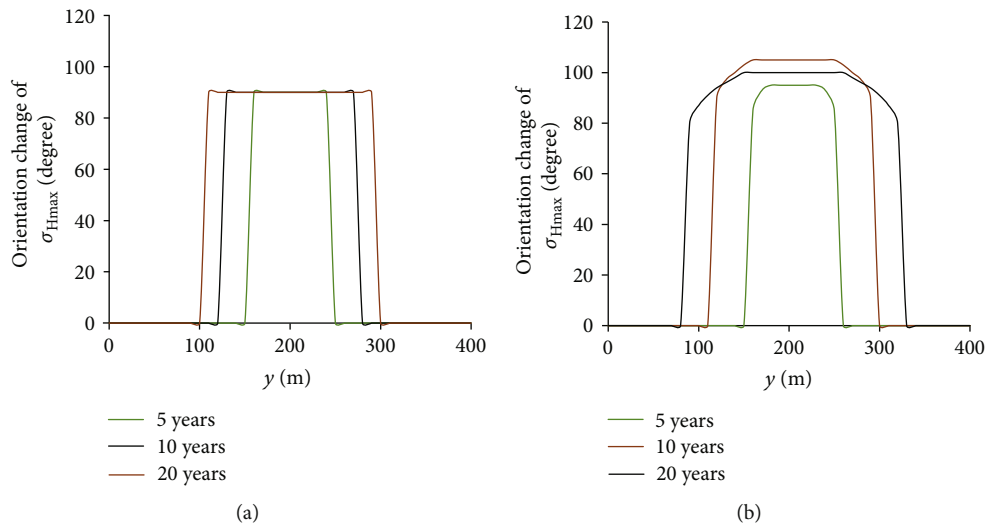


FIGURE 14: (a) and (b) present the steering angle of the maximum horizontal principal stress along Path B without and with considering the influence of natural fractures in different production years, respectively.

50 m. The three hydraulic fractures are considered as production fractures. It was assumed that all three clusters of fractures pass through the reservoir in the z-direction. The other calculation parameters are the same as those in Table 1. Under this condition, the reservoir stress distribution after 1, 5, and 10 years of production was simulated.

Figure 15 presents the pore pressure distribution after 1, 5, and 10 years of nonplanar fracture production using the conventional model. The pore pressure distribution in the domain was axially symmetric. However, under the influence of natural fractures, there was an initial decrease in the pore pressure along the strike direction of the natural

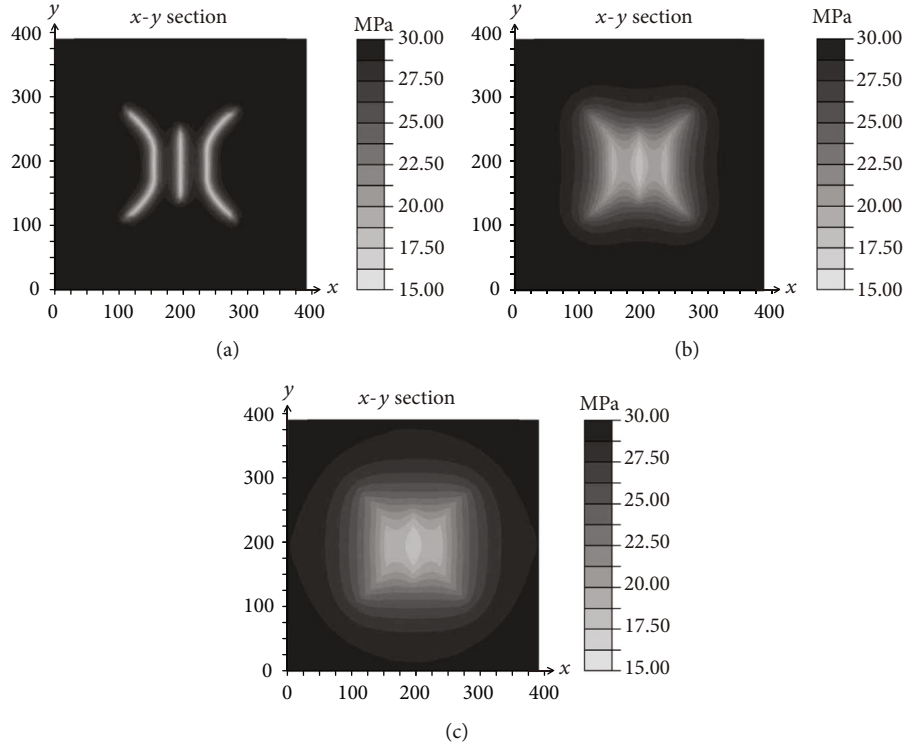


FIGURE 15: (a), (b), and (c) present the pore pressure distribution after 1, 5, and 10 years of nonplanar fracture production without considering the influence of natural fractures.

fractures, and the distribution exhibited central symmetry rather than axial symmetry (as shown in Figure 16). The upper left part and the lower right part of the domain are underexploited areas under such reservoir geological conditions and distributed fractures.

Due to the influence of the nonplanar fracture geometry, the stress distribution after production exhibited a high complexity. Without considering the effect of natural fractures, the stress distribution of the conventional model was axially symmetric. Compared with a single fracture, there was an increase in the rates of the pore pressure dissipation and stress decrease and there was an increase in the size of the influence range, as shown in Figures 17(a), 17(b), and 17(c). The stress (σ_{xx}) on the left and right of the domain and the stress (σ_{yy}) on the top and bottom of the domain increased to support the pressure depletion of the middle area. When the influence of natural fractures was considered, the stress distribution in the proposed model exhibited a significant degree of deflection, as shown in Figures 18(a), 18(b), and 18(c). The deflection of the stress distribution confirms that natural fractures have a significant influence on the reservoir fluid flow and production.

Compared with a single crack, the distribution of the principal stress was more complex. The change in reorientation of $\sigma_{H \max}$ was $\theta'_1 > \theta_1$, $\theta'_2 > \theta_2$, as shown in Figure 19. Due to the influence of the nonplanar crack geometry, the rotation angle of the maximum principal stress direction in the conventional model reached 135° . In the proposed model, the rotation angle of the principal stress direction

near the crack was concentrated at 140° . The reorientation region affected by the natural fractures was larger than those of the conventional models. Therefore, under the action of the nonplanar fracture geometry and natural fractures, the evolution of the reservoir stress tends to be complex in the production process. From a comparison of Figures 20(a) and Figure 18(a), the profile of the change in reorientation on Path B was found to be significantly different due to the influence of the hydraulic fracture geometry. During the first year of production, the central region did not turn; however, it turned in accordance with an increase in the production time. From a comparison of Figures 20 and Figure 18, there was a similarity in that the greatest change in the reorientation of $\sigma_{H \max}$ occurred in the 10th year and the change in reorientation was correlated with the reservoir depletion time.

5. Conclusion

A fully coupled 3D pore elastic model based on the FEM was developed to analyze the stress evolution and stress reorientation in heterogeneous porous media in the reservoir depletion process. In the model, the continuous natural fracture model is used to characterize the effect of natural fractures on the reservoir fluid flow. The relationship between the natural fracture width and effective stress was used to establish a fluid cluster single fracture model and a three-cluster nonplane fracture model for an example analysis. There was a good agreement between the analytical solutions and

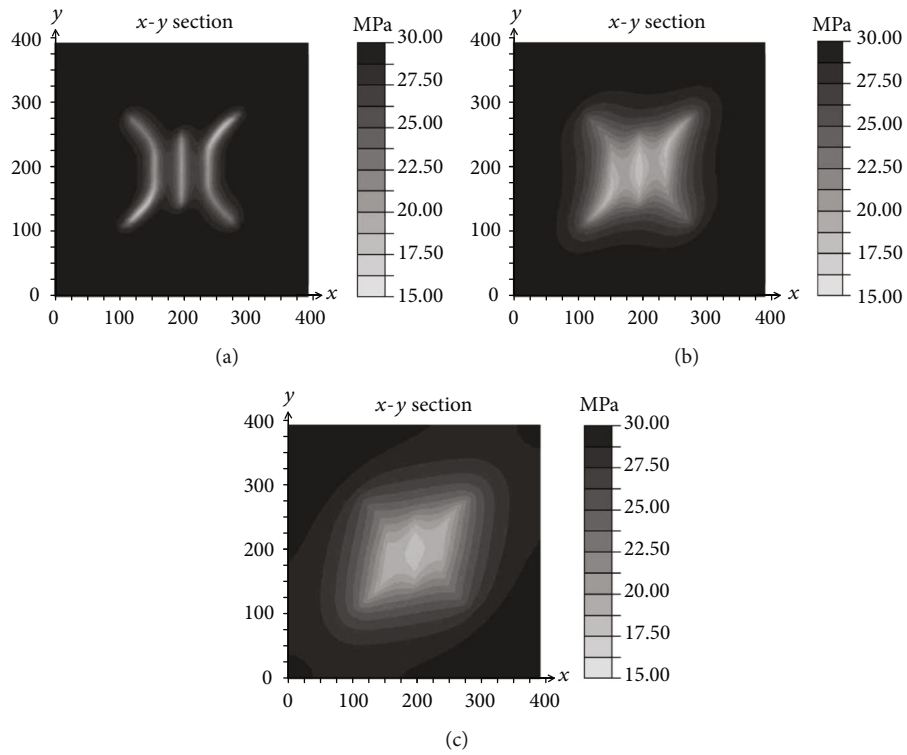


FIGURE 16: (a), (b), and (c) present the pore pressure distribution after 1, 5, and 10 years of nonplanar fracture production considering the influence of natural fractures.

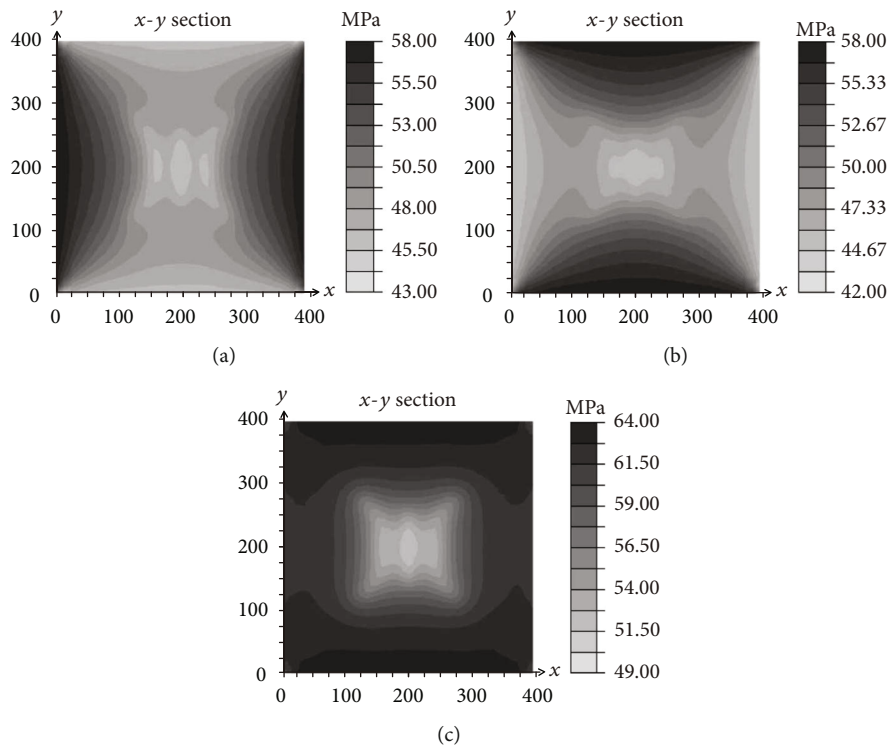


FIGURE 17: (a), (b), and (c) present the σ_x , σ_y , and σ_z stress distributions after 10 years of nonplanar fracture production without considering the influence of natural fractures.

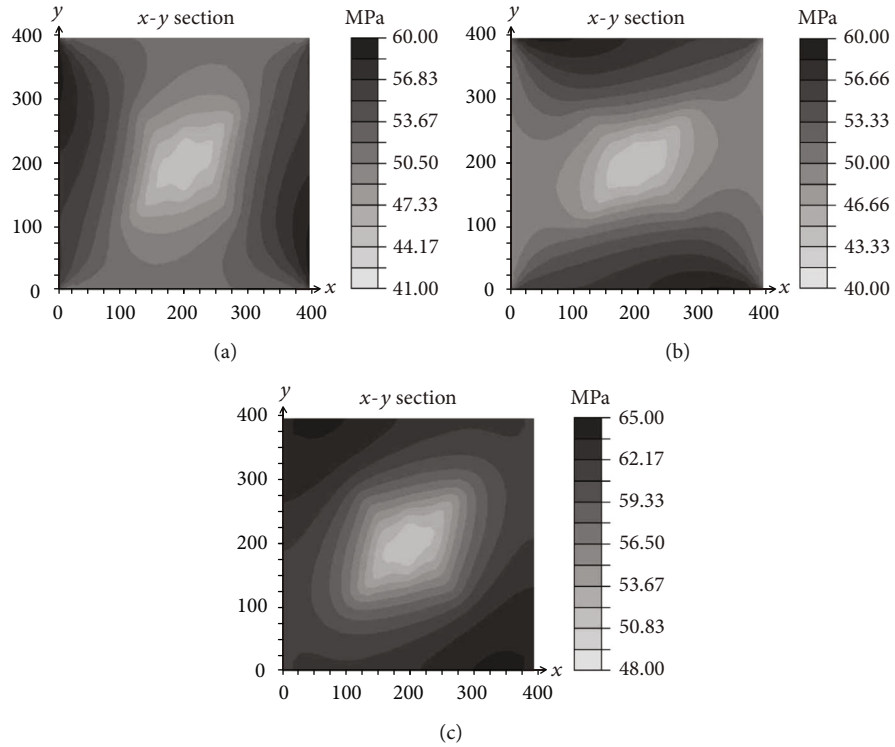


FIGURE 18: (a), (b), and (c) present the $\sigma_x, \sigma_y, \sigma_z$ stress distribution after 10 years of nonplanar fracture production considering the influence of natural fractures.

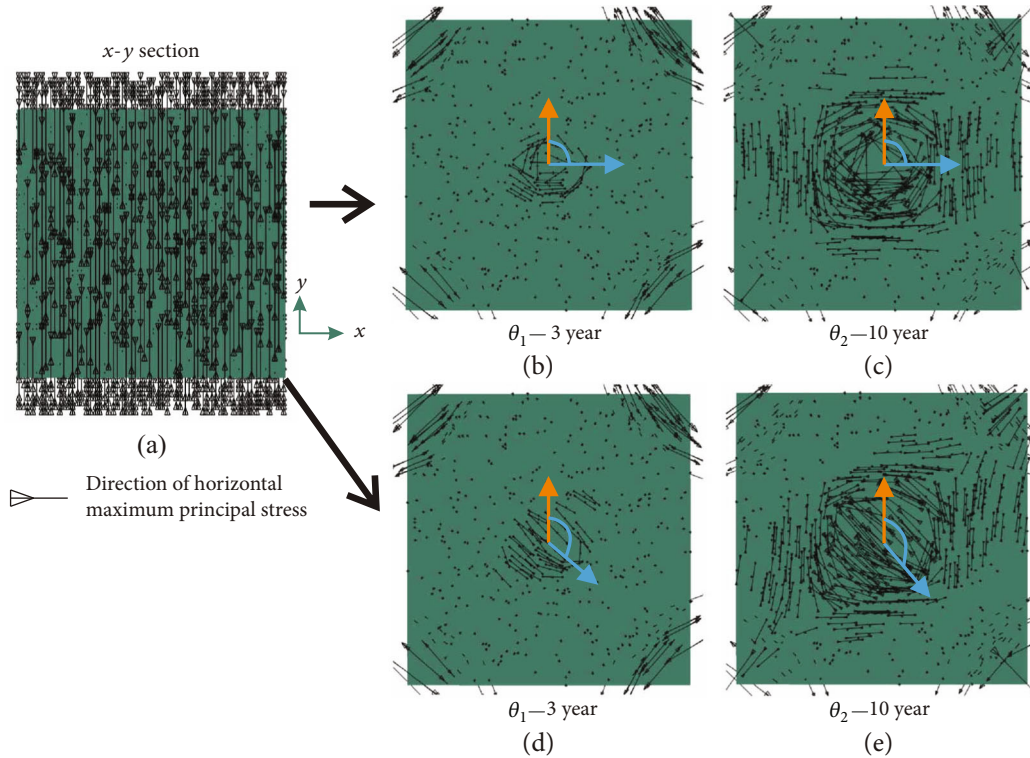


FIGURE 19: (a) presents the direction of the initial maximum horizontal principal stress on the $x-y$ section. (b) and (c) present the direction of the maximum horizontal principal stress after 3 years of depletion without considering the natural cracks. (d) and (e) present the direction of the maximum horizontal principal stress after 10 years of production considering the natural cracks.

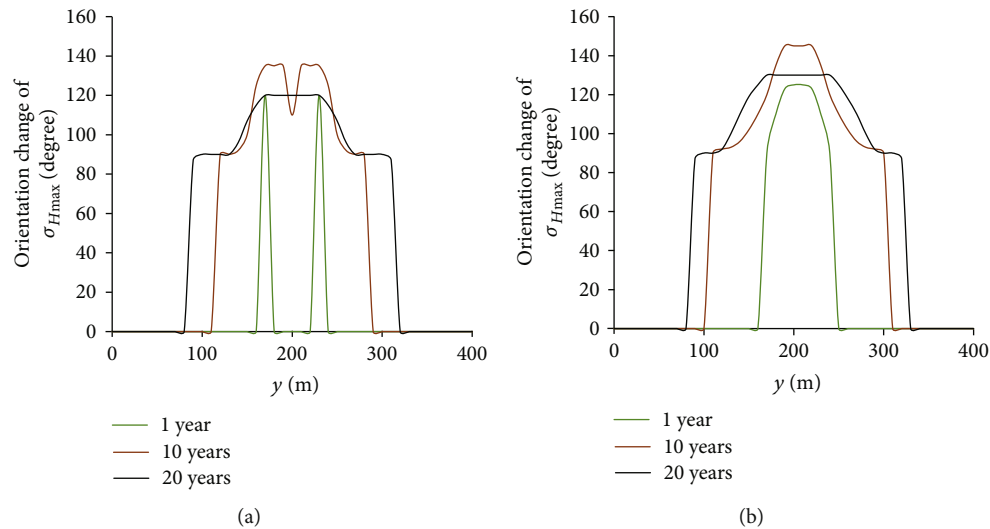


FIGURE 20: (a) and (b) present the change in reorientation of $\sigma_{H \max}$ along Path B without and with considering the influence of natural fractures and under different depletion years, respectively.

numerical results. By comparing the conventional models, it was confirmed that natural cracks have a significant influence on the stress evolution, surrounding drainage, and change in reorientation in the depletion process. Under the influence of natural fractures, the fluids in reservoirs along the direction of the natural fractures are easier to recover, and areas that are perpendicular to the natural fracture surface are prone to underconsumption. In addition, under the flow mode dominated by natural fractures, the stress distribution in the proposed model is deflected to a certain extent, especially in the nonplanar fracture model. Due to the action of natural cracks, the absolute values of the stress, displacement, and stress difference in the proposed model are relatively greater and the change in the reorientation of the maximum principal stress steering is significantly different. After considering the natural cracks, the steering angle and steering range increased. Moreover, this directly results in significant differences in the design of the late-stage fracturing temporary plugging steering and refracturing technology for conventional reservoirs. The simulation results revealed that it is very important to consider the effects of natural fractures on the stress redistribution, surrounding drainage, and reorientation in production. The findings of this study can serve as a theoretical guide for the design of refracturing, temporary plugging steering, and infilling wells and help predict the direction of new fractures and the trajectory of fracture extensions.

Data Availability

The data used to support the findings of this study are available from the corresponding author upon request.

Conflicts of Interest

The authors declare that they have no conflicts of interest.

Acknowledgments

The work presented in this paper was supported by the main program of the China National Petroleum Corporation (2016E-01), National Science and Technology Major Special Project-Fu Ling Shale Gas Development Demonstration Project (2016ZX05060), and the China National Scholarship Fund.

References

- [1] A. Sangnimmuan, J. Li, and K. Wu, "Development of efficiently coupled fluid-flow/geomechanics model to predict stress evolution in unconventional reservoirs with complex-fracture geometry," *SPE Journal*, vol. 23, no. 03, pp. 640–660, 2018.
- [2] M. Chen, M. Bai, and J. C. Roegiers, "Permeability tensors of anisotropic fracture networks," *Mathematical Geology*, vol. 31, no. 4, pp. 335–373, 1999.
- [3] X. Weng, V. Sesetty, and O. Kresse, "Investigation of shear-induced permeability in unconventional reservoirs," in *49th U.S. Rock Mechanics/Geomechanics Symposium*, San Francisco, California, November 2015.
- [4] R. H. Richard, "The influence of fracture stiffness and the in situ stress field on the closure of natural fractures," *Petroleum Geoscience*, vol. 4, no. 1, pp. 57–65, 1998.
- [5] T. K. Perkins and J. A. Gonzalez, "The effect of thermoelastic stresses on injection well fracturing," *Society of Petroleum Engineers Journal*, vol. 25, no. 01, pp. 78–88, 1985.
- [6] Y. Q. Hu, Q. Wang, J. Z. Zhao, Z. Guo, Y. Zhang, and C. Mao, "Development of efficiently coupled thermo-hydro-mechanical model to predict hydraulic fracture morphology in heavy oil reservoirs," *Environmental Earth Sciences*, vol. 77, no. 23, p. 778, 2018.
- [7] L. Ren, R. Lin, J. Z. Zhao, V. Rasouli, J. Zhao, and H. Yang, "Stimulated reservoir volume estimation for shale gas fracturing: mechanism and modeling approach," *Journal of Petroleum Science and Engineering*, vol. 166, pp. 290–304, 2018.

- [8] Q. Wang, Y. Hu, J. Z. Zhao, L. Ren, C. Zhao, and J. Zhao, "Multiscale apparent permeability model of shale nanopores based on fractal theory," *Energies*, vol. 12, no. 17, p. 3381, 2019.
- [9] J. Z. Zhao, Q. Wang, Y. Q. Hu, L. Ren, and C. Zhao, "Numerical investigation of shut-in time on stress evolution and tight oil production," *Journal of Petroleum Science and Engineering*, vol. 179, pp. 716–733, 2019.
- [10] J. Z. Zhao, Q. Wang, Y. Q. Hu, C. Zhao, and J. Zhao, "Prediction of pore pressure-induced stress changes during hydraulic fracturing of heterogeneous reservoirs through coupled fluid flow/geomechanics," *Journal of Engineering Mechanics*, vol. 145, no. 12, article 05019001, 2019.
- [11] N. P. Roussel and M. M. Sharma, "Role of stress reorientation in the success of refracture treatments in tight gas sands," *SPE Production & Operations*, vol. 27, no. 04, pp. 346–355, 2012.
- [12] R. Safari, R. Lewis, X. Ma, O. Mutlu, and A. Ghassemi, "Infill well fracturing optimization in tightly spaced horizontal wells," *SPE Journal*, vol. 22, no. 02, pp. 582–595, 2016.
- [13] D. Kumar and A. Ghassemi, "Three-dimensional poroelastic modeling of multiple hydraulic fracture propagation from horizontal wells," *International Journal of Rock Mechanics and Mining Sciences*, vol. 105, pp. 192–209, 2018.
- [14] A. Ghassemi, X. X. Zhou, and C. Rawal, "A three-dimensional poroelastic analysis of rock failure around a hydraulic fracture," *Journal of Petroleum Science and Engineering*, vol. 108, pp. 118–127, 2013.
- [15] S. Salimzadeh, A. Paluszny, and R. W. Zimmerman, "Three-dimensional poroelastic effects during hydraulic fracturing in permeable rocks," *International Journal of Solids and Structures*, vol. 108, pp. 153–163, 2017.
- [16] Q. Gao and A. Ghassemi, "Pore pressure and stress distributions around a hydraulic fracture in heterogeneous rock," *Rock Mechanics and Rock Engineering*, vol. 50, no. 12, pp. 3157–3173, 2017.
- [17] Y. Zeng, Z. Wang, Y. Zang et al., "Pore pressure disturbance induced by multistage hydraulic fracturing in shale gas: modelling and field application," *Geofluids*, vol. 2019, Article ID 1315451, 11 pages, 2019.
- [18] H. Zhu, X. Tang, Q. Liu, K. Li, and J. D. McLennan, "4D multiphysical stress modelling during shale gas production: a case study of Sichuan Basin shale gas reservoir, China," *Journal of Petroleum Science and Engineering*, vol. 167, pp. 929–943, 2018.
- [19] H. Zhu, X. Tang, Q. Liu et al., "Permeability stress-sensitivity in 4D flow-geomechanical coupling of Shouyang CBM reservoir, Qinshui Basin, China," *Fuel*, vol. 232, pp. 817–832, 2018.
- [20] D. Kumar and A. Ghassemi, "A three-dimensional analysis of simultaneous and sequential fracturing of horizontal wells," *Journal of Petroleum Science and Engineering*, vol. 146, pp. 1006–1025, 2016.
- [21] R. Safari and A. Ghassemi, "Three-dimensional poroelastic modeling of injection induced permeability enhancement and microseismicity," *International Journal of Rock Mechanics and Mining Sciences*, vol. 84, pp. 47–58, 2016.
- [22] R. Safari and A. Ghassemi, "3D thermo-poroelastic analysis of fracture network deformation and induced micro-seismicity in enhanced geothermal systems," *Geothermics*, vol. 58, pp. 1–14, 2015.
- [23] M. Lin, S. Chen, E. Mbia, and Z. Chen, "Application of reservoir flow simulation integrated with geomechanics in unconventional tight play," *Rock Mechanics and Rock Engineering*, vol. 51, no. 1, pp. 315–328, 2018.
- [24] A. Morales, K. Zhang, K. Gakhar et al., "Advanced modeling of interwell fracturing interference: an Eagle Ford shale oil study-refracturing," in *SPE Hydraulic Fracturing Technology Conference*, Woodlands, TX, USA, February 2016.
- [25] A. Rezaei, G. Bornia, M. Rafiee, M. Soliman, and S. Morse, "Analysis of refracturing in horizontal wells: insights from the poroelastic displacement discontinuity method," *International Journal for Numerical and Analytical Methods in Geomechanics*, vol. 42, no. 11, pp. 1306–1327, 2018.
- [26] Q. Zhang, *A Boundary Element Method for Thermo-Poroelasticity with Applications in Rock Mechanics*, University of North Dakota, Grand Forks, ND, USA, 2004.
- [27] A. Ghassemi and Q. Zhang, "Porothermoelastic analysis of the response of a stationary crack using the displacement discontinuity method," *Journal of Engineering Mechanics*, vol. 132, no. 1, pp. 26–33, 2006.
- [28] K. H. Chun, *Thermo-Poroelastic Fracture Propagation Modeling with Displacement Discontinuity Boundary Element Method*, Ph. D. Dissertation, Texas A & M University, College Station, TX, USA, 2013.
- [29] I. Walton and J. McLennan, "The role of natural fractures in shale gas production," in *ISRM International Conference for Effective and Sustainable Hydraulic Fracturing*, Brisbane, Australia, May 2013.
- [30] N. R. Warpinski, "Hydraulic fracturing in tight, fissured media," *Journal of Petroleum Technology*, vol. 43, no. 02, pp. 146–209, 1991.
- [31] S. A. McKenna and P. C. Reeves, *Fractured Continuum Approach to Stochastic Permeability Modeling*, American Association of Petroleum Geologists, Tulsa, Oklahoma, 2006.
- [32] E. Kalinina, S. A. McKenna, K. Klise, K. T. Hadgu, and T. S. Lowry, "Incorporating complex three-dimensional fracture network into geothermal reservoir simulations," *Transactions-Geothermal Resources Council*, vol. 36, pp. 493–497, 2012.
- [33] S. C. Bandis, A. C. Lumsden, and N. R. Barton, "Fundamentals of rock joint deformation," *International Journal of Rock Mechanics and Mining Sciences*, vol. 20, no. 6, pp. 249–268, 1983.
- [34] M. A. Biot, "General theory of three-dimensional consolidation," *Journal of Applied Physics*, vol. 12, no. 2, pp. 155–164, 1941.
- [35] M. A. Biot, "Theory of elasticity and consolidation for a porous anisotropic solid," *Journal of Applied Physics*, vol. 26, no. 2, pp. 182–185, 1955.
- [36] R. W. Zimmerman, "Coupling in poroelasticity and thermoelasticity," *International Journal of Rock Mechanics and Mining Sciences*, vol. 37, no. 1-2, pp. 79–87, 2000.
- [37] D. W. Peaceman, "Interpretation of well-block pressures in numerical reservoir simulation (includes associated paper 6988)," *SPE Journal*, vol. 18, no. 03, pp. 183–194, 1978.

Research Article

A Fractal Model for Characterizing Hydraulic Properties of Fractured Rock Mass under Mining Influence

Xiaoli Liu ¹, Tao Liang,¹ Sijing Wang,^{1,2} and Kumar Nawnit¹

¹The State Key Laboratory of Hydro-Science and Engineering, Tsinghua University, Beijing 100084, China

²Institute of Geology and Geophysics of the Chinese Academy of Sciences, Beijing 100029, China

Correspondence should be addressed to Xiaoli Liu; xiaoli.liu@tsinghua.edu.cn

Received 18 May 2019; Revised 6 November 2019; Accepted 14 November 2019; Published 20 December 2019

Guest Editor: Frédéric Nguyen

Copyright © 2019 Xiaoli Liu et al. This is an open access article distributed under the Creative Commons Attribution License, which permits unrestricted use, distribution, and reproduction in any medium, provided the original work is properly cited.

In this paper, two basic assumptions are introduced: (1) The number and length distribution of fractures in fractured rock mass are in accordance with the fractal law. (2) Fluid seepage in the fractures satisfies the cubic law. Based on these two assumptions, the fractal model of parallel seepage and radial seepage in fractured rock mass is established, and the seepage tensor of fracture network which reflects the geometric characteristics and fractal characteristics of fracture network under two kinds of seepage is derived. The influence of fracture geometry and fractal characteristics on permeability is analyzed, and the validity and accuracy of the model are verified by comparing the calculated results of the theoretical model and physical model test. The results show that the permeability coefficient K of fracture network is a function of the geometric (maximum crack length L_{\max} , fractured horizontal projection length L_0 , diameter calculation section porosity Φ , fracture strike α , and fracture angle θ) and fractal characteristics (fracture network fractal dimension D_f and seepage flow fractal dimension D_T). With the increase of fractal dimension D_f , the permeability coefficient increases. With the increase of D_T , the permeability coefficient decreases rapidly. And the larger the D_f ($D_f > 1.5$), the greater the change of permeability coefficient K with D_T .

1. Introduction

A large number of fractures are distributed in the natural rock mass and artificially disturbed rock mass, which provide channels for fluid seepage. To determine the permeability characteristic of fractured rock is important in the field of geology, geotechnical engineering, petrochemical resource exploitation, groundwater resource development and protection, nuclear waste disposal, and storage of carbon dioxide and others [1–9]. Generally, it is assumed that the fluid flows only in the interconnected fractures, and the permeability characteristics of equivalent fracture network is determined by analyzing the permeability characteristics of the different characteristic fractures [10, 11]. This method is called the discrete fracture network (DFN) method, which has been widely used and developed in recent decades [12–16].

The permeability characteristics of the fracture network mainly depend on the fracture characteristics (spatial distribution, density, connectivity, etc.) at the macroscopic level and the fracture characteristics (length, gap width, directiv-

ity, roughness, etc.) at the microscopic level. Liu et al. [8] reviewed the current research on the influence of geometrical characteristics of fractured rock mass on the permeability of two-dimensional discrete fracture network and summed up nine parameters which have great influence on the permeability of fracture network. It is the length and distribution of fractures, the width and distribution, fractured surface roughness, dead fracture, fracture cross point, hydraulic gradient, stress condition, anisotropy, and size effect and listed the analytical expressions of the relationship between the relevant fracture parameters and permeability. de Dreuzy and Philippe [17] studied the effect of fracture length and gap width distribution on the infiltration characteristics of two-dimensional random fracture networks. Based on the fractal network statistics and fractal characteristics, a practical method to determine the permeability of fracture network was proposed by Jafari and Babadagli [18, 19]. Sensitivity analysis of the permeability of each parameter was carried out. The results showed that the fracture density and length have the greatest influence on the permeability of fracture

network. The permeability of fracture network with exponential distribution was studied by Rossen and Gu [20]. It is found that the single large scale fracture plays a major role in the permeability of the fracture network. The permeability of the study area increases with the increase of the study size. Under normal circumstances, it is very difficult to quantitatively describe the fracture characteristics of the fracture network due to its complexity [21, 22]. Studies have shown that natural fractures have fractal properties that have the same effect on the permeability of fracture networks as well as fracture geometries [18, 23–26].

A series of studies have been made on the influence of geometric characteristics and fractal features of fractures on permeability. A two-dimensional random fracture network model considering the characteristics of fracture network (density, length, gap width, directionality, and connectivity) was established. The fracture network statistics and the relationship between fractal characteristics and fracture network permeability were obtained through the multiple regression analysis and artificial neural network processing. An estimation method was proposed to estimate the permeability of multilayer complex fracture network, in order to obtain a good estimate result, which was recommended for comprehensive utilization of drill core data (1D), bedrock exposed data (2D), and drilling test data (3D). Another key factor that affects the permeability of fracture network is the connectivity between fractures. Based on the fractal geometry and percolation theory, the two-dimensional fracture network connectivity was defined, and the relationship between fracture network permeability and fractal dimension and dimensionless fracture density and percolation threshold was given and analyzed. It is pointed out that the estimated value obtained by fractal dimension of fractured network was more accurate than that of fractal dimension of fracture intersections, fracture connectivity rate, and intersection fractal dimension in the X-direction and Y-direction.

In recent years, many scholars have established the fractal model of pore and fractured media based on the fractal characteristics of porosity and fractures and have made great achievements in studying fluid seepage, solute transport, and heat conduction [27–32]. Zheng and Yu [33] deduced the seepage characteristics of the gas in the porous media model composed of porous rock and fractal tree fractures. It is shown that the pore fractal dimension, pore bending degree, porosity, the ratio of maximum pore diameter to fractal tree fracture network length, diameter ratio, bifurcation angle, and bifurcation level are the key factors that have significant effects on gas permeability. Yun et al. [34] analyzed the plane radial seepage and parallel seepage of Newtonian fluid in porous media and deduced the permeability coefficient and flow rate and velocity expression in the two seepage cases. The fractal theory and the Monte Carlo method were used to establish the probability model of radial percolation in porous media by Xu et al. [35]. The results showed that the effective radial permeability coefficient decreased drastically with the radial distance increase and the porosity and pore fractal dimension of the radial seepage interface had a significant effect on the effective permeability coefficient. Based on the fractal geometry theory and the laminar cube

law of fluid in fractures, a fractal model of seepage in fractured rock mass was deduced by Miao et al. [36]. The theoretical model showed that the permeability coefficient of fractured rock mass was a function of fracture fractal dimension, porosity, fracture density, maximum fracture length, gap width, fracture direction, and inclination angle. Miao et al. [37] assumed that the fractures in the fractured rock mass were randomly distributed, the fluid flow in the fracture was in accordance with the law of cube, the pores in the rock mass connected into tortuous channels, the fracture length and pore diameter distribution had fractal characteristics, and a fractal model of seepage flow in a two-hole media model was established. The Monte Carlo method was used to generate the fractured network, and a fractal flow model was established to reflect the geometrical characteristics of fractured rock mass. It is revealed that the bending degree, the gap width and the random number that reflects fractal regularity of fracture length distribution, had a significant influence on the permeability of fracture network [38]. The seepage fractal model of discrete fracture network was established by using the fractal dimension of fracture geometrical distribution and the fractal dimension of flow line which reflects the surface roughness of fractures. By simulating and calculating the equivalent permeability coefficient of fluid flowing through different geometric characteristics of discrete fractures, it was found that when the fractal dimension of the fractured network is less than 1.5, the seepage of the fracture network is mainly controlled by the small fracture with the length less than the width of the fracture network. With the increase of fractal dimension, the effect of long fractures on fracture network seepage is increasing [7, 8].

The permeability of fractured rock mass is influenced by the heterogeneity of fracture direction, inclination, and length distribution, which lead to the fact that the permeability of the fractured rock mass is directional, and many scholars have carried on fruitful research in this area [9, 10, 12, 13, 39, 40]. Based on the previous research, this paper is aimed at establishing a parallel seepage and radial seepage fractal model of fractured rock mass considering the effect of fracture surface roughness in Section 2 and deducing the seepage tensor of the fracture network which reflects the geometrical and fractal characteristics of fracture network in Section 3. The influence of fracture geometry and fractal characteristics on the permeability is analyzed in Section 4. The validity and accuracy of the model are verified by comparing the theoretical model and the physical model water injection test in Section 5.

2. Fractal Characteristics of Fractured Network of Rock Mass

Studies have shown that the cumulative surface area distribution of the Earth's surface islands is subject to power distribution [36, 41], i.e.,

$$N(A > a) \propto a^{-D/2}, \quad (1)$$

where N is the total number of islands with area A greater than constant a and D is the fractal dimension representing

the area distribution of the island. On this basis, a_{\max} is used to represent the area of the largest island [42]. Equation (2) is given:

$$N(A > a) = \left(\frac{a_{\max}}{a}\right)^{D/2}. \quad (2)$$

The relationship between the equivalent gap width and the crack length can be expressed [36, 43–45]:

$$e = \beta l^n, \quad (3)$$

where e is the equivalent gap width; β is the proportional coefficient, which is related to the mechanical properties of the surrounding rock and in the range of 0.001–0.1 [37, 44]; l is the fracture length; and n is a constant that reflects the fracture characteristics, which ranges from 0.5 to 2.0 [37, 44, 45]. When $n = 1$, it indicates that the equivalent gap width and the length of the fracture are linearly distributed. The fractured network has self-similarity and fractal characteristics [37, 38, 43, 45]. Equation (3) can be written as follows:

$$e = \beta l. \quad (4)$$

Many studies have shown that the fracture length distribution satisfies the fractal law [15, 36, 45–49]. Therefore, equation (2), which describes the distribution law of island area, is used to describe the distribution of fractures area in fractured media:

$$N(A \geq a) = \left(\frac{e_{\max} l_{\max}}{el}\right)^{D_f/2}, \quad (5)$$

where e_{\max} and l_{\max} are the maximum gap width and maximum length, respectively, and e and l are the fracture width and length, respectively. Equation (4) is substituted into equation (5), and equation (6) is given as follows:

$$N(L \geq l) = \left(\frac{l_{\max}}{l}\right)^{D_f}, \quad (6)$$

where D_f is the fractal dimension of the fracture length, for the two-dimensional problem $0 < D_f < 2$ and for the three-dimensional problem $0 < D_f < 3$. By substituting l in equation (6) with l_{\min} , the total number of fractures in the fracture network can be expressed as follows:

$$N_t(L > l_{\min}) = \left(\frac{l_{\max}}{l_{\min}}\right)^{D_f}. \quad (7)$$

In general, the number of fractures in the fracture network is large, so equation (6) can be approximated as a continuous differential equation and equation (8) can be obtained by solving differential l in equation (6):

$$-dN(l) = D_f l_{\max}^{D_f} l^{-(D_f+1)} dl. \quad (8)$$

Equation (8) indicates the number of fractures in $[l, l + dl]$, and the negative sign indicates that the number of fractures decreases with increasing fracture length. Equation (8) divided by equation (7) is equal to the following equation:

$$-\frac{dN}{N_t} = D_f l_{\min}^{D_f} l^{-(D_f+1)} dl = f(l) dl, \quad (9)$$

where $f(l) = D_f l_{\min}^{D_f} l^{-(D_f+1)}$ is the probability density function, which is satisfied by equation (10) by the definition of the probability function:

$$\int_{-\infty}^{+\infty} f(l) dl = \int_{l_{\min}}^{l_{\max}} f(l) dl = 1 - \left(\frac{l_{\min}}{l_{\max}}\right)^{D_f} \equiv 1. \quad (10)$$

Therefore, equation (11) is given as follows:

$$\left(\frac{l_{\min}}{l_{\max}}\right)^{D_f} \equiv 0. \quad (11)$$

In general, $l_{\min} \ll l_{\max}$ in equation (11) is a necessary condition for the fractal network to show fractal characteristics. Many researchers [22, 38] used $l_{\min}/l_{\max} \leq 0.001$ as a threshold for the fractal model considering the two-dimensional fracture network seepage. This criterion is also used in this paper.

The relationship between porosity and fractal dimension can be expressed [37, 50, 51]:

$$D_f = d_E + \frac{\ln \Phi}{\ln (l_{\max}/l_{\min})}, \quad (12)$$

where D_f is the fractal dimension of the fracture length; Φ is the porosity of the fracture network; l_{\min} and l_{\max} are the minimum and maximum values of the fracture length; d_E is the European dimension, in which for the two-dimensional problem $d_E = 2$ and for the three-dimensional problem $d_E = 3$.

According to the definition of porosity, the following equation is available:

$$\phi = \frac{A_f}{A_0}, \quad (13)$$

where Φ is the porosity of the fracture network, A_0 is the area of the cross section, and A_f is the pore area.

$$A_f = - \int_{l_{\min}}^{l_{\max}} e l dN(l) = \frac{\beta D_f l_{\max}^2}{2 - D_f} \left[1 - \left(\frac{l_{\min}}{l_{\max}}\right)^{2-D_f} \right]. \quad (14)$$

By solving simultaneously equations (12) and (14), the following equation becomes available:

$$A_f = \frac{\beta D_f l_{\max}^2}{2 - D_f} (1 - \phi). \quad (15)$$

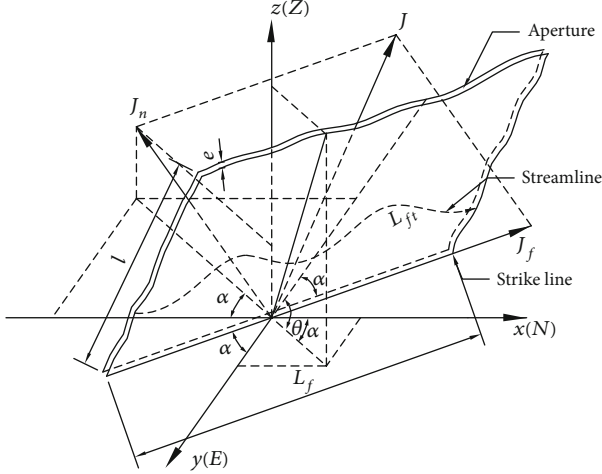


FIGURE 1: Three-dimensional fracture seepage diagram.

By substituting equation (13) into equation (15), the following equation becomes available:

$$A_0 = \frac{\beta D_f l_{\max}^2 (1 - \phi)}{2 - D_f} \frac{1}{\phi}. \quad (16)$$

3. Fractal Model of Permeability of Fractured Rock Mass

3.1. Formula Derivation. In a three-dimensional space, the direction of the fracture is determined by the direction and inclination, as shown in Figure 1. The x -axis and the y -axis are the two coordinate directions of the horizontal plane, which is in the same direction as the geodetic coordinate; that is, the x -axis is N and the y -axis is E ; α is the angle between the trend line and the y -axis, θ is the angle between the fracture plane and the horizontal plane (inclination), l is the fracture length, e is the fracture width, L_{ft} is the seepage length of the fluid in the fracture considering the fracture roughness, L_f is the linear length in the direction of fracture seepage, J_f is the tangential component of the hydraulic gradient in the fracture, and J_n is the normal component of the hydraulic gradient in the fracture. L_0 is the linear length of L_f projected to the x -axis direction.

Usually, there are a large number of cracks in the fractured rock mass, and it is impossible to determine the direction and inclination of the fractures one by one. Studies have shown that the directionality of many fractures in a given area is not exactly the same but can usually show a tendency [36, 52]. For example, the results of 1878 fractures in the study showed an average inclination of 70° and an average orientation of N-S [53]. Furthermore, the fracture network studied at present is only caused by mining. Compared with the natural fracture networks affected by complex geological factors, the fracture network studied here is more regular. Therefore, we take the trend and dip angle in the calculation model for a certain range of statistical average.

It is assumed that the flow of fluid in the fracture can be described by the cubic law [39, 44, 54]:

$$q(l) = \frac{e^3 l \Delta P}{12\mu L_{ft}}, \quad (17)$$

where $q(l)$ is a single fracture flow, μ is the dynamic viscosity coefficient, e is the fracture width, l is the fracture length, L_{ft} is the length of the seepage of the fluid in the fracture considering the fracture roughness, and ΔP is the pressure difference across the fracture.

Because of the rough surface of the fracture, the fluid flow path in the fracture is a curve, which leads to the extension of the flow path and the decrease of the effective flow capacity, as shown in Figure 1. The relationship between L_{ft} and L_f can be expressed as follows:

$$L_{ft} = e^{1-D_T} L_f^{D_T}, \quad (18)$$

where D_T is the fractal dimension of the flow line of the seepage flow. D_T reflects the nonlinearity of the streamline, and the streamline is a straight line when $D_T = 1$, $L_{ft} = L_f$.

By substituting equations (4) and (18) into equation (17), the following equation becomes available:

$$q(l) = \frac{\beta^{2+D_T} l^{3+D_T} \Delta P}{12\mu L_f^{D_T}} = \frac{\beta^{2+D_T} l^{3+D_T}}{12\mu D_T L_f^{D_T-1}} \frac{dP}{dL_f}. \quad (19)$$

In a three-dimensional space, the hydraulic gradient is divided into normal and tangential components along the fracture, as shown in Figure 1. Only the tangential hydraulic gradient produces the seepage flow, that is,

$$\mathbf{q}(\mathbf{l}) = \frac{\beta^{2+D_T} l^{3+D_T}}{12\mu D_T L_f^{D_T-1}} \mathbf{J}_f. \quad (20)$$

By substituting $L_0 = L_f \sin \alpha$ into equation (20), the following equation becomes available:

$$q(l) = \frac{\beta^{2+D_T} l^{3+D_T}}{12\mu D_T} \left(\frac{L_0}{\sin \alpha} \right)^{1-D_T} \mathbf{J}_f. \quad (21)$$

It is assumed that the angle between the normal direction of the fracture surface and the coordinate axes is α_1 , α_2 , and α_3 , respectively. The normal direction vector of the fracture surface can be expressed as

$$\mathbf{n}_n = \cos \alpha_1 \mathbf{i} + \cos \alpha_2 \mathbf{j} + \cos \alpha_3 \mathbf{k}. \quad (22)$$

At the same time, the hydraulic gradient vector is decomposed along the fracture plane normal and tangential components [55]:

$$\mathbf{J} = \mathbf{J}_f + \mathbf{J}_n. \quad (23)$$

Taking equation (24) into consideration,

$$\mathbf{J}_n = (\mathbf{J} \cdot \mathbf{n}_n) \mathbf{n}_n. \quad (24)$$

The hydraulic gradient is decomposed in the direction of the coordinate axis; equation (25) is available.

$$\mathbf{J} = \mathbf{J}_x + \mathbf{J}_y + \mathbf{J}_z = J_x \mathbf{i} + J_y \mathbf{j} + J_z \mathbf{k}. \quad (25)$$

According to theorem of vector operation, equation (26) is available.

$$\mathbf{J}_f = \mathbf{J} - \mathbf{J}_n. \quad (26)$$

Equations (22), (23), (24), (25), and (26) are simultaneously solved; equation (27) is available.

$$\begin{aligned} \mathbf{J}_f = & [J_x(1 - \cos \alpha_1 \cos \alpha_1) - J_y \cos \alpha_2 \cos \alpha_1 \\ & - J_z \cos \alpha_3 \cos \alpha_1] \mathbf{i} + [-J_x \cos \alpha_1 \cos \alpha_2 \\ & + J_y(1 - \cos \alpha_2 \cos \alpha_2) - J_z \cos \alpha_3 \cos \alpha_2] \mathbf{j} \\ & + [-J_x \cos \alpha_1 \cos \alpha_3 - J_y \cos \alpha_2 \cos \alpha_3 \\ & + J_z(1 - \cos \alpha_3 \cos \alpha_3)]. \end{aligned} \quad (27)$$

Equation (27) is written in a matrix form:

$$\mathbf{J}_f = \begin{bmatrix} 1 - \cos^2 \alpha_1 & -\cos \alpha_2 \cos \alpha_1 & -\cos \alpha_3 \cos \alpha_1 \\ -\cos \alpha_1 \cos \alpha_2 & 1 - \cos^2 \alpha_2 & -\cos \alpha_3 \cos \alpha_2 \\ -\cos \alpha_1 \cos \alpha_3 & -\cos \alpha_2 \cos \alpha_3 & 1 - \cos^2 \alpha_3 \end{bmatrix} \begin{bmatrix} J_x \\ J_y \\ J_z \end{bmatrix}. \quad (28)$$

The total seepage flow can be obtained by integrating seepage flow of single fracture along the fracture length on the calculated cross section.

$$Q = - \int_{l_{\min}}^{l_{\max}} q(l) dN(l). \quad (29)$$

By substituting equations (8), (21), and (28) into equation (29), equation (30) becomes available:

$$\begin{aligned} Q &= \int_{l_{\min}}^{l_{\max}} \frac{\beta^{2+D_T} l_{\max}^{3+D_T}}{12\mu D_T} \left(\frac{L_0}{\sin \alpha} \right)^{1-D_T} \mathbf{J}_f D_T l_{\max}^{D_T} \Gamma^{-(D_T+1)} dl \\ &= \frac{\beta^{2+D_T} l_{\max}^{3+D_T}}{12\mu D_T} \left(\frac{L_0}{\sin \alpha} \right)^{1-D_T} \frac{D_f}{3 + D_T - D_f} \left[1 - \left(\frac{l_{\min}}{l_{\max}} \right)^{3+D_T-D_f} \right] \\ &\cdot \begin{bmatrix} 1 - \cos^2 \alpha_1 & -\cos \alpha_2 \cos \alpha_1 & -\cos \alpha_3 \cos \alpha_1 \\ -\cos \alpha_1 \cos \alpha_2 & 1 - \cos^2 \alpha_2 & -\cos \alpha_3 \cos \alpha_2 \\ -\cos \alpha_1 \cos \alpha_3 & -\cos \alpha_2 \cos \alpha_3 & 1 - \cos^2 \alpha_3 \end{bmatrix} \begin{bmatrix} J_x \\ J_y \\ J_z \end{bmatrix}. \end{aligned} \quad (30)$$

Considering $l_{\min} \ll l_{\max}$, $1 < D_T < 2$, $1 < D_f < 2$, $(l_{\min}/l_{\max})^{3+D_T-D_f} \ll 1$, equation (30) is simplified and rewritten as a matrix:

$$\begin{bmatrix} \mathbf{q}_x \\ \mathbf{q}_y \\ \mathbf{q}_z \end{bmatrix} = \frac{\beta^{2+D_T} l_{\max}^{3+D_T}}{12\mu D_T} \left(\frac{L_0}{\sin \alpha} \right)^{1-D_T} \frac{D_f}{3 + D_T - D_f} \cdot \begin{bmatrix} 1 - \cos^2 \alpha_1 & -\cos \alpha_2 \cos \alpha_1 & -\cos \alpha_3 \cos \alpha_1 \\ -\cos \alpha_1 \cos \alpha_2 & 1 - \cos^2 \alpha_2 & -\cos \alpha_3 \cos \alpha_2 \\ -\cos \alpha_1 \cos \alpha_3 & -\cos \alpha_2 \cos \alpha_3 & 1 - \cos^2 \alpha_3 \end{bmatrix} \cdot \begin{bmatrix} J_x \\ J_y \\ J_z \end{bmatrix}. \quad (31)$$

Figure 1 shows that the relationship between the direction cosine of fracture normal plane and the direction and inclination of the geodetic coordinate is as follows:

$$\begin{cases} \cos \alpha_1 = -\sin \theta \cos \alpha, \\ \cos \alpha_2 = -\sin \theta \sin \alpha, \\ \cos \alpha_3 = \cos \theta. \end{cases} \quad (32)$$

By substituting equation (32) into equation (31), equation (33) can be obtained as follows:

$$\begin{bmatrix} \mathbf{q}_x \\ \mathbf{q}_y \\ \mathbf{q}_z \end{bmatrix} = \frac{\beta^{2+D_T} l_{\max}^{3+D_T}}{12\mu D_T} \left(\frac{L_0}{\sin \alpha} \right)^{1-D_T} \frac{D_f}{3 + D_T - D_f} \cdot \begin{bmatrix} 1 - \sin^2 \theta \cos^2 \alpha & -\sin^2 \theta \sin \alpha \cos \alpha & \sin \theta \cos \theta \cos \alpha \\ -\sin^2 \theta \sin \alpha \cos \alpha & 1 - \sin^2 \theta \sin^2 \alpha & \sin \theta \cos \theta \sin \alpha \\ \sin \theta \cos \theta \cos \alpha & \sin \theta \cos \theta \sin \alpha & \sin^2 \theta \end{bmatrix} \cdot \begin{bmatrix} J_x \\ J_y \\ J_z \end{bmatrix}. \quad (33)$$

The permeability coefficient can be expressed as

$$K = \frac{\mu Q}{A_0 J}. \quad (34)$$

By substituting equations (16) and (33) into equation (34), equation (35) is obtained as follows:

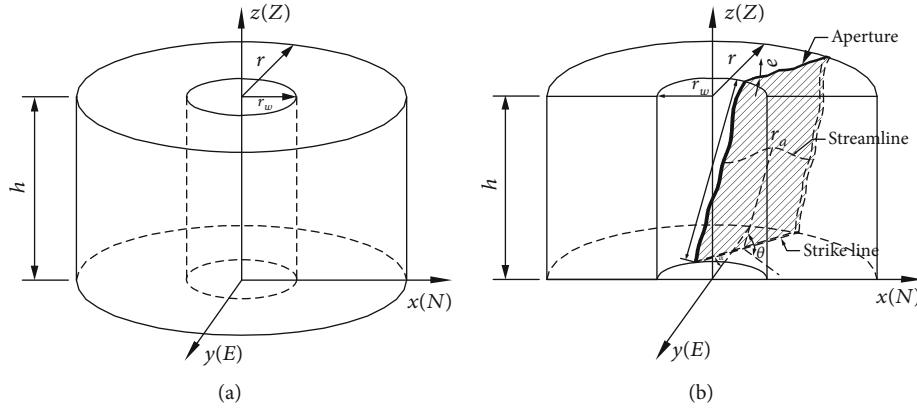


FIGURE 2: Radial flow diagram: (a) elevation view and (b) section view.

$$\mathbf{K} = \frac{\beta^{1+D_T} l^{1+D_T}}{12D_T} \left(\frac{L_0}{\sin \alpha} \right)^{1-D_T} \frac{2-D_f}{3+D_T-D_f} \frac{\emptyset}{1-\emptyset} \cdot \begin{bmatrix} 1 - \sin^2 \theta \cos^2 \alpha & -\sin^2 \theta \sin \alpha \cos \alpha & \sin \theta \cos \theta \cos \alpha \\ -\sin^2 \theta \sin \alpha \cos \alpha & 1 - \sin^2 \theta \sin^2 \alpha & \sin \theta \cos \theta \sin \alpha \\ \sin \theta \cos \theta \cos \alpha & \sin \theta \cos \theta \sin \alpha & \sin^2 \theta \end{bmatrix}. \quad (35)$$

3.2. Radial Seepage. In a three-dimensional space, the radial flow diagram is shown in Figure 2. Map coordinates and parameter definitions are consistent with Figure 1. The x - and y -axes are two coordinate directions, which are consistent with the direction of geodetic coordinates. It is assumed the x -axis is N , the y -axis is E . α is the angle between the strike line and the y -axis, and θ is the angle between the fracture plane and the horizontal plane (inclination). l is the fracture length, e is the fracture width, r_a is the seepage length of the fluid in the fracture considering the fracture roughness, r is taken as the straight line length along fracture seepage direction, r_w is radius of the hole, J_f is the tangential component of the hydraulic gradient in the fracture, and J_n is the normal component of the hydraulic gradient in the fracture.

It is assumed that the flow of fluid in the fracture can be described by the cubic law [39, 44, 54]. Equation (17) can be rewritten as follows under the condition of radial flow:

$$q(l) = \frac{e^3 l}{12\mu} \frac{dp}{dr_a}, \quad (36)$$

where $q(l)$ is a single fracture flow, μ is the dynamic viscous coefficient, e is the fracture width, l is the fracture length, and p is the water pressure. Due to the rugged surface of the fracture, the fluid seepage path in the fracture is a curve, resulting in a decrease in the flow path and an effective overcurrent capacity, as shown in Figure 2.

The relation between r_a and r can be rewritten according to equation (18) as follows:

$$r_a = e^{1-D_T} r^{D_T}. \quad (37)$$

Equation (38) can be obtained by substituting equations (4) and (37) into equation (36) as follows:

$$q(l) = \frac{\beta^{2+D_T} l^{3+D_T}}{12\mu D_T} \frac{dp}{dr}. \quad (38)$$

Similarly, the hydraulic gradient vector will be decomposed along the fracture plane in normal and tangential components [55]. Only the hydraulic gradient along the tangential direction of the fracture will produce seepage flow [12], i.e.,

$$\mathbf{q}(\mathbf{l}) = \frac{\beta^{2+D_T} l^{3+D_T}}{12\mu D_T r^{D_T-1}} \mathbf{J}_f. \quad (39)$$

On the inner side of the radial hole wall, the seepage flow of single fracture is integrated along the fracture length, and the total seepage flow can be obtained.

$$\mathbf{Q} = \frac{2\pi r_w h}{A_0} \int_{l_{\min}}^{l_{\max}} \mathbf{q}(\mathbf{l}) dN = \frac{\pi h r_w \beta^{2+D_T} l_{\max}^{3+D_T}}{6\mu D_T A_0 r^{D_T-1}} \frac{D_f}{3+D_T-D_f} \cdot \begin{bmatrix} 1 - \sin^2 \theta \cos^2 \alpha & -\sin^2 \theta \sin \alpha \cos \alpha & \sin \theta \cos \theta \cos \alpha \\ -\sin^2 \theta \sin \alpha \cos \alpha & 1 - \sin^2 \theta \sin^2 \alpha & \sin \theta \cos \theta \sin \alpha \\ \sin \theta \cos \theta \cos \alpha & \sin \theta \cos \theta \sin \alpha & \sin^2 \theta \end{bmatrix} \cdot \begin{bmatrix} J_x \\ J_y \\ J_z \end{bmatrix}. \quad (40)$$

Equation (16) is substituted into equation (40) and is rewritten in a matrix form:

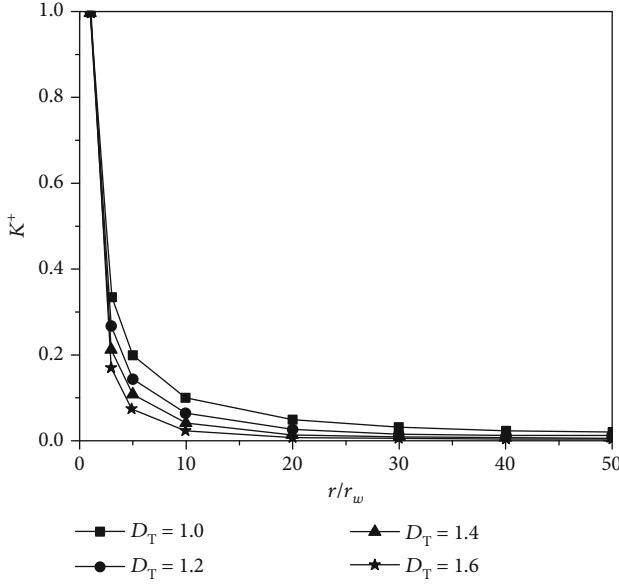


FIGURE 3: The relationship between K^+ and r/r_w .

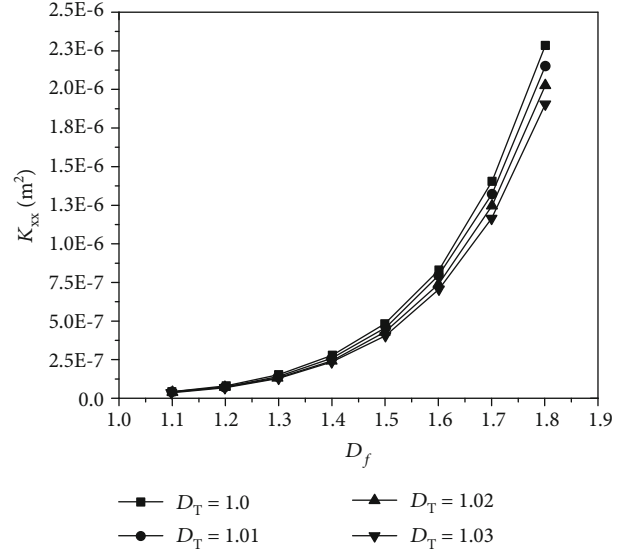


FIGURE 4: The relationship between K_{xx} and D_f ($\beta = 0.01$, $\theta = \pi/6$, and $\alpha = \pi/2$).

TABLE 1: List of calculation parameters.

Parameter	Value	Parameter description
D_f	1.1-1.8	Fractal dimension of fracture
D_T	1.0-1.7	Fractal dimension of seepage streamline
β	0.001-0.1	Ratio of fracture width and length
α	$0-\pi$	Trend
θ	$0-\pi/2$	Dip angle
l_{max}	3-30 m	Maximum fracture length
l_{min}/l_{max}	0.001	Minimum fracture length/maximum fracture length
L_0	3-180 m	Computational element length

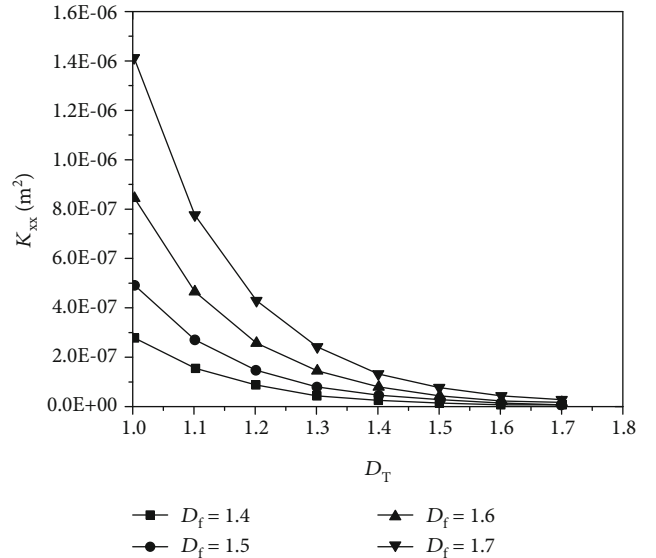


FIGURE 5: The relationship between K_{xx} and D_T ($\beta = 0.01$, $\theta = \pi/6$, and $\alpha = \pi/2$).

$$\begin{bmatrix} \mathbf{q}_x \\ \mathbf{q}_y \\ \mathbf{q}_z \end{bmatrix} = \frac{\pi h r_w \beta^{1+D_T} l_{max}^{1+D_T}}{6 \mu D_T r^{D_T-1}} \frac{2-D_f}{3+D_T-D_f} \frac{\Phi}{1-\Phi} \cdot \begin{bmatrix} 1 - \sin^2 \theta \cos^2 \alpha & -\sin^2 \theta \sin \alpha \cos \alpha & \sin \theta \cos \theta \cos \alpha \\ -\sin^2 \theta \sin \alpha \cos \alpha & 1 - \sin^2 \theta \sin^2 \alpha & \sin \theta \cos \theta \sin \alpha \\ \sin \theta \cos \theta \cos \alpha & \sin \theta \cos \theta \sin \alpha & \sin^2 \theta \end{bmatrix} \cdot \begin{bmatrix} \mathbf{J}_x \\ \mathbf{J}_y \\ \mathbf{J}_z \end{bmatrix} \quad (41)$$

Combining equations (41) and (34) and A_0 being replaced by $A_r = 2\pi r h$, equation (42) is obtained as follows:

$$\mathbf{K}(\mathbf{r}) = \frac{r_w \beta^{1+D_T} l_{max}^{1+D_T}}{12 D_T r^{D_T}} \frac{2-D_f}{3+D_T-D_f} \frac{\Phi}{1-\Phi} \cdot \begin{bmatrix} 1 - \sin^2 \theta \cos^2 \alpha & -\sin^2 \theta \sin \alpha \cos \alpha & \sin \theta \cos \theta \cos \alpha \\ -\sin^2 \theta \sin \alpha \cos \alpha & 1 - \sin^2 \theta \sin^2 \alpha & \sin \theta \cos \theta \sin \alpha \\ \sin \theta \cos \theta \cos \alpha & \sin \theta \cos \theta \sin \alpha & \sin^2 \theta \end{bmatrix} \quad (42)$$

The permeability coefficient can be expressed as follows at the inner side of the radial hole wall:

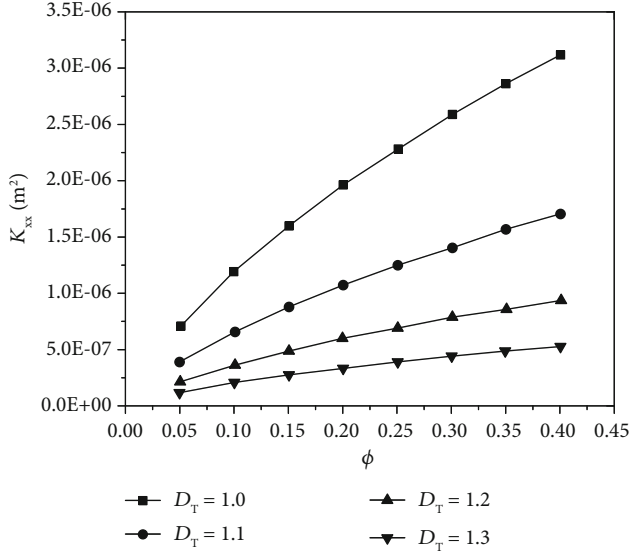


FIGURE 6: The relationship between K_{xx} and Φ ($\beta = 0.01$, $\theta = \pi/6$, and $\alpha = \pi/2$).

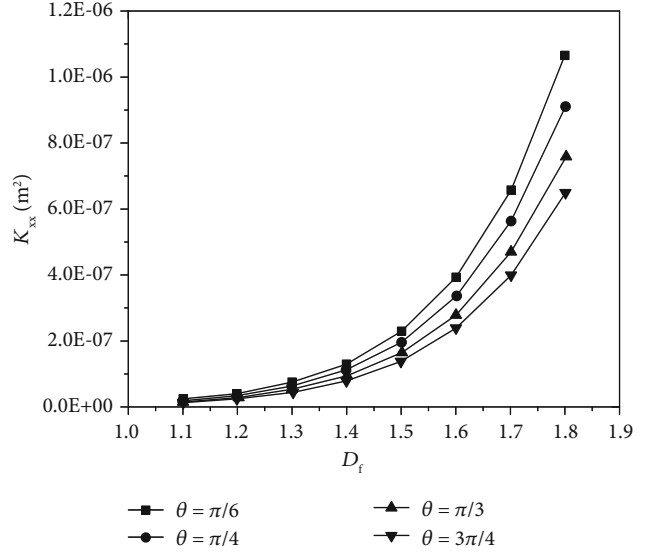


FIGURE 8: The relationship between K_{xx} and D_f ($D_T = 1.1$, $\beta = 0.01$, and $\alpha = \pi/4$).

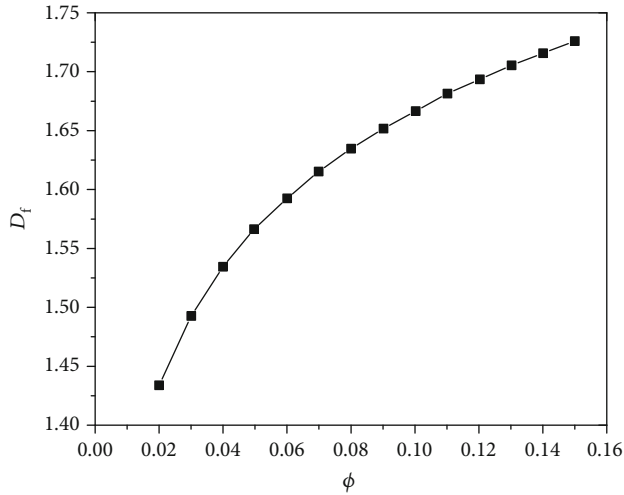


FIGURE 7: The relationship between Φ and D_f .

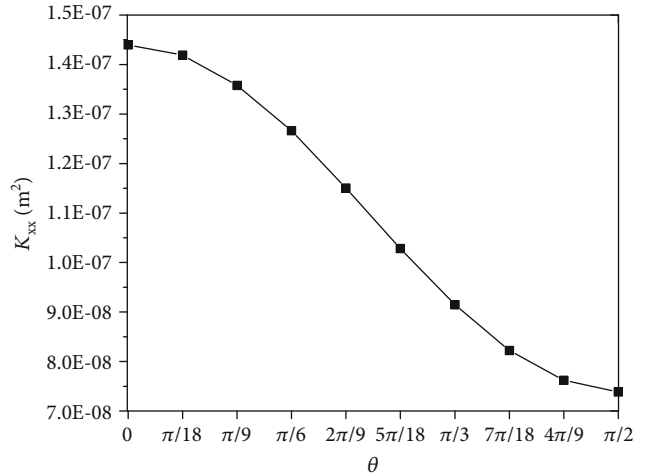


FIGURE 9: The relationship between K_{xx} and θ ($D_f = 1.4$, $D_T = 1.1$, $\beta = 0.01$, and $\alpha = \pi/4$).

$$K_w = \frac{\beta^{1+D_T} l_{\max}^{1+D_T}}{12D_T r_w^{D_T-1}} \frac{2-D_f}{3+D_T-D_f} \frac{\Phi}{1-\Phi} \cdot \begin{bmatrix} 1 - \sin^2\theta \cos^2\alpha & -\sin^2\theta \sin\alpha \cos\alpha & \sin\theta \cos\theta \cos\alpha \\ -\sin^2\theta \sin\alpha \cos\alpha & 1 - \sin^2\theta \sin^2\alpha & \sin\theta \cos\theta \sin\alpha \\ \sin\theta \cos\theta \cos\alpha & \sin\theta \cos\theta \sin\alpha & \sin^2\theta \end{bmatrix}. \quad (43)$$

From equations (42) and (43), the dimensionless permeability coefficient is obtained as follows:

$$K^+ = \frac{K_r}{K_w} = \left(\frac{r_w}{r} \right)^{D_T}. \quad (44)$$

Equation (44) shows that the dimensionless permeability coefficient is closely related to D_T and r/r_w . It decreases with the increase of D_T and decreases with the increase of r/r_w , as shown in Figure 3.

3.3. Parameter Impact Analysis. This section mainly analyzes the influence of the parameters of equations (35) and (42) on the permeability coefficient K , and the values of each parameter are shown in Table 1.

Figure 4 shows the relationship between the fractal dimension D_f and the permeability coefficient K_{xx} in the case of different D_T , and the other parameters are $\beta = 0.01$, $\theta = \pi/6$, and $\alpha = \pi/2$. As shown in Figure 4, the permeability coefficient increases with the increase of fractal dimension D_f . And with the increase of D_T , the permeability coefficient K_{xx}

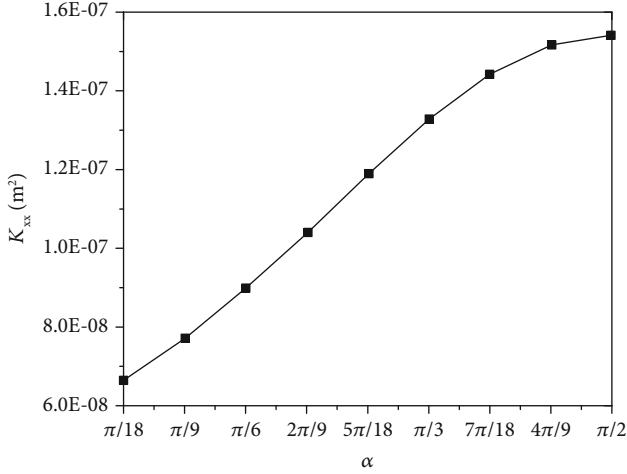


FIGURE 10: The relationship between K_{xx} and α ($D_f = 1.4$, $D_T = 1.1$, $\beta = 0.01$, and $\alpha = \pi/4$).

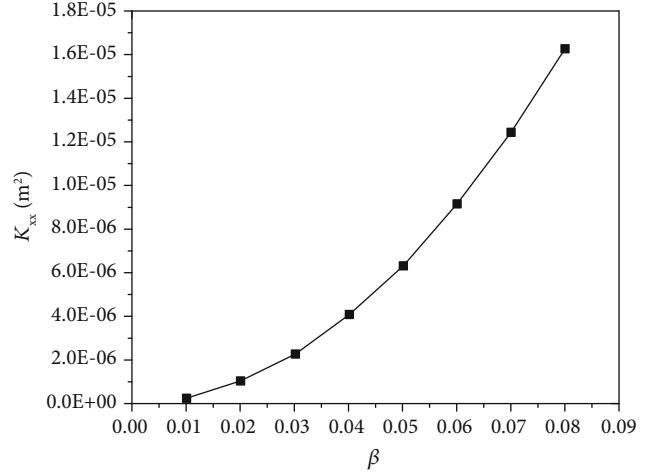


FIGURE 12: The relationship between β and K_{xx} ($D_f = 1.4$, $D_T = 1.01$, $\theta = \pi/6$, and $\alpha = \pi/2$).

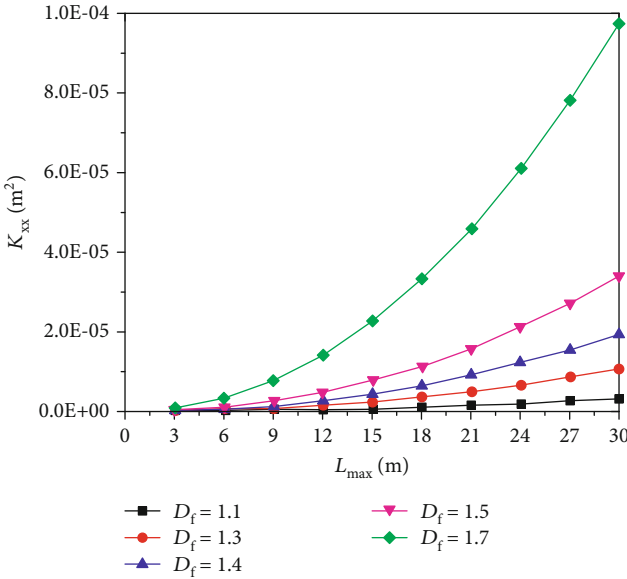


FIGURE 11: The relationship between L_{max} and K_{xx} ($D_T = 1.1$, $\beta = 0.01$, $\theta = \pi/6$, and $\alpha = \pi/2$).

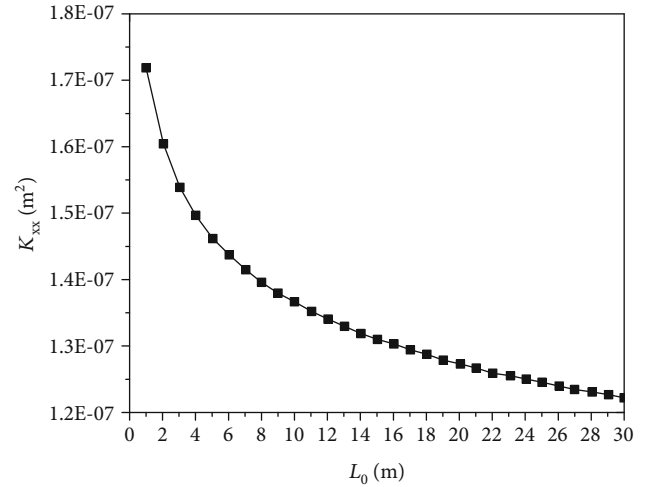


FIGURE 13: The relationship between L_0 and K_{xx} ($D_f = 1.4$, $D_T = 1.1$, $\beta = 0.01$, $\theta = \pi/4$, and $\alpha = \pi/2$).

decreases. The results show that the increase of the fracture surface roughness leads to the increase of the flow path and the decrease of flow velocity.

Figure 5 shows the relationship between D_T and permeability coefficient K_{xx} in the case of different D_f , and the other parameters are $\beta = 0.01$, $\theta = \pi/6$, and $\alpha = \pi/2$. As shown in Figure 5, with the increase of D_T , the permeability coefficient decreases rapidly. The overall permeability coefficient increases with the increase of D_f , and the larger the D_f ($D_f > 1.5$), the greater the change rate of K_{xx} with D_T , which means that when $D_f > 1.5$, the weakening effect of the fracture surface roughness on the permeability of the fracture network increases rapidly.

As can be seen from Figures 4 and 5, D_f and D_T have a significant effect on the permeability of the fracture network, but they have different physical meanings and influences. The larger the value of D_f , the more complex the fractured network, the higher the fracture density [18], and the greater the permeability coefficient. D_T reflects the flexural degree of the fluid seepage path in the fracture due to fracture surface roughness. With the increase of D_T , the seepage path is lengthened and the effective overcurrent capacity of the fracture is reduced, which leads to the decrease of the permeability coefficient of the fracture network.

Figure 6 shows the relationship between porosity Φ and permeability coefficient K_{xx} in the case of different D_T , and the other parameters are $\beta = 0.01$, $\theta = \pi/6$, and $\alpha = \pi/2$. As shown in the figure, the permeability coefficient increases with the increase of porosity Φ . In general, it can be seen from Equation (12) and Figure 7 that, assuming $l_{min}/l_{max} =$

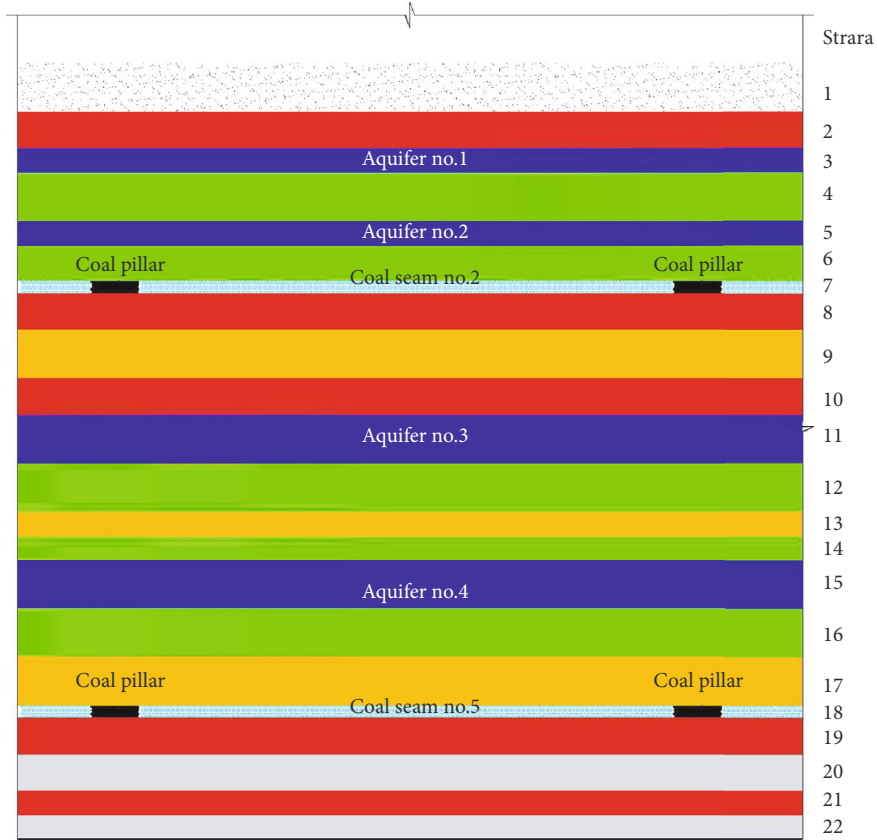


FIGURE 14: Physical model (partial) profile.

0.001, Φ is positively correlated with D_f , and thus the increase of porosity Φ and D_f increase have identity, and all reflect the increase of seepage cross section. It also shows in Figure 6 that the overall permeability coefficient decreases with the increase of D_T , and the larger the D_T ($D_T > 1.2$), the smaller the change rate of K_{xx} with Φ , which indicates that when $D_T > 1.2$, the roughness of the fracture surface will greatly offset the effect of increased permeability of the fracture network due to the increase of the seepage area.

Figure 8 shows the relationship between fractal dimension D_f and permeability coefficient K_{xx} of the fracture network under the condition of the change of the fracture dip angle θ , and the other parameters are $D_T = 1.1$, $\beta = 0.01$, and $\alpha = \pi/4$. As shown in the figure, the permeability coefficient increases with the increase of porosity D_f , which is the same as that of Figure 4. At the same time, as the fracture dip angle θ increases, the permeability coefficient K_{xx} decreases.

Figure 9 shows the relationship between the fracture dip angle θ and the permeability coefficient K_{xx} , and the other parameters are $D_f = 1.4$, $D_T = 1.1$, $\beta = 0.01$, and $\alpha = \pi/4$. As shown in Figure 9, the permeability coefficient K_{xx} decreases with the increasing of fracture dip angle θ from 0 to $\pi/2$. Figure 10 shows the relationship between the fracture strike α and the permeability coefficient K_{xx} , and the other parameters are $D_f = 1.4$, $D_T = 1.1$, $\beta = 0.01$, and $\theta = \pi/4$. As shown in Figure 10, the permeability coefficient K_{xx} increases as

the dip angle α of fracture increases from $\pi/18$ to $\pi/2$. The variation of the permeability coefficient component with the fracture strike and dip angle reflects the nonuniformity and seepage directivity of fractured rock mass.

Figure 11 shows the relationship between the maximum fracture length L_{max} and permeability coefficient K_{xx} under condition of different D_f . The other parameters are $D_T = 1.1$, $\beta = 0.01$, $\theta = \pi/6$, and $\alpha = \pi/2$. As shown in Figure 11, the permeability coefficient increases with the increase of L_{max} . At the same time, with the increase of D_f , the overall permeability coefficient will increase, and with the increase of D_f ($D_f > 1.5$), the change rate of K_{xx} with L_{max} get sharply greater, indicating that when $D_f > 1.5$, with the increase of fractal dimension, the influence of long fractures on fracture network seepage is increasing, which is consistent with the results of Li et al. [22].

Figure 12 shows the relationship between β and the permeability coefficient K_{xx} , and the other parameters are $D_f = 1.4$, $D_T = 1.01$, $\theta = \pi/6$, and $\alpha = \pi/2$. As shown in Figure 12, the permeability coefficient increases with the increase of β . Considering equation (4), this also reflects the relationship between the fracture width and the permeability coefficient to a certain extent.

Figure 13 shows the relationship between L_0 and permeability coefficient K_{xx} , and the other parameters are $D_f = 1.4$, $D_T = 1.1$, $\beta = 0.01$, $\theta = \pi/4$, and $\alpha = \pi/2$. As shown in Figure 13, the permeability coefficient decreases gradually

TABLE 2: Generalized stratigraphic parameters.

No.	Stratum	Thickness (m)	σ (MPa)	ρ (kg/m ³)
1	Aeolian sand and loess	30		2000
2	Mudstone	15	34.86	2304
3	Fine sandstone and siltstone (aquifer no.1)	10	50.00	2550
4	Mudstone	20	25.22	2204
5	Fine sandstone and siltstone (aquifer no.2)	10	5.26	2133
6	Mudstone	15	25.22	2204
7	Coal seam no. 2	5	20.07	1233
8	Mudstone	15	34.86	2304
9	Fine sandstone and siltstone	20	5.26	2133
10	Mudstone	15	34.86	2304
11	Medium-thick grained sandstone (aquifer no.3)	20	50.00	2550
12	Mudstone	20	25.22	2204
13	Fine sandstone and siltstone	10	5.26	2133
14	Mudstone	10	25.22	2204
15	Medium-thick grained sandstone (aquifer no.4)	20	50.00	2550
16	Mudstone	20	25.22	2204
17	Medium-thick grained sandstone	20	5.26	2133
18	Coal seam no. 5	5	20.07	1233
19	Mudstone	15	34.86	2304
20	Medium-thick grained sandstone	15	50.00	2550
21	Mudstone	10	34.86	2304
22	Medium-thick grained sandstone	10	50.00	2550

with the increase of L_0 . This is because the increase in L_0 is the growth of the seepage path, which means that the seepage resistance increases and the hydraulic gradient decreases.

4. Experimental Verification

4.1. Physical Model Test. Figure 14 shows a large physical model (partial) profile. According to the generalized stratigraphic parameters shown in Table 2, the similar materials arranged according to a similarity ratio are poured up and down, and the bottom pouring height of no. 2 coal seam and no. 5 coal seam was 2.25 m and 0.5 m, respectively. The thickness of the layer is 0.05 meters, the net length of working face is 2.1 meters, and the reserved pillar width is 0.3 meters. The displacement and stress changes of the overlying strata and the expansion and evolution of the fractures are studied under the conditions of different burial depth and mining speed. Figure 15 shows the distribution of the fractures of the overlying strata after the mining of no. 5 coal seam.

4.2. Water Injection Test in the Physical Model. In order to obtain the permeability parameters of the rock mass in different fracture zones and verify the fractal model of the fractured rock mass, the water injection test in the physical model was carried out after the physical model excavation was completed. In order to compare with the evolution of fracture expansion, the working face is divided into seven zones along the excavation direction, and the width of each

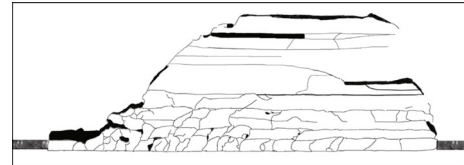


FIGURE 15: Distribution map of mining-induced fractures of no. 5 coal seam mining.

zone is 30 cm. In order to reduce the interaction of the boundary effect and the water injection holes, the water injection holes were arranged in plum blossom in the middle of the partition, as shown in Figure 16.

The location of water injection test sites is carried out at the top of the model in accordance with Figure 16 when constructing, and then the hydraulic drill is set up to conduct drilling construction, as shown in Figures 17 and 18. The water injection test is carried out by the top-down stratified water injection method to obtain the permeability parameters of different plane positions and different elevation rocks in the mining face. Meanwhile, the corresponding fracture distribution images are obtained by drilling imaging an analyzer, and the fracture images are processed digitally to obtain the fracture expansion images, as shown in Figure 19. The fracture expansion images are analyzed to extract the fracture geometric characteristic parameters, and thus the fractal

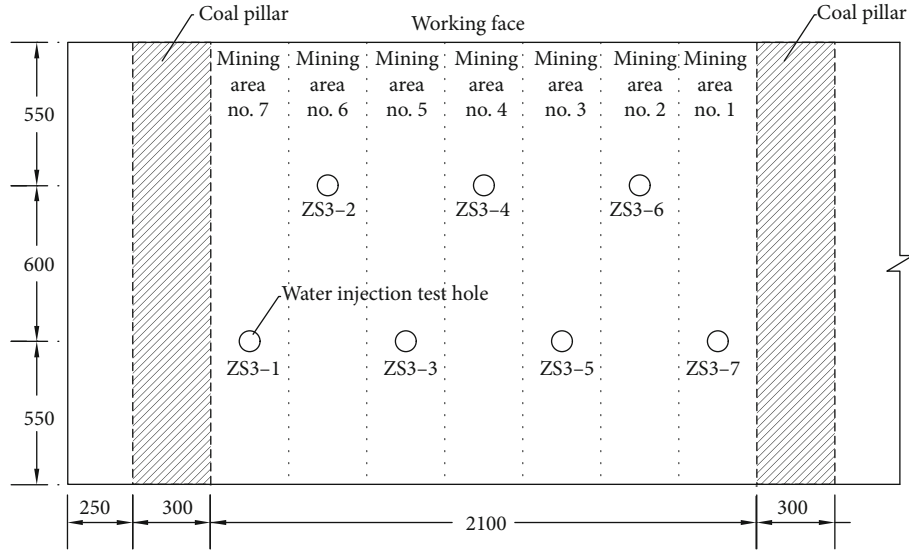


FIGURE 16: Plane layout of water injection test points (units: mm).

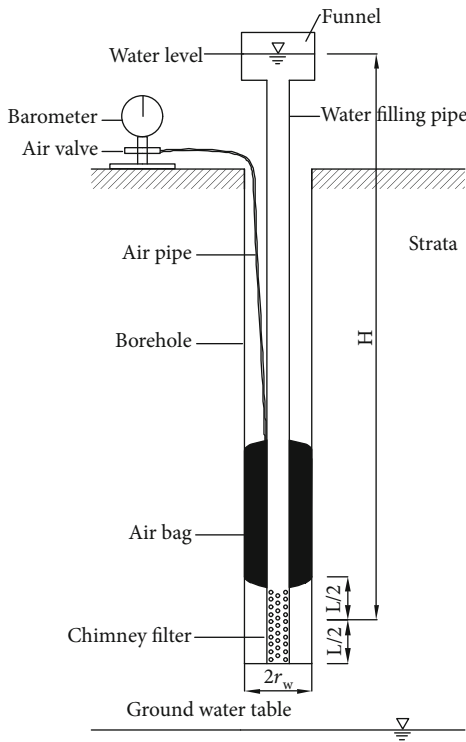


FIGURE 17: Water injection test profile.

characteristic parameters, D_T and D_f , are calculated by the box counting method [51, 56–59].

5. Analysis and Discussion

According to the field test conditions, the continuous head water injection test is used to determine the seepage per unit time in the case of constant water head and then calculate the

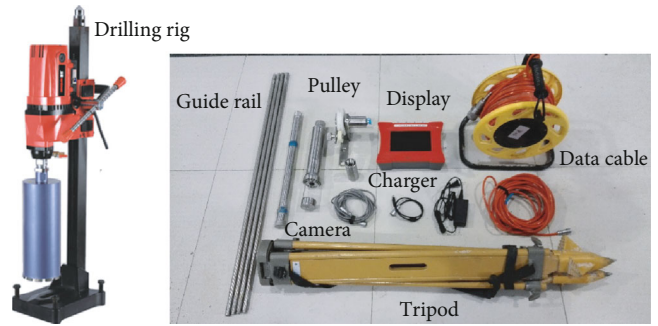


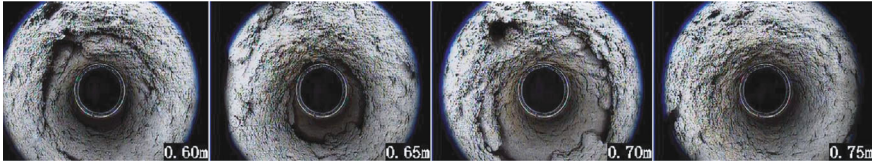
FIGURE 18: Bench drill and drilling imaging analyzer.

permeability coefficient of the simulated strata according to equation (44).

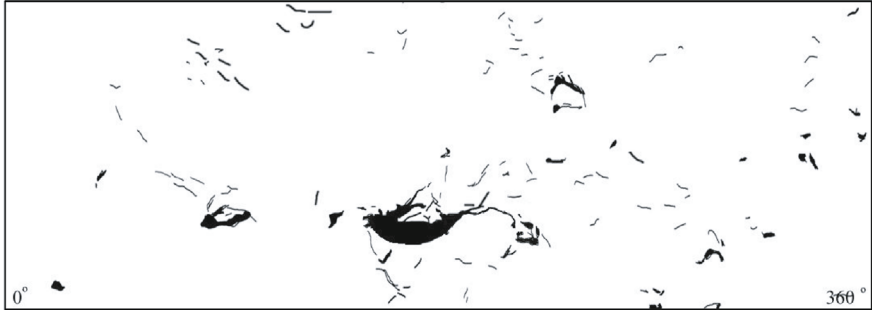
$$K = \frac{0.423Q}{lH} \lg \frac{2H}{r}, \quad (45)$$

where K is the permeability coefficient of the soil layer (cm/s), Q is the stable water flow (cm³/s), H is the test water head (cm), l is the length of the water injection section (cm), and r is the water injection test hole radius (cm).

Fracture development images are analyzed in the previous section; then the fractal characteristic parameters are extracted, and the relevant parameters are substituted into equation (42). The calculated results are compared with the K_{xx} values calculated by equation (43), as shown in Table 3. And the fractal characteristics are calculated, as shown in Figure 20. The relevant parameters are substituted into equation (41); then the calculated results are compared with the measured Q values for the water injection test, as shown in Figure 21. The calculated values of K_{xx} and Q are compared with the measured values of water injection, as shown in Figure 22. From Figures 20–22, it shows that the theoretical



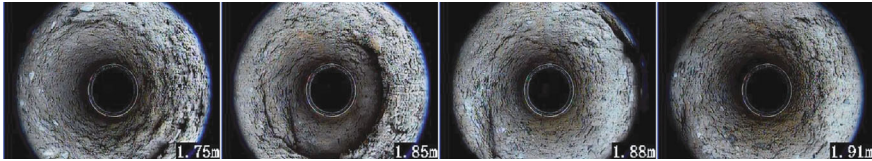
(a) Inner view in ZS3-6 (60-75 cm)



(b) Fractures developed pattern in ZS3-6 (55-65 cm)



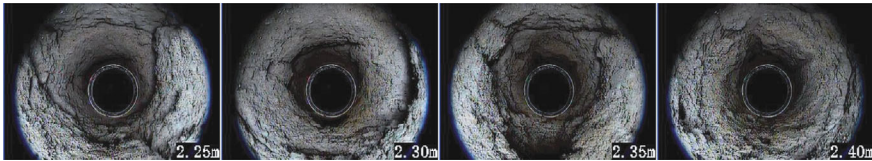
(c) Fractures developed pattern in ZS3-6 (65-75 cm)



(d) Inner view in ZS3-6 (175-191 cm)

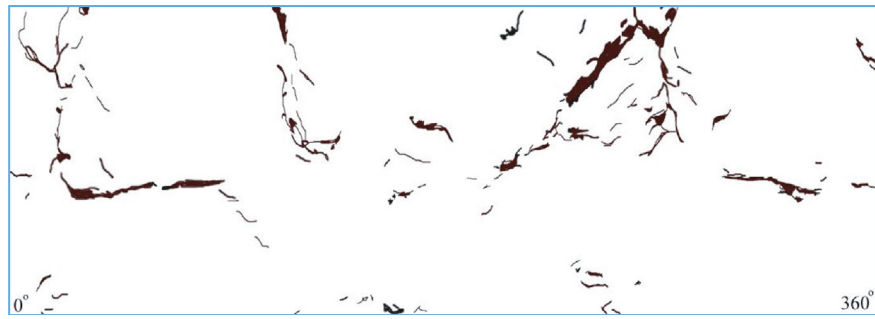


(e) Fractures developed pattern in ZS3-6 (175-191 cm)

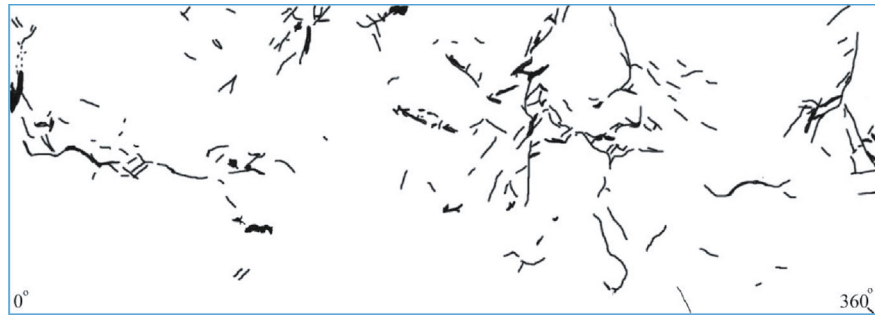


(f) Inner view in ZS3-6 (225-240 cm)

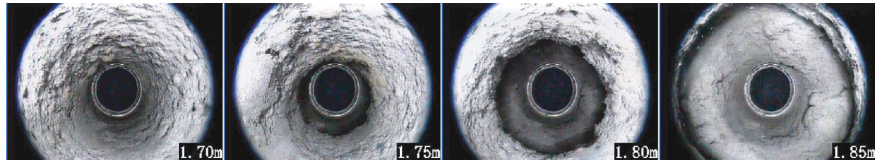
FIGURE 19: Continued.



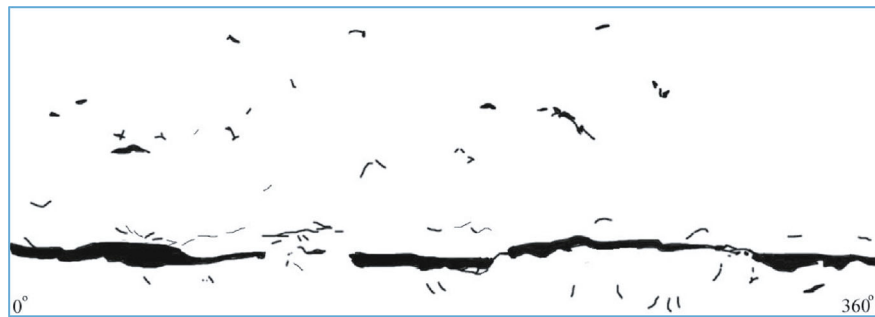
(g) Fractures developed pattern in ZS3-6 (225-235 cm)



(h) Fractures developed pattern in ZS3-6 (235-245 cm)



(i) Inner view in ZS3-4 (170-185 cm)



(j) Fractures developed pattern in ZS3-4 (175-185 cm)

FIGURE 19: Inner view of different holes and their fractures developed pattern in different depth.

TABLE 3: List of theoretical models and water injection test.

D_f	K_{xx} calculated value (cm/s)	K_{xx} test value (cm/s)	K_{xx} calculated value/ K_{xx} test value	Q calculated value (L/min)	Q test value (L/min)	Q calculated value/ Q test value
1.266	0.16	0.15	107.26%	13.16	13.68	96.19%
1.324	0.36	0.36	101.06%	19.20	21.46	89.48%
1.306	0.10	0.10	98.36%	21.90	20.00	109.51%
1.313	0.15	0.16	96.41%	32.37	29.53	109.61%
1.401	1.26	1.18	106.76%	175.53	157.95	111.13%
1.451	2.31	2.22	103.95%	322.91	298.43	108.21%

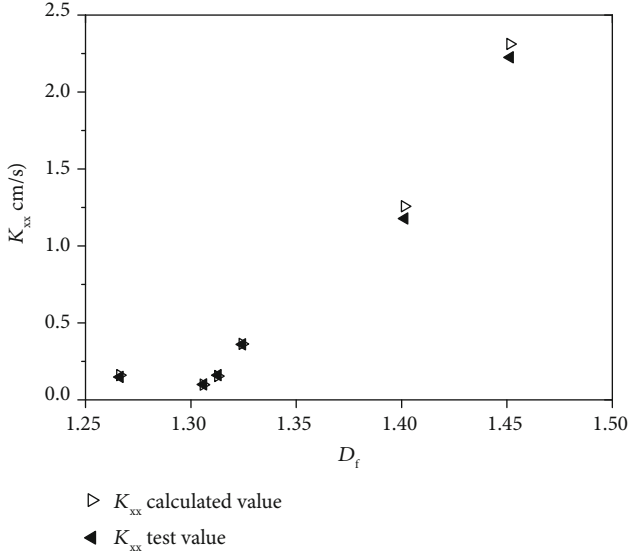


FIGURE 20: Comparison of theoretical model and water injection test K_{xx} .

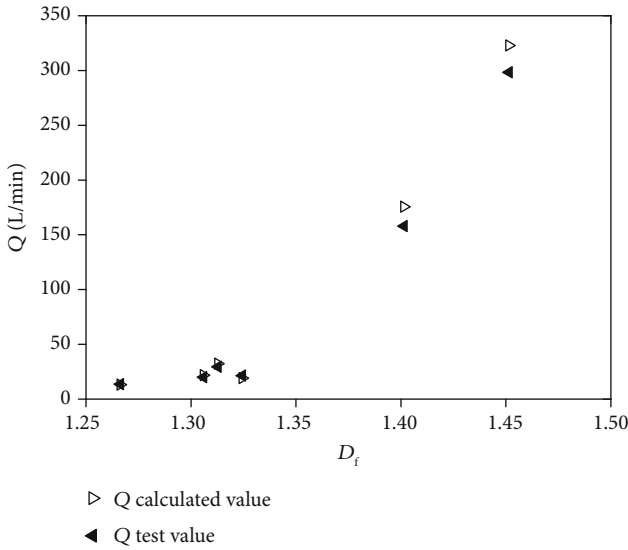


FIGURE 21: Comparison of theoretical model and water injection test Q.

calculation is in good agreement with the experimental results, which proves the validity of the theoretical model.

6. Conclusions

In this paper, a fractal model for characterizing hydraulic properties of fractured rock mass under mining influence considering fracture surface roughness is established, and the infiltration tensor of fracture network is deduced under two kinds of seepage conditions. The effects of fractal geometry and fractal characteristics on the permeability are analyzed. The validity and accuracy of the model are verified by comparing the theoretical model with the physical model water injection test. The results show the following:

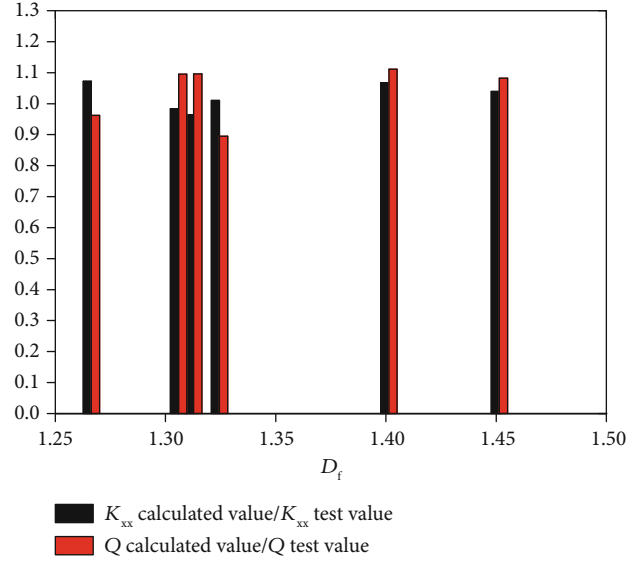


FIGURE 22: Theoretical calculated value/water injection test measured histogram of K_{xx} and Q.

- (1) The permeability coefficient K of the fracture network is a function of the geometric of fracture network. In general, the maximum fracture length L_{max} , calculation section porosity Φ and fracture network fractal dimension D_f reflect the related indicators of the calculation section, such as the fracture length, discharge area, and density, which play a role in promoting permeability. The horizontal projection length L_0 and the fractal dimension D_T of the seepage flow line reflect the obstacle of the surface roughness and the increase of the seepage path to the seepage fluid, which inhibit the permeability
- (2) With the increase of fractal dimension D_f , the permeability coefficient increases. While with the increase of D_T , the permeability coefficient decreases rapidly, and the larger the D_f ($D_f > 1.5$), the greater the change of permeability coefficient K with D_T , which indicates that when $D_f > 1.5$, the weakening effect of fracture surface roughness on the permeability of fracture network increases rapidly
- (3) D_f and D_T have a greater impact on the permeability of the fracture network, but their physical meanings and influences are different. The larger the D_f value, the more complex the fractured network in the cross section, and the higher the fracture density, thus the higher the permeability coefficient. D_T reflects the rupture degree of the fluid seepage path in the fracture due to the rough surface of the fracture. With the increase of D_T , the seepage path is lengthened and the effective overcurrent capacity of the fracture is reduced, which leads to the decrease of the permeability coefficient of the fracture network
- (4) With the increase of porosity Φ , the permeability coefficient increases. While with the increase of D_T ,

the permeability coefficient decreases. The higher the D_T ($D_T > 1.2$), the smaller the change of permeability coefficient K with the change of Φ , which shows that when $D_T > 1.2$, the fracture surface roughness will be greatly offset due to the increase of water seepage area leading to increasing effect on permeability coefficient

- (5) With the increase of L_{\max} , the permeability coefficient increases. Simultaneously, with the increase of D_f , the overall permeability coefficient will increase, and with the increase of D_f ($D_f > 1.5$), the rate of permeability coefficient K with L_{\max} change sharply increases, which shows that when $D_f > 1.5$, with the increase of fractal dimension, the influence of long fractures on fracture network seepage is increasing

Data Availability

The data used to support the findings of this study are available from the corresponding author upon request.

Conflicts of Interest

The authors declare that they have no conflicts of interest.

Acknowledgments

The authors would like to acknowledge the support from the National Key Research and Development Plan (Grant No. 2016YFC0501104), the National Natural Science Foundation of China (Grant Nos. 51522903, 51479094, and 41772246), and the Key Research and Development Plan of Ningxia Hui Autonomous Region (Grant No. 2018BCG01003).

References

- [1] V. Cvetkovic, S. Painter, N. Outters, and J. O. Selroos, "Stochastic simulation of radionuclide migration in discretely fractured rock near the Äspö Hard Rock Laboratory," *Water Resources Research*, vol. 40, no. 2, article W02404, 2004.
- [2] H. Murphy, C. Huang, Z. Dash, G. Zyvoloski, and A. White, "Semianalytical solutions for fluid flow in rock joints with pressure-dependent openings," *Water Resources Research*, vol. 40, no. 12, 2004.
- [3] R. Juanes, E. J. Spiteri, F. M. Orr Jr., and M. J. Blunt, "Impact of relative permeability hysteresis on geological CO₂ storage," *Water Resources Research*, vol. 42, no. 12, 2006.
- [4] Å. Haugen, M. A. Fernø, A. Graue, and H. J. Bertin, "Experimental study of foam flow in fractured oil-wet limestone for enhanced oil recovery," *SPE Reservoir Evaluation & Engineering*, vol. 15, no. 2, pp. 218–228, 2012.
- [5] A. Jafari and T. Babadagli, "Equivalent fracture network permeability of multilayer-complex naturally fractured reservoirs," *Transport in Porous Media*, vol. 91, no. 1, pp. 339–362, 2012.
- [6] A. Jafari and T. Babadagli, "Estimation of equivalent fracture network permeability using fractal and statistical network properties," *Journal of Petroleum Science and Engineering*, vol. 92–93, pp. 110–123, 2012.
- [7] R. Liu, B. Li, and Y. Jiang, "A fractal model based on a new governing equation of fluid flow in fractures for characterizing hydraulic properties of rock fracture networks," *Computers and Geotechnics*, vol. 75, pp. 57–68, 2016.
- [8] R. Liu, B. Li, Y. Jiang, and N. Huang, "Review: mathematical expressions for estimating equivalent permeability of rock fracture networks," *Hydrogeology Journal*, vol. 24, no. 7, pp. 1623–1649, 2016.
- [9] R. Liu, L. Yu, and Y. Jiang, "Fractal of directional permeability of gas shale fracture networks: a numerical study," *Journal of Natural Gas Science and Engineering*, vol. 33, pp. 1330–1341, 2016.
- [10] K. Min, L. Jing, and O. Stephansson, "Determining the equivalent permeability tensor for fractured rock masses using a stochastic REV approach: method and application to the field data from Sellafeld, UK," *Hydrogeology Journal*, vol. 12, no. 5, pp. 497–510, 2004.
- [11] A. Jafari and T. Babadagli, "Effective fracture network permeability of geothermal reservoirs," *Geothermics*, vol. 40, no. 1, pp. 25–38, 2011.
- [12] J. C. S. Long, J. S. Remer, C. R. Wilson, and P. A. Witherspoon, "Porous media equivalents for networks of discontinuous fractures," *Water Resources Research*, vol. 18, no. 3, pp. 645–658, 1982.
- [13] J. Long, P. Gilmour, and P. A. Witherspoon, "A model for steady fluid flow in random three-dimensional networks of disc-shaped fractures," *Water Resources Research*, vol. 21, no. 8, pp. 1105–1115, 1985.
- [14] J. Bear, C. F. Tsang, and G. de Marsily, *Flow and Contaminant Transport in Fractured Rocks*, United States, Academic Press, San Diego, CA, USA, 1993.
- [15] M. Sahimi, "Flow phenomena in rocks: from continuum models to fractals, percolation, cellular automata, and simulated annealing," *Reviews of Modern Physics*, vol. 4, no. 65, pp. 1393–1534, 1993.
- [16] M. Sahimi, *Flow and Transport in Porous Media and Fractured Rock: From Classical Methods to Modern Approaches*, John Wiley & Sons, 2011.
- [17] J. de Dreuzy D. Philippe et al., "Hydraulic properties of two-dimensional random fracture networks following a power law length distribution: 1. Effective connectivity," *Water Resources Research*, vol. 37, no. 8, pp. 2065–2078, 2001.
- [18] A. Jafari and T. Babadagli, "A sensitivity analysis for effective parameters on fracture network permeability," in *SPE Western Regional and Pacific Section AAPG Joint Meeting*, Bakersfield, CA, USA, 2008.
- [19] A. Jafari and T. Babadagli, "Relationship between percolation-fractal properties and permeability of 2-D fracture networks," *International Journal of Rock Mechanics and Mining Sciences*, vol. 60, pp. 353–362, 2013.
- [20] W. R. Rossen, Y. Gu, and L. W. Lake, "Connectivity and permeability in fracture networks obeying power-law statistics," in *SPE Permian Basin Oil and Gas Recovery Conference*, Midland, TX, USA, 2000.
- [21] R. Parashar and D. M. Reeves, "On iterative techniques for computing flow in large two-dimensional discrete fracture networks," *Journal of Computational and Applied Mathematics*, vol. 236, no. 18, pp. 4712–4724, 2012.
- [22] B. Li, R. Liu, and Y. Jiang, "A multiple fractal model for estimating permeability of dual-porosity media," *Journal of Hydrology*, vol. 540, pp. 659–669, 2016.
- [23] C. C. Barton and E. Larsen, "Fractal geometry of two-dimensional fracture networks at Yucca Mountain,

- Southwestern Nevada," in *Fundamentals of Rock Joints: Proceedings of the International Symposium on Fundamentals of Rock Joints*, Björkliden, Lapland, Sweden, 1985.
- [24] P. R. La Pointe, "A method to characterize fracture density and connectivity through fractal geometry," *International Journal of Rock Mechanics and Mining Sciences & Geomechanics Abstracts*, vol. 25, no. 6, pp. 421–429, 1988.
- [25] C. C. Barton and P. A. Hsieh, "Physical and hydrologic-flow properties of fractures," in *28th International Geological Congress Field Trip Guidebook*, 1989.
- [26] B. Berkowitz and A. Hadad, "Fractal and multifractal measures of natural and synthetic fracture networks," *Journal of Geophysical Research: Solid Earth*, vol. 102, no. B6, pp. 12205–12218, 1997.
- [27] B. Yu and P. Cheng, "A fractal permeability model for bi-dispersed porous media," *International Journal of Heat and Mass Transfer*, vol. 45, no. 14, pp. 2983–2993, 2002.
- [28] B. Yu, M. Zou, and Y. Feng, "Permeability of fractal porous media by Monte Carlo simulations," *International Journal of Heat and Mass Transfer*, vol. 48, no. 13, pp. 2787–2794, 2005.
- [29] P. Xu, B. Yu, Y. Feng, and Y. Liu, "Analysis of permeability for the fractal-like tree network by parallel and series models," *Physica A: Statistical Mechanics and its Applications*, vol. 369, no. 2, pp. 884–894, 2006.
- [30] J. Cai, B. Yu, M. Zou, and M. Mei, "Fractal analysis of invasion depth of extraneous fluids in porous media," *Chemical Engineering Science*, vol. 65, no. 18, pp. 5178–5186, 2010.
- [31] P. Xu, "A discussion on fractal models for transport physics of porous media," *Fractals*, vol. 23, no. 3, article 1530001, 2015.
- [32] T. Miao, S. Cheng, A. Chen, and B. Yu, "Analysis of axial thermal conductivity of dual-porosity fractal porous media with random fractures," *International Journal of Heat and Mass Transfer*, vol. 102, pp. 884–890, 2016.
- [33] Q. Zheng and B. Yu, "A fractal permeability model for gas flow through dual-porosity media," *Journal of Applied Physics*, vol. 111, no. 2, article 024316, 2012.
- [34] M. Yun, B. Yu, and J. Cai, "Analysis of seepage characters in fractal porous media," *International Journal of Heat and Mass Transfer*, vol. 52, no. 13–14, pp. 3272–3278, 2009.
- [35] P. Xu, B. Yu, X. Qiao, S. Qiu, and Z. Jiang, "Radial permeability of fractured porous media by Monte Carlo simulations," *International Journal of Heat and Mass Transfer*, vol. 57, no. 1, pp. 369–374, 2013.
- [36] T. Miao, B. Yu, Y. Duan, and Q. Fang, "A fractal analysis of permeability for fractured rocks," *International Journal of Heat and Mass Transfer*, vol. 81, pp. 75–80, 2015.
- [37] T. Miao, S. Yang, Z. Long, and B. Yu, "Fractal analysis of permeability of dual-porosity media embedded with random fractures," *International Journal of Heat and Mass Transfer*, vol. 88, pp. 814–821, 2015.
- [38] R. Liu, Y. Jiang, B. Li, and X. Wang, "A fractal model for characterizing fluid flow in fractured rock masses based on randomly distributed rock fracture networks," *Computers and Geotechnics*, vol. 65, pp. 45–55, 2015.
- [39] R. W. Parsons, "Permeability of idealized fractured rock," *Society of Petroleum Engineers Journal*, vol. 6, no. 2, pp. 126–136, 1966.
- [40] D. T. Snow, "Anisotropic permeability of fractured media," *Water Resources Research*, vol. 5, no. 6, pp. 1273–1289, 1969.
- [41] B. B. Mandelbrot, *The Fractal Geometry of Nature*, Freeman, San Francisco, 1982.
- [42] A. Majumdar and B. Bhushan, "Role of fractal geometry in roughness characterization and contact mechanics of surfaces," *Journal of Tribology*, vol. 112, no. 2, pp. 205–216, 1990.
- [43] R. A. Schultz, R. Soliva, H. Fossen, C. H. Okubo, and D. M. Reeves, "Dependence of displacement-length scaling relations for fractures and deformation bands on the volumetric changes across them," *Journal of Structural Geology*, vol. 30, no. 11, pp. 1405–1411, 2008.
- [44] C. Klimczak, R. A. Schultz, R. Parashar, and D. M. Reeves, "Cubic law with aperture-length correlation: implications for network scale fluid flow," *Hydrogeology Journal*, vol. 18, no. 4, pp. 851–862, 2010.
- [45] A. Torabi and S. S. Berg, "Scaling of fault attributes: a review," *Marine and Petroleum Geology*, vol. 28, no. 8, pp. 1444–1460, 2011.
- [46] J. Chang and Y. C. Yortsos, "Pressure-transient analysis of fractal reservoirs," *SPE Reservoir Evaluation & Engineering*, vol. 5, no. 1, pp. 31–38, 1990.
- [47] K. Watanabe and H. Takahashi, "Fractal geometry characterization of geothermal reservoir fracture networks," *Journal of Geophysical Research: Solid Earth*, vol. 100, no. B1, pp. 521–528, 1995.
- [48] E. Bonnet, O. Bour, N. E. Odling et al., "Scaling of fracture systems in geological media," *Reviews of Geophysics*, vol. 39, no. 3, pp. 347–383, 2001.
- [49] J. S. Andrade, E. A. Oliveira, A. A. Moreira, and H. J. Herrmann, "Fracturing the optimal paths," *Physical Review Letters*, vol. 103, no. 22, article 225503, 2009.
- [50] B. Yu and J. Li, "Some fractal characters of porous media," *Fractals*, vol. 09, no. 3, pp. 365–372, 2001.
- [51] B. Yu, "Analysis of flow in fractal porous media," *Applied Mechanics Reviews*, vol. 61, article 050801, 2008.
- [52] M. Khamforoush, K. Shams, J. F. Thovert, and P. M. Adler, "Permeability and percolation of anisotropic three-dimensional fracture networks," *Physical Review E*, vol. 77, no. 5, article 056307, 2008.
- [53] B. Massart, M. Paillet, V. Henrion et al., "Fracture characterization and stochastic modeling of the granitic basement in the HDR Soultz Project (France)," in *Proceedings World Geothermal Congress 2010*, Bali, Indonesia, 2010.
- [54] C. E. Neuzil and J. V. Tracy, "Flow through fractures," *Water Resources Research*, vol. 1, no. 17, pp. 191–199, 1981.
- [55] Q. Zhong, J. S. Chen, and L. Chen, "Symmetry certification of permeability tensor and derivation of principal permeability of fractured rock mass," *Journal of Rock Mechanics and Engineering*, vol. 25, no. S1, pp. 2997–3002, 2006.
- [56] M. Madadi, C. D. Van Siclen, and M. Sahimi, "Fluid flow and conduction in two-dimensional fractures with rough, self-affine surfaces: a comparative study," *Journal of Geophysical Research*, vol. 108, no. B8, p. 2396, 2003.
- [57] M. Madadi and M. Sahimi, "Lattice Boltzmann simulation of fluid flow in fracture networks with rough, self-affine surfaces," *Physical Review E*, vol. 67, no. 2, article 026309, 2003.
- [58] A. Yazdi, H. Hamzehpour, and M. Sahimi, "Permeability, porosity, and percolation properties of two-dimensional disordered fracture networks," *Physical Review E*, vol. 84, no. 4, article 046317, 2011.
- [59] T. A. Tafti, M. Sahimi, F. Aminzadeh, and C. G. Sammis, "Use of microseismicity for determining the structure of the fracture network of large-scale porous media," *Physical Review E*, vol. 87, no. 3, article 032152, 2013.

Research Article

The Role of In Situ Stress in Organizing Flow Pathways in Natural Fracture Networks at the Percolation Threshold

Chuanyin Jiang,¹ Xiaoguang Wang ,² Zhixue Sun,^{1,2} and Qinghua Lei³

¹School of Petroleum Engineering, China University of Petroleum (East China), Qingdao, China

²Hydrosociences Montpellier, UMR 5569 CNRS-IRD-UM, Montpellier, France

³Department of Earth Sciences, ETH Zurich, Switzerland

Correspondence should be addressed to Xiaoguang Wang; x.wang0127@gmail.com

Received 24 July 2019; Accepted 13 November 2019; Published 16 December 2019

Guest Editor: Tanguy Robert

Copyright © 2019 Chuanyin Jiang et al. This is an open access article distributed under the Creative Commons Attribution License, which permits unrestricted use, distribution, and reproduction in any medium, provided the original work is properly cited.

We investigated the effect of in situ stresses on fluid flow in a natural fracture network. The fracture network model is based on an actual critically connected (i.e., close to the percolation threshold) fracture pattern mapped from a field outcrop. We derive stress-dependent fracture aperture fields using a hybrid finite-discrete element method. We analyze the changes of aperture distribution and fluid flow field with variations of in situ stress orientation and magnitude. Our simulations show that an isotropic stress loading tends to reduce fracture apertures and suppress fluid flow, resulting in a decrease of equivalent permeability of the fractured rock. Anisotropic stresses may cause a significant amount of sliding of fracture walls accompanied with shear-induced dilation along some preferentially oriented fractures, resulting in enhanced flow heterogeneity and channelization. When the differential stress is further elevated, fracture propagation becomes prevailing and creates some new flow paths via linking preexisting natural fractures, which attempts to increase the bulk permeability but attenuates the flow channelization. Comparing to the shear-induced dilation effect, it appears that the propagation of new cracks leads to a more prominent permeability enhancement for the natural fracture system. The results have particularly important implications for predicting the hydraulic responses of fractured rocks to in situ stress fields and may provide useful guidance for the strategy design of geofluid production from naturally fractured reservoirs.

1. Introduction

Fractured rocks host a significant proportion of the world's georesources, e.g., groundwater, hydrocarbon, and geothermal energy. Fractured reservoirs are known to be highly heterogeneous with the main flow paths dominated by intricate fracture networks. The spatial distribution and organization of natural fractures in the subsurface are highly complex, often exhibiting long-range correlation and spatial. Furthermore, the transmissivity of fractures shows strong variations in both magnitude and space. As a result, fractured reservoirs often accommodate strong flow heterogeneities across multiple length scales [1–3].

A typical workflow for fractured reservoir characterization starts by constructing a flow model, which requires the geometrical and hydraulic properties of the studied fracture network to be defined [4]. Such a model is often difficult to

build due to limited subsurface measurements. Therefore, fracture patterns from outcrop analogues are commonly used to enhance the understanding regarding the key characteristics of the fracture network [5–8]. With a thorough fracture characterization, the emergent geological model may provide a good geometrical representation of the studied fracture system; however, it may still fail completely to reproduce the system's hydrodynamic behavior. This failure arises from the difficulties in relating surface characterization to subsurface fracture network properties (e.g., fracture aperture and connectivity), due to resolution limits of geophysical tools [9]. Moreover, since fractures are subject to *in situ* stresses in the subsurface environment, fracture apertures can be often strongly modified from their initial values and exhibit a highly heterogeneous distribution [10–12]. The aperture heterogeneity may lead to a highly channelized flow pattern [7, 13–15]. Extensive field observations have shown that the

contribution of individual fractures in the network to the total flow is not equal [16–18]. Instead, the majority of the fluid flow is restricted to only a small number of fractures [19–22]. Consequently, in order to predict the hydrodynamic behavior of fractured rocks, it is crucial to include the impact of in situ stresses on fluid flow.

A few recent studies have shown that the *in situ* stresses may exert a complex impact on the bulk hydraulic properties of fractured rocks due to a variety of fracture responses such as closure, sliding, dilatancy, and propagation [23–29]. Based on orthogonally imposed stress boundary conditions, numerical simulations have revealed that confining stresses tend to reduce fracture apertures and flow magnitude [23, 28], while large differential stresses often cause strong sliding along preferentially oriented rough fractures, which dilates fracture aperture and leads to permeability enhancement and flow channelization [7, 14, 25, 26, 28, 30]. On the other hand, the propagation of new cracks may also generate changes to the bulk flow properties through modifying the connectivity of fracture networks. This effect may be significant as natural fracture networks are often found to be close to the percolation threshold, i.e., critically connected [31, 32].

In reviewing the literature, it is found that little effort has been devoted to quantifying the changes of flow structures in critically connected fracture systems due to stress loading and understanding the mechanisms of geomechanical effects that alter fluid flow. In particular, which geomechanical process (e.g., fracture dilation or propagation) dominates flow structure alteration remains an open question. In this work, we perform a generic study using high-fidelity numerical simulations with representative parameters to explore how the fluid flow properties change with in situ stresses for a natural fracture network whose connectivity state is close to the percolation threshold and further elucidate the mechanisms underpinning the changes. The remainder of the paper is organized as follows. In Section 2, we present the numerical methods used in this work for modeling fracture network geometry, geomechanical deformation, and fluid flow of a naturally fractured rock. The set-up and boundary conditions of numerical experiments are presented in Section 3. The numerical simulation results are given in Section 4 with an emphasis on comparing the relative change in flow magnitude and organization caused by shear-induced dilation and fracture propagation. Finally, a brief discussion and conclusions are given in Section 5.

2. Models and Methods

2.1. Natural Fracture Network. The natural fracture network used in our simulations was mapped on a field outcrop of the Devonian sandstone at the Hornelen Basin, Norway (Figure 1(a)) [33]. Due to direct field measurements for a complete 3D characterization which is difficult to obtain, the sampled fracture patterns are limited to 2D. The fracture network covering an area of 18 m × 18 m consists three major fracture sets of mean set orientation of 5°, 50°, and 120° (Figures 1(b)–1(d)). This 2D natural fracture network has a connectivity close to the percolation threshold such that the system is in a critical state in between well-connected and

disconnected [34, 35]. The fracture network has been studied extensively in the past to investigate the geometrical organization and distribution of fractures [2, 34, 36] and their influence on fluid flow [8, 37] and mass transport [5, 33] properties of fractured rocks. In this paper, we use this fracture network to further examine the impact of in situ stresses on the flow structure.

2.2. Geomechanical Model. The geomechanical deformation of the fracture network in response to in situ stresses is simulated using a hybrid finite-discrete element method [38]. The geomechanical model can realistically capture the deformation of intact rock, interaction of matrix blocks, variability of local stresses, displacement of preexisting fractures, and propagation of new cracks [14, 27]. The closure of rock fractures under compression is calculated based on a hyperbolic relation (Bandis et al., 1983):

$$v_n = \frac{\sigma_n v_m}{k_{n0} v_m + \sigma_n}, \quad (1)$$

where v_n is the normal closure, σ_n is the effective normal compressive stress, k_{n0} is the initial normal stiffness, and v_m is the maximum allowable closure. The dependency of the shear behaviour of fractures on the normal stress loading is described using a constant displacement model parameterised with fixed u_p and u_r values [39]. In this model, the peak shear stress τ_p is given by [40]:

$$\tau_p = \sigma_n \tan(\phi_b + \phi_i)(1 - a_s) + a_s c, \quad (2)$$

where a_s is the proportion of total fracture area sheared through asperities, i is the dilation angle, c is the shear strength of the asperity (i.e., cohesion of the intact rock), and ϕ_b is the basic friction angle which is substituted using the residual friction angle ϕ_r [41]. If σ_n does not exceed the uniaxial compressive strength of the intact rock σ_u , the values of a_s and ϕ_i are, respectively, given as [40]:

$$a_s = 1 - \left(1 - \frac{\sigma_n}{\sigma_u}\right)^{m_1},$$

$$\tan \phi_i = \begin{cases} \left(1 - \frac{\sigma_n}{\sigma_u}\right)^{m_2} \tan \phi_{i0}, & \text{for } u \leq u_r, \\ 0, & \text{for } u > u_r, \end{cases} \quad (3)$$

where ϕ_{i0} is the initial dilation angle when $\sigma_n = 0$, and m_1 and m_2 are empirical parameters with suggested values of 1.5 and 4.0, respectively. The residual shear stress τ_r is given as [41]:

$$\tau_r = \sigma_n \tan \phi_r. \quad (4)$$

The dilational displacement v_s is related to the shear displacement u in an incremental form as [40]:

$$dv_s = -\tan \phi_i du. \quad (5)$$

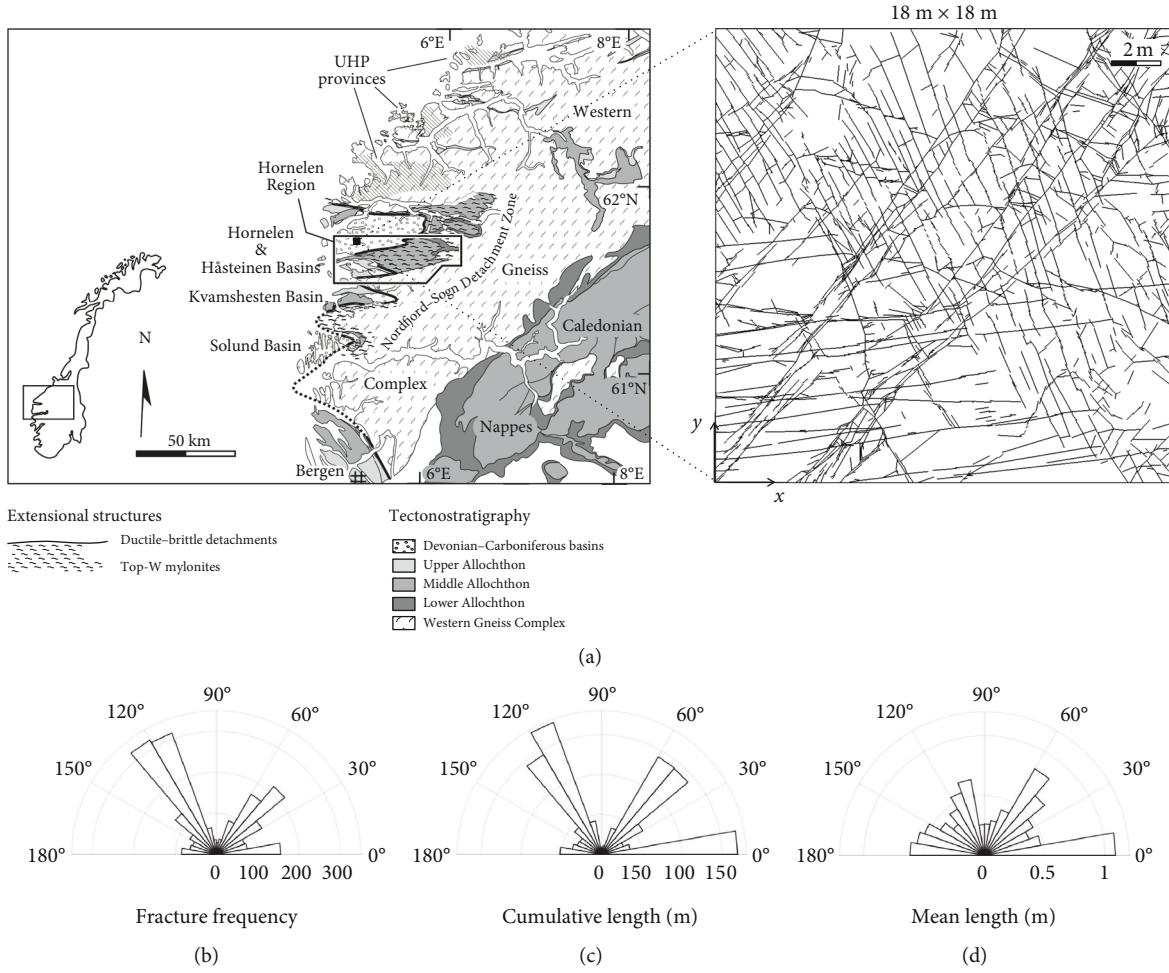


FIGURE 1: (a) The location of the outcrop. (b) A natural fracture network mapped at Hornelen Basin, Norway [33]. (b–d) Fracture statistics.

The fracture aperture h under coupled normal and shear loadings is thus given by [10]:

$$h = \begin{cases} h_0 + w, & \sigma_n < 0, \\ h_0 - \nu_n - \nu_s, & \sigma_n \geq 0, \end{cases} \quad (6)$$

where h_0 is the initial aperture, and w is the separation of opposing fracture walls if the fracture is under tension.

2.3. Fluid Flow Model. We model a single-phase steady-state flow of incompressible fluids through the fractured rock (formed by a fracture population and permeable matrix) by solving the Laplace equation,

$$\nabla \cdot (k \nabla p) = 0, \quad (7)$$

where k is the intrinsic permeability and p is the fluid pressure. The model domain is discretized by an unstructured mesh with 2D triangular matrix elements and 1D lower dimensional fracture elements. The pressure field is solved using the finite element method. The flow velocity at the barycenter of each element is

computed based on the pressure gradient vector field by applying Darcy's law:

$$\mathbf{u}^e = -\frac{k^e}{\mu} \nabla p^e, \quad (8)$$

while \mathbf{u}^e is the velocity vector field, p^e is the local pressure at element nodes, μ is the dynamic fluid viscosity, and k^e is the local permeability. In the computational mesh, the local permeability is constant for all matrix elements while spatially variable for fracture elements. The fracture permeabilities are determined according to the cubic law [42] based on the stress-dependent fracture apertures.

2.4. Quantitative Indices for Flow Field Evaluation. To quantify the stress effects on fluid flow, we compute three network-scale indices: (i) the network equivalent permeability, (ii) the correlation dimension of the flow rate field, and (iii) the flow channeling density indicator. The network equivalent permeability provides a measure of the overall flow capacity [43, 44] of the fracture network, while the correlation dimension and flow channeling density indicator characterize how the flow is spatially organized in the system [30, 45–48].

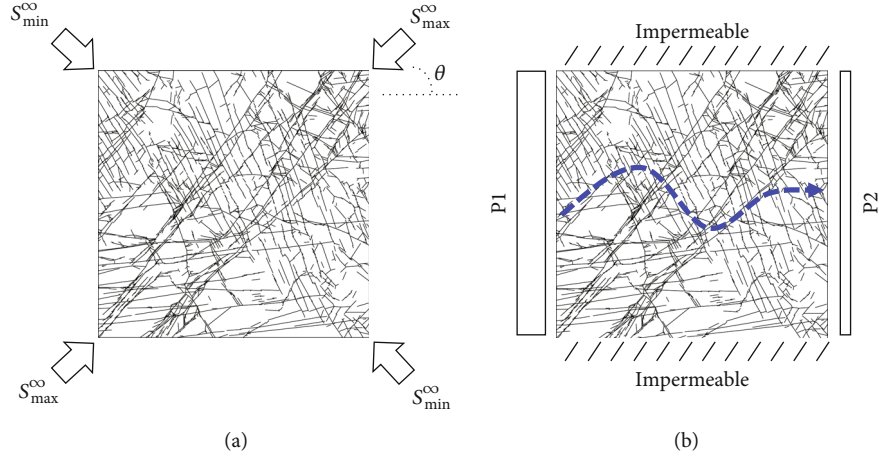


FIGURE 2: (a) Far-field stress boundary conditions for geomechanical simulation. (b) Hydraulic boundary conditions for fluid flow simulation.

The network equivalent permeability is obtained using Darcy's law:

$$k_{\text{eff}} = \frac{\mu QL}{A(p_{\text{in}} - p_{\text{out}})}, \quad (9)$$

where Q is the volumetric flow rate through the inlet face of the fractured rock, L is the length of the model domain, A is the outlet cross-section area, and p_{in} and p_{out} are the hydraulic head at inlet and outlet, respectively.

The correlation dimension of the flow rate field D_2 is defined as [49, 50]:

$$D_2 = \lim_{r \rightarrow 0} \frac{\log \sum_{k=1}^M P_k^2}{\log r}, \quad (10)$$

where P_k is the proportion of flow within an elemental area to the cumulative amount of flow in the entire grid, and r is the dimension of the grid elements. In this work, we use a 30 by 30 square grid in our calculation of D_2 , thus r equals to 0.6 m.

The flow channeling density indicator d_Q , similar to the participation ratio in the physics literature [51, 52], is defined as [46, 47]:

$$d_Q = \frac{1}{S} \cdot \frac{(\sum_f L_f \cdot Q_f)^2}{(\sum_f L_f \cdot Q_f^2)}, \quad (11)$$

where Q_f is the fracture flow rate, L_f is the fracture length, S is the cumulative fracture length of the entire network. The inverse of d_Q defines the average spacing of main flow paths [46]. A small d_Q indicates a large distance between main flow paths, and thus a highly channeled flow pattern.

3. Model Set-Up

In this study, the stress-dependent fracture aperture fields are obtained by imposing effective far-field stresses to the fracture network at various angles ranging from 0° to 170° with an increment of 10° (Figure 2(a)). We consider five

TABLE 1: Material properties for geomechanical computation.

Properties	Value	Unit
Density	2500	kg·m ⁻³
Young's modulus	20	GPa
Poisson's ratio	0.25	—
Internal friction coefficient	0.85	—
Intact rock cohesion	40	MPa
Tensile strength	20	MPa
Mode I energy release rate	396	J/m ²
Mode II energy release rate	495	J/m ²
Fracture initial normal stiffness	50	GPa/m
Fracture residual friction angle	30	deg
Fracture initial dilation angle	10	deg
Fluid density	1000	kg/m ³
Dynamic viscosity	0.001	Pa·s
Rock density	2650	kg/m ³
Gravity acceleration	9.8	m/s ²
Initial fracture aperture	0.1	mm
Matrix permeability	1.0×10^{-15}	m ²

different stress scenarios: (i) $S_{\text{max}} = S_{\text{min}} = 0.0$ MPa (reference case); (ii) $S_{\text{max}} = S_{\text{min}} = 5.0$ MPa; (iii) $S_{\text{max}} = 10.0$ MPa, $S_{\text{min}} = 5.0$ MPa; (iv) $S_{\text{max}} = 15.0$ MPa, $S_{\text{min}} = 5.0$ MPa; and (v) $S_{\text{max}} = 20.0$ MPa, $S_{\text{min}} = 5.0$ MPa. The initial aperture field is assumed constant as $h_0 = 0.1$ mm, which is representative for nature fractures [53–55].

We simulate a single-phase steady-state flow through the deformed fracture networks by applying the classical permeameter-type boundary condition (Figure 2(b)): two opposite model boundaries have constant hydraulic heads, which create a fixed pressure gradient (i.e., 10 kPa), while the two orthogonal boundaries parallel to the flow direction are impervious. The matrix permeability k_m is assumed constant in space with a value of 1×10^{-15} m². The material properties of the fractured rocks and fluids used in the simulations (Table 1) are typical for sandstone formations [5]. In this work, we focus on discussing the cases where the flow is

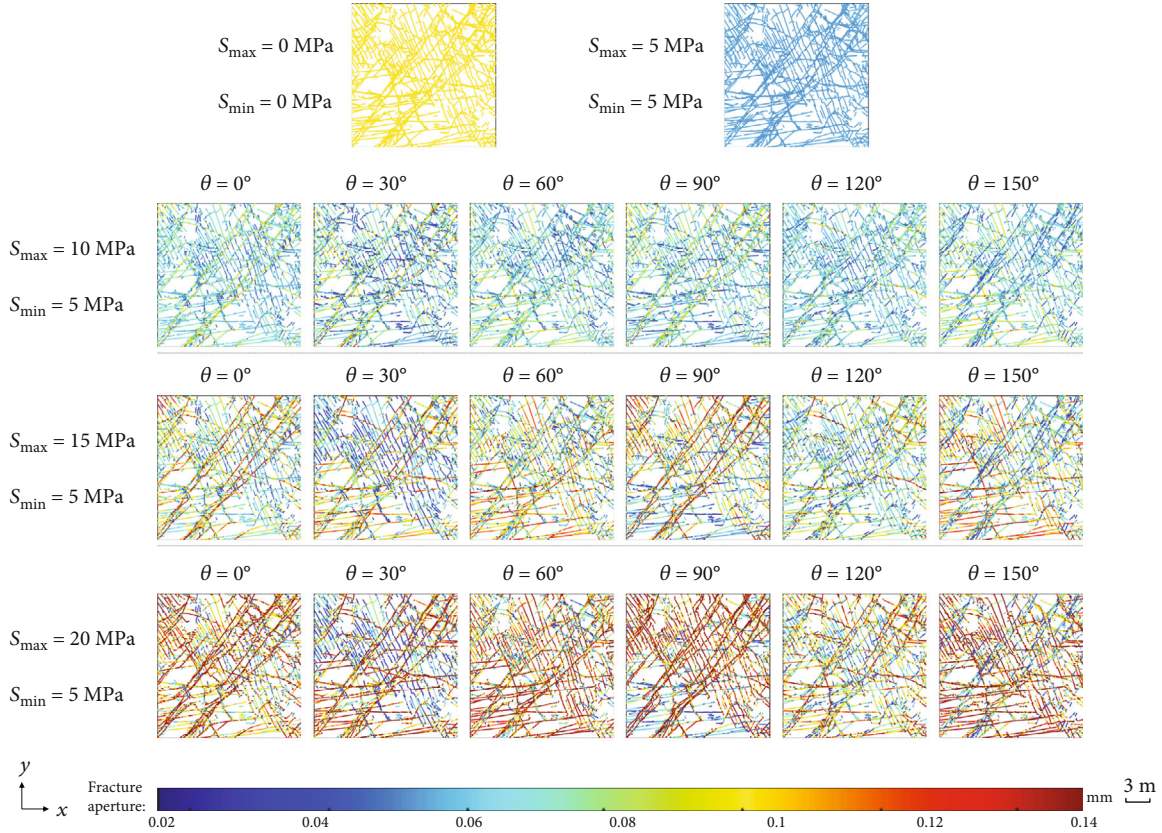


FIGURE 3: Distributions of fracture apertures in the fracture network under different stress conditions.

along the x -direction; the results for y -direction flow are given in the supplementary document (available here).

4. Results

We analyze the geomechanical responses of the fractured rocks under different far-field stress conditions. Figure 3 shows the distributions of fracture apertures in the fractured rocks under various stress conditions for representative cases of $\theta = 0^\circ, 30^\circ, 60^\circ, 90^\circ, 120^\circ$, and 150° . The probability density functions (PDFs) of these cases are given in Figure 4.

When $S_{\max} = S_{\min} = 0$ MPa, all fractures have an identical aperture, i.e., the prescribed initial value of 0.1 mm (Figures 3 and 4). If the fractured rock is isotropically stressed with $S_{\max} = S_{\min} = 5.0$ MPa, all fractures tend to be uniformly compressed such that the deformed apertures are lower than the initial value. If the fractured rock is anisotropically stressed, the fracture network becomes to accommodate heterogeneous aperture distribution as a result of the superimposed effects of shear-induced dilation and compression-induced closure (Figures 3 and 4). When $S_{\max} = 10$ MPa and $S_{\min} = 5$ MPa, most fractures are closed by compression, while only a few small fractures exhibit apertures larger than the initial value of 0.1 mm (Figures 3 and 4). When $S_{\max} = 15$ MPa and $S_{\min} = 5$ MPa, the shear-induced dilation of fracture apertures is more prevailing along some long fractures (Figure 3). When S_{\max} is further increased to 20 MPa, the number of fractures with large apertures

greatly increases due to enhanced shear displacements driven by elevated differential stresses (Figure 3). The fractures' shear behavior is strongly controlled by the relative angle between the orientation of far-field stresses and the mean orientation of fracture sets. For example, when the rotation angle of far-field stresses equals to 30° , the 0° and 50° fracture sets exhibit enhanced shear displacements, while the 120° set is more suppressed for shearing because it is oriented almost perpendicularly to the maximum principal stress, S_{\max} . The anisotropic geomechanical response of the fractured rock is further revealed by the different shape of aperture PDFs for different orientations of far-field stress field (Figure 4).

We obtain the flow velocity fields of the deformed fractured rocks by solving the single-phase steady-state flow equations (i.e., Equations (7) and (8)). Figure 5 displays the flow fields for various stress loading cases. The PDFs of fracture flow velocities are provided in Figure 6. As shown in Figure 5, the flow is highly channelized in a subnetwork consisting mainly of fractures from the 5° and the 30° sets, if zero far-field stresses are applied. When the fractured rock is isotropically loaded (i.e., $S_{\max} = S_{\min} = 5$ MPa), the flow velocity in the fracture network is systematically reduced due to the compression-induced normal closure of fractures (Figures 5 and 6). If the fractured rock is loaded with the anisotropic stress field of $S_{\max} = 10$ MPa and $S_{\min} = 5$ MPa, the main flow network still shows an overall reduction in flow velocity due to compression-induced aperture closure

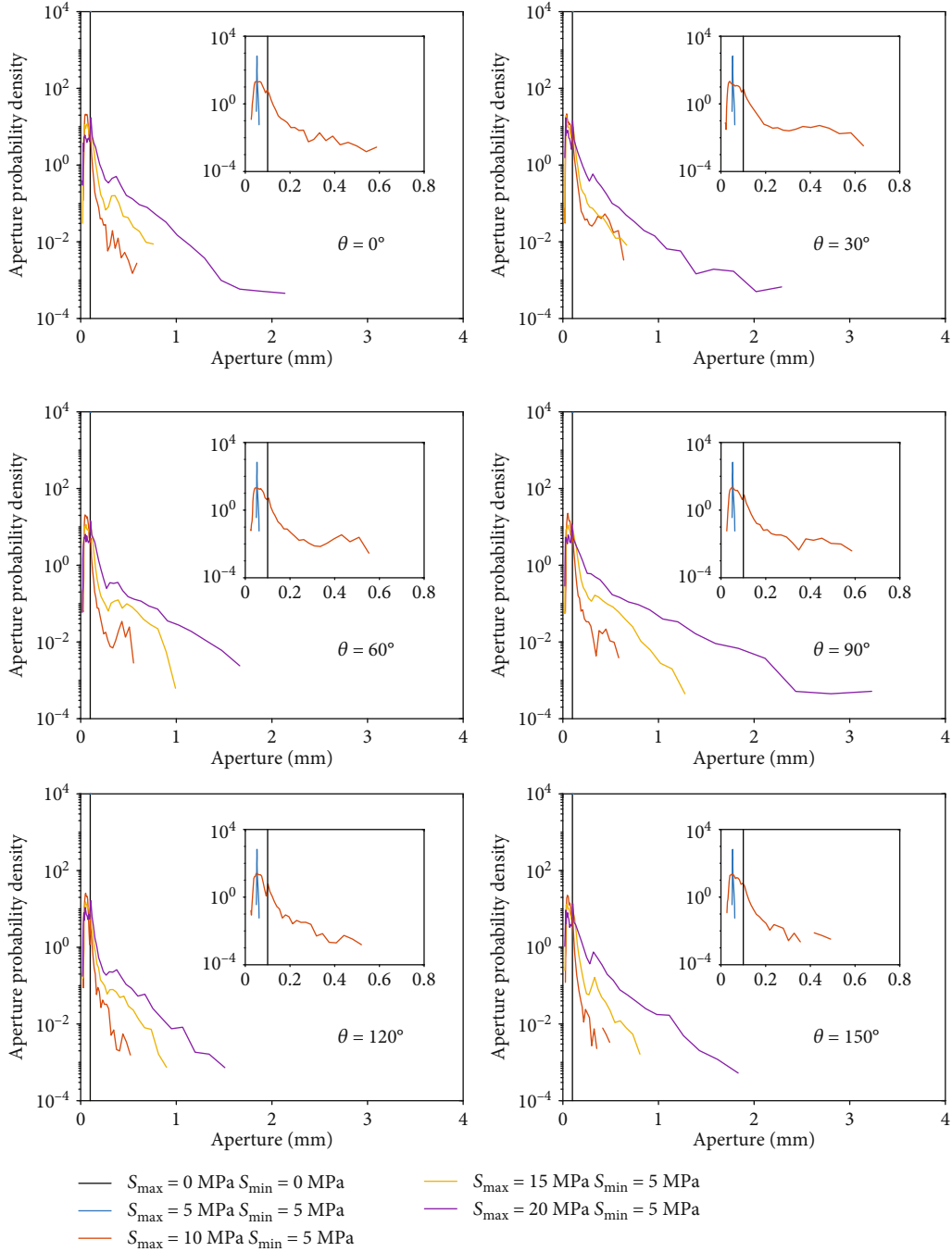


FIGURE 4: Probability density function of fracture apertures in the fracture network under various stress conditions.

(Figures 5 and 6), while locally some fractures exhibit increased velocity values due to moderate shear-induced aperture dilation (Figure 5). The flow velocity fields for various far-field stress orientations are similar (Figure 5). This similarity of flow distribution is also revealed by the resembled shape of PDFs for various θ cases (Figure 6). When $S_{\max} = 15 \text{ MPa}$ and $S_{\min} = 5 \text{ MPa}$, the flow fields become more heterogeneous and sensitive to the variation in θ (Figure 5). Visible variations of flow field, reflected by differences in PDF shape and range, with far-field stress

orientation occurs (Figure 6). At specific orientations of far-field stress field, e.g., 30° and 60° , we observe a conspicuous increase in flow velocity in some fracture clusters in the lower-right part of the fracture network, which is not a part of the original main flow network under zero stress loadings (Figure 5). When S_{\max} is further increased to 20 MPa , a stronger dependence of the flow field on the far-field stress orientation is observed (Figure 5). The extent of PDFs' spreading towards high velocities varies with stress (Figure 6). It seems that the flow field alteration under the two high stress ratio

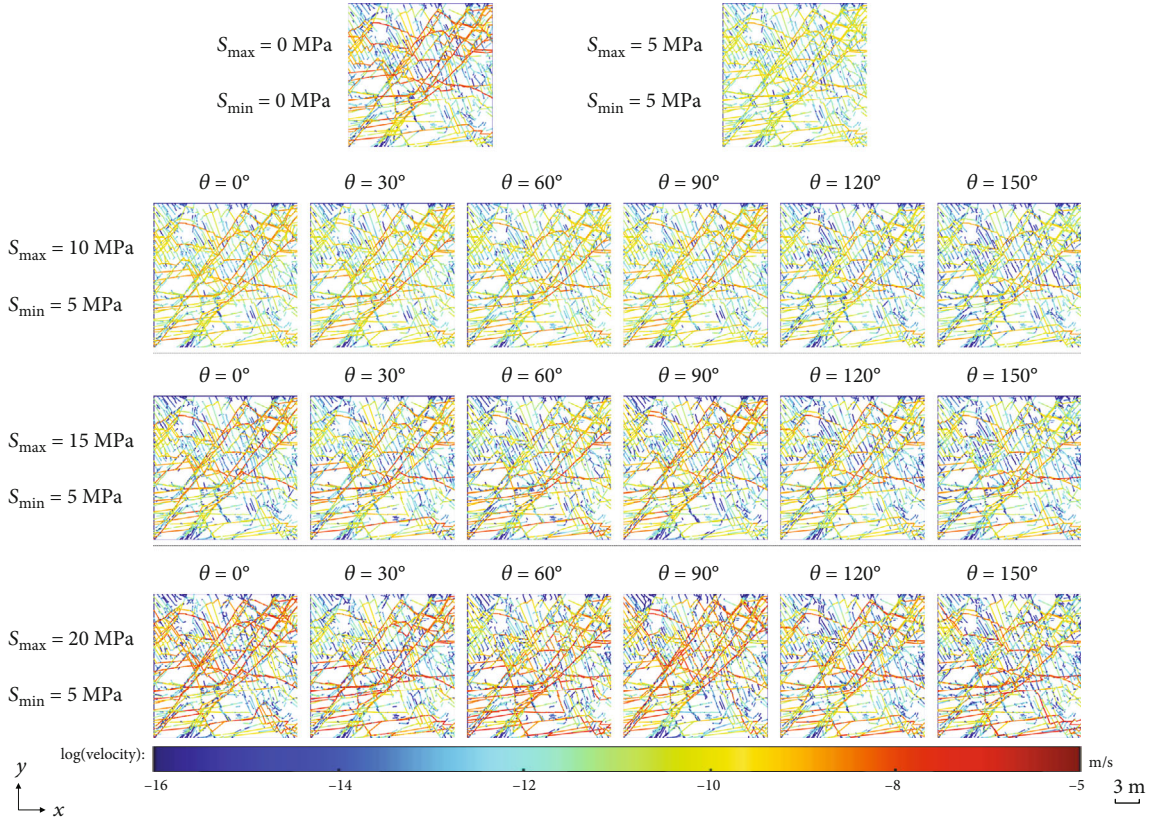


FIGURE 5: Distributions of flow velocity in the fracture network under different stress conditions.

conditions (i.e., $S_{\max} = 15$ or 20 MPa) is driven by a different mechanism compared with the isotropic stress cases and anisotropic cases with a low stress contrast (i.e., the case of $S_{\max} = 10$ MPa and $S_{\min} = 5$ MPa). Indeed, we observe numerous new cracks formed in the cases of high differential stresses (Figure 7). These propagated fractures, although small in size, may create new flow paths connecting preexisting disconnected clusters in the fractured rock. To further elucidate this effect, we plot flow distributions in fractures intersecting the outlet, i.e., the right model boundary (Figure 8). We note that a change in the relative flow magnitude of effluent fractures may indicate an alteration of internal flow organization. When $S_{\max} = 10$ MPa and $S_{\min} = 5$ MPa, there is only a quantitative variation in the relative magnitude of fracture flow when θ is varied; however, when $S_{\max} = 15$ MPa and $S_{\min} = 5$ MPa or $S_{\max} = 20$ MPa and $S_{\min} = 5$ MPa, except for a more drastic variation in flow magnitude with stress, the locations of flowing fractures are also changed qualitatively as θ varies (Figure 8). We will further analyze which geomechanical effect, i.e., shear-induced dilation or new crack propagation, dominates this enhanced sensitivity to stress towards the end of this section.

To quantify the impact of stress variation on flow magnitude and organization, we further derive three flow indicators, i.e., the equivalent network permeability k_{eff} , the correlation dimension of flow rate D_2 , and the flow channeling density indicator d_Q , for various stress condi-

tions. The equivalent permeability may quantify the bulk flow magnitude through the fractured rock, while D_2 and d_Q further indicate the flow distribution within the fracture network.

As shown in Figure 9(a), if the fractured rock is isotropically loaded ($S_{\max} = S_{\min} = 0$ or 5 MPa), k_{eff} does not vary with the stress field rotation, and neither does the flow distribution (Figures 9(b) and 9(c)). As the stress level increases (i.e., in the case of $S_{\max} = 5$ MPa and $S_{\min} = 5$ MPa), k_{eff} decreases by about several times due to compression-induced aperture closure (Figure 3). On the other hand, both D_2 and d_Q increase, indicating a less channelized flow distribution in the fractured rock. If the fractured rock is anisotropically stressed, k_{eff} varies with the far-field stress orientation. When $S_{\max} = 10$ MPa and $S_{\min} = 5$ MPa, the k_{eff} becomes larger than that of the isotropic stress loading cases of $S_{\max} = 5$ MPa and $S_{\min} = 5$ MPa but is still smaller than that of the zero-stress loading case (i.e., $S_{\max} = 0$ MPa and $S_{\min} = 0$ MPa) due to the dominant normal closure effect under confining stresses. The variation of k_{eff} with far-field stress orientation is quite small. A variation in D_2 and d_Q also occurs. This indicates that the flow structure becomes dependent on the far-field stress orientation. With the increase of the differential stress magnitude (i.e., when $S_{\max} = 15$ MPa and $S_{\min} = 5$ MPa), the k_{eff} variation as a function of far-field stress orientation becomes very complex under the combined effects of compression-induced closure, shear-induced dilation, and formation of new cracks. In general, k_{eff} increases as the increase of differential stress so far but

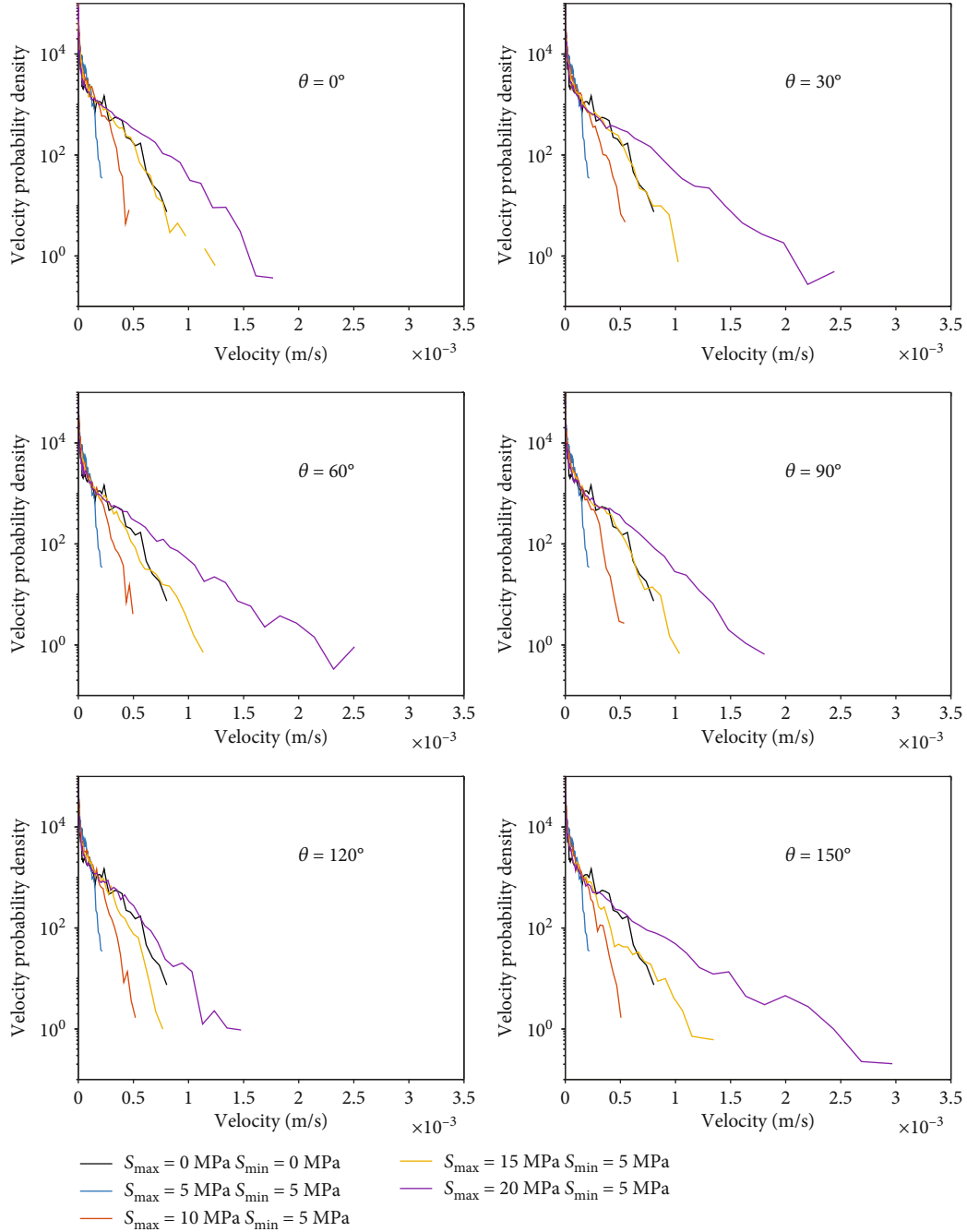


FIGURE 6: Probability density function of the flow velocity in the fracture network under various stress conditions.

is still smaller than the that of the fractured rocks under the zero-stress loading. Moreover, D_2 and d_Q also become smaller, indicating a higher level of flow channelization. The variation magnitude of D_2 and d_Q with stress becomes more prominent. The variation trends of D_2 and d_Q as the far-field stress field orientation appear similar (Figures 9(b) and 9(c)). As S_{\max} is further increased to 20 MPa, there is a significant overall increase in k_{eff} (Figure 9(a)). For all far-field stress orientations, the k_{eff} values are now larger than that of the fractured rock under the zero-stress loading. Both D_2 and d_Q exhibit an increased variability with far-field stress

orientation. Moreover, their variation trends are no longer similar. When θ falls in the range between 70° and 90° , the D_2 and d_Q values remain high and similar to those of the case of $S_{\max} = 10 \text{ MPa}$ and $S_{\min} = 5 \text{ MPa}$. When $\theta = 0^\circ$, 130° , and 140° , an enhanced reduction in d_Q is observed (Figures 9(b) and 9(c)), while there is a slightly less decrease in D_2 . It seems that the cases with high bulk permeability have less localized flow, although this correlation is associated with large uncertainties.

To further investigate the relative contribution of shear displacement and new fracture propagation to the

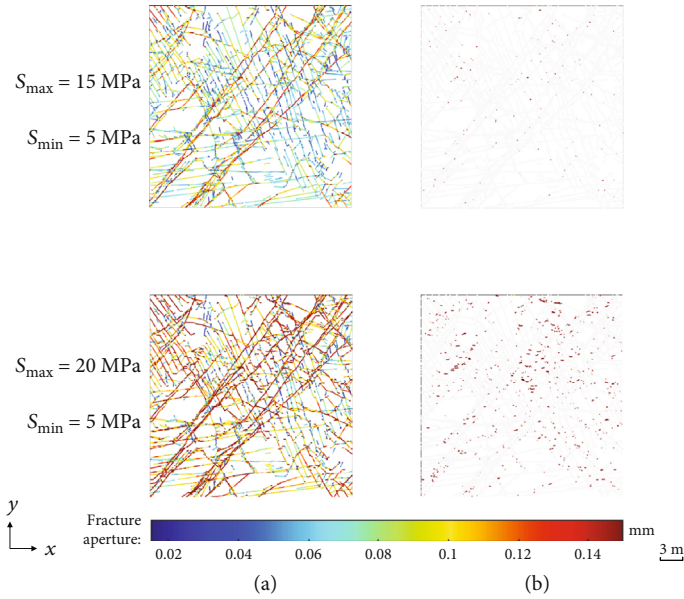


FIGURE 7: Formation of new cracks under high differential stress conditions. (a) All fractures; (b) location and aperture of new cracks.

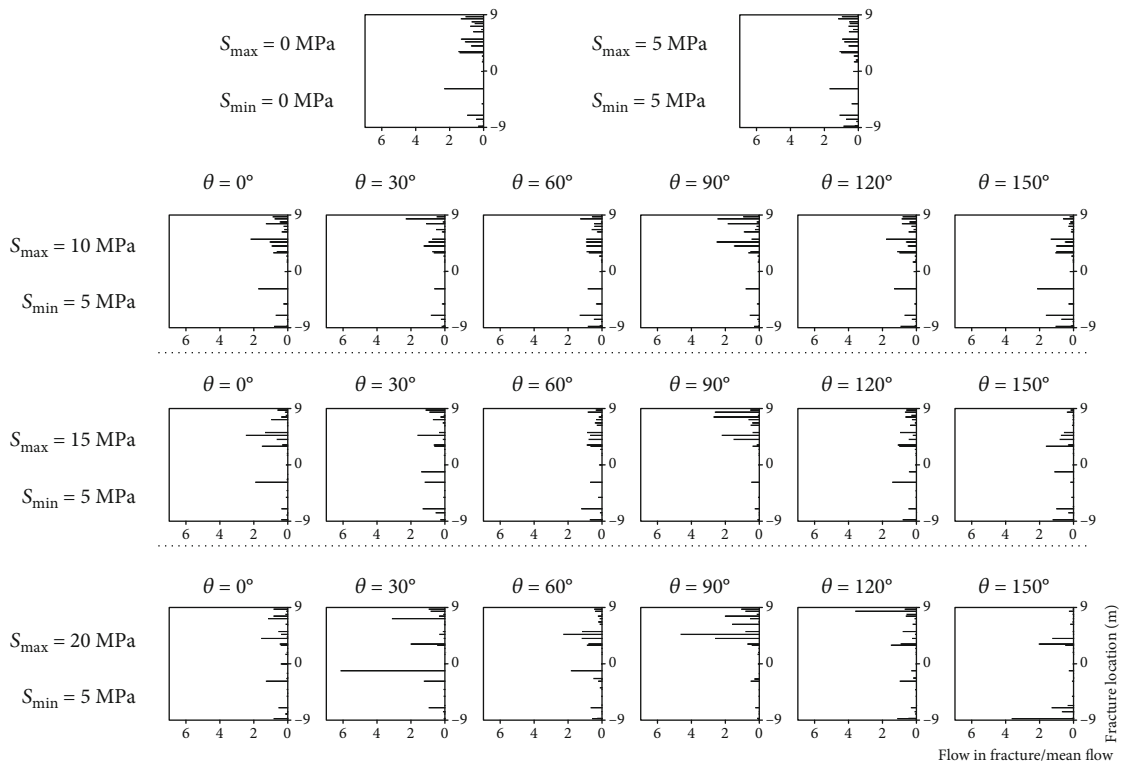


FIGURE 8: Flow rate distributions at the outlet of fracture networks under different stress condition.

permeability enhancement and flow structure alternation under high differential stresses (Figure 7), we show, in Figure 10, the derived k_{eff} , D_2 , and d_Q values after removing all newly propagated cracks from the stressed fracture network. By comparing Figure 10 against Figure 9, it can be seen that the bulk permeability decreases by several times with the removal of new cracks. In addition, there is also a system-

atic decrease in both D_2 and d_Q , implying a higher level of flow channelization without the new cracks. These results are consistent with our observations of new flow paths created by the propagated cracks (Figures 5 and 8). The comparison between Figures 9 and 10 further suggests that the permeability enhancement may be more dominated by the propagation of new fractures while shear-induced dilation plays a

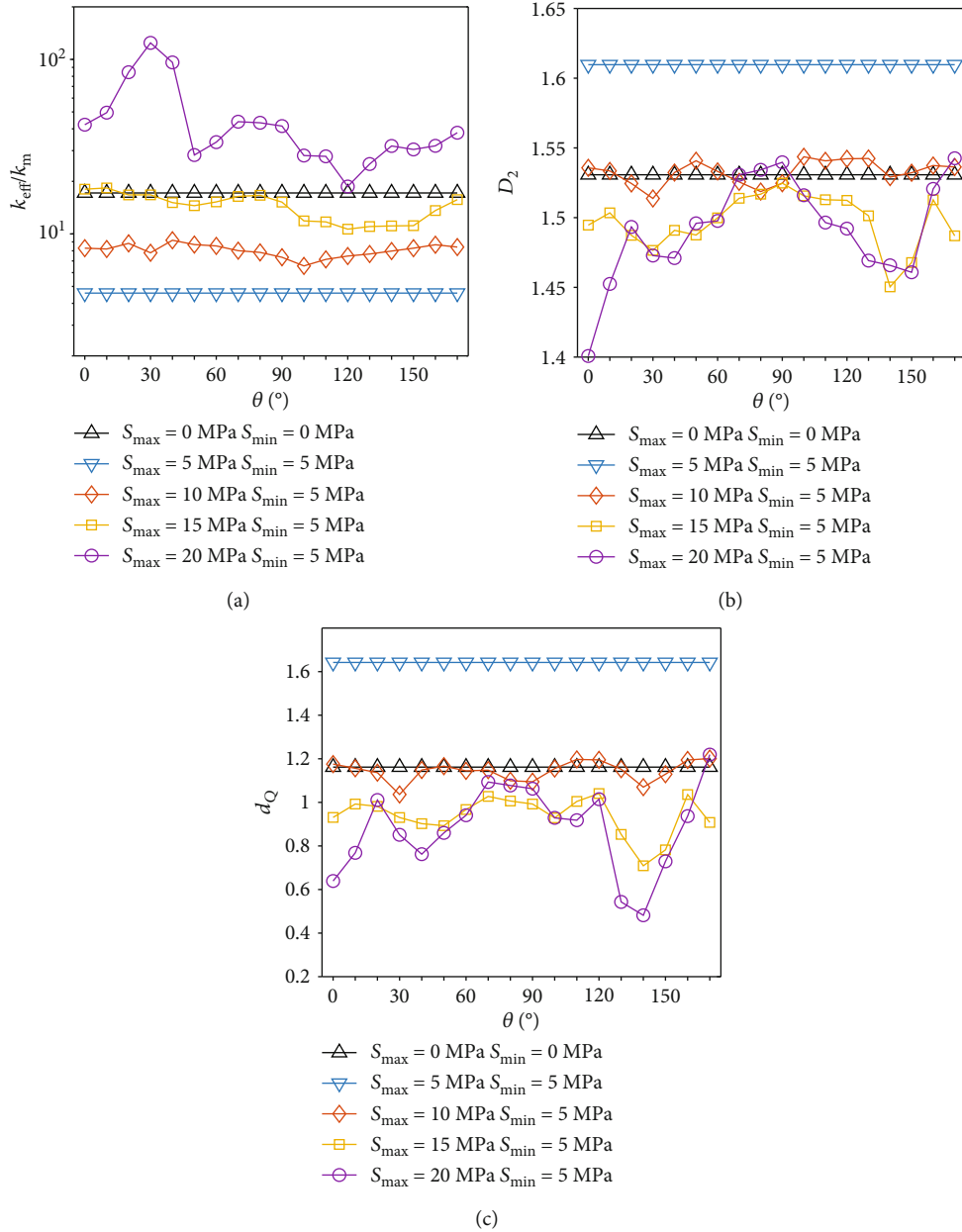


FIGURE 9: Quantitative indices for evaluating flow magnitude and distribution in fracture networks under different stress conditions: (a) effective permeability, (b) correlation dimension of flow rate, and (c) flow channeling density indicator.

second-order role. It is also evident that the elevated flow channelization due to shear displacement has been attenuated by the presence of new flow paths created by propagated cracks. This phenomenon is considered to be related to the fact that the natural fracture network is close to the percolation threshold such that new cracks can critically transition the system from disconnected to connected (see more discussions in the following section).

5. Discussions and Conclusions

In this study, we have demonstrated how in situ stress variations impact fluid flow in a 2D natural fracture network that is critically connected (i.e., the network connec-

tivity is close to the percolation threshold). We have shown that the stress variation may induce changes in the bulk permeability and flow organization. As the stress magnitude increases, fracture apertures decrease systematically, which in turn reduces fracture flow velocities and the bulk permeability. For anisotropic stress conditions, significant shear-induced dilation may occur along preferentially oriented fractures with respect to the anisotropic stress field. Although the shear displacement may cause a significant change in the internal flow organization (generally enhances the flow channelization intensity), its impact on the network's macroscopic hydraulic properties is mild. These observations are consistent with previous studies where similar results about the stress-dependent

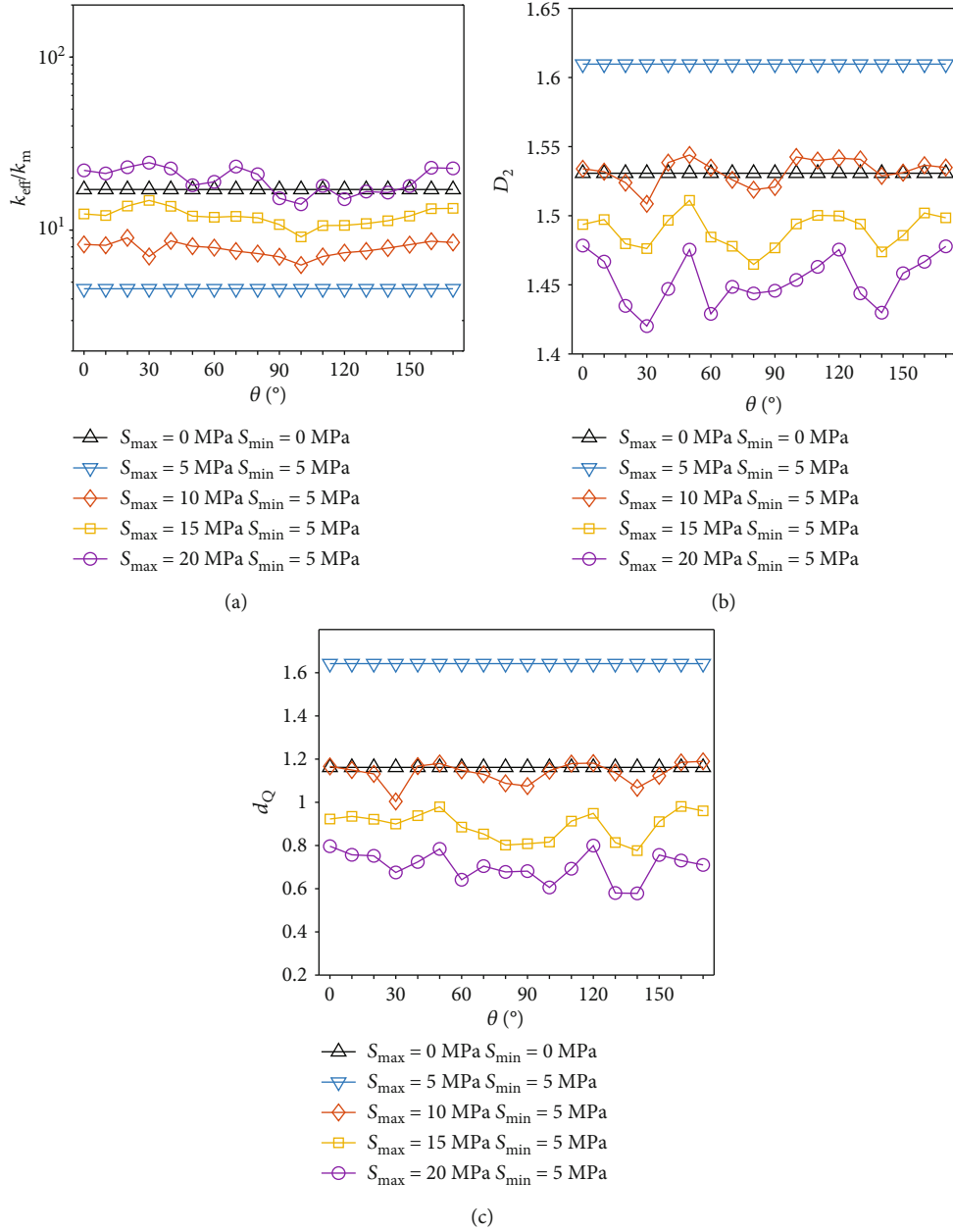


FIGURE 10: Quantitative indices for evaluating flow magnitude and distribution in fracture networks under different stress condition after removing the new cracks: (a) effective permeability, (b) correlation dimension of flow rate, and (c) flow channeling density indicator.

permeability of 2D fracture networks were reported [7, 11, 14, 23, 26, 28]. We further show that under high differential stress conditions, the formation of new cracks is also prevailing in the fracture network, which may change the number and location of preferential flow paths. As a result, the bulk permeability may increase significantly. The new cracks in general reduce the level of flow channelization within the network as they may bridge unconnected fractures or clusters to form new paths branching the flow. This effect is particularly prominent when the fractured rock is critically stressed (i.e., with a stress ratio larger than 3).

These observations indicate that in natural fracture networks close to the percolation threshold, the network

connectivity has a primary control on fluid flow, while the shear-related geomechanical effects only pose a second-order impact on the hydraulic properties of the fractured rock. However, the effect of fracture propagation still reserves the power to regulate the hydraulic connectivity of the fracture network. These research findings highlight the importance of integrating geomechanical analyses in the practice of understanding and prediction of fluid flow in natural fracture systems as they are mostly critically connected [32] and under critical stress condition [56]. Our numerical simulations clearly show that without taking into account the stress effects, we may largely underestimate the level of flow channelization and overestimate the bulk permeability of naturally fractured rocks

subjecting to anisotropic loadings with intermediate stress magnitude. However, when the fractured rock is loaded by anisotropic stress of high magnitudes, we tend to underestimate the bulk permeability and overestimate the flow channeling intensity without considering the fracture propagation process. Moreover, the reduction in hydraulic connection caused by stress orientation variation may also be overlooked, which may cause complexities or even the failure of the production scheme under implementation, since stress redistributions often occur during the production of geofluids.

Although the present work provides a better understanding of hydromechanical behavior of a nature fracture network under different stress conditions, particularly the evolution of flow paths with *in situ* stresses, a number of issues remain to be addressed in future work. First, the present work needs to be extended to 3D to further verify the consistency and generality of the main results discovered based on 2D simulations. The geometry and connectivity of 3D fracture networks are intricate (Bour and Davy, 1998). The stress effects are thus expected to be much more complex. Based on the findings from our recent 3D modeling work (e.g., [27]), the 2D analysis presented here may provide some indicative approximations, but certainly cannot reveal fully the polyaxial stress-dependent behavior of 3D fracture networks. However, due to the very expensive run time of 3D FEMDEM simulations, the number of fractures in the 3D model has to be very limited. The challenges in performing large-scale simulations need to be addressed before they can be used to drive pertinent 3D characterizations of stress effects at the scale of natural fracture systems. Moreover, our work only examined the hydromechanical behavior of a specific natural fracture network. The validity and universality of the findings for other natural fracture systems require further investigations. Furthermore, spatial variability and correlation of initial fracture aperture may also need to be integrated into the model to more realistically simulate the actual systems.

Data Availability

The simulation data used to support the findings of this study are available from the corresponding author upon request.

Additional Points

Highlights. (1) Stress effect on flow organization in a natural fracture network is investigated. (2) The role of shear-induced dilation and stress-driven fracture on fluid flow is evaluated. (3) New cracks may serve as red links to critically enhance the network connectivity. (4) Shear-induced dilation tends to be a second-order factor on altering permeability

Conflicts of Interest

The authors declare that they have no conflicts of interest.

Acknowledgments

ZS acknowledges funding from the National Natural Science Foundation of China (No. 51774317), the Fundamental Research Funds for the Central Universities (No. 18CX2100A), and the National Science and Technology Major Project (No. 2016ZX05011004-004). All the data of numerical simulation results in this paper are available upon request to the correspondence author X. Wang (xiaoguang.wang@umontpellier.fr).

Supplementary Materials

In this supplementary file, we provide flow simulation results in the y -direction for various stress cases. As shown in Figure S1, when calculating the flow field, a vertical hydraulic gradient is applied to the fracture networks, where the fracture apertures are derived from geomechanical simulations with zero, isotropic, and anisotropic far-field stress loadings. The material properties of the fracture networks and fluids used in these simulations are the same as listed in Table 1. Figure S2 displays the flow fields for various stress loading cases. Overall, the results in the y -direction (Figures S2, S3, S4, and S5) are similar to those in the x -direction (Figures 5, 6, 9, and 10), revealing that the effect of geomechanical deformation depends on the angle between maximum stress and flow direction. The y -direction flow is mainly restricted to the 50° and 120° fracture sets. The large extent of PDFs' spreading towards high velocities tends to occur when $\theta = 90^\circ$ in the cases of y -direction, whereas it occurs when $\theta = 30$ and 150° in x -direction (Figure S3 and Figure 6). Note that θ is the angle between maximum stress and x positive direction. The variation tendency of the quantitative flow indices (k_{eff}/k_m , D_2 , and d_Q) under different stress conditions (Figures S4 and S5) is coincident with the cases in the x -direction (Figures 9 and 10), except that the corresponding transition points are shifted and the shape of the curves is changed compared to the respective case for x -direction flow. The difference between the results of x - and y -directions may be caused by the interplay among the maximum stress direction, mean flow direction, and fracture network geometry (e.g., the direction of the main fracture sets and the organization of fractures of different sets). (*Supplementary Materials*)

References

- [1] P. M. Adler and J.-F. Thovert, *Fractures and Fracture Networks, Theory and Applications of Transport in Porous Media*, Kluwer Academic Publishers, Dordrecht, Netherlands, 1999.
- [2] B. Berkowitz, "Characterizing flow and transport in fractured geological media: a review," *Advances in Water Resources*, vol. 25, no. 8-12, pp. 861-884, 2002.
- [3] S. P. Neuman, "Trends, prospects and challenges in quantifying flow and transport through fractured rocks," *Hydrogeology Journal*, vol. 13, no. 1, pp. 124-147, 2005.
- [4] I. Miller, G. Lee, and W. Dershowitz, "MAFIC-matrix/fracture interaction code with heat and solute transport-user

- documentation, version 1.6,” Golder Associates Inc., Redmond, WA, USA, 1999.
- [5] S. Geiger and S. Emmanuel, “Non-Fourier thermal transport in fractured geological media,” *Water Resources Research*, vol. 46, no. 7, 2010.
- [6] N. J. Hardebol, C. Maier, H. Nick, S. Geiger, G. Bertotti, and H. Boro, “Multiscale fracture network characterization and impact on flow: a case study on the Latemar carbonate platform,” *Journal of Geophysical Research Solid Earth*, vol. 120, no. 12, pp. 8197–8222, 2015.
- [7] Q. Lei, X. Wang, J. Xiang, and J.-P. Latham, “Polyaxial stress-dependent permeability of a three-dimensional fractured rock layer,” *Hydrogeology Journal*, vol. 25, no. 8, pp. 2251–2262, 2017.
- [8] N. E. Odling, P. Gillespie, B. Bourgin et al., “Variations in fracture system geometry and their implications for fluid flow in fractures hydrocarbon reservoirs,” *Petroleum Geoscience*, vol. 5, no. 4, pp. 373–384, 1999.
- [9] F. D. Day-Lewis, K. Singha, and A. M. Binley, “Applying petrophysical models to radar travel time and electrical resistivity tomograms: resolution-dependent limitations,” *Journal of Geophysical Research: Solid Earth*, vol. 110, no. B8, 2005.
- [10] Q. Lei, J.-P. Latham, and J. Xiang, “Implementation of an empirical joint constitutive model into finite-discrete element analysis of the geomechanical behaviour of fractured rocks,” *Rock Mechanics and Rock Engineering*, vol. 49, no. 12, pp. 4799–4816, 2016.
- [11] Q. Lei, J.-P. Latham, J. Xiang, C.-F. Tsang, P. Lang, and L. Guo, “Effects of geomechanical changes on the validity of a discrete fracture network representation of a realistic two-dimensional fractured rock,” *International Journal of Rock Mechanics and Mining Sciences*, vol. 70, pp. 507–523, 2014.
- [12] X. Zhang and D. J. Sanderson, “Numerical study of critical behaviour of deformation and permeability of fractured rock masses,” *Marine and Petroleum Geology*, vol. 15, no. 6, pp. 535–548, 1998.
- [13] S. Follin, L. Hartley, I. Rhén et al., “A methodology to constrain the parameters of a hydrogeological discrete fracture network model for sparsely fractured crystalline rock, exemplified by data from the proposed high-level nuclear waste repository site at Forsmark, Sweden,” *Hydrogeology Journal*, vol. 22, no. 2, pp. 313–331, 2014.
- [14] Q. Lei, J.-P. Latham, J. Xiang, and C.-F. Tsang, “Polyaxial stress-induced variable aperture model for persistent 3D fracture networks,” *Geomechanics for Energy and the Environment*, vol. 1, pp. 34–47, 2015.
- [15] C.-F. Tsang and I. Neretnieks, “Flow channeling in heterogeneous fractured rocks,” *Reviews of Geophysics*, vol. 36, no. 2, pp. 275–298, 1998.
- [16] H. Abelin, L. Birgersson, H. Widen, T. Ågren, L. Moreno, and I. Neretnieks, “Channeling experiment,” Swedish Nuclear Fuel and Waste Management Co., 1990.
- [17] H. Abelin, I. Neretnieks, S. Tunbrant, and L. Moreno, “Final report of the migration in a single fracture-experimental results and evaluation,” Swedish Nuclear Fuel and Waste Management Co., 1985.
- [18] P. A. Hsieh, S. P. Neuman, G. K. Stiles, and E. S. Simpson, “Field determination of the three-dimensional hydraulic conductivity tensor of anisotropic media: 2. Methodology and application to fractured rocks,” *Water Resources Research*, vol. 21, no. 11, pp. 1667–1676, 1985.
- [19] H. Abelin, L. Birgersson, T. Ågren, and I. Neretnieks, “A channeling experiment to study flow and transport in natural fractures,” in *MRS Online Proceedings Library Archive*, 1988.
- [20] H. Abelin, L. Birgersson, J. Gidlund et al., “3–D migration experiment in sparsely fractured crystalline rock,” *MRS Proceedings*, vol. 112, p. 199, 1987.
- [21] Y. W. Tsang and C. F. Tsang, “Channel model of flow through fractured media,” *Water Resources Research*, vol. 23, no. 3, pp. 467–479, 1987.
- [22] Y. W. Tsang and C. F. Tsang, “Flow channeling in a single fracture as a two-dimensional strongly heterogeneous permeable medium,” *Water Resources Research*, vol. 25, no. 9, pp. 2076–2080, 1989.
- [23] A. Baghbanan and L. Jing, “Stress effects on permeability in a fractured rock mass with correlated fracture length and aperture,” *International Journal of Rock Mechanics and Mining Sciences*, vol. 45, no. 8, pp. 1320–1334, 2008.
- [24] W. Dang, W. Wu, H. Konietzky, and J. Qian, “Effect of shear-induced aperture evolution on fluid flow in rock fractures,” *Computers and Geotechnics*, vol. 114, article 103152, 2019.
- [25] P. K. Kang, Q. Lei, M. Dentz, and R. Juanes, “Stress-induced anomalous transport in natural fracture networks,” *Water Resources Research*, vol. 55, no. 5, pp. 4163–4185, 2019.
- [26] J.-P. Latham, J. Xiang, M. Belayneh, H. M. Nick, C.-F. Tsang, and M. J. Blunt, “Modelling stress-dependent permeability in fractured rock including effects of propagating and bending fractures,” *International Journal of Rock Mechanics and Mining Sciences*, vol. 57, pp. 100–112, 2013.
- [27] Q. Lei, J.-P. Latham, and C.-F. Tsang, “The use of discrete fracture networks for modelling coupled geomechanical and hydrological behaviour of fractured rocks,” *Computers and Geotechnics*, vol. 85, pp. 151–176, 2017.
- [28] K.-B. Min, J. Rutqvist, C.-F. Tsang, and L. Jing, “Stress-dependent permeability of fractured rock masses: a numerical study,” *International Journal of Rock Mechanics and Mining Sciences*, vol. 41, no. 7, pp. 1191–1210, 2004.
- [29] J. Rutqvist and O. Stephansson, “The role of hydromechanical coupling in fractured rock engineering,” *Hydrogeology Journal*, vol. 11, no. 1, pp. 7–40, 2003.
- [30] D. J. Sanderson and X. Zhang, “Critical stress localization of flow associated with deformation of well-fractured rock masses, with implications for mineral deposits,” *The Geological Society*, vol. 155, no. 1, pp. 69–81, 1999.
- [31] Q. Lei and X. Wang, “Tectonic interpretation of the connectivity of a multiscale fracture system in limestone,” *Geophysical Research Letters*, vol. 43, no. 4, pp. 1551–1558, 2016.
- [32] C. E. Renshaw, “Mechanical controls on the spatial density of opening-mode fracture networks,” *Geology*, vol. 25, no. 10, pp. 923–926, 1997.
- [33] N. E. Odling, “Scaling and connectivity of joint systems in sandstones from western Norway,” *Journal of Structural Geology*, vol. 19, no. 10, pp. 1257–1271, 1997.
- [34] O. Bour, “A statistical scaling model for fracture network geometry, with validation on a multiscale mapping of a joint network (Hornelen Basin, Norway),” *Journal of Geophysical Research*, vol. 107, no. B6, article 2113, 2002.

- [35] Q. Lei and K. Gao, "Correlation between fracture network properties and stress variability in geological media," *Geophysical Research Letters*, vol. 45, no. 9, pp. 3994–4006, 2018.
- [36] A. Roy, E. Perfect, W. M. Dunne, N. Odling, and J.-W. Kim, "Lacunarity analysis of fracture networks: evidence for scale-dependent clustering," *Journal of Structural Geology*, vol. 32, no. 10, pp. 1444–1449, 2010.
- [37] N. E. Odling, "The scaling of hydraulic conductivity in rock fracture zones," *Geophysical Research Letters*, vol. 28, no. 15, pp. 3019–3022, 2001.
- [38] A. Munjiza, *The Combined Finite-Discrete Element Method: Munjiza/Discrete Element Method*, John Wiley & Sons, Ltd, Chichester, UK, 2004.
- [39] R. Goodman, *Methods of Geological Engineering*, St Paul. West Publishing Company, 1976.
- [40] S. Saeb and B. Amadei, "Modelling rock joints under shear and normal loading," *International Journal of Rock Mechanics and Mining Sciences & Geomechanics Abstracts*, vol. 29, no. 3, pp. 267–278, 1992.
- [41] N. Barton and V. Choubey, "The shear strength of rock joints in theory and practice," *Rock Mechanics*, vol. 10, no. 1-2, pp. 1–54, 1977.
- [42] P. A. Witherspoon, J. S. Y. Wang, K. Iwai, and J. E. Gale, "Validity of cubic law for fluid flow in a deformable rock fracture," *Water Resources Research*, vol. 16, no. 6, pp. 1016–1024, 1980.
- [43] P. S. Lang, A. Paluszny, and R. W. Zimmerman, "Permeability tensor of three-dimensional fractured porous rock and a comparison to trace map predictions," *Journal of Geophysical Research: Solid Earth*, vol. 119, no. 8, pp. 6288–6307, 2014.
- [44] P. Renard and G. de Marsily, "Calculating equivalent permeability: a review," *Advances in Water Resources*, vol. 20, no. 5-6, pp. 253–278, 1997.
- [45] C. Bruderer-Weng, P. Cowie, Y. Bernabé, and I. Main, "Relating flow channelling to tracer dispersion in heterogeneous networks," *Advances in Water Resources*, vol. 27, no. 8, pp. 843–855, 2004.
- [46] J. Maillot, P. Davy, R. Le Goc, C. Darcel, and J. R. de Dreuzy, "Connectivity, permeability, and channeling in randomly distributed and kinematically defined discrete fracture network models," *Water Resources Research*, vol. 52, no. 11, pp. 8526–8545, 2016.
- [47] A. Sornette, P. Davy, and D. Sornette, "Fault growth in brittle-ductile experiments and the mechanics of continental collisions," *Journal of Geophysical Research*, vol. 98, no. B7, pp. 12111–12139, 1993.
- [48] X. Wang, Q. Lei, L. Lonergan, H. Jourde, O. Gosselin, and J. Cosgrove, "Heterogeneous fluid flow in fractured layered carbonates and its implication for generation of incipient karst," *Advances in Water Resources*, vol. 107, pp. 502–516, 2017.
- [49] E. Bonnet, O. Bour, N. E. Odling et al., "Scaling of fracture systems in geological media," *Reviews of Geophysics*, vol. 39, no. 3, pp. 347–383, 2001.
- [50] P. A. Cowie, D. Sornette, and C. Vanneste, "Multifractal scaling properties of a growing fault population," *Geophysical Journal International*, vol. 122, no. 2, pp. 457–469, 1995.
- [51] R. J. Bell and P. Dean, "Atomic vibrations in vitreous silica," *Discussions of the Faraday Society*, vol. 50, p. 55, 1970.
- [52] J. T. Edwards and D. J. Thouless, "Numerical studies of localization in disordered systems," *Journal of Physics C: Solid State Physics*, vol. 5, no. 8, pp. 807–820, 1972.
- [53] W. C. Belfield, "Multifractal characteristics of natural fracture apertures," *Geophysical Research Letters*, vol. 21, no. 24, pp. 2641–2644, 1994.
- [54] K. Bisdom, G. Bertotti, and H. M. Nick, "The impact of different aperture distribution models and critical stress criteria on equivalent permeability in fractured rocks," *Journal of Geophysical Research: Solid Earth*, vol. 121, no. 5, pp. 4045–4063, 2016.
- [55] P. Szymczak and A. J. C. Ladd, "The initial stages of cave formation: beyond the one-dimensional paradigm," *Earth and Planetary Science Letters*, vol. 301, no. 3-4, pp. 424–432, 2011.
- [56] C. A. Barton, M. D. Zoback, and D. Moos, "Fluid flow along potentially active faults in crystalline rock," *Geology*, vol. 23, no. 8, p. 683, 1995.

Research Article

How Do Secondary Minerals in Granite Help Distinguish Paleo- from Present-Day Permeable Fracture Zones? Joint Interpretation of SWIR Spectroscopy and Geophysical Logs in the Geothermal Wells of Northern Alsace

Carole Glaas ^{1,2,3}, Jeanne Vidal ^{2,4}, Patricia Patrier,³ Jean-François Girard,¹ Daniel Beaufort,³ Sabine Petit,³ and Albert Genter²

¹UMR 7516 IPGS, University of Strasbourg, CNRS, 5 Rue René Descartes, 67084 Strasbourg Cedex, France

²ES-Géothermie, Bat Le Belem 5 Rue de Lisbonne, 67300 Schiltigheim, France

³UMR 7285 IC2MP, HydrASA, University of Poitiers, CNRS, Bat B8 Rue Albert Turpain, TSA51106, F-86073 Poitiers Cedex 9, France

⁴FCFM, Department of Geology, Andean Geothermal Center of Excellence (CEGA), University of Chile, Plaza Ercilla 803, Santiago, Chile

Correspondence should be addressed to Carole Glaas; carole.glaas@es.fr

Received 17 May 2019; Revised 11 September 2019; Accepted 24 September 2019; Published 11 December 2019

Guest Editor: Tanguy Robert

Copyright © 2019 Carole Glaas et al. This is an open access article distributed under the Creative Commons Attribution License, which permits unrestricted use, distribution, and reproduction in any medium, provided the original work is properly cited.

The investigation of permeable hydrothermally altered and fractured zones and their distribution is a key issue for the understanding of fluid circulation in granitic rocks, on which the success of geothermal projects relies. Based on the use of short-wave infrared (SWIR) spectroscopy applied to rock cuttings coupled with interpretation of geophysical logs, we propose an investigation of the clay signature of fault and fracture zones (FZ) inside the granitic basement. This methodology was applied to two geothermal wells: GRT-2 from the Rittershoffen and GPK-1 from the Soultz-sous-Forêts (Soultz) geothermal sites, both located in the Upper Rhine Graben (URG). A total of 1430 SWIR spectra were acquired and analysed. Variations in the 2200 nm absorption band area are correlated with hydrothermal alteration grades. The 2200 nm absorption band area is found to reflect the illite quantity and its variations in the granitic basement. Low, stable values are observed in the unaltered granite facies, showing good reproducibility of the method, whereas scattered high values are associated with high hydrothermal alteration and FZs. Variations in the 2200 nm absorption band area were correlated with the gamma ray and electrical resistivity logs. This procedure allowed us to confirm that illite mainly controls the resistivity response except inside the permeable FZs, where the resistivity response is controlled by the geothermal brine. Thus, the architecture of these permeable FZs was described precisely by using a combination of the 2200 nm absorption band area data and the electrical resistivity log. Moreover, by correlation with other geophysical logs (temperature (T), porosity, and density), paleo-permeable and currently permeable FZs inside the reservoir were distinguished. The correlation of SWIR spectroscopy with electrical resistivity logs appears to be a robust tool for geothermal exploration in granitic reservoirs in the URG.

1. Introduction

The mid-Carboniferous granitic basement of the Upper Rhine Graben (URG) has been affected by several extensional and compressional tectonic phases that developed a multiscale fracture network during the Tertiary [1, 2]. Today, the network hosts hydrothermal circulations and acts as the

main pathway through which the natural brine sustains wide convection cells [3–5]. More than 30 years of geothermal research in the pilot geothermal project of Soultz-sous-Forêts (Soultz) (Alsace, France) led to a 3D knowledge of those multiscale fault and fracture networks [6, 7]. Fault and fracture networks will be designated by the general term “FZ” in this paper. Their internal complexity in terms of

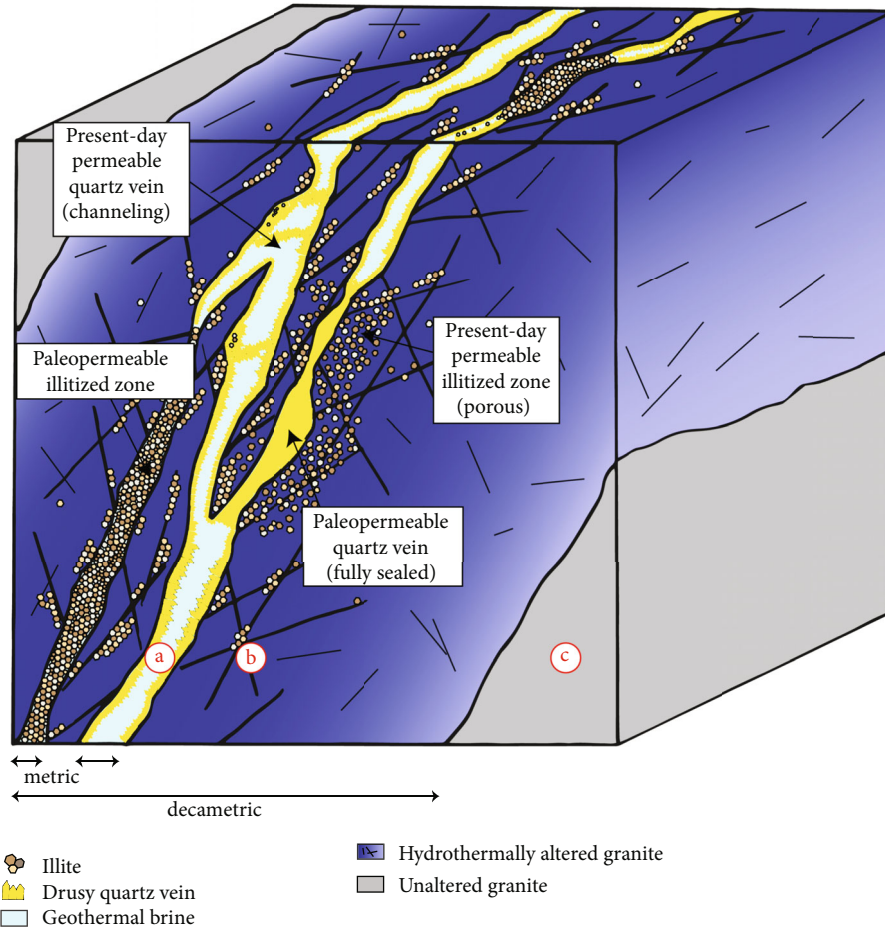


FIGURE 1: Complexity of a FZ after Caine et al. [71]. We can differentiate three zones: (a) the fault core, which can be a pathway for fluid if illite and quartz veins are not totally sealing the zone, (b) the damage zone, which can be sealed or opened with fractures that are acting as fluid pathways, and (c) the unaltered granite, which shows generally very low permeability.

architecture and associated permeability is a key question that must be answered when granitic rocks are used as hydrogeological reservoirs, for nuclear waste disposal, or as deep geothermal systems (Figure 1) [4, 8–12]. In the URG, the current targets for geothermal projects are hydrothermal fractured reservoirs in granitic rocks lying under a thick sedimentary cover [13]. Benefitting from lessons learned during the Soultz project and gained on several deep geothermal wells in Northern Alsace, we decided to avoid drilling subvertical wells in nearly vertical fracture systems to maximize the intersection of permeable FZs. Accordingly, a new drilling approach consisting of targeting deviated well trajectories crosscutting highly dipped FZs in the granitic basement was developed. However, these FZs can act either as permeable conduits and as paleo-permeable barriers for natural fluid transport (Figure 1). Therefore, due to primary mineral dissolution and/or secondary mineral precipitation related to fluid-rock interaction, the resulting permeability of FZs can increase or even decrease, increasing the challenge of obtaining successful geothermal wells [14–18].

This paper aims to develop a method to both characterize the hydrothermal alteration and evaluate the degree of per-

meability of the granitic reservoir intersected by geothermal wells in the context of the URG. Hydrothermal alteration of the buried granitic basement in the URG wells is systematically expressed by an illitization process [6, 7, 13, 19, 20]. Routinely used for the mining industry, short-wave infrared (SWIR) spectroscopy is an innovative method for geothermal systems [21]. Here, SWIR spectroscopy was used to detect illitic minerals (illite and illite-rich illite/smectite mixed layers) in the studied geothermal wells. However, the use of SWIR spectroscopy alone does not permit differentiation of whether this high illitization is the clay signature of permeable FZs contributing to the well's productivity or injectivity, or a signature of paleo-permeable FZs that are now sealed by secondary minerals. To distinguish paleo-permeable from currently permeable FZs, we propose an innovative method based on the correlation between SWIR signature, geophysical logs (T , gases, porosity, density, gamma ray, and electrical resistivity), and cuttings observations.

After describing the SWIR method and the several geophysical logs used in this study, the SWIR results will be presented for two geothermal wells drilled in Rittershoffen (GRT-2) and Soultz (GPK-1), respectively, and the specific

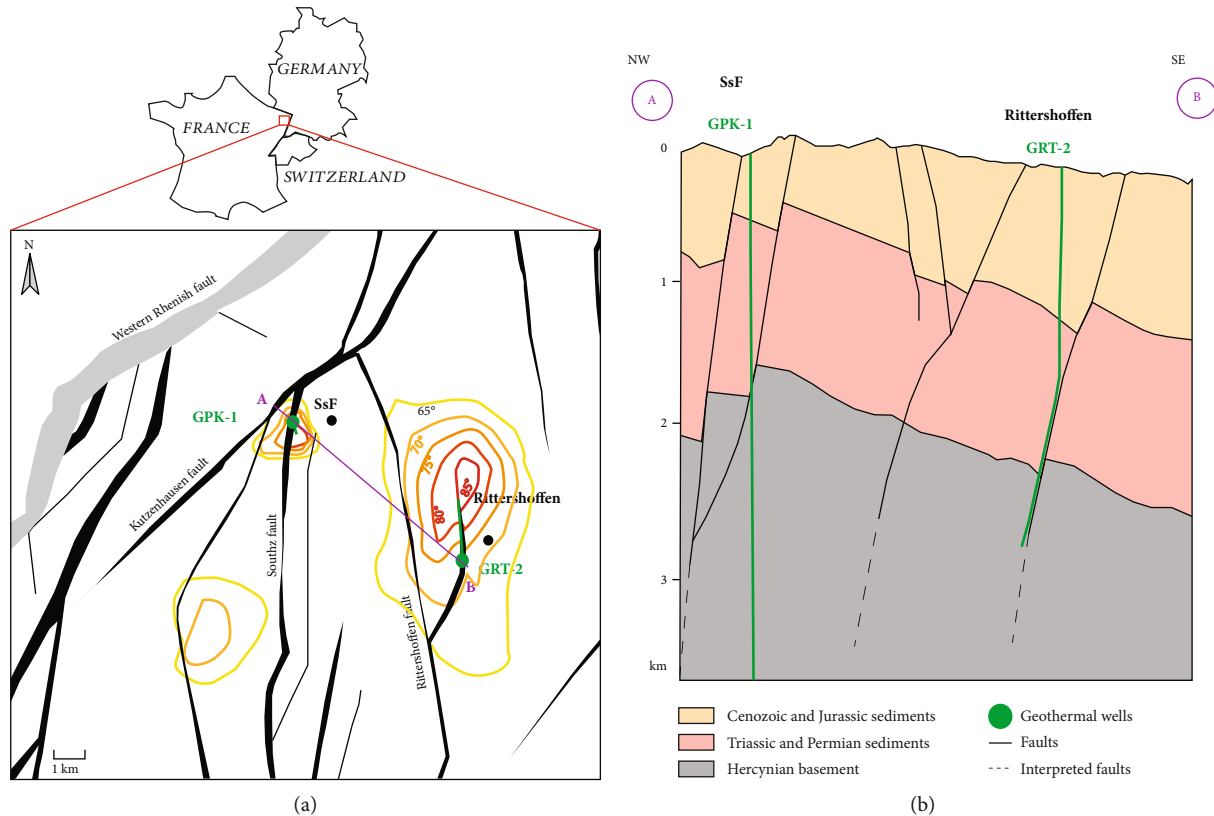


FIGURE 2: (a) Structural map of the top of the granitic basement from the GeOrg geoportal with the well trajectories (green), the thermal anomalies [3], and the Soutz (SsF) and Rittershoffen localizations. (b) Geological cross section through the GPK-1 and GRT-2 wells crossing the URG sedimentary cover and granitic basement; the well trajectory of the GRT-2 well is a NW-SE projection on the cross section, from the last 3D seismic campaign [72].

signatures and architectures of the FZs will be detailed. In the next step, the geophysical logs and SWIR results will be correlated and used to differentiate paleo- and present-day permeable zones. Finally, we will discuss the applicability of the SWIR method and its implications for the understanding of the mineralogy and the distribution of illitization at the well scale.

2. Geological Setting

2.1. Soutz and Rittershoffen Sites. In 2019, two deep geothermal plants exploiting deep fractured granite are operating in France. These plants produce a total of 24 MWth for industrial use at Rittershoffen and 1.7 MWe for the electrical grid at Soutz. Both sites are located in the URG approximately 40 km north of Strasbourg and target the hydrothermally altered granitic basement as a geothermal reservoir (Figure 2(a)).

The Soutz GPK-1 well was drilled vertically from 0 to approximately 2000 m measured depth (MD) in 1987 and was then deepened almost vertically to 3590 m MD in 1992 (Figure 2(b)). It crosses the Cenozoic and Mesozoic sedimentary covers before reaching the top of the Paleozoic granitic basement at 1376 m MD. The drilling of this well in 1987 was conducted according to an old geothermal concept, involving the creation of an artificial heat exchanger by

hydraulic stimulation created by vertical wells [22–25]. The well was hydraulically stimulated several times to enhance the connection between the well and the reservoir [26, 27]. The FZs in the granitic basement are mainly oriented N160–170°E and subvertical, and most of them dip more steeply than 65° eastward or westward [14]. On drilling, natural very saline brines were encountered in fractured and altered zones bearing secondary minerals of hydrothermal origin [28]. Five main permeable FZs ranging from 20 to 40 m in apparent thickness are intersected at 1645, 1814, 2000, 2818, and 3495 m MD. In 2004, the Soutz site was composed of five deep wells that in fact revealed numerous permeable FZs [28].

The Rittershoffen project was initiated in 2008, and its target was the Rittershoffen normal fault, which is crossed by two deep wells, GRT-1 and GRT-2. The production well GRT-2 was drilled subvertically from 0 to 2480 m MD crossing the sedimentary cover to the top basement and was highly deviated (40° to the north) down to 3196 m MD crossing the granitic basement (Figure 2(b)). The target was to crosscut the main local fault as long as possible. This normal fault, which is located approximately 15 km east of the western Rhenish border fault, is oriented N5°E based on subsurface geological data [29, 30]. The GRT-2 well is therefore slightly deviated but tangent to the local fault over its approximately 400 m apparent length (Figure 2(b)). The GRT-2 well

revealed a high productivity index of 4 L/s/bar without any stimulation; thus, a hydrothermal concept could be implemented [13, 31]. Achieved in 2016, this Rittershoffen project proved to be a great success, with an operational plant producing a flow rate of 70 L/s at surface T of 168°C [32]. In the granitic section of the open hole of the GRT-2 well, four main permeable FZs ranging from 15 to 40 m in apparent thickness were intersected at 2533, 2770, 2950, and 3052 m MD [31, 33, 34].

Observations conducted on continuous and high-quality coring of the EPS-1 well from Soultz highlighted a multiscale fracture network [35]. Small-scale fractures with no evidence of displacement are filled with carbonates, chlorite, iron oxides, epidote, and sulphides, and faults visible at the core scale are filled with drusy quartz (euhedral quartz crystals as coatings on or infillings in fractures), carbonates, barite, and clay minerals. In the case of the Rittershoffen wells, for which no core was available, only the largest faults could be identified (small-scale fractures were hardly identified) because only cuttings and acoustic image logs were available.

2.2. Alterations of the Granitic Basement. During the cooling of the crystalline pluton, the granite underwent a pervasive alteration that presents the petrographic and mineralogical features of the propylitic facies. Today, it exhibits several grades of hydrothermal alteration that are also related to fluid circulation [36, 37]. The unaltered crystalline granitic basement at Rittershoffen and Soultz is composed of primary muscovite, biotite, K-feldspar, plagioclase, and quartz [37, 38]. This primary mineralogy is affected by hydrothermal alteration, and specific mineralogical associations reflect the various alteration grades encountered. According to previous studies of the Soultz geothermal wells, the hydrothermal alteration grades in the granite are well known from core observations [16, 17, 37, 39–41]. In this study, the core mineralogy and hydrothermal alteration grades were crossreferenced with the minerals observed in the cuttings using a binocular magnifier, although the texture information and the mineral assemblage were not reflected in the cuttings (Figure 3). The mineralogy of the cuttings was determined through a semiquantitative approach using a three-class scale [18, 33]. The hydrothermal alteration grades—low (HLOW), moderate (HMOD), high (HHIG), and extreme (HEXT)—are described in Figure 3 [42–46]. The granitic facies identified in the cuttings include two types of granite, “unaltered” granite (GRAN), affected by a propylitic alteration related to the cooling of the pluton [14, 47], and the presence of locally reddish granite (RED), containing a large number of red K-feldspar megacrysts that have been oxidized through intense exposure to weathering fluids. The presence of illite in the granitic basement as a major signature of hydrothermal alteration was confirmed by complementary laboratory analyses. In previous studies of the GRT-2 well, X-ray diffraction (XRD) was performed on the $<5 \mu\text{m}$ fraction of selected cuttings; in this way, three groups of illitic minerals (well-crystallized illite, poorly crystallized illite, and illite-rich illite/smectite mixed layers) were identified [18]. The chemical composi-

tions of the clay minerals were obtained using a scanning electron microscope (SEM) coupled with energy-dispersive X-ray spectroscopy (EDS). This study showed that permeable FZs were associated with the occurrence of poorly crystallized illite and illite/smectite mixed layers that crystallized during hydrothermal circulation [18]. XRD measurements of the GPK-1 well’s cuttings were also performed in this study; the results showed the presence of illite in fractured and altered zones as well as the presence of chlorite and biotite in HLOW and GRAN.

3. Materials and Methods

3.1. SWIR Spectroscopy Method

3.1.1. Materials. The cuttings (chip samples) collected during the drilling of the wells were first washed using sieves and then dried on-site in an oven at 80°C for 40 minutes, by the mud logger unit. In the case of the GRT-2 well, the cuttings were sampled every 3 m in depth in the studied 8 1/2” drilled section. Thus, one bag of cuttings represents approximately 0.1 m³ of rock. For the GPK-1 well, the cuttings were sampled every 1 m in depth; thus in the 9 5/8” drilled section from 1400 to 2850 m MD, one bag of cuttings represents approximately 0.04 m³ of rock, and in the 7 5/8” drilled section from 2850 to 3590 m MD, one bag of cuttings represents approximately 0.025 m³ of rock. The sampling included in this study encompasses all the facies described in the foregoing section (Figure 3). The average grain size of the cuttings chips in each sample varies between 0.5 and 2 mm. The chip size can be highly influenced by drilling tool wear. For this reason and because the chip size of the cuttings influences the SWIR intensity (the higher the chip size, the higher the SWIR intensity), the changes of drilling tool are also presented in this work.

3.1.2. Measurement Conditions. The SWIR spectral domain extends from 1000 to 2500 nm. If the wavelength of the infrared radiation is close to the vibrational energy of the eigenmode of the molecule, it causes vibration of some bonds and the infrared radiation energy is absorbed. This is conveyed by absorption bands on the infrared spectrum acquired at the corresponding wavelength in the midinfrared (MIR) domain. In the SWIR domain, we can observe the harmonics and the combinations of these absorption bands [48]. In total, 240 cuttings samples from the GRT-2 well and 1190 cuttings samples from the GPK-1 well were analysed. The SWIR measurements were performed at the same time for each well; thus, the acquisition conditions (hygrometry of the room, ambient temperature) are homogeneous for each well. Because very few expandable clay minerals are present in the granite, even when it has been hydrothermally altered, the SWIR data are not very sensitive to the hygrometry parameter. This is confirmed by the reproducibility of the low values of the 2200 nm absorption band area in the unaltered granite for all the geothermal wells studied in the URG. The spectrometer used is a TerraSpec 4 Standard Res Mineral Analyzer created by Analytical Spectral Devices, Inc. (Malvern PANalytical company) equipped with two SWIR

	Granite hydrothermal alteration grades	Core samples Sultz-sous-Forêts 4 cm	Cuttings samples Rittershoffen 3 mm
 + hydrothermal alteration	GRAN (unaltered granite): - Bt - Hem - Cal - Red Kfs megacrysts (large amount)		
	HLOW (low hydrothermal alteration): - Chl - Primary Bt (few) - Absence/minor amount of secondary Illt - Unaltered primary Pl+Kfs		
	HMOD (moderate hydrothermal alteration): - Illt (further alteration of Chl) - Pl+Kfs (weakly altered) - Fresh and weakly altered Bt (minor amounts)		
	HHIG (high hydrothermal alteration): - Illt (abundant) - Chl (very few) - Pl+Kfs (strongly altered) - Altered Bt (relics)		
	HEXT (extreme hydrothermal alteration): - Depletion of Bt - Illt (abundant) replacing primary Bt - Pl+Kfs - Drusy Qz linked to hydrothermal circulation		
	VEIN (quartz vein): core of the FZs - Highest amount of secondary drusy Qz associated with a high Cal content		

FIGURE 3: Examples of mineralogical assemblages of the granitic basement observed in cores (middle) and in cuttings (right); these assemblages define the different hydrothermal alteration grades (left). GRAN: unaltered granite; HLOW: low hydrothermal alteration; HMOD: moderate hydrothermal alteration; HHIG: high hydrothermal alteration; HEXT: extreme hydrothermal alteration; VEIN: secondary drusy quartz vein; Anh: anhydrite; Bt: biotite; Cal: calcite; Chl: chlorite; Hem: hematite; Illt: illite; Kfs: potassic feldspars; Pl: plagioclase; Qz: quartz.

detectors. The spectral domain from 350 to 2500 nm is covered at a spectral resolution of 3 nm from 350 to 1000 nm and at a spectral resolution of 10 nm from 1000 to 2100 nm. The scanning time of 100 milliseconds made it possible to

conduct the measurements rapidly for all granitic sections. The wavelength reproducibility is 0.1 nm with an accuracy of 0.5 nm. The reproducibility of the measurement was tested by measuring the same sample five times; this resulted in a

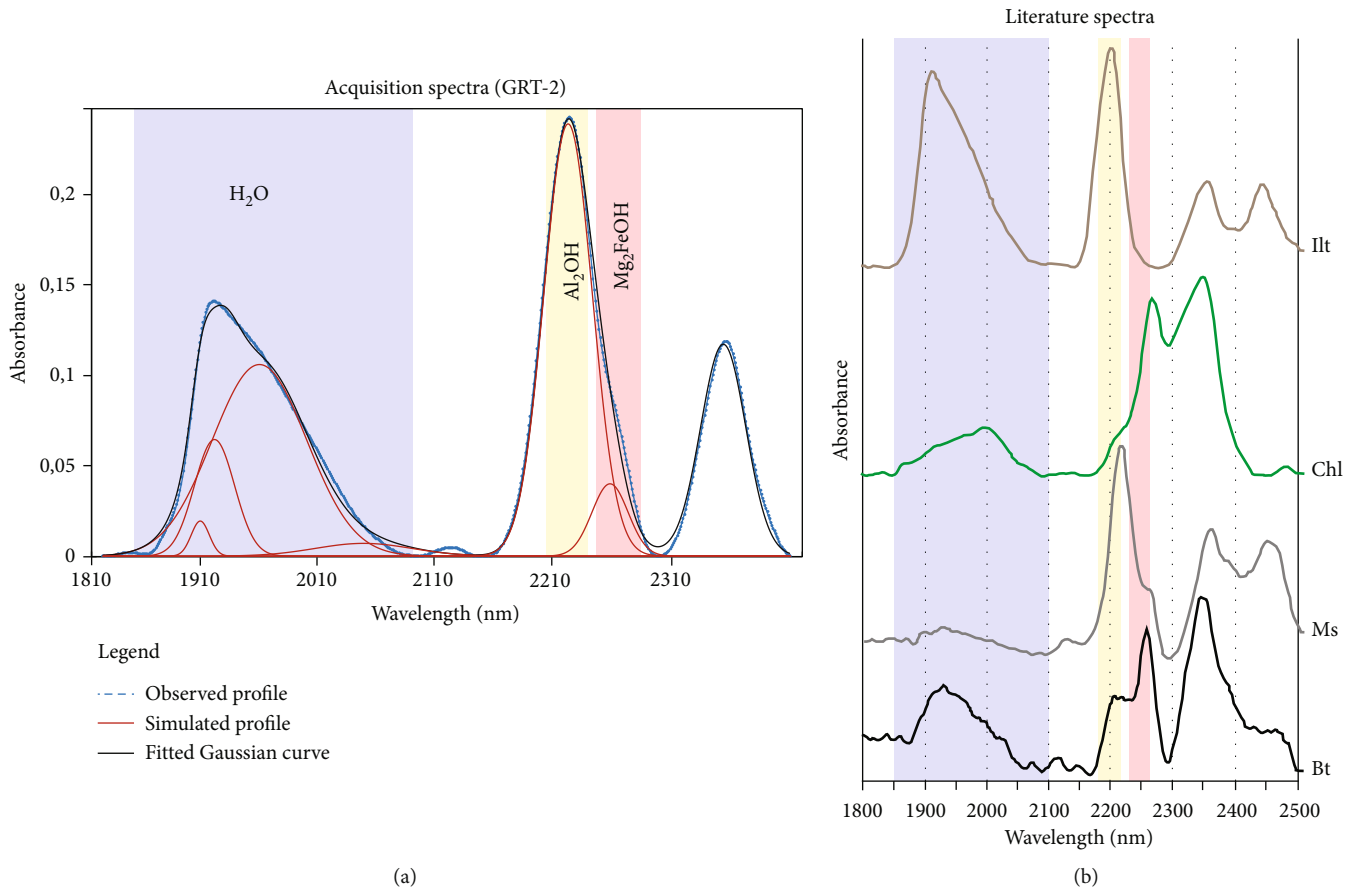


FIGURE 4: (a) Example of an absorption spectrum and a simulated profile in the GRT-2 well at 2800 m. (b) Reference spectra from Pontual et al. [52] for biotite (Bt), muscovite (Ms), chlorite (Chl), and illite (Ill).

variation of 1% for the 2200 nm absorption band area, by performing five measurements without moving the sample and five measurements after mixing the sample (personal communication). Before measurements are taken, the ASD TerraSpec requires a warm-up period of approximately 30 minutes. It is also necessary to conduct a calibration with the “Spectralon” reference material provided with the machine before the first measurement and thereafter regularly every hour during the measurement period [49].

3.1.3. Processing. After the measurement, the SWIR spectra were processed with “the Spectral Swagger” (TSS), an in-house Visual Basic Macro developed at Poitiers University that runs on Microsoft Excel [49]. First, the baseline was removed automatically by the software; then, spectra were fitted with few Gaussian curves (four and two for the water and the 2200 nm absorption band areas, respectively). To create a profile simulation, the user must set the position and the half width at half maximum (HWHM). The height parameter is automatically deduced from the baseline-removed spectrum; its initial height equals 90% of the y -axis value of the baseline-removed spectrum at the Gaussian centre wavelength. The user can designate the parameter that will be allowed to change. The final simulated profile is the sum of all Gaussian curves. The quality of the fit between the simulated

and observed profile is verified against the weighted profile R -factor (Rwp), which is commonly used in Rietveld refinements [50]. In this study, six Gaussian curves were used to fit the spectrum from 1820 to 2300 nm (Figure 4). For the GRT-2 well, position and HWHM were locked for each simulation profile. However, different sets of position and HWHM were used. Simulation profiles with an Rwp lower than 0.05 were accepted. For the GPK-1 well, for which a very large number of profiles (1190) were calculated, position and HWHM were free-fitted by TSS for each simulation profile. The areas of the water absorption band and the 2200 nm absorption band were also fitted manually for some profiles to determine whether there was a significant deviation in the area with respect to the free fitting. The results showed that there was no significant change in the area between profiles fitted manually and those free-fitted by TSS (see Figure S3 in the supplementary materials). Thus, the results presented in this study for the GPK-1 well are profiles that were free-fitted by TSS.

3.1.4. Mineralogical Identification. In the SWIR spectral domain, the phyllosilicates are detected, and they are not influenced by feldspars and quartz, which do not present absorption bands in this domain. Four Gaussian curves were used to fit the absorption band spanning the

wavelength range from 1900 to 2060 nm (Figure 4); this range corresponds to the stretching and bending vibrations of H₂O molecules. This absorption band exists not only for the hydrated phyllosilicates but also for some other hydrated minerals such as zeolites, opal, and amorphous silica. This absorption band can also vary according to the humidity of the environment. Hence, not only it is linked to clay minerals but also, under constant humidity conditions, the area of this absorption band will vary according to the quantity of clay minerals present in the sample. This aspect will be discussed in Section 5.2. Two Gaussian curves were used to fit the absorption band spanning the wavelength range from 2200 to 2255 nm, which mainly corresponds to the vibrations of the bonds between the cations of the octahedral sheets and the structural OH groups in the aluminous phyllosilicates, i.e., corresponding to the combination modes of the stretching and bending vibrations of the Al₂OH groups [51]. Thus, the 2200 nm absorption band represents Al-rich dioctahedral clay minerals [52]. The shoulder observed between 2247 and 2253 nm is more complex in terms of absorption band and mainly reflects the occurrence of biotite and chlorite trioctahedral clay minerals as well as of muscovite (Figure 4(a)). The Gaussian curves used to fit the spectrum from 2300 to 2400 nm are not presented in this study because we are focusing on the relative quantification of illitic minerals associated with the “Al₂OH” absorption band. In our study, the mineralogy of the granitic basement in the wells is thoroughly described by binocular magnifier observation of 240 cuttings from the GRT-2 well [33] and 1190 cuttings from the GPK-1 well [37, 53]. Thus, the variation in the relative integrated intensity of the 2200 nm absorption band is considered to represent illite variations, except in the GRT-2 well from 2950 to 3200 m MD, where significant amounts of biotite were observed, and in the GPK-1 well, in which biotite is present in the unaltered granite. Based on a comparison with spectra reported in the literature (Figure 4(b)), the influence of chlorite on the 2200 nm absorption band area is not significant, but the influence of biotite and muscovite could be significant if these minerals were present in high amounts in the studied samples. Beyond the mineralogical signature of the absorption bands, this methodology was used for a broad quantification of clay minerals based on the Beer-Lambert law, which establishes proportionality between the absorbed energy and the concentration of chemical bonds in the analysed material [54]. In this study, the area of the 2200 nm absorption band is expressed in arbitrary units (a.u.) which represents the area of the absorption band considered.

3.1.5. Intrasample Variability. Because each cuttings bag contains sections of the drilled rocks (see Section 3.1.1) and because the cuttings could not be homogeneously mixed in the bag, several measurements were performed on each cuttings bag (see Figures S1 and S2 in the supplementary materials). In the GRT-2 well, 10 measurements were performed on the same cuttings bag, whereas only 5 measurements were performed in the GPK-1 well due to the lower amount of cuttings available. Error bars were calculated for each cuttings bag to determine whether the range of variation exceeds the scattering of the data.

Because the results were found to be reliable, they are not presented in this study; however, figures showing the results are provided as supplementary materials.

3.2. X-Ray Diffraction. X-ray diffraction data were acquired from selected cuttings samples of the GPK-1 well and used to identify the clay minerals present in the samples. The XRD results of Vidal et al. [18] for the GRT-2 well were also used in this study. Twenty-eight cuttings samples were collected from the GPK-1 well. The sampling was concentrated in the permeable and altered FZs as well as in the unaltered granite that was used as a reference material, as the latter is believed to be representative of rocks preserved from actual fluid circulation. The samples were not ground; they were dispersed in distilled water by ultrasonic vibration. Oriented powders on glass slides were prepared from a <5 μm clay mineral suspension obtained by sedimentation. Clay minerals were identified by XRD of air-dried and ethylene glycol-saturated oriented powders conducted on a Bruker D8 Advance diffractometer (CuKα radiation, 40 kV, 40 mA). The analytical conditions were as follows: angular domain, 2.5–30° 2θ; step increment, 0.025 2θ; and counting time per step, 1 s. XRD data acquisition and treatment were conducted using the X'Pert HighScore software (PANalytical B.V.). The clay minerals were identified according to the literature [55].

3.3. Geophysical Logs. The geophysical logs and mud logging data are presented in this study to highlight their correlations with evidence of present-day circulation (*T* log, He, CO₂, CH₄, and Rn), FZ evidence (neutron porosity, density, and resistivity), and evidence of the presence of paleo-circulation zones rich in illite (total gamma ray, spectral potassium gamma ray (GR-K), and electrical resistivity).

3.3.1. Temperature. The *T* log is expressed in °C. Measurements were made every 50 cm and 10 cm in the GRT-2 and GPK-1 wells, respectively. *T* anomalies are interpreted as the signatures of fluid circulations between the well and the formation [30, 56–58]. For this study, the *T* log of the GRT-2 well was shifted upwards by 2 m from 2480 to 2650 m MD and upwards by 10 m from 2650 to 3196 m MD because stretching of the cable occurred during the measurement as a function of depth. Moreover, because the *T* log of the GRT-2 well was acquired separately, it could not be correlated in depth with another reference. Thus, in this study, the *T* log was correlated with the resistivity and porosity logs because they obviously presented the same types of anomalies preceding the four main *T* anomalies. For similar reasons, the *T* log of the GPK-1 well was shifted downwards by 7 m to vertically fit the *T* anomalies and the permeable FZs [30].

3.3.2. Gas Content (He, CO₂, and CH₄). The occurrence of alkanes as well as of other gas species such as He, CO₂, and CH₄ indicates permeable FZs [59, 60]. For reference, the abundances of He and CH₄ in the atmosphere are approximately 5.24 ppm and 1.75 ppm, respectively. He, CO₂, and CH₄ were monitored in GPK-1 [59]. Only CH₄ was monitored in GRT-2 [34].

3.3.3. Porosity. The neutron porosity log (NPHI) which is supposed to quantify the porosity filled with water is deduced from measurements of the hydrogen content of the formation (fast neutrons emitted by the tool are slowed down by elastic scattering, mainly due to collision with hydrogen atoms). Neutron porosity can also be highly influenced by clay minerals, which often contain bound water. It is expressed in m^3/m^3 and sometimes in %. It was sampled at every 15 cm depth in the GRT-2 and GPK-1 wells. The parameter has an investigation depth of several cm behind the borehole wall, which can correspond to the flushed zone. Porosity logs do not directly indicate true porosity in this context, a specific calibration should be performed, and the influence of the granitic matrix on the neutron porosity can be as high as 7% [61]. Nevertheless, the neutron porosity measured here provides a global signal for FZs to the extent that they are porous and contain fluids and/or clay minerals.

3.3.4. Density. The density log (RHOB) is calculated from returning gamma rays following the interaction of gamma rays emitted from a chemical source (Ce^{137} and Co^{60}) with the electrons present in the elements in the formation. These gamma rays are related to the electron density of the formation, which itself depends on the formation density. RHOB is given in g/cm^3 and was acquired every 15 cm in depth for both the GRT-2 and the GPK-1 wells. A negative peak in a density curve could be due to the occurrence of secondary clay minerals and high porosity and thus should reveal alterations associated with a fracture zone, whereas positive peaks are associated with high-density minerals or changes in lithology.

3.3.5. Gamma Ray. The gamma ray (GR) log measures natural radioactivity (cumulative emissions, mainly from uranium (U), potassium (K), and thorium (Th)) in gAPI; vertical sampling of the GRT-2 and GPK-1 wells was performed every 15 cm. The GR log is aimed at interpreting lithology and rock composition by detecting clay minerals rich in potassium (illite and muscovite). In the altered crystalline basement, negative GR peaks in the lower positive domain can reflect drusy quartz veins in illitized host rock [14]. In the context under study, GR data are an indicator of hydrothermal alteration and thus provide information regarding paleo-permeability.

3.3.6. Electrical Resistivity. In unaltered hard rocks, the electrical resistivity log is mainly controlled by the electrical conductivity of the fluid contained in the rock porosity, a factor that is particularly significant in FZs. Electrical resistivity decreases with water saturation and is even lower for conductive fluids that contain salts, such as brines. Similarly, the electrical resistivity of clay minerals, which are conductive minerals, is low [62]. Hence, laterologs and focused resistivity arrays are sensitive to fracturation and alteration. Resistivity laterologs measure an apparent electrical resistivity that needs to be corrected for the probe characteristics, the hole effect, and spatial variations in electrical resistivity (dipping). In the zones in which hydrothermally altered granite may

coexist with unaltered granite, electrical resistivity modelling should be applied to obtain the “true” electrical resistivity by taking into account the 2D/3D geometry of the zone [63]. Although petrophysical models are commonly used to evaluate hydrocarbon saturation in sedimentary formations [64]; for instance, the estimation of porosity changes from electrical resistivity is not so straightforward in fractured granitic environments. The electrical conductivity can vary by several orders of magnitudes in zones and areas with different clay mineral contents and fracture densities, whether or not the zones are sealed. In the GRT-2 well, the electrical resistivity was measured with a five-electrode configuration, yielding five apparent resistivity values (RLA1–5) [65]. The contribution of the matrix to the electrical conductivity is supposed to be far lower than that of fractures, and it can vary by several orders of magnitude among unaltered and altered granite zones [33]. Measurements were obtained every 15 cm in depth. These configurations are sensitive to the distance beyond the borehole wall. The shallowest resistivity (RLA1) mainly reflects the average resistivity of the borehole mud, and the deepest resistivity (RLA5) mainly reflects the average resistivity of the formation (granite matrix). In the GPK-1 well, the electrical resistivity was measured in 1989 using a laterolog tool with a two-electrode configuration every 15 cm in depth, yielding a shallow laterolog (LLS) and a deep laterolog (LLD). In this paper, only the most far-reaching resistivity curves (RLA5 and LLD) are presented on an inverted scale with highly resistive values on the left and conductive values on the right, allowing the reader to easily correlate GR, SWIR, and conductive peaks.

4. Results

4.1. GRT-2 Well

4.1.1. Dataset. The petrographical log of the GRT-2 well (Figure 5) was built from the macroscopic description of the alteration mineralogy in the cuttings. The hydrothermal alteration grades were determined according to the occurrence of the secondary minerals (chlorite, illite, and drusy quartz) in the cuttings samples. This petrographical log presents three major units: reddish, oxidized granite at the top of the granitic basement, an altered zone from 2535 to 3060 m MD with a highly altered core from 2737 to 2875 m MD, and unaltered granite at the bottom of the well from 3060 to 3196 m MD. These main sections correlate well with the SWIR values; more precisely, we can distinguish four sections in which the variations in the 2200 nm absorption band area are indicative of the alteration grades around the permeable FZs.

4.1.2. SWIR Variations and Hydrothermal Alteration Grades. The first section, from 2514 to 2570 m MD around the FZ1, is characterized by a small increase in the SWIR 2200 nm absorption band area, with scattered values between 6 and 10 a.u. It corresponds to the RED and HHIG facies observed with a binocular magnifier.

The second section, from 2570 to 2970 m MD, comprises the FZ2 and the FZ3 and corresponds to the HHIG and

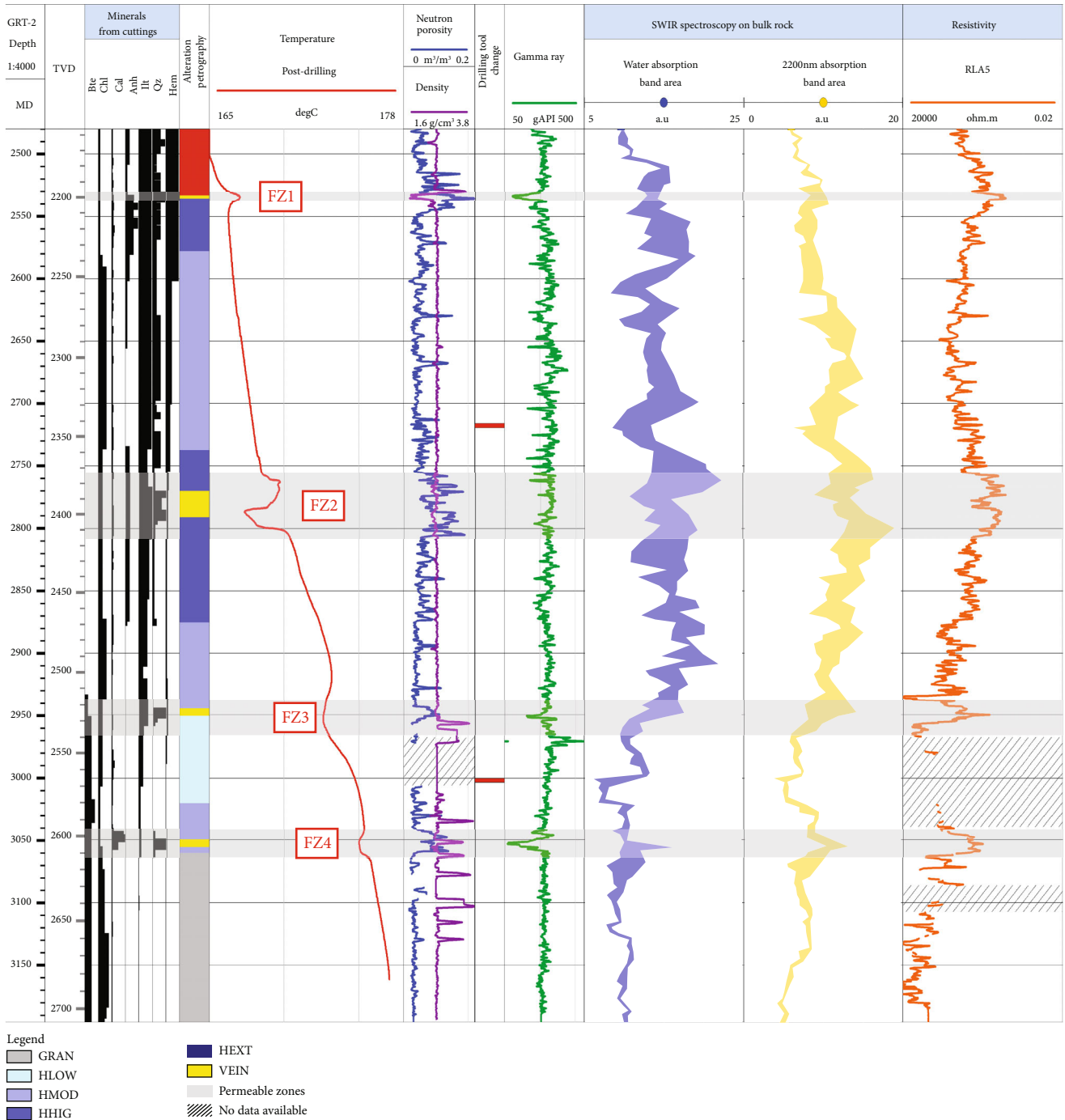


FIGURE 5: Composite log of the GRT-2 well at Rittershoffen presenting the mineral quantity, petrographical log, T log, porosity and density logs, drilling tool change, total GR, SWIR results with water and the 2200 nm absorption band areas, and resistivity log. Petrographical facies abbreviations are defined in the legend in Figure 3.

HMOD facies observed with a binocular magnifier. This zone is characterized by the highest values of the 2200 nm absorption band area observed for the well. These values are highly scattered between 10 and 20 a.u., and because the acoustic image logs for GRT-2 are of poor quality, it is difficult to correlate the lowest values with opened fractures. The illitization appears to increase with the alteration grade, reaching its highest value (20 a.u.) in the fracture wall (FW) at 2780 m MD. In the FZ2, minimal values of the 2200 nm absorption

band area are observed for a few samples located approximately 2773 m MD. In the acoustic image logs, an opened fracture filled with secondary drusy quartz (VEIN) is observed at 2773 m MD. Below, in the deepest section, acoustic image logs are not available.

The third section, from 2970 to 3070 m MD, comprises the FZ4. The 2200 nm absorption band area appears to increase with the alteration grade, reaching its highest value (14 a.u.) in the FW at 3055 m MD, associated with a

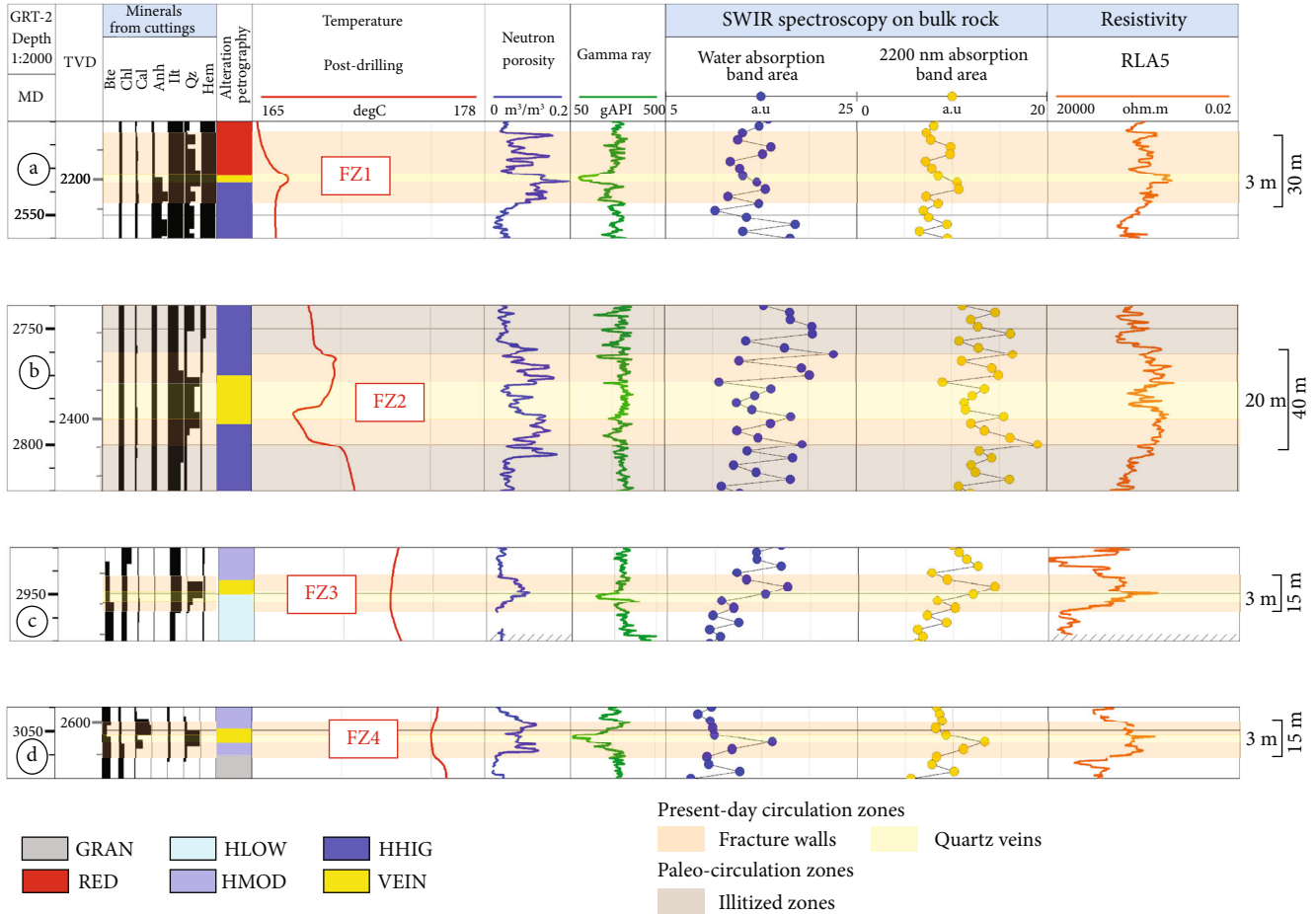


FIGURE 6: Magnified view of the four (a, b, c, and d) main permeable FZs of the GRT-2 well at Rittersshoffen, presenting the mineral quantity, petrographical log, T log, porosity and density logs, total GR, SWIR results with water and the 2200 nm absorption band areas, and resistivity log (low values to the right). Petrographical facies abbreviations are defined in the legend in Figure 3.

permeable FZ and a quartz vein at 3050 m MD. This zone corresponds to the HMOD and HLOW facies observed with a binocular magnifier.

The fourth section, from 3070 to 3196 m MD, corresponds to the GRAN facies observed with a binocular magnifier. The values of the 2200 nm absorption band area are stable and low, ranging from 5 to 8 a.u.

The resistivity log also appears to correlate relatively well with the trend of the SWIR log (2200 nm absorption band area). In the open hole of the GRT-2 well, 500 m is altered granite and 200 m is unaltered granite. Thus, altered granite represents 70% of the open-hole section.

4.1.3. Permeable FZs. The four permeable FZs of the GRT-2 well are shown in Figure 6 and are discussed below.

(1) *FZ1 (2533 m MD)*. From the ultrasonic borehole images (UBI), no small-scale fracture is observed around the quartz vein for this FZ [34]. The porosity log shows high, scattered values in the entire FZ, the GR log exhibits a low peak correlated with the quartz vein, and the resistivity log shows a high conductivity peak that is also correlated with the quartz vein (Figure 6(a)). The thermal anomaly is localized at the quartz vein depth. The SWIR absorption band area at 2200 nm

shows scattered and average values. According to the geophysical logs, the natural flow appears to be spatially correlated with the occurrence of a quartz vein. The observed conductivity peak in this permeable quartz vein could be due to the presence of geothermal brine, which is a very conductive fluid [66].

(2) *FZ2 (2770 m MD)*. The UBI is not available over the entire zone, but open fractures are observed at 2767, 2770, and 2774 m MD and are associated with the occurrence of quartz veins, translating into potential open pathways for fluids. Below these open fractures, smaller sealed fractures are observed from 2786 to 2789 m MD [34]. Whereas the GR is quite stable with some small negative peaks, the porosity, electrical conductivity, and SWIR 2200 nm absorption band area present two positive humps extending vertically over a length of 40 m (Figure 6(b)). This zone is the most contributive according to hydraulic tests [31], but the intra-FZ section reveals a complex architecture. At the centre of the zone, resistive values are observed (from 2776 to 2783 m MD), correlating with low neutron porosity, whereas the GR is unaffected, which goes along with the presence of the quartz vein observed in the cuttings. More generally, the observations in this FZ are consistent with a permeable FZ and brine

circulations. The lack of UBI data in this zone does not help support our interpretation. However, the fact that the unavailability of UBI data is due to difficulties in running the tool in this zone because of cavings also suggests the existence of an FZ.

(3) *FZ3 and FZ4 (2950 and 3052 m MD)*. No UBI is available for this zone; thus, we are unable to describe the architecture of the FZs. The presence of *T* anomalies implies circulation in both FZs. These two FZs look alike. In fact, they present a neutron porosity increase over 10 m, a low GR, and a sharp peak in electrical conductivity correlated with the quartz veins (Figures 6(b) and 6(c)). Two higher resistivity values are observed above and below the FW, surrounding the zone of higher neutron porosity. These peaks appear to be related to the presence of unaltered (or slightly altered) granite, which occurs from 2934 m MD according to the high resistive values and also appears to be correlated with the SWIR values, which are stable and low at this depth. The SWIR 2200 nm absorption band area is high in both of these FZs. For both FZs, the sharp increase in electrical conductivity appears to be linked to brine circulation in the quartz veins, whereas the lower conductive values above and below the quartz veins appear to be linked to the occurrence of illite in the FW. The abrupt decrease in electrical conductivity suggests a closely delimited hydrothermal circulation zone.

4.2. GPK-1 Well

4.2.1. *Dataset*. The petrographical log of the GPK-1 well was compiled by Genter et al. [42, 43] and Traineau et al. [37] from cuttings samples based on macroscopic observations with a binocular magnifier. The grades of hydrothermal alteration were determined according to the occurrence of the secondary minerals (chlorite, illite, and drusy quartz) in the cuttings samples. This petrographical log presents three major hydrothermally altered granite units surrounded by unaltered granite. These three units extend from 1580 to 1830 m MD, from 2600 to 2800 m MD, and from 3200 to 3500 m MD.

4.2.2. *SWIR Variations and Hydrothermal Alteration Grades*. The first section, from 1580 to 1830 m MD, is characterized by very scattered high values between 3 and 26 a.u. for the 2200 nm absorption band area. The shift of the SWIR values to high values in this section could be due to a granulometry effect, as this section was drilled first and was then deepened, resulting in a change in the cuttings grain size. Based on binocular magnifier observations, this section corresponds to GRAN with hydrothermally altered zones of HMOD-HHIG facies. These altered zones appear to correlate with the SWIR values, which are higher, i.e., between 8-17 a.u. for the 2200 nm absorption band area for HMOD (1547-1553 m MD, 1579-1606 m MD, and 1650-1656 m MD) and approximately 25 a.u. for HHIG (at 1620-1640 m MD). Quartz veins were identified at 1645 m MD (FZ1) and at 1814 m MD (FZ2), where drusy quartz was visible by observations of cuttings. The latter corresponds to a fracture vein that is visible in core samples (Figure 7).

The second section, from 2605 to 2827 m MD, is characterized by high, scattered values between 3 and 19 a.u. for the 2200 nm absorption band area. Based on binocular magnifier observations, it corresponds to GRAN with occurrences of low to high hydrothermal alterations. The HLOW grade appears to correlate with the 2200 nm absorption band area, with values between 5 and 10 a.u. at 2600-2603 m MD, 2610-2612 m MD, 2676-2679 m MD, 2681 m MD, 2693-2701 m MD, and 2731-2733 m MD. Occurrences of HMOD suggest a good correlation with the 2200 nm absorption band area, with values between 7 and 15 a.u. at 2625-2632 m MD, 2679-2681 m MD, 2685-2692 m MD, 2701-2731 m MD, and 2733-2736 m MD. The HHIG occurrences also suggest a good correlation with the stable values of the 2200 nm absorption band area, which range from 14 to 19 a.u. A quartz vein is observed in the cuttings from 2817 to 2818 m MD (FZ3). An open fracture is observed on the FMI log and is characterized by the occurrence of He and CO₂ content, evidencing the presence of geothermal fluid.

The third section, from 3203 to 3523 m MD, is characterized by high, scattered values between 3 and 19 a.u. for the 2200 nm absorption band area. Based on binocular magnifier observations, it corresponds to GRAN with occurrences of hydrothermal alterations of HLOW to HEXT facies. HLOW appears to correlate with values of the 2200 nm absorption band area between 4 and 8 a.u. Two quartz veins are observed in the same fracture zone at 3489 and 3496 m MD in the cuttings. These open fractures, which match the flow log anomalies, are observed on the acoustic image logs at 3490 and at 3495 m MD (FZ4).

Outside of these sections, from 2065 to 2605 m MD and from 2827 to 3203 m MD, we observe low, very stable values between 2 and 9 a.u. for the 2200 nm absorption band area. Based on binocular magnifier observations, these correspond to GRAN, with HLOW-HMOD from 2505 to 2530 m MD. These hydrothermal alteration grades suggest a good correlation with the 2200 nm absorption band area which presents higher values of approximately 9 a.u.

In the open-hole section of the GPK-1 well, 500 m is hydrothermally altered granite and 2200 m is unaltered granite; thus, the hydrothermally altered granite represents only 20% of the open hole.

4.2.3. *Permeable FZs*. The two FZs of the upper section of the GPK-1 well (1540-2000 m MD) are shown in Figure 8 and are discussed below.

(1) *FZ1 (1645 m MD)*. A quartz vein was observed, and a *T* anomaly above the quartz vein proves a contributive flow zone (Figure 8(a)). The porosity presents high values above and below the quartz vein, whereas low values are observed at the quartz vein depth. The GR-K is also slightly higher above and below the quartz vein, whereas it is low at the quartz vein. Very small He content is also visible above the quartz vein. The laterolog resistivity (LLD) presents high conductivity values above the quartz vein and high resistivity values at the quartz vein depth. He content is also observed in this section, indicating the occurrence of dissolved gas in the geothermal fluid (Figures 7 and 8). The SWIR values are high

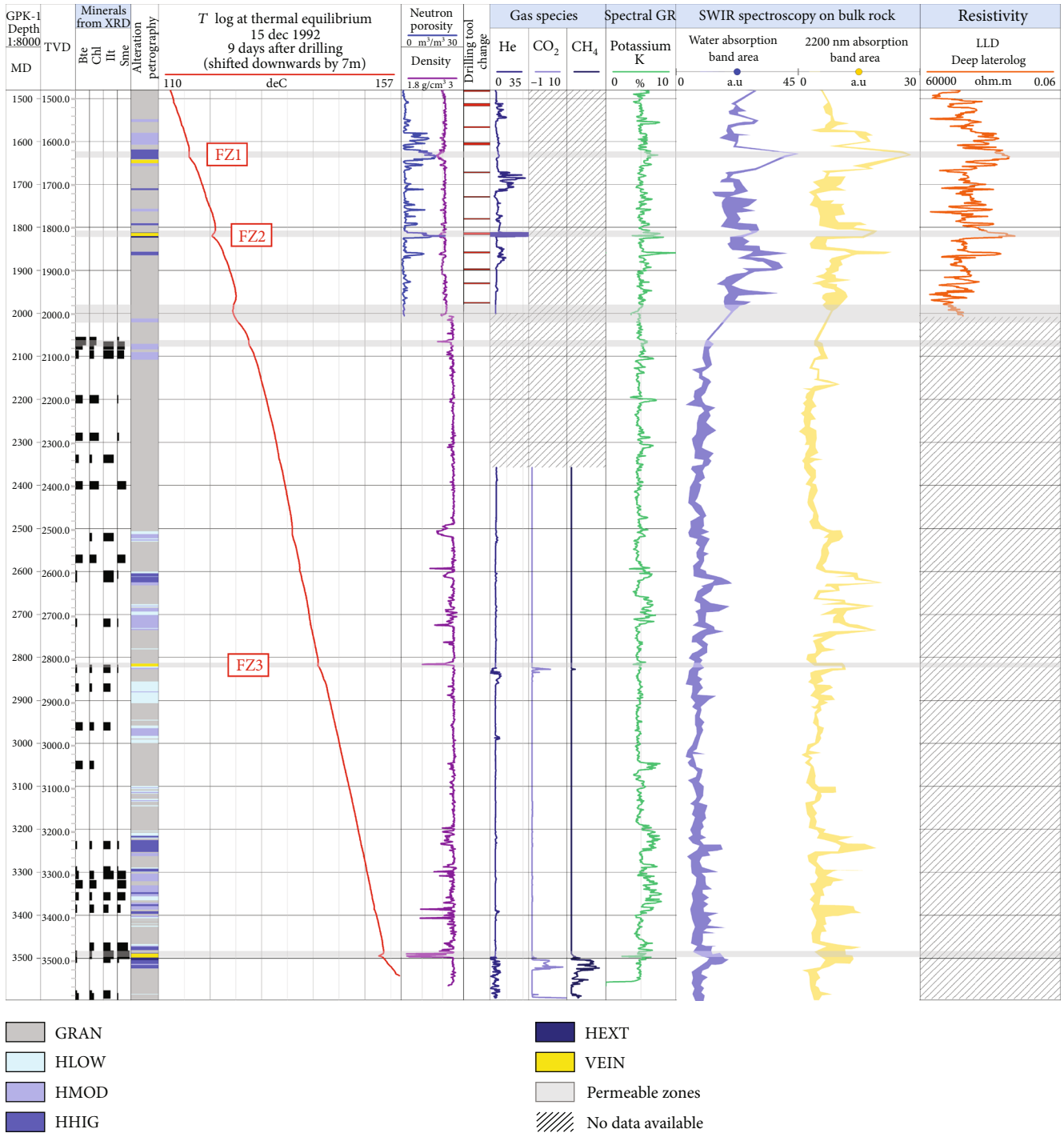


FIGURE 7: Composite log of the GPK-1 well at Soultz-sous-Forêts, presenting the mineral quantity, petrographical log, *T* log, porosity and density logs, drilling tool change, gas species, spectral GR-K, SWIR results with water and 2200 nm absorption band areas, and resistivity log. Petrographical facies abbreviations are defined in the legend in Figure 3.

in the FZ, particularly above the quartz vein. The hydraulic data show that flow anomalies are mainly due to the FZ core [67]. However, surprisingly, the quartz vein presents neither a sharp *T* anomaly nor evidence of fluid circulations from geophysical logs. The geophysical anomalies associated with the FW above the sealed quartz vein could suggest that the FW corresponds to porous granite which allows a good connection between the well and the near-well field. On the other

hand, the geophysical anomalies of the FW below the quartz vein could indicate that the FW acts as a tight zone possibly caused by secondary mineral precipitations.

(2) FZ2 (1814 m MD). This FZ presents a localized *T* anomaly correlated with the quartz vein (Figure 8(b)). According to this *T* anomaly and considering the section between 1400 and 2000 m, the majority of the fluid flows from this FZ

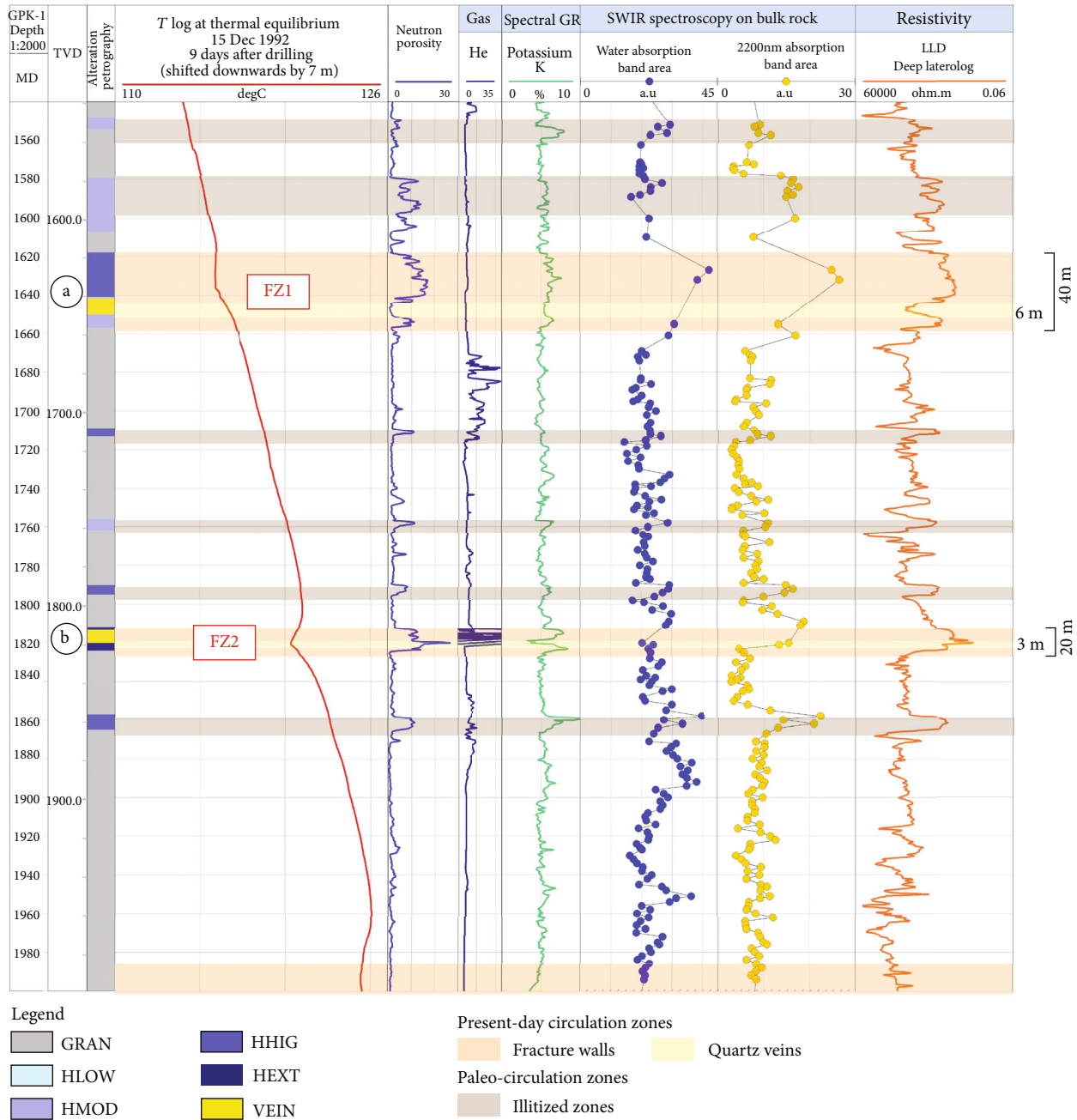


FIGURE 8: Magnified view of two (a and b) main permeable FZs of the GPK-1 well at Soultz-sous-Forêts, presenting the petrographical log, T log, porosity and density logs, spectral GR-K, SWIR results with water and 2200 nm absorption band areas, and resistivity log. Petrographical facies abbreviations are defined in the legend in Figure 3.

[67, 68]. The porosity is high and shows a sharp peak in its centre that is correlated with the drusy quartz vein. The GR-K presents a low peak at the quartz vein depth and high peaks in the FW above and below the quartz vein. The resistivity laterolog presents high electrical conductivity values, with a sharp very conductive peak at the quartz vein depth, and lower-than-average resistivity values above and below that are correlated with the FWs. The SWIR 2200 nm absorption band area presents higher values in the FZ. As for FZ3 and FZ4 in the GRT-2 well, the sharp and very high conductivity values could be associated with the brine circulating in

the quartz vein since high GR-K and the conductive zone above and below coincide with the high amount of clay minerals (illite) in the FW. The very high He content matching the quartz vein (>200 ppm) evidences the occurrence of permeability indicators such as geothermal gases dissolved in the brine.

5. Discussion

5.1. SWIR as a Permeability Indicator. The SWIR method showed good reproducibility of the measurements obtained

on cuttings samples. Stable and low values appear to be systematically observed in conjunction with the unaltered or slightly hydrothermally altered granite (Figures 5, 7, and 9). The geothermal reservoirs of the Soultz and Rittershoffen geothermal sites are highly fractured, with fracture infillings corresponding to secondary drusy quartz and some carbonates, and present hydrothermally altered zones. The heterogeneity of the hydrothermal facies encountered produces heterogeneity in the SWIR signal that appears on the SWIR log as peaks exceeding the mean values, surely reflecting the presence of mineralizations associated with hydrothermal circulations. Because the primary and secondary mineralogy of the deep granites in the URG basement does not vary significantly, the SWIR method is easily applicable to the detection of fluid-rock interaction processes linked to geothermal fluid circulation in the granitic fractured reservoirs of geothermal wells. More generally, the combination of the SWIR 2200 nm absorption band area and the spectral GR-K is a strong illite indicator. On a large scale, the scattering (linked to quartz vein occurrences in the FZs) and the high values of the SWIR 2200 nm absorption band area localize the highly altered zones crossed by the wells. These highly altered zones are linked to the main faults and are interpreted as the permeable zones of the well (Figures 6 and 8). The vertical extent of this scattering provides in-depth information on the extent of the well volume that is affected by hydrothermal circulations. This initial study applying the SWIR method to the Soultz and Rittershoffen geothermal sites will soon be reinforced by an ongoing study in which the SWIR method is applied to the new Illkirch geothermal site. This will help us confirm our interpretation and extend the interpretation to the URG.

Based only on geophysical logs (acoustic image logs were not acquired below 2850 m MD), the main permeable FZ of GRT-2 was identified from 2766-2800 m MD with a true thickness of 35 m by Vidal et al. [34]. Our SWIR method yields new complementary results that provide new information about the FZ architecture, and we observe that the FZ is more extended than was described by Vidal et al. [34] based on geophysical logs. SWIR helps distinguish the part of the actual FZ that controls the present-day circulations and the part of the FZ that has been affected by paleo-circulations. In fact, this study using SWIR data reveals that this zone presents an intense illitization extending from 2743 to 2884 m MD and thus a true thickness of 112 m. Previous mineralogical studies of the GRT-2 well suggested that a low intensity of illitization could explain the high permeability of the well [18]. However, the GRT-2 well presents high values of the 2200 nm absorption band area (20 a.u.); these are higher than the values measured in the GPK-1 well (13 a.u.) and also higher than those measured in other wells such as GRT-1 and GPK-4 [69]. These high SWIR 2200 nm absorption band area values are surprising considering the results of Vidal et al. [18]. The advantage of the SWIR method is that it provides a general and continuous overview of the well in terms of permeability indicators that prevents over-interpretation of punctual localized data.

5.2. SWIR Correlation. From simple observations, for both the GRT-2 and GPK-1 wells, the water absorption band area and the 2200 nm absorption band area appear to be correlated (Figures 5 and 7). In fact, the ratio between the water absorption band area and the 2200 nm absorption band area varies significantly according to the species of aluminous phyllosilicates considered (illite and micas) [21].

The correlation between these two absorption bands was tested for both wells (Figure 9). For the GRT-2 well, the correlation appears to be linear with a correlation coefficient of 0.62 (Figure 9(a)). For the GPK-1 well, the correlation presents two linear tendencies (Figure 9(a)). After classifying the samples into altered and unaltered granite on the basis of petrographic observations, it was found that these two tendencies correspond to hydrothermally altered granite with a coefficient of 0.53 and to unaltered granite with a coefficient of 0.26 (Figure 9(a)).

From mineralogical identifications (XRD and binocular magnifier observations), the unaltered granite in both wells is characterized by the presence of biotite and chlorite whereas the altered granite is essentially characterized by the presence of illite and illite-rich illite/smectite mixed layers in considerable amounts (Figures 9(b) and 9(c)).

Based on the phyllosilicate mineralogy of the unaltered and altered granite, it seems relevant to use the 2200 nm absorption band area as an indicator of the illitization rate of the granitic rocks of Northern Alsace. In the GPK-1 well, we can clearly see that for a similar value of the water absorption band area (e.g., a water absorption band area of 20 a.u.), we observe values of the 2200 nm absorption band area of the illitized granite more than two times higher than those observed for the unaltered granite (17 a.u. and 7 a.u., respectively). Considering the absorption band area at 2200 nm, the lower absorption depth noted for the samples of unaltered granite (Figure 9) can be explained by a weak to very weak contribution of both primary biotite and chlorite to the absorption band near 2200 nm (Figure 4(b)). The correlation between the water absorption band area and the 2200 nm absorption band area indicates that the mineralogy of the GRT-2 well is more homogeneous than that of the GPK-1 well (Figure 9).

From the SWIR results, the GRT-2 well showed a higher degree of hydrothermal alteration all along the well compared to the GPK-1 well. In this well, unaltered granite presents some localized sharp peaks of the 2200 nm absorption band area that correspond to the fracture-controlled altered zones. The interpretation of the two correlation tendencies of the GPK-1 well is consistent along with the petrographical observations: localized FZs are intersected on small apparent depth extents (Figures 7 and 9). These mineralogical and structural differences between the wells are explained by their different trajectories and concepts. Notably, the GPK-1 well was drilled nearly vertically and intersects few localized FZs at a higher angle, whereas the GRT-2 well is highly deviated but has an orientation parallel to the Rittershoffen local fault over its approximately 400 m apparent length. In fact, the GPK-1 well required stimulation, whereas the GRT-2 well did not, suggesting that intense illitization is a good indicator of permeability.

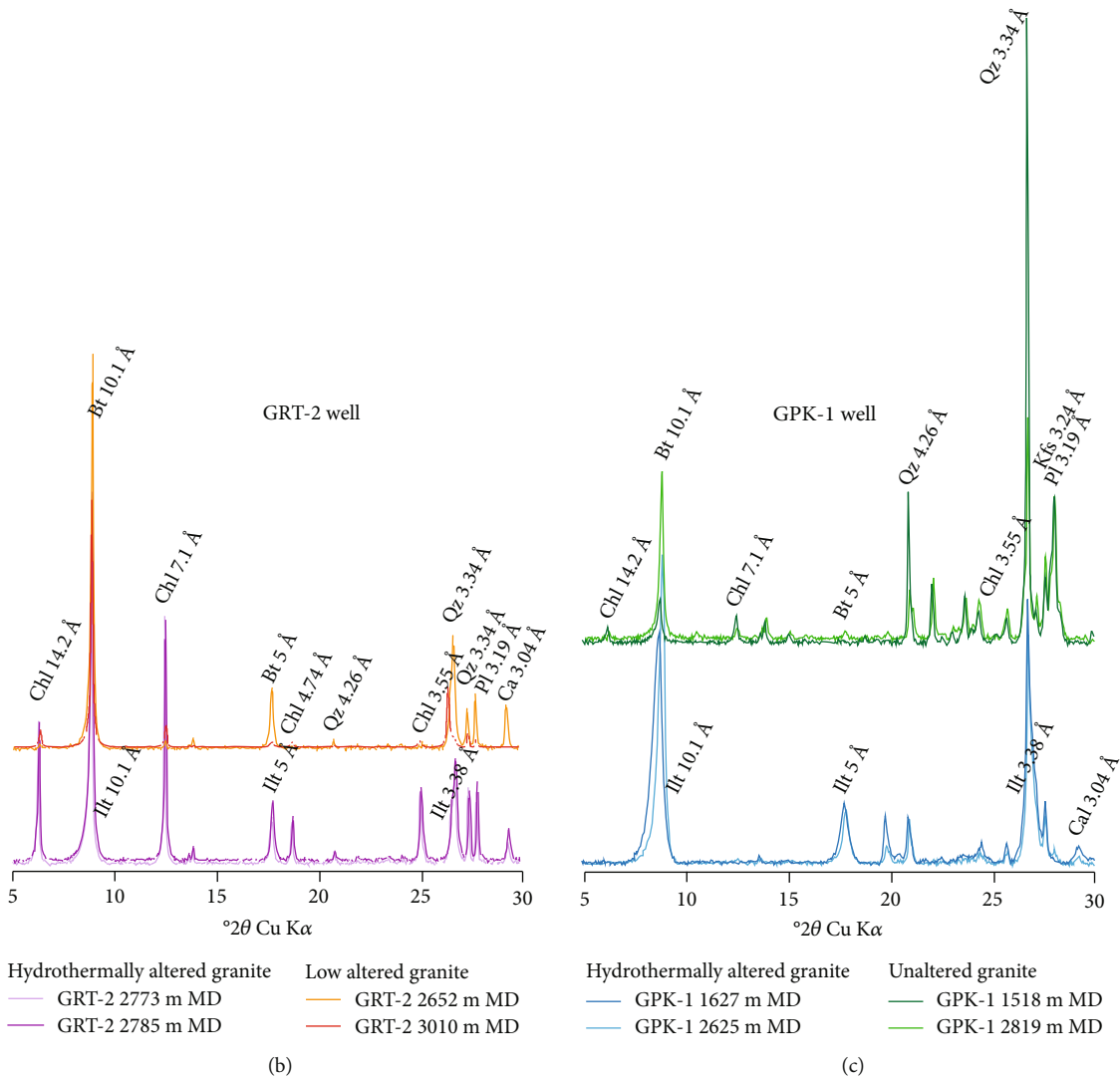
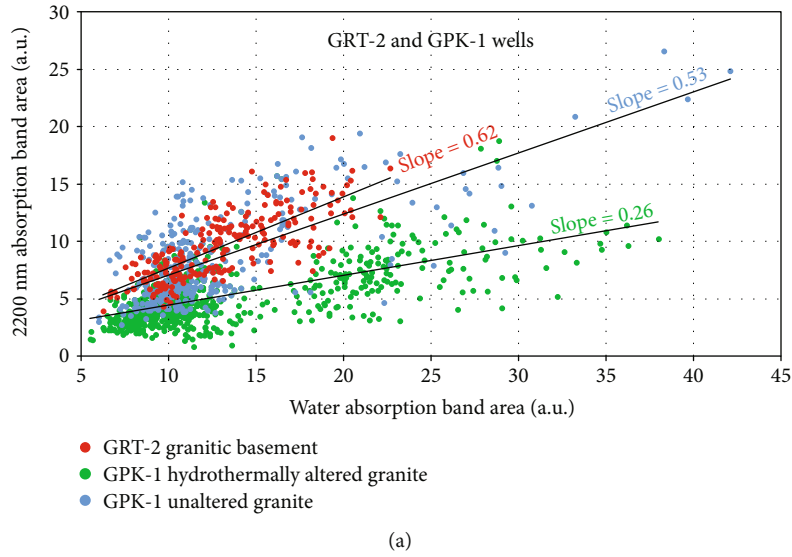


FIGURE 9: Correlation of the SWIR water and 2200 nm absorption band area for (a) the GRT-2 and GPK-1 wells, (b) XRD results for the slightly altered granite and the hydrothermally altered granite in the GRT-2 well, and (c) XRD results for the unaltered granite and the hydrothermally altered granite in the GPK-1 well.

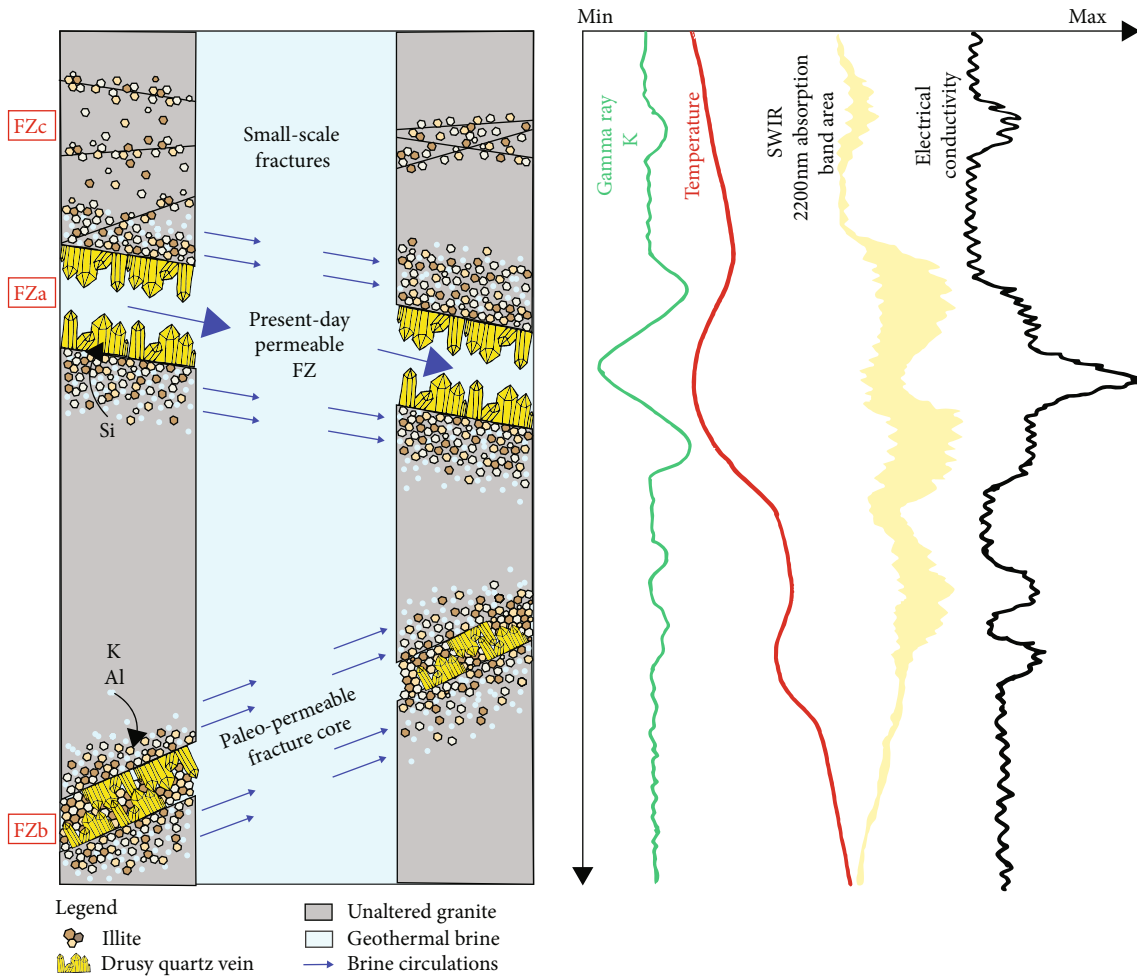


FIGURE 10: Model showing the variation in the 2200 nm absorption band area and its correlation with geophysical logs (gamma ray, temperature, and electrical conductivity) in response to different grades of hydrothermal alteration of the granite and different FZ architectures.

5.3. Electrical Logs and SWIR. The similar shapes and tendencies observed for the electrical logs and the SWIR data, outside of brine circulation in FZs, at first show a considerable control of illite on the electrical properties measured in the GRT-2 and GPK-1 wells (Figure 10). Very conductive zones are often associated with the SWIR 2200 nm absorption band area and with high GR-K peaks pointing to highly hydrothermally altered zones rich in illite. This type of zone could be observed either associated with a T anomaly, yielding an altered zone that is contributive (in FZ1 at 1620–1640 m MD in GPK-1) (Figure 8(a)), or with a straight T profile, yielding a sealed illitized zone (at 1550, 1579–1606, 1710, 1758, 1792, and 1860 m MD in GPK-1), which could be paleo-circulation zones (Figure 8). Resistive peaks can correlate with negative 2200 nm absorption band area peaks and the occurrence of a quartz vein, suggesting a fracture core plugged with secondary drusy quartz filling with insufficient residual porosity for abundant circulation and no abundant illite (low GR) (FZ1 at 1645 m MD in GPK-1) (Figure 8(a)). At a more restricted level, positive conductivity peaks can also correlate with negative GR-K peaks, low SWIR 2200 nm absorption band area, and T anomalies, translating

into the presence of brine such as in the cores of FZs (FZ2 at 1814 m in GPK-1, FZ1 at 2534 m MD, FZ3 at 2950 m MD, and FZ4 at 3050 m MD in GRT-2) (Figures 6 and 8).

5.4. FZ Signatures. In the GRT-2 well, FZs are always correlated with T anomalies and VEIN facies. This observation is probably related to the drusy euhedral quartz geometry, which keeps the space open and prevents plugging of the fracture. In contrast, the textural organization of illite in the FWs tends to plug the zone (Figure 10).

A specific signature of the resistivity laterolog is observed in both the GRT-2 and GPK-1 wells (FZ3 and FZ4 in GRT-2 and FZ2 in GPK-1), with very low resistivity values (20 ohm-m) corresponding to the occurrence of geothermal brine within the quartz vein as well as low resistivity values (20 ohm-m) corresponding to illite occurrence in the FW (Figures 6, 8, and 10).

We can distinguish three types of FZs (Figure 10):

- (i) FZa: permeable FZs with localized brine contributions, such as FZ1, FZ3, and FZ4 in GRT-2

(Figures 6(a), 6(c), and 6(d)) and FZ2 in GPK-1 (Figures 6(a), 6(c), 6(d), 8(b), and 10)

- (ii) FZb: permeable FZs with multiple brine contributions, such as FZ2 in GRT-2 and FZ1 in GPK-1 (Figures 6(b), 8(a), and 10)
- (iii) FZc: paleo-permeable FZs, such as those at 1550, 1579-1606, 1710, 1758, 1792, and 1860 m MD in GPK-1 (Figures 8 and 10)

Evans et al. [70] showed that in the open-hole section of GPK-1, the poststimulated flow zones systematically match the permeable and paleo-permeable FZs.

5.5. Applications. In future geothermal projects in the URG, the SWIR method could be a routine mud logging method. As a matter of fact, along with GR measurements obtained while drilling (MWD), cuttings provide the first data obtained during drilling. The use of SWIR measurements during drilling, when previously calibrated with the granitic analogue signature, could be helpful in determining the extent of the hydrothermally altered fault damage zone and in quantifying the alteration grade encountered in the granite. This could help determine when the exploration well leaves the altered zone and thus when to stop drilling. The SWIR method could be used as a routine mud logging analysis on-site during drilling after washing and drying the cuttings samples. It could also be further refined for the alteration mineralogy identification in geothermal systems [21].

In enhanced geothermal system projects, SWIR could be used to target paleo-permeable zones that could be reopened (sealed fractures and damage zones), thereby enhancing the permeability between the well and the reservoir during stimulation operations. In a similar manner, for existing geothermal wells in the URG drilled in granite, SWIR could be used as a complementary method to precisely characterize the hydrothermal alterations around the FZs and to target potential stimulation zones in cases of decreased productivity.

6. Conclusion

In this paper, the analysis of the correlation between the SWIR water and 2200 nm absorption bands areas confirms the petrography observed in both wells. By showing that the mineralogy is more homogeneous in the GRT-2 well than in the GPK-1 well, the results confirm that the two wells do not crosscut the circulation zones in the same way. Showing that the fluid-rock ratio is higher in the GRT-2 well than in the GPK-1 well, these results are consistent, according to hydrothermal concepts, with the higher productivity of the GRT-2 well compared to the GPK-1 well, which required stimulation. In this study, we observe three types of FZs: FZs with a localized contribution, FZs with multiple contributions, and paleo-permeable FZs. In conclusion, the SWIR method is a robust method for the detection of paleo- and present circulation zones for geothermal applications. By the joint interpretation of SWIR data and other geophysical logs,

this method could be used to determine whether the studied zone is a currently active circulation zone or a paleo-circulation zone. According to the values of the SWIR 2200 nm absorption band area, grades of alteration as well as the fluid-rock ratio trend can be determined. The similar variations in the SWIR 2200 nm absorption band area and the electrical logs demonstrate a significant influence of the rock clay mineral content (quantity of illitic minerals) on the electrical response. A specific electrical signature is observed in each well, indicating the FZ architecture and brine or illite contributions.

Data Availability

Data of the Rittershoffen wells belong to ECOGI. Please contact ES-Géothermie for data requests at geothermie@es.fr. Data of the Soultz wells can be requested at guichet.H@brgm.fr. SWIR data belong to ES-Géothermie and Poitiers University; for data request, please contact geothermie@es.fr.

Conflicts of Interest

The authors declare that they have no competing interests.

Authors' Contributions

CG acquired the SWIR data in GPK-1. JV acquired the SWIR data in GRT-2. CG, JV, PP, DB, SP, and AG worked on the interpretation of SWIR data and the correlation with other geophysical logs. CG and J-FG worked on the interpretation of the electrical logs. All authors approved the final manuscript.

Acknowledgments

This manuscript was prepared as a contribution to the PhD thesis (University of Strasbourg) of Carole Glaas which is cofunded by ES-Géothermie and ANRT (French Agency for Research and Technology). The authors warmly thank Benoît Hébert for allowing them to use his in-house Visual Basic software (TSS) and the Poitiers University team for the use of the TerraSpec on the Soultz site. They warmly thank Chrystel Dezayes from BRGM for the access to the Soultz cuttings samples. The authors acknowledge the EGS Alsace and DEEP-EM projects funded by ADEME (French Agency for Environment), GEIE EMC, and ECOGI for providing the Soultz and Rittershoffen cuttings samples and logs. Sophie Funfrock is thanked for improving the manuscript with English revision. Tom Schintgen is also thanked for the review of the manuscript.

Supplementary Materials

This supporting information provides details on the SWIR results acquired in the GRT-2 and GPK-1 wells. Figure S1 shows the intrasample variability in the GPK-1 well, presenting the results of multiple measurements of the same cuttings samples. Figure S2 shows the intrasample variability in the GRT-2 well, presenting the results of multiple measurements

of the same cuttings samples. Figure S3 presents a comparison between manual fitting of the data for the GPK-1 well and automatic fitting of the same data using the TSS software. (*Supplementary Materials*)

References

- [1] M. E. Schumacher, "Upper Rhine Graben: role of preexisting structures during rift evolution," *Tectonics*, vol. 21, no. 1, pp. 6-1-6-17, 2002.
- [2] T. Villemin and F. Bergerat, "L'évolution structurale du fossé rhénan au cours du Cénozoïque : un bilan de la déformation et des effets thermiques de l'extension," *Bulletin de la Société Géologique de France*, vol. 8, pp. 245-255, 1987.
- [3] P. Baillieux, E. Schill, J.-B. Edel, and G. Mauri, "Localization of temperature anomalies in the Upper Rhine Graben: insights from geophysics and neotectonic activity," *International Geology Review*, vol. 55, no. 14, pp. 1744-1762, 2013.
- [4] C. Dezayes and C. Lerouge, "Reconstructing paleofluid circulation at the Hercynian basement/Mesozoic sedimentary cover interface in the Upper Rhine Graben," *Geofluids*, vol. 2019, Article ID 4849860, 30 pages, 2019.
- [5] R. Schellschmidt and C. Clauser, "The thermal regime of the Upper Rhine Graben and the anomaly at Soultz," *Zeitschrift für Angewandte Geologie*, vol. 42, pp. 40-44, 1996.
- [6] C. Dezayes, A. Genter, and B. Valley, "Structure du réseau de fractures naturelles dans le réservoir géothermique peu perméable de Soultz," *Comptes Rendus Geoscience*, vol. 342, no. 7-8, pp. 517-530, 2010.
- [7] J. Sausse and A. Genter, "Types of permeable fractures in granite," *Geological Society, London, Special Publications*, vol. 240, no. 1, pp. 1-14, 2005.
- [8] V. F. Bense, T. Gleeson, S. E. Loveless, O. Bour, and J. Scibek, "Fault zone hydrogeology," *Earth-Science Reviews*, vol. 127, pp. 171-192, 2013.
- [9] S. S. Berg and E. Øian, "Hierarchical approach for simulating fluid flow in normal fault zones," *Petroleum Geoscience*, vol. 13, no. 1, pp. 25-35, 2007.
- [10] J.-H. Choi, P. Edwards, K. Ko, and Y.-S. Kim, "Definition and classification of fault damage zones: a review and a new methodological approach," *Earth-Science Reviews*, vol. 152, pp. 70-87, 2016.
- [11] D. R. Faulkner, C. A. L. Jackson, R. J. Lunn et al., "A review of recent developments concerning the structure, mechanics and fluid flow properties of fault zones," *Journal of Structural Geology*, vol. 32, no. 11, pp. 1557-1575, 2010.
- [12] C. E. Manning and S. E. Ingebritsen, "Permeability of the continental crust: implications of geothermal data and metamorphic systems," *Reviews of Geophysics*, vol. 37, no. 1, pp. 127-150, 1999.
- [13] J. Vidal and A. Genter, "Overview of naturally permeable fractured reservoirs in the central and southern Upper Rhine Graben: insights from geothermal wells," *Geothermics*, vol. 74, pp. 57-73, 2018.
- [14] A. Genter, H. Traineau, B. Ledésert, B. Bourguine, and S. Gentier, "Over 10 Years of Geological Investigations within the HDR Soultz Project, France," in *Presented at the World Geothermal Congress*, pp. 3707-3712, Kyushu, Japan, 2000.
- [15] G. R. Hooijkaas, A. Genter, and C. Dezayes, "Deep-seated geology of the granite intrusions at the Soultz EGS site based on data from 5 km-deep boreholes," *Geothermics*, vol. 35, no. 5-6, pp. 484-506, 2006.
- [16] B. Ledésert, G. Berger, A. Meunier, A. Genter, and A. Bouchet, "Diagenetic-type reactions related to hydrothermal alteration in the Soultz-sous-Forêts granite, France," *European Journal of Mineralogy*, vol. 11, no. 4, pp. 731-742, 1999.
- [17] C. Meller and T. Kohl, "The significance of hydrothermal alteration zones for the mechanical behavior of a geothermal reservoir," *Geothermal Energy*, vol. 2, no. 1, pp. 1-21, 2014.
- [18] J. Vidal, P. Patrier, A. Genter et al., "Clay minerals related to the circulation of geothermal fluids in boreholes at Rittershoffen (Alsace, France)," *Journal of Volcanology and Geothermal Research*, vol. 349, pp. 192-204, 2018.
- [19] B. Ledésert, R. Hebert, A. Genter, D. Bartier, N. Clauer, and C. Grall, "Fractures, alterations hydrothermales et perméabilité dans l'échangeur géothermique de Soultz," *Comptes Rendus Geoscience*, vol. 342, no. 7-8, pp. 607-615, 2010.
- [20] Y. Rotstein, J.-B. Edel, G. Gabriel, D. Boulanger, M. Schaming, and M. Munsch, "Insight into the structure of the Upper Rhine Graben and its basement from a new compilation of Bouguer gravity," *Tectonophysics*, vol. 425, no. 1-4, pp. 55-70, 2006.
- [21] M. P. Simpson and A. J. Rae, "Short-wave infrared (SWIR) reflectance spectrometric characterisation of clays from geothermal systems of the Taupō Volcanic Zone, New Zealand," *Geothermics*, vol. 73, pp. 74-90, 2018.
- [22] J. D. Garnish, *Hot dry rock - a European perspective*, GRC Hawaï, 1985.
- [23] A. Gérard and O. Kappelmeyer, "The Soultz-sous-Forêts project," *Geothermics*, vol. 16, no. 4, pp. 393-399, 1987.
- [24] A. Gérard, A. Menjoz, and P. Schwoerer, "L'anomalie thermique de Soultz-sous-Forêts," *Géothermie Actualités*, vol. 3, pp. 35-42, 1984.
- [25] O. Kappelmeyer, "European HDR project at Soultz-sous-Forêts general presentation," *Geothermal Science and Technology*, vol. 4, pp. 263-289, 1991.
- [26] R. Jung, "Connecting a borehole to a nearby fault by means of hydraulic fracturing," in *Geothermal Resources Council Transactions*, vol. 16, pp. 433-437, 1992.
- [27] E. Schill, A. Genter, N. Cuenot, and T. Kohl, "Hydraulic performance history at the Soultz EGS reservoirs from stimulation and long-term circulation tests," *Geothermics*, vol. 70, pp. 110-124, 2017.
- [28] A. Genter, K. Evans, N. Cuenot, D. Fritsch, and B. Sanjuan, "Contribution of the exploration of deep crystalline fractured reservoir of Soultz to the knowledge of enhanced geothermal systems (EGS)," *Comptes Rendus Geoscience*, vol. 342, no. 7-8, pp. 502-516, 2010.
- [29] T. GeOrg, "EU-Projekt GeORG - Geoportail [WWW Document]," 2017, <http://www.geopotenziale.org/home?lang=3>.
- [30] J. Vidal, R. Hehn, C. Glaas, and A. Genter, "How can temperature logs help identify permeable fractures and define a conceptual model of fluid circulation? An example from deep geothermal wells in the Upper Rhine Graben," *Geofluids*, vol. 2019, Article ID 3978364, 14 pages, 2019.
- [31] C. Baujard, A. Genter, E. Dalmais et al., "Hydrothermal characterization of wells GRT-1 and GRT-2 in Rittershoffen, France: implications on the understanding of natural flow systems in the Rhine Graben," *Geothermics*, vol. 65, pp. 255-268, 2017.
- [32] C. Baujard, A. Genter, N. Cuenot et al., "Experience from a Successful Soft Stimulation and Operational Feedback after 2

- Years of Geothermal Power and Heat Production in Rittershoffen and Soultz-sous-Forêts Plants (Alsace, France),” in *Presented at the Geothermal Resource Council*, pp. 2241–2252, Reno, Nevada, USA, 2018.
- [33] C. Glaas, A. Genter, J. F. Girard, P. Patrier, and J. Vidal, “How do the geological and geophysical signatures of permeable fractures in granitic basement evolve after long periods of natural circulation? Insights from the Rittershoffen geothermal wells (France),” *Geothermal Energy*, vol. 6, no. 1, pp. 1–25, 2018.
- [34] J. Vidal, A. Genter, and F. Chopin, “Permeable fracture zones in the hard rocks of the geothermal reservoir at Rittershoffen, France,” *Journal of Geophysical Research: Solid Earth*, vol. 122, no. 7, pp. 4864–4887, 2017.
- [35] A. Genter and H. Traineau, “Analysis of macroscopic fractures in granite in the HDR geothermal well EPS-1, Soultz-sous-Forêts, France,” *Journal of Volcanology and Geothermal Research*, vol. 72, no. 1–2, pp. 121–141, 1996.
- [36] A. Cocherie, C. Guerrot, C. M. Fanning, and A. Genter, “U-Pb dating of two granite types from Soultz (Rhine Graben, France),” *Comptes Rendus Geoscience*, vol. 336, no. 9, pp. 775–787, 2004.
- [37] H. Traineau, A. Genter, J.-P. Cautru, H. Fabriol, and P. Chèvremont, “Petrography of the granite massif from drill cutting analysis and well log interpretation in the geothermal HDR borehole GPK-1 (Soultz, Alsace, France),” in *Geothermal Energy in Europe: The Soultz Hot Dry Rock Project*, J. C. Bresee, Ed., pp. 1–29, Geothermal Science and Technology, Montreux, Switzerland, 1992.
- [38] J.-M. Stussi, A. Cheilletz, J.-J. Royer, P. Chèvremont, and G. Féraud, “The hidden monzogranite of Soultz-sous-Forêts (Rhine Graben, France),” *Mineralogy, petrology and genesis. Géologie de la France*, vol. 1, pp. 45–64, 2002.
- [39] C. Meller, A. Kontny, and T. Kohl, “Identification and characterization of hydrothermally altered zones in granite by combining synthetic clay content logs with magnetic mineralogical investigations of drilled rock cuttings,” *Geophysical Journal International*, vol. 199, no. 1, pp. 465–479, 2014.
- [40] C. Meller and B. Ledésert, “Is There a Link Between Mineralogy, Petrophysics, and the Hydraulic and Seismic Behaviors of the Soultz-sous-Forêts Granite During Stimulation? A Review and Reinterpretation of Petro-Hydromechanical Data Toward a Better Understanding of Induced Seismicity and Fluid Flow,” *Journal of Geophysical Research: Solid Earth*, vol. 122, no. 12, pp. 9755–9774, 2017.
- [41] J. Sausse, M. Fourar, and A. Genter, “Permeability and alteration within the Soultz granite inferred from geophysical and flow log analysis,” *Geothermics*, vol. 35, no. 5–6, pp. 544–560, 2006.
- [42] A. Genter, C. Castaing, C. Dezayes, H. Tenzer, H. Traineau, and T. Villemin, “Comparative analysis of direct (core) and indirect (borehole imaging tools) collection of fracture data in the hot dry rock Soultz reservoir (France),” *Journal of Geophysical Research: Solid Earth*, vol. 102, no. B7, pp. 15419–15431, 1997.
- [43] A. Genter, H. Traineau, and D. Artignan, *Synthesis of Geological and Geophysical Data at Soultz-sous-Forêts (France)*, BRGM, Orléans, France, 1997.
- [44] R. L. Hébert, B. Ledésert, D. Bartier, C. Dezayes, A. Genter, and C. Grall, “The Enhanced Geothermal System of Soultz-sous-Forêts: A study of the relationships between fracture zones and calcite content,” *Journal of Volcanology and Geothermal Research*, vol. 196, no. 1–2, pp. 126–133, 2010.
- [45] B. Ledésert, R. L. Hébert, C. Grall et al., “Calcmetry as a useful tool for a better knowledge of flow pathways in the Soultz-sous-Forêts Enhanced Geothermal System,” *Journal of Volcanology and Geothermal Research*, vol. 181, no. 1–2, pp. 106–114, 2009.
- [46] S. Nishimoto and H. Yoshida, “Hydrothermal alteration of deep fractured granite: effects of dissolution and precipitation,” *Lithos*, vol. 115, no. 1–4, pp. 153–162, 2010.
- [47] B. Jacquemont, “Etude des interactions eaux-roches dans le granite de Soultz-sous-Forêts. Quantification et modélisation des transferts de matière par les fluides,” (PhD). Université de Strasbourg, France, 2002.
- [48] G. L. Hunt and J. W. Salisbury, “Visible and near infrared spectra of minerals and rocks: I. Silicate minerals,” *Modern Geology*, vol. 1, pp. 283–300, 1970.
- [49] B. Hébert, *Approche quantitative par spectrométrie Vis-NIR des minéraux argileux et uranifères dans les sables du gisement de Tortkuduk, Kazakhstan*, Université de Poitiers, Poitiers, 2018.
- [50] B. H. Toby, “R factors in Rietveld analysis: how good is good enough?,” *Powder Diffraction*, vol. 21, no. 1, pp. 67–70, 2006.
- [51] J. Madejová, W. P. Gates, and S. Petit, “IR spectra of clay minerals,” in *Developments in Clay Science*, pp. 107–149, Elsevier, 2017.
- [52] S. Pontual, N. Merry, and P. Gamson, *G-Mex Vol.1, Spectral interpretation field manual*, Ausspec international Pty. Ltd., Kew, Victoria 3101, Australia, 1997.
- [53] A. Genter, H. Traineau, C. Dezayes et al., “Fracture analysis and reservoir characterization of the granitic basement in the HDR Soultz Project (France),” *Geothermal Science and Technology*, vol. 4, pp. 189–214, 1995.
- [54] J. H. Duckworth, “Spectroscopic quantitative analysis,” in *Applied Spectroscopy: A Compact Reference for Practitioners*, Academic Press, 1998.
- [55] G. W. Brindley and G. Brown, *Crystal Structures of Clay Minerals and Their X-Ray Identification*, Mineralogical Society of Great Britain and Ireland, 1980.
- [56] C. A. Barton, M. D. Zoback, and D. Moos, “Fluid flow along potentially active faults in crystalline rock,” *Geology*, vol. 23, no. 8, pp. 683–686, 1995.
- [57] J. Bradford, J. McLennan, J. Moore et al., “Recent Developments at the Raft River Geothermal Field,” in *Presented at the Thirty-Eighth Workshop on Geothermal Reservoir Engineering, Stanford University, California, USA, 2013*.
- [58] N. C. Davatzes and S. H. Hickman, “Controls on Fault-Hosted Fluid Flow; Preliminary Results from the Coso Geothermal Field, CA,” in *Presented at the Geothermal Resources Council Transactions, Geothermal Resources Council*, pp. 343–348, Davis, California, 2005.
- [59] L. Aquilina, M. Brach, J. C. Foucher, A. De Las Heras, and G. Braibant, *Deepening of GPK-1 HDR borehole 2000-3600m (Soultz-sous-Forêts, France), geochemical monitoring of drilling fluids (open file no. R36619)*, BRGM, Orléans, France, 1993.
- [60] F.-D. Vuataz, M. Brach, A. Criaud, and C. Fouillac, “Geochemical monitoring of drilling fluids: a powerful tool to forecast and detect formation waters,” *SPE Formation Evaluation*, vol. 5, no. 2, pp. 177–184, 1990.
- [61] C. Gallé, “Neutron porosity logging and core porosity measurements in the Beauvoir granite, Massif Central Range, France,” *Journal of Applied Geophysics*, vol. 32, no. 2–3, pp. 125–137, 1994.

- [62] L. Lévy, B. Gibert, F. Sigmundsson et al., “The role of smectites in the electrical conductivity of active hydrothermal systems: electrical properties of core samples from Krafla volcano, Iceland,” *Geophysical Journal International*, vol. 215, no. 3, pp. 1558–1582, 2018.
- [63] B. I. Anderson, *Modeling and inversion methods for the interpretation of resistivity logging tool response*, Technische Universiteit Delft, Netherlands, 2001.
- [64] O. Serra, *Fundamentals of Well-Log Interpretation*, Elsevier, Ed., ELF Aquitaine, Pau, France, 1984.
- [65] Schlumberger, “HRLA High-Resolution Laterolog Array | Schlumberger [WWW Document],” Schlumberger, 2018, March 2018, https://www.slb.com/services/characterization/petrophysics/wireline/legacy_services/high_res_array.aspx.
- [66] B. Sanjuan, R. Millot, C. Innocent, C. Dezayes, J. Scheiber, and M. Brach, “Major geochemical characteristics of geothermal brines from the Upper Rhine Graben granitic basement with constraints on temperature and circulation,” *Chemical Geology*, vol. 428, pp. 27–47, 2016.
- [67] R. Jung, “Hydraulic fracturing and hydraulic testing in the granitic section of borehole GPK-1, Soultz-sous-Forêts,” in *Geothermal Energy in Europe, The Soultz Hot Dry Rock Project*, vol. 3, pp. 149–198, Geothermal Science and Technology, 1992.
- [68] R. Schellschmidt and R. Schulz, “Hydrogeothermic studies in the Hot Dry Rock Project at Soultz-sous-Forêts,” in *Geothermal Energy in Europe: The Soultz Hot Dry Rock Project*, vol. 3, pp. 217–238, Geothermal Science and Technology, 1992.
- [69] C. Glaas, J. Vidal, P. Patrier, D. Beaufort, and A. Genter, “Contribution of SWIR to the Clay Signature of Permeable Fracture Zones in the Granitic Basement. Overview of Soultz and Rittershoffen wells,” in *Presented at the European Geothermal Congress*, p. 11, Den Haag, The Netherlands, 2019.
- [70] K. F. Evans, A. Genter, and J. Sausse, “Permeability creation and damage due to massive fluid injections into granite at 3.5 km at Soultz: 1. Borehole observations,” *Journal of Geophysical Research*, vol. 110, no. B4, 2005.
- [71] J. S. Caine, J. P. Evans, and C. B. Forster, “Fault zone architecture and permeability structure,” *Geology*, vol. 24, no. 11, pp. 1025–1028, 1996.
- [72] A. Richard, É. Gillot, V. Maurer, N. Cuenot, and J. Klee, “Upper Rhine Graben: The Largest Exploration by 3D Seismic Reflection,” in *Presented at the European Geothermal Congress*, Den Haag, Netherlands, 2019.

Research Article

Applying Rare Earth Elements, Uranium, and $^{87}\text{Sr}/^{86}\text{Sr}$ to Disentangle Structurally Forced Confluence of Regional Groundwater Resources: The Case of the Lower Yarmouk Gorge

Christian Siebert ¹, Peter Möller,² Fabien Magri ^{3,4}, Eyal Shalev ⁵, Eliahu Rosenthal ⁶,
Marwan Al-Raggad,⁷ and Tino Rödiger⁸

¹Dept. of Catchment Hydrology, Helmholtz Centre for Environmental Research (UFZ), Halle/Saale, Germany

²Helmholtz Centre Potsdam, German Research Centre for Geosciences (GFZ), Section 3.4, Potsdam, Germany

³Dept. of FA 2, Federal Office for the Safety of Nuclear Waste Management (BfE), Berlin, Germany

⁴Hydrogeology, Freie Universität, Berlin, Germany

⁵Geological Survey of Israel (GSI), Jerusalem, Israel

⁶The School of Earth Sciences, Tel Aviv University, Tel Aviv, Israel

⁷The Inter-Islamic Network on Water Resources Development and Management (NWRDAM), Amman, Jordan

⁸Dept. of Computational Hydrosystems, Helmholtz Centre for Environmental Research (UFZ), Leipzig, Germany

Correspondence should be addressed to Christian Siebert; christian.siebert@ufz.de

Received 24 May 2019; Revised 23 September 2019; Accepted 3 October 2019; Published 3 December 2019

Guest Editor: Tanguy Robert

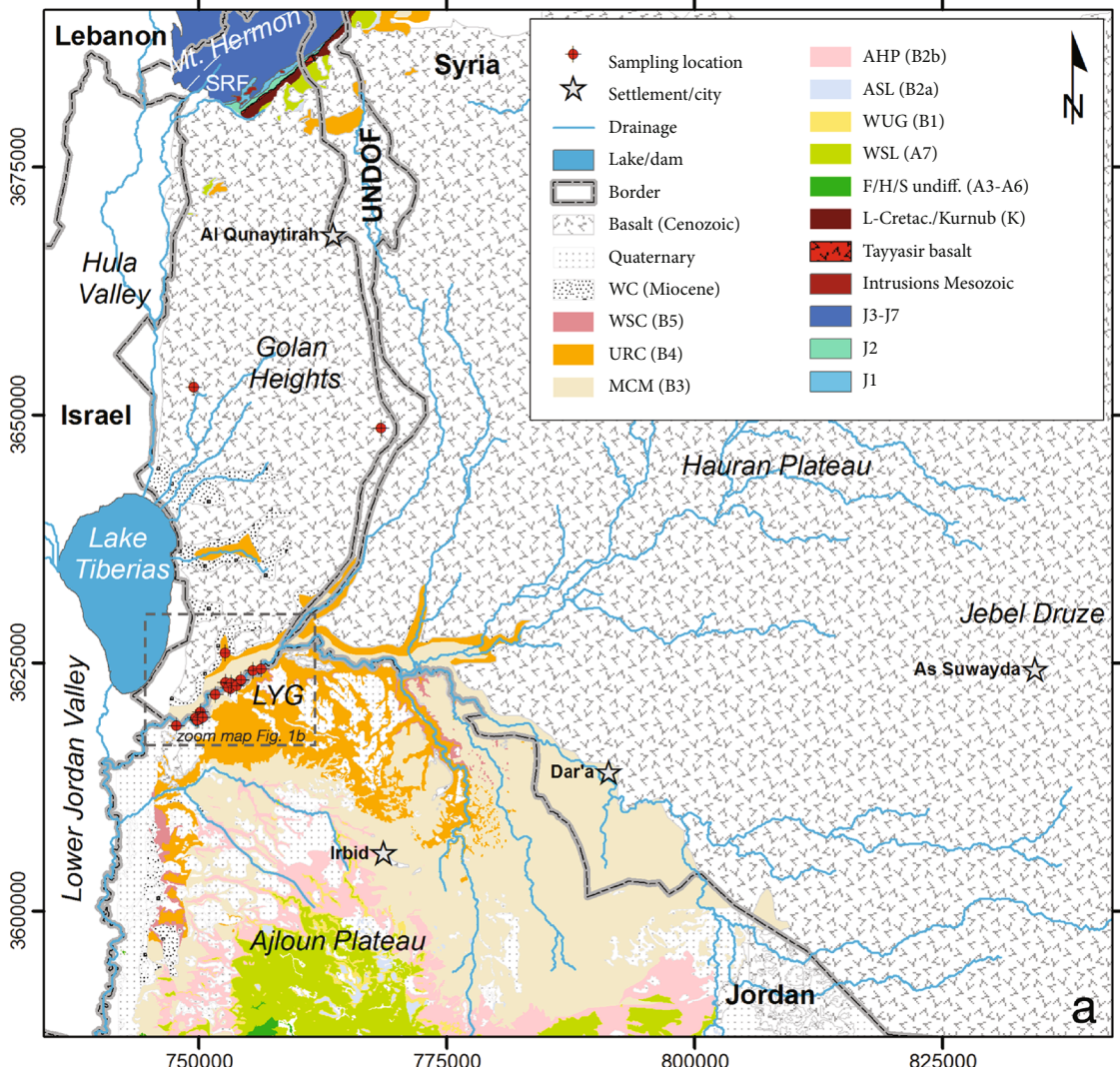
Copyright © 2019 Christian Siebert et al. This is an open access article distributed under the Creative Commons Attribution License, which permits unrestricted use, distribution, and reproduction in any medium, provided the original work is properly cited.

The conjoint discussion of tectonic features, correlations of element concentrations, $\delta^{18}\text{O}$, δD , and $^{87}\text{Sr}/^{86}\text{Sr}$ of groundwater leads to new insight into sources of groundwater, their flow patterns, and salinization in the Yarmouk Basin. The sources of groundwater are precipitation infiltrating into basaltic rock or limestone aquifers. Leaching of relic brines and dissolution of gypsum and calcite from the limestone host rocks generate enhanced salinity in groundwater in different degrees. High U(VI) suggests leaching of U from phosphorite-rich Upper Cretaceous B2 formation. Both very low U(VI) and specific rare earth element including yttrium (REY) distribution patterns indicate interaction with ferric oxyhydroxides formed during weathering of widespread alkali olivine basalts in the catchment area. REY patterns of groundwater generated in basaltic aquifers are modified by interaction with underlying limestones. Repeated sampling over 18 years revealed that the flow paths towards certain wells of groundwater varied as documented by changes in concentrations of dissolved species and REY patterns and U(VI) contents. In the Yarmouk Gorge, groundwater with basaltic REY patterns but high U(VI) and low Sr^{2+} and intermediate sulfate concentrations mainly ascends in artesian wells tapping a buried flower structure fault system crossing the trend of the gorge.

1. Introduction

Since Roman times, the hot springs of Hamat Gader (HG), Israel, and Ain Himma, Jordan, in the Lower Yarmouk Gorge (LYG) were used for health care (Figure 1). At present, only Ein Balsam at HG is publically in use. Hydrogeological and hydrochemical studies of springs and well waters in the gorge reveal that groundwater of widely different composition discharges at short distances [1]. By major and minor elements and distribution patterns of rare earth elements including

yttrium (henceforth termed REY), it was ascertained that thermal groundwater discharging through springs in the LYG is infiltrated in basaltic regions of the Hauran plateau, Syria [1]. Parts of these waters are mixed in various proportions with limestone water from Ajloun. The hot waters of Hamat Gader and Meizar get salinized by either mixing with relic seawater evaporation brines [2, 3] or leaching of evaporites. The recent study is based on 18 years of repeated sampling of wells and springs and reveals significant variations in REY patterns and element concentrations suggesting



Sampling location	X (UTM)	Y (UTM)	Short
<i>Groundwater wells</i>			
Mukheibeh 1	753119	3622154	M1
Mukheibeh 2	753241	3622342	M2
Mukheibeh 4	753212	3622331	M4
Mukheibeh 5	747753	3618570	M5
Mukheibeh 6	753018	3622417	M6
Mukheibeh 7	754257	3623142	M7
Mukheibeh 8	755495	3624134	M8
Mukheibeh 9	756312	3624296	M9
Mukheibeh 10	753267	3622856	M10
Mukheibeh 11	753845	3622588	M11
Mukheibeh 13	754268	3623212	M13
Meizer 1	752652	3625884	Me1
Meizer 2	752706	3622894	Me2
Meizer 3	752725	3622926	Me2
<i>Spring (Hamat Gader)</i>			
Ein Balsam	749705	3619324	EB
Ein Makla	749859	3619141	EM
Ein Reach	750014	3619198	ER
Ein Sahina	750190	3619926	ES
Ain Saraya	750429	3619424	EB
<i>Spring (Himma)</i>			
Ain Himma	751661	3621700	AH
<i>Spring (Golan Hieghts)</i>			
Umm Abu ad Danar	763884	3648639	AS
Amphy spring	748804	3653081	AM
<i>River</i>			
Yarmouk River	756255	3624301	YR

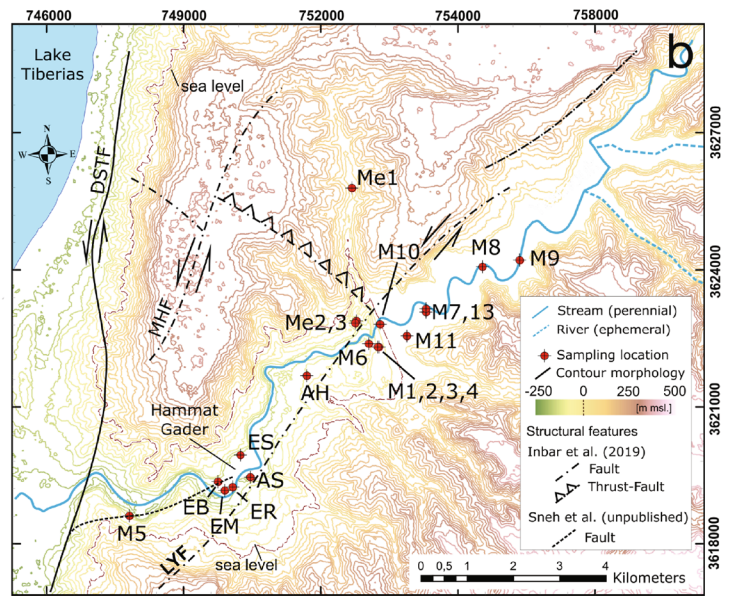


FIGURE 1: Overview of the study area, showing geological background (a) and sampling locations (b) including structural features recently introduced by Inbar et al. [15] and Sneh (unpublished).

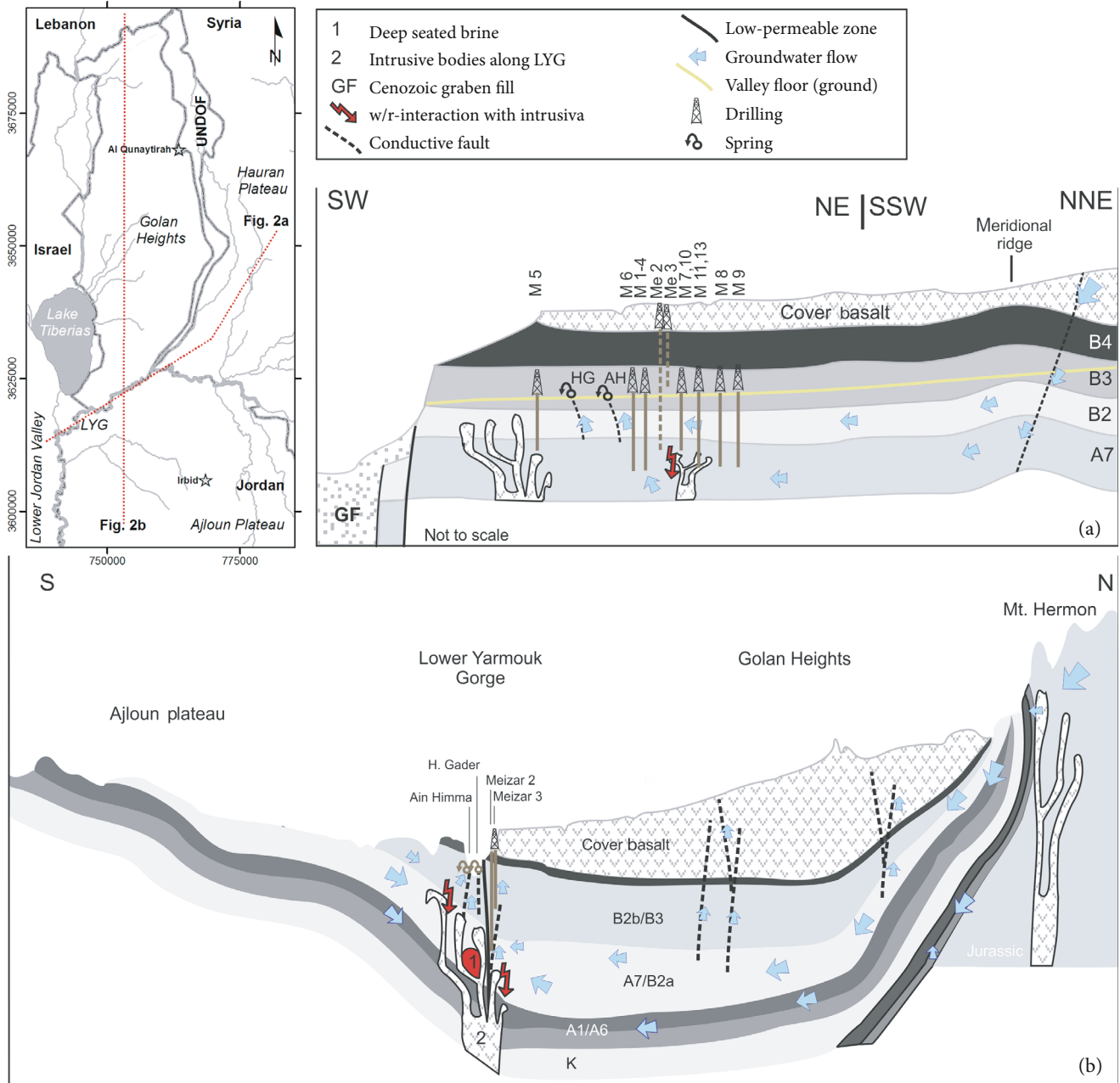


FIGURE 2: Schematic geological cross sections (not to scale). Section (a) starts in the Lower Jordan Valley, continues through the LYG, and branches into the Hauran NE-ward, while section (b) cuts from the Ajloun northward across the LYG and the Golan Heights into Mt. Hermon. The map shows the location of cross sections in red.

variation of flow paths and associated interactions with host rocks and leaching residual brines and evaporites.

The chemical and isotopic composition of the large amounts of fresh artesian groundwater produced in the Jordanian Mukheibeh well field contrasts with that of the saline groundwater in the Meizar wells and the springs of Hamat Gader. This gave rise to the conceptual model that the LYG is the surface expression of a fault zone, preventing transboundary flow [1]. 2D and 3D modelling supported that concept of continuous groundwater aquifers with the absence of transboundary groundwater exchange due to a zone of high hydraulic anisotropy underneath the gorge's centerline

[4–7]. The gorge seemingly acts as a complex conduit-barrier system, along which groundwater from the Golan in the north and Ajloun in the south converges and drains towards the Lower Jordan Valley (Figure 2). Flow paths in the underground of the gorge possibly occur along faults oriented perpendicular to the major axis of the gorge [5, 6, 8].

Based on stratigraphic data [9, 10], topographic data, deep seismic survey data [11, 12], shallow fault mapping [13], and thickness irregularities of the Turonian and Senonian sequences in the study area [14–17] support the occurrence of strike-slip flower structure faults along and across the gorge creating a series of structural fault blocks and

numerous buried faults at close proximity to the Dead Sea Transform Fault (DSTF) (Figure 1).

Applying REY distribution patterns, U(VI), $^{87}\text{Sr}/^{86}\text{Sr}$, and water isotopes in a new, complete, and synchronous set of sampled spring and well waters in 2016, we aim for joint discussion of hydrochemical and geological features to improve the knowledge of the sources of groundwater and of their flow paths.

After the introduction (Section 1), we will present the hydrogeological setting of the studied area (Section 2), the sample acquisition and the techniques used to analyze them (Section 3), the results on major and minor element, particularly on REY and U(VI), and Sr isotopes (Section 4), and a detailed discussion (Section 5). Section 6 concludes this study.

2. Hydrogeological Setting

Geographically, the Yarmouk drainage basin comprises (i) the volcanic Hauran plateau and the western flank of the Jebel Druze volcano [18], (ii) the southern and southeastern slopes of Hermon, (iii) the Golan Heights with numerous volcanic cones, (iv) the northern plunges of the Ajloun anticline, and (v) the Azraq-Dhuleil basin ENE of Ajloun (Figure 1(a)).

The Mediterranean climate in the Yarmouk basin causes rainy and cool winters and hot and dry summers. The distinct differences in altitude and the distance from the Mediterranean force strong gradients in annual precipitation. Highest values (up to 1300 mm/a) fall in the Hermon Massif and the highest parts of Jebel Druze; medium elevated regions such as the Hauran and Ajloun plateaus and the Golan Heights receive 600–800 mm/a, while the low-lying LYG and the xeric region SE of the surface drainage basin receive <500 mm/a only (e.g., [18–21]). The resulting recharge fractions are calculated to range from 0.06 to 0.1 [20, 22–24].

In the south of the Yarmouk River, geological formations dip NW-ward (Figure 2). Here, the oldest hydrogeological relevant formations comprise the highly karstified lime- and dolostones of the Upper Cretaceous A7 aquifer and the overlying heavily fractured silicified limestones of the Eocene B2 aquifer, altogether forming the 160 m thick regional A7/B2 aquifer system (Figure 3). This system becomes efficiently confined due to its descent and the appearance of the covering B3 aquiclude. On top of the southern flank of the LYG, remnants of the B4 sequence form a local limestone aquifer.

All formations older than B4 continue in the underground of the Golan Heights syncline before they partly resurface in the foothills of the Hermon anticline [25]. Underneath the Golan Heights, Jurassic limestones form the base of the formations before they become uplifted in the Hermon anticline in the north (Figures 1(a) and 2(b)). Since the drainage basin extends into three nations with different geological terminologies, Figure 3 compiles the relevant parts of the stratigraphic columns for the entire region.

Morphologically, the Golan Heights is restricted southward by the LYG, westward by the Hula Valley and Lake Tiberias, northward by Wadi Sa'ar at the foothills of Mt.

Hermon, and eastward by Wadi Raqqad. The entire Golan Heights is unconformably overlain by Plio-Pleistocene cover basalts, which continue E- and SE-ward into the Hauran plateau, Jebel Druze, and Azraq-Dhuleil Basin and form the uppermost supraregional aquifer in the area [26, 27]. Within the Golan Heights, the thickness of the basalts varies with more than 750 m in the central part and less than 50 m along the LYG (Figure 2(b)) and B3 layers form the impervious base of the basaltic aquifer [28–30]. However, the basaltic aquifer is connected to underlying aquifers at certain locations [31], either where B3 was already eroded or where structurally prominent features of post-Pliocene age cut the formations [12, 28, 32, 33]. An aeromagnetic survey in N Jordan revealed a SW-NE lineament branching from the DSTF towards Hamat Gader in the LYG [34], which was later proven to be a fault by geological mapping (Sneh et al., unpublished) (Figure 1(b)).

The groundwater in the phreatic and shallow basaltic aquifer mainly follows the morphology. Within the Golan Heights, it flows W- and SW-ward towards the Hula Valley, the Lake Tiberias, and the LYG [28, 33]. In the east, a subterranean meridional ridge forms a water divide against the Hauran [19] (Figure 2(a)). The thin lava flows east of the water divide, hosts only modest amounts of groundwater, and discharges locally into incised wadis, e.g., the Raqqad. The basaltic cover of the Hauran plateau is mainly recharged at the elevated southeastern flanks of the Hermon Massif and western piedmont of Jebel Druze, from where the groundwater flows SE- and W-ward, respectively. The groundwater most probably converges in the central part of the Hauran and flows from there SW-ward towards the LYG. There, the observed groundwater of this study discharges either naturally at the valley floor through springs in Hamat Gader, Suraya, and Himma or artificially through the (mostly) artesian wells of Mukheibeh and Meizar, located in the flanks of the gorge, either north (Meizar wells) or south (Mukheibeh wells) (Figure 1(b)).

3. Analytical Procedures

The elements Ca^{2+} , Mg^{2+} , U(VI), and REY are determined by ICP-MS (Elan DRC-e). K^{+} and Na^{+} were analyzed by ICP-AES (Spectro Arcos) using matrix-adjusted standard solution for calibration. Cl^{-} , Br^{-} , and SO_4^{2-} are determined with Dionex ICS (AS18 column). The alkalinity is titrated to pH 4.3 with H_2SO_4 and given as HCO_3^{-} .

To determine REY and U(VI), preconcentration is required. Therefore, about 4 l of sample is filtered in the field by using a peristaltic pump coupled to 0.2 μm filters (Sartorius, Germany). The samples are acidified by subboiled (index sbb) HCl, and 1 ml of Tm spike solution is added. At the same day, the samples are adjusted to pH = 2 using HCl_{sbb} and subsequently passed through preconditioned C_{18} Sep-Pak cartridges (Waters, USA), loaded with an ethylhexyl phosphate (Merck, Germany) liquid ion exchanger, at a rate of 1 l/h. Thereafter, each cartridge is washed with 50 ml of 0.01 M HCl_{sbb} and subsequently eluted with 40 ml of 6 M HCl_{sbb} at a rate of 3 ml/min. The eluates are evaporated to incipient dryness, and the residues are dissolved in 1 ml of

System	Age		Group			Formation			Hydrogeological properties		
	Period	GH/Mt.H	Ajloun	DB/H	GH/Mt.H	Ajloun	DB/H	Golan/Mt. Hermon	Ajloun	Damascus Basin/Hauran	
Quaternary	Quaternary				Yarmouk Basalt			Alkaline-olivine basalt	Alkaline-olivine basalt	Gravel, gypseous marl, siltite, clay	
					Cover basalt		n3				Sandstone, siltite
Neogene	Pliocene	Kefar Giladi		Jeribe Chilou	Bira/Gesher				Silicified limest., dolomite	Alternation congl., marl, limest.	
	Miocene				Hordos	Waaqas conglomerate (WC) - Jordan Valley	n2	Conglomerates in siltand clay matrice	Marl, sand	Limestone	
Paleogene	Oligocene	Avedat	Belqa	Kermev Bardeh	Lower basalt				Alkali olivine basalt	Conglomerates in limy matrix	
	Eocene				Susita/Fiq		n1		Marlist., sandy dolomite	Marl, clay, conglomerates	
Cretaceous	Upper Maastricht-Paleocene	Mt. Scopus		Soubine	Jaddala	Wadi Shallalah chalk (WSC) (B5)	e5		Chalk, bituminous	Thick banked limestone, upper part chalky, marly	
	Massstrichtian				Maresha/Adulam	Umm Rijam (URC) (B4)	e4	Marl, chalk, limestone	chalky limest., chert beds	Massive limestone	
Cretaceous	Campanian	Kurnub		Soubine	Taqiye	Murwaqqar chalk (MCM) (B3)	e1-e3	Marly limestone, bituminous, chert, phosphorite	Micritic limest., bituminous (oil shale)	Alternating chak, marl	
	Santonian				Ghareb	Al Hasa phosphorite (AHP) (B2-b)	m1, m2		Calcareous, phosphorite beds, limest., chalk, marl	Alternating chalk, marl, limest., cherts	
Cretaceous	Turonian	Judea		Judea	Mishash	Amman silicified limestone (ASL) (B2a)	s		Limestone, dolomite, chalky, phosphate, chert	Chalk, marl	
	Cenomanian-Turonian				Menuha	Wadi Umm Ghudran (WUG) (B1)			Massive chalk, limest., phosphatic sandst., chert		
Cretaceous	Albian	Kurnub		Judea	Bina	Wadi Es Sir Limest. (WSL) (A7)	t2	Limestone, dolomite, marly limest.	Dolomitic limest., sandst., cherts	Banked limestone	
	Aptian				F/H/S-undifferentiated		t1		Marl and gypsum		
Cretaceous	Barremian	Kurnub		Judea	Saknin	Hummar (H) (A4)		Dolomitic limestone	Dolomitic limestone, karstic limestone	Banked limestone, partly dolomite	
	Hauterivian-Berriasian				Deir Hanna	Fuheis (F) (A3)	c		Chalk beds, thin dolost.		Calcareous siltst., marly lime-/dolost., chalk beds
Jurassic	Malm	Arad	Zarqa		Na'ur (NL) (A1-2)			Dolomite, limestone	Limest., dolomite	Marly limestone	
	Dogger				Yagur		ab		Sandstone		
Jurassic	Lias				Yakhini			Basalts		Clayey sandstone, limestone intercalated	
					Banias, Tayassir basalt	Subeihi (K2)	a1-a3				
Jurassic					Aarda (K1)						
Jurassic	Malm	Arad	Zarqa		J6-J7 (Nahal Saar)		j5-j7	Limestone	Sandstone, siltstone, limestones	basalts	
	Dogger				J5 (Kidod)	Azab			Marl, shale		Marl
Jurassic	Lias				J4 (Hermon/Zohar)		j2-j4	Limestone		Dolomitic limestone at base, limestone on top	
					J1-J3		j1	Dolomite, limestone		Marl lignite, dolomite, sand- and limestone	

GH = Golan Heights, Mt.H = Mount Hermon, DB = Damascus Basin, H = Hauran; Syrian geology taken from Brew et al. [26] and Wolfart [27]

FIGURE 3: Stratigraphic table of the hydrogeological formation in the Yarmouk Basin.

5 M HNO₃ sbb (Merck, Germany) and transferred into 10 ml volumetric flasks. 1 ml of spike solution is added which is used, if necessary, for drift corrections of the response factors during the ICP-MS measurements.

Stable isotopes of oxygen and hydrogen are determined in separate filtered samples (0.2 μm) using laser cavity ring-down spectroscopy (Picarro L2120-i, USA) without further treatment of the water samples. The respective analytical precision is ±0.1‰ and ±0.8‰ for δ¹⁸O and δD, respectively. The results are reported relative to Vienna Standard Mean Ocean Water (VSMOW).

Analyses of ⁸⁷Sr/⁸⁶Sr in water samples were performed at TUBAF, Freiberg, Germany. Samples were prepared and analyzed after Tichomirova et al. [35] by applying TIMS (Finnigan MAT 262) with an acceptable relative error of ±0.005% for ⁸⁷Sr/⁸⁶Sr. Sr-isotope ratios are given in respect to NBS-987. To analyze Sr²⁺ in basaltic rock samples, rocks have been powdered to <150 μm, pressed to pellets, and analyzed applying energy-dispersive X-ray fluorescence (EDXRF) (Spectro XEPOS HE 2000). Chemical and isotopic analyses are given in Tables 1–3.

4. Results

Depending on the sampling location, the results are classified in the following way: Mukheibeh well field (M1-M13), Ain Himma (AH), Hamat Gader springs (HG), Meizar wells (Me1-Me3), and the Yarmouk River (YR). Sampling locations, which have been repeatedly sampled, are indicated by the year of sampling given in parentheses. The Hebrew and Arabic term of springs is transliterated as Ein and Ain, respectively.

4.1. Major and Minor Element Correlations with Cl⁻. From the low-salinity Mukheibeh clusters, two (Figures 4(a)–4(f)) or one (Figures 4(g)–4(j)) mixing lines evolve with high-salinity end members. They indicate that two end member brines occur in the study area: one is salinizing the Meizar wells and Ain Himma and the other the springs of Hamat Gader (Ein Maqla, Ein Reach, Ein Balsam, and Ain Sarayah). The Ca²⁺ concentration in Ain Himma switches between the two trends, probably because the access point to sample the spring water within the increasingly ruined Himma resort

TABLE 1: Compilation of groundwater analyses from the Lower Yarmouk Gorge and surrounding areas.

ID	Source	Abbr.	X	Y	Sampling Date	pH	Eh mV	Temp °C	EC μ S/cm	Alk mg/cm	Ca mg/l	Mg mg/l	K mg/l	Sr mg/l	Na mg/l	Cl mg/l	SO ₄ mg/l	Br mg/l	HCO ₃ mg/l	U nmol/l	$\delta^{18}\text{O}$ VSMOW	$\delta^2\text{H}$
Groundwater wells																						
01-128	Mukheibeh 1	M1 (01)	753119	3622154	#####	7	67	29.1	797	5.93	91.3	30	3.1	0.69	39	57.2	54.3	0.20	358	105.2	-5.65	-27.40
13/803	Mukheibeh 2	M2 (13)	753243	3622340	#####	7.12	65	28.14	809	5.18	96	30	3.02	0.54	38.7	58.4	57.2	0.09	312	88.2	-5.64	-26.40
16/08	Mukheibeh 2	M2 (16)	753241	3622342	#####	6.13	18	28.9	830	4.56	78	26	2.9	0.51	39	56.4	56.1	0.1	274	88.2	-5.38	-25.51
13/802	Mukheibeh 4	M4 (13)	753209	3622333	#####	7.1	63	28.8	807	5.18	96	29	3	0.51	38.5	55.4	54.7	0	312	96.6	-5.26	-25.40
16/09	Mukheibeh 4	M4 (16)	753212	3622331	#####	7.04	273	29.1	827	4.76	84	28	2.9	0.5	40	56.5	57.1	0.09	286	92.4	-5.50	-25.47
16/12	Mukheibeh 5	M5 (16)	747753	3618570	#####	7.32	162	40.9	876	5.08	71	24	3.8	0.94	47	57.2	36.3	0.11	305	4.6	-5.16	-24.54
16/10	Mukheibeh 6	M6 (16)	753018	3622417	#####	7.06	-40	31	667	5.08	86	29	3.4	0.66	49	73.3	59.8	0.26	306	58.8	-5.43	-26.28
16/14	Mukheibeh 7	M7 (16)	754257	3623142	#####	7.17	-17	38.5	774	4.8	84	29	2.9	0.54	40	60.5	35.5		288	63.0	-5.58	-27.04
13/804	Mukheibeh 8	M8 (13)	755490	3624127	#####	7.45	-123	44.9	701	4.72	68	20	5.25	1.4	53.3	64.5	27.8	0.12	283	0.0462	-6.28	-30.99
16/16	Mukheibeh 8	M8 (16)	755495	3624134	#####	7.16	-62	44.9	723	4.1	59	20	5.1	1.3	56	66.6	12.7	5.55	246		-6.09	-30.01
16/17	Mukheibeh 9	M9 (16)	756312	3624296	#####	7.2	-67	28.9	1157	7.6	54	29	16	5.3	120	82.6	21	0.19	459		-6.54	-32.16
16/11	Mukheibeh 10	M10 (16)	753267	3622856	#####	6.96	-117	39	710	4.34	72	25	3.7	0.96	47	59.9	39.5		261	5.0	-5.67	-27.37
16/13	Mukheibeh 11	M11 (16)	753845	3622588	#####	6.92	200	31.9	821	4.8	76	39	2.8	0.87	44	56.4	53.3	0.09	289		-5.34	-25.75
13/805	Mukheibeh 13	M13 (13)	754280	3623202	#####	7.38	-76	38.5	752	5.12	81	25	3.74	0.94	43.6	59.1	24.5	0.1	307	3.7	-5.69	-27.78
16/15	Mukheibeh 13	M13 (16)	754268	3623212	#####	7.12	-47	38.9	778	4.4	72	25	3.7	0.88	46	61.7	34		264	8.0	-5.65	-27.04
16/07	Meizar 1	Me1	752652	3625884	#####	7.38	-79	35.2	1630	3.64	52	17	13	2.1	230	386	12.7	2.39	217		-5.98	-29.13
01-166	Meizar 2	Me2 (01)	752700	3622914	#####	6.63	-102	60	1650	4.06	142	34.8	21.8	5.16	178	317	27.8	3.90	244	0.059	-5.90	-29.40
08/753	Meizar 2	Me2 (08)	752715	3622884	#####	6.75	-106	57.1	2060	3.76	178	42.1	24.6	5.8	201	373	32.8	4.44	225	0.063	-6.87	-36.61
16/02	Meizar 2	Me2 (16)	752706	3622894	#####	6.4	-77	60.6	2080	3.68	170	37	24	5.5	210	392	33.8	3.6	221		-6.89	-35.25
01-167	Meizar 3	Me3 (01)	752707	3622923	#####	7.09	-129	41.8	664	5.24	65.3	20.9	4.7	1.25	48.5	61.6	4	0.20	315	0.045	-6.84	-33.00
08/752	Meizar 3	Me3 (08)	752721	3622900	#####	6.6	-117	57.4	2090	3.72	177	42.2	24.2	5.8	200	365	30.6	3.97	223	0.078	-6.87	-36.61
16/01	Meizar 3	Me3 (16)	752725	3622926	#####	6.81	-120	42.2	810	5.48	71	25	3.9	1.1	53	78.7	19.3	0.35	330		-5.85	-28.29
Springs (Hamat Gader fresh)																						
16/03	Ein Sahina	ES	750190	3619926	#####	7.04	454	28	844	5	87	28	3.3	0.56	44	66.5	48.9	0.2	301	19.3	-5.57	-26.13
Springs (Hamat Gader thermohaline, incl. Ain Saraya)																						
16/04	Ein Balsam	EB	749705	3619324	#####	6.76	11	41.9	1600	4.8	120	34	12	3.5	130	325	13.3	2.92	289	4.6	-5.84	-28.53
00-107	Ein Reach	ER (00)	750349	3619399	#####	6.85	-96	38	1728	6	142	39.5	12.2	2.94	143	309	11.5	3.82	362	9.1	-5.84	-29.90
04-585	Ein Reach	ER (04)	749985	3618816	#####	6.81	-147	41.5	1759	5.86	134	39.5	12.6	3.44	156	345	11.9	4.25	353	7.9	-5.99	-29.90
16/05	Ein Reach	ER (16)	750014	3619198	#####	6.69	-76	43.4	1860	4.84	130	37	14	4.2	160	376	12.8	3.37	291	7.6	-5.93	-28.59
00-108	Ein Makla	EM (00)	749909	3619091	#####	6.64	-131	47.3	2190	5.64	178	44.2	18	5.21	212	488	15.8	6.55	340	5.8	-6.00	-31.60
04-586	Ein Makla	EM (04)	749811	3618793	#####	6.73	-167	49.6	2160	5.42	152	42	17.2	5.19	209	465	15.1	5.98	327	5.7	-6.15	-31.30
16/06	Ein Makla	EM (16)	749859	3619141	#####	6.59	-116	49.5	2160	3.64	150	39	17	5.5	210	475	15.0	4.51	218	5.9	-6.08	-29.59
16/20	Ain Saraya	AS	750429	3619424	#####	6.83	-16	38.3	1655	4.54	130	38	12	3.8	160	342	12.0	3.02	273	8.0	-5.85	-28.56

TABLE 1: Continued.

ID	Source	Abbr.	X	Y	Sampling Date	pH	Eh mV	Temp °C	EC µS/cm	Alk mg/l	Ca mg/l	Mg mg/l	K mg/l	Sr mg/l	Na mg/l	Cl mg/l	SO ₄ mg/l	Br mg/l	HCO ₃ mg/l	U nmol/l	δ ¹⁸ O VSMOW	δ ² H
Springs (Himma thermohaline)																						
01-12	Ein Himma	AH (01)	751665	3621722	#####	7.06	-145	41.5	1418	5.59	108	34.9	13.9	2.88	124	208	148	2.25	337	4.1	-6.08	-32.00
07/624	Ein Himma	AH (07)	751665	3621722	#####	7.02	-28	40	1433		113	34	13.8	3.7	122	244	212	2.9	330	2.3	-6.16	-31.13
11/140	Ein Himma	AH (11)	751568	3621767	#####	7.11	492	27.5	1071	5.56	105	34.5	8.7		82.3	143	124	0.97	335	9.3	-5.29	-23.86
13/807	Ein Himma	AH (13)	751600	3621710	#####	7.1	72	37.7	1130	4.84	118	32	8.89	1.9	84.4	150	125	1.06	291	8.4	-6.16	-31.13
16/19	Ein Himma	AH (16)	751661	3621700	#####	7.03	85	40	499	4.06	110	30	9.5	2	94	161	129	1.32	244	6.7	-6.13	-28.98
Springs (Golan Heights, cover basalt, fresh)																						
18/920	Umm Abu ad Dananir		763884	3648639	#####	6.68	468	17.8	349		22.4	13.7	5.69	0.25	23.8	25.7	11.8		128	0.06	-6.11	-27.3
18/921	Ayit fall		757703	3649486	#####	7.61	433	18	1010		85	43	4.47	0.83	64.5	108	24.9		408	0.02	-4.94	-21.6
18/922	Amphy spring		748804	3653081	#####	7.69	460	18.6	363		26.1	15.4	4.31	0.21	25.5	17.3	5.7		168	0.05	-6.97	-30.0
Springs (Mt. Hermon, limestone, fresh)																						
08/786	Ein Dan		751017	3682076	#####	7.39	445	15.9	472	3.44	65.9	5.44	0.65	0.09	4.34	9.77	8.99		211	1.01	-7.36	-38.34
08/787	Ein Banyas		746939	3682079	#####	7.49	497	18.4	358	3.52	72.3	12.4	1.46	0.30	9.87	12.9	57.3		206	1.00	-7.29	-37.59
	Average										69.1	8.92	1.06		7.11	11.3	33.1					
River																						
16/18	Yarmouk River	YR	756255	3624301	#####	8.4	191	23.5	961	3.18	55	30	5.7	0.57	97	110	147	0.2	184	5.9	-4.32	-21.34

TABLE 2: REY composition of the discussed groundwater from the Lower Yarmouk Gorge.

ID	Location	Short	La pmol/l	Ce pmol/l	Pr pmol/l	Nd pmol/l	Pm	Sm pmol/l	Eu pmol/l	Gd pmol/l	Tb pmol/l	Dy pmol/l	Y pmol/l	Ho pmol/l	Er pmol/l	Tm pmol/l	Yb pmol/l	Lu pmol/l
01-128	Mukheibeh 1	2001	M1 (01)	2.35	4.31	0.58	2.33	0.48	0.17	0.54	0.09	0.70	17.71	0.17	0.72		1.01	0.20
13/803	Mukheibeh 2	2013	M2 (13)	1.40	2.11	0.28	1.14	0.22	0.08	0.35	0.06	0.54	14.84	0.14	0.58		0.86	0.17
16-08	Mukheibeh 2	2016	M2 (16)	2.21	3.75	0.43	1.98	0.74	0.08	0.42	0.06	0.65	18.59	0.17	0.67		0.89	0.17
13/802	Mukheibeh 4	2013	M4 (13)	1.51	2.47	0.31	1.42	0.26	0.08	0.29	0.06	0.44	11.57	0.11	0.48		0.72	0.13
16-09	Mukheibeh 4	2016	M4 (16)	22.21	41.72	5.15	21.76	4.34	1.02	3.99	0.54	3.43	52.06	0.70	2.10		1.89	0.31
16-12	Mukheibeh 5	2016	M5 (16)	1.18	1.84	0.18	0.81	0.23	0.09	0.09		0.11	2.90				0.16	
16-10	Mukheibeh 6	2016	M6 (16)	1.54	2.57	0.23	1.03	0.28		0.21	0.05	0.42	14.17	0.12	0.49		0.77	0.15
16-14	Mukheibeh 7	2016	M7 (16)	4.62	9.02	0.90	3.47	0.63	0.17	0.69	0.10	0.79	17.05	0.18	0.66		0.79	0.13
13/804	Mukheibeh 8	2013	M8 (13)	5.14	8.87	1.10	4.53	0.89	0.23	0.91	0.15	0.90	12.69	0.19	0.56		0.46	0.08
16-16	Mukheibeh 8	2016	M8 (16)	4.66	6.57	0.79	3.02	0.49	0.12	0.53	0.06	0.54	9.73	0.11	0.36		0.34	0.05
16-17	Mukheibeh 9	2016	M9 (16)	14.58	29.29	2.84	8.76	0.51	0.11	0.92	0.07	0.47	8.02	0.09	0.32		0.49	0.12
16-11	Mukheibeh 10	2016	M10 (16)	3.63	7.27	0.79	3.40	0.81	0.18	0.71	0.09	0.62	8.73	0.12	0.38		0.42	0.08
16-13	Mukheibeh 11	2016	M11 (16)	4.22	7.74	0.84	3.60	0.82	0.21	0.89	0.14	1.22	27.90	0.29	0.96		0.99	0.16
13/805	Mukheibeh 13	2013	M13 (13)	7.48	11.31	1.19	4.65	0.77	0.23	0.86	0.10	0.75	11.11	0.16	0.50		0.54	0.09
16-15	Mukheibeh 13	2016	M13 (16)	2.97	6.20	0.62	2.67	0.62	0.16	0.59	0.09	0.69	12.51	0.16	0.49		0.50	0.08
16-07	Meizar 1		Me1	1.40	2.21	0.18	0.96	0.42	0.28	0.53		0.18	3.23				0.14	
01-166	Meizar 2	2001	Me2 (01)	4.38	10.32	1.33	4.80	1.03	0.23	1.05	0.14	0.88	15.75	0.17	0.49		0.40	0.06
08/753	Meizar 2	2008	Me2 (08)	7.17	18.48	3.23	15.86	5.48	1.40	6.32	0.84	4.18	34.51	0.75	1.91		1.21	0.15
16-02	Meizar 2	2016	Me2 (16)	6.14	10.28	1.14	4.51	0.85	0.22	1.09	0.16	1.15	24.60	0.25	0.72		0.51	0.07
01-167	Meizar 3	2001	Me3 (01)	9.98	18.14	2.48	10.12	2.24	0.56	2.25	0.31	1.81	23.87	0.35	1.02		0.86	0.14
08/752	Meizar 3	2008	Me3 (08)	30.39	86.80	17.80	96.20	31.56	7.83	36.36	4.79	23.55	140.96	3.97	8.98		5.48	0.77
16-01	Meizar 3	2016	Me3 (16)	1.33	2.39	0.25	1.03	0.20		0.20	0.04	0.22	4.63	0.05	0.17		0.25	0.05
16-03	Ein Sahina		ES	1.84	3.24	0.32	1.43	0.28		0.33		0.35	9.18	0.09	0.30		0.30	0.04
16-04	Ein Balsam	2016	EB	4.68	9.13	0.98	4.20	0.75	0.20	0.80	0.10	0.76	17.16	0.16	0.53		0.61	0.10
00-108	Ein Makla	2000	ER (00)	12.49	25.59	1.87	11.20	1.81	0.49	2.16	0.33	2.26	50.15	0.55	1.91		2.03	0.35
04-586	Ein Makla	2004	ER (04)	10.31	14.67	1.81	7.43	1.28	0.38	1.83	0.31	1.99	47.02	0.48	1.84		1.92	0.33
16-06	Ein Makla	2016	ER (16)	8.81	11.05	1.44	6.23	1.26	0.38	1.70	0.27	2.23	50.26	0.52	1.84		2.03	0.36
00-107	Ein Reach	2000	EM (00)		19.71	1.46	9.53	1.35	0.38	1.50	0.24	1.50	27.60	0.31	1.17		1.25	0.22
04-585	Ein Reach	2004	EM (04)	4.75	7.70	0.98	3.61	0.62	0.21	0.84	0.15	1.04	19.69	0.22	0.73		0.92	0.17
16-05	Ein Reach	2016	EM (16)	14.61	25.69	2.88	12.01	2.16	0.60	2.41	0.33	2.40	43.53	0.53	1.75		1.72	0.30
16-20	Ain Saraya		AS	12.27	18.80	2.33	7.34	0.49	0.11	0.84	0.08	0.64	15.98	0.16	0.62		0.85	0.17
01-12	Ain Himma	2001	AH (01)	4.31	23.39	3.48	13.06	2.98	0.78	3.38	0.52	3.33	51.76	0.73	2.21		2.02	0.34
07/624	Ain Himma	2007	AH (07)	16.34	65.43	3.42	14.15	3.38	0.92	4.19	0.68	4.29	62.85	0.93	2.79		2.57	0.42
13/807	Ain Himma	2013	AH (13)	4.06	7.58	0.74	2.91	0.53	0.13	0.53	0.09	0.61	13.83	0.16	0.52		0.66	0.11
16-19	Ain Himma	2016	AH (16)	43.50	61.06	8.54	25.95	0.76	0.19	2.11	0.12	0.92	19.85	0.21	0.80		1.05	0.23

TABLE 2: Continued.

ID	Location	Short	La pmol/l	Ce pmol/l	Pr pmol/l	Nd pmol/l	Pm	Sm pmol/l	Eu pmol/l	Gd pmol/l	Tb pmol/l	Dy pmol/l	Y pmol/l	Ho pmol/l	Er pmol/l	Tm pmol/l	Yb pmol/l	Lu pmol/l
08/787	Ein Banyas	EBY	45.10	5.39	9.80	45.24		8.29	2.26	10.58	1.52	11.14	249.79	2.71	8.08		6.35	0.96
08/786	Ein Dan	ED	50.63	23.07	12.00	54.53		10.48	2.86	12.74	1.82	12.55	240.58	2.91	8.78		7.57	1.22
16-18	Yarmouk	YR	38.37	82.25	8.18	34.96		5.88	1.53	6.64	0.83	5.92	153.95	1.43	4.93		5.54	1.07

TABLE 3: Sr²⁺ concentration and ⁸⁷Sr/⁸⁶Sr isotope signatures of groundwater and rocks from the Lower Yarmouk Gorge and surrounding areas.

ID	Well/spring	Sr (mg/l)	⁸⁷ Sr/ ⁸⁶ Sr
16/08	Mukheibeh 2	0.51	0.70769
16/09	Mukheibeh 4	0.5	0.70764
16/12	Mukheibeh 5	0.94	0.70770
16/10	Mukheibeh 6	0.66	0.70767
16/14	Mukheibeh 7	0.54	0.70757
16/16	Mukheibeh 8	1.3	0.70748
16/17	Mukheibeh 9	5.3	0.70778
16/11	Mukheibeh 10	0.96	0.70757
16/13	Mukheibeh 11	0.87	0.70767
16/15	Mukheibeh 13	0.88	0.70757
16/07	Meizar 1	2.1	0.70754
16/02	Meizar 2	5.5	0.70760
16/01	Meizar 3	1.1	0.70755
16/03	Ein Sahina	0.56	0.70763
16/04	Ein Balsam	3.5	0.70765
16/06	Ein Makla	5.5	0.70767
16/05	Ein Reach	4.2	0.70776
16/20	Ain Saraya	3.8	0.70771
16/19	Ain Himma	2	0.70759
18/920	Umm Abu ad Dananir	0.252	0.70458
18/922	Amphy spring	0.21	0.70457
16/18	Yarmouk	0.57	0.70708
ID	Rock sample	Sr (mg/kg)	⁸⁷ Sr/ ⁸⁶ Sr
18/A	Golan Heights 1	1934	0.70330
18/B	Golan Heights 2	1040	0.70350

varied over the years. Hamat Gader brines are lower in SO₄²⁻ but higher in Cl⁻ and Br⁻ than Meizar brines. Waters from wells such as Meizar 1 and Mukheibeh 8, 9, and 11 sometimes deviate from the indicated trend lines. The Yarmouk River water is mostly comparable to Mukheibeh water, but not in diagrams with Na⁺, Cl⁻ and SO₄²⁻.

4.2. *Uranium*. U(VI) is correlated neither with any other element mentioned before nor with Eh varying between -200 and +200 mV (Table 1). The Mukheibeh field splits into three subgroups (Figure 5). U(VI) with 80-105 nmol/l has the highest values in Mukheibeh groundwater. Groundwater from wells Mukheibeh 5 and 11, Ain Himma, Hamat Gader shows values between 3 and 10 nmol/l. The groundwater with <0.1 nmol/l and that with U(VI) below the detection limit comprise all well waters from Meizar 2 and 3 and Mukheibeh 1, 8, and 9. The lowest U(VI) values are either in the lowest or in the highest sulfate groundwater (Figure 5(b)).

4.3. *Rare Earths and Yttrium*. Weathering of omnipresent alkali olivine basalts in the Yarmouk basin releases Fe(II) which precipitates as colloidal ferric oxyhydroxides (HFO)

under oxidizing conditions. These colloids later aggregate to gels on all solid surfaces along the pathways within and below the basaltic layer. In aqueous systems, however, HREE and Y are slightly fractionated. The REY patterns of samples in this study are subdivided into 6 types. The first group (t1) typifies groundwater derived from weathered alkali olivine basalts. The patterns t2 and t3 show the results of increasing mixing with limestone water (t4) (Figures 6(a)–6(d)). In Figure 6(e), three REY patterns of type t2* are compiled which show very high LREE contents but low HREE and Y. Otherwise, they resemble type t2. Another different feature of t2* is that positive Gd anomalies exceed those of Y.

All of the above patterns show positive Y anomalies. The dissolution of REY-enriched HFO yields convex patterns of type t5 with enhanced abundances of medium REE compared to light and heavy REE and negative Y anomalies (Figure 6(f)). These Y anomalies develop because Y prefers to stay in the aqueous phase during the stage of REY adsorption by HFO [36].

The water from Ain Himma in 2001 and 2007 and well Mukheibeh 4(16) shows REY patterns, typical of water from limestone aquifers such as those of Ein Dan and Ein Banyas in the Mt. Hermon Massif but without the negative Ce anomalies typical of spring waters from karstic limestones (Figure 6(g)) or from Cretaceous limestones along the rift valley [37]. Note that the REY abundance in waters from Mukheibeh 4(16) and Ain Himma from years 2000 and 2007 is lower than that in the spring waters of Dan and Banyas, which may be a result of interaction with HFO.

4.4. *⁸⁷Sr/⁸⁶Sr*. Although the waters show a wide spread in Sr²⁺, their ⁸⁷Sr/⁸⁶Sr isotope ratios vary only between 0.7070 and 0.7077 (Figure 7). This corresponds with the range of ⁸⁷Sr/⁸⁶Sr in Cretaceous limestones of Israel, which is about 0.7070-0.7086 (Wilske et al., unpublished data). Only the Yarmouk River with 0.70710 points to mixing with basaltic rock drainage water which shows an ⁸⁷Sr/⁸⁶Sr value of 0.70455, slightly above Phanerozoic upper mantle alkali olivine basalts from Israel with ⁸⁷Sr/⁸⁶Sr of 0.7033-0.7035 (Table 3).

In the plot of Sr²⁺ vs. ⁸⁷Sr/⁸⁶Sr, Mukheibeh field groundwater clusters at low Sr²⁺, whereas the samples from Hamat Gader, Meizar 2, and Himma show a wide spread. Mukheibeh 8 water fits into the Hamat Gader-Meizar 2-Himma trend, whereas Meizar 3 approaches the Mukheibeh field.

4.5. *δ¹⁸O vs. δD*. The stable water isotopes in the LYG range from low values of Meizar 2 in the southern Golan Heights and springs and wells on the eastern plunge of the Mt. Hermon Massif towards the Hauran plateau to high values in water of the Yarmouk River (Figure 8). All data from the LYG are plotted between the Syrian and Mt. Hermon meteoric water lines (MWL). The Mukheibeh waters like the groundwater from the Hauran plateau nearly cover the whole array, whereas the samples of Meizar, Hamat Gader, and Himma cluster. Ein Sahina, located uphill of the Hamat Gader group, is plotted among the Mukheibeh field. Ain Sarayah, located close to Ein Reach of the Hamat Gader

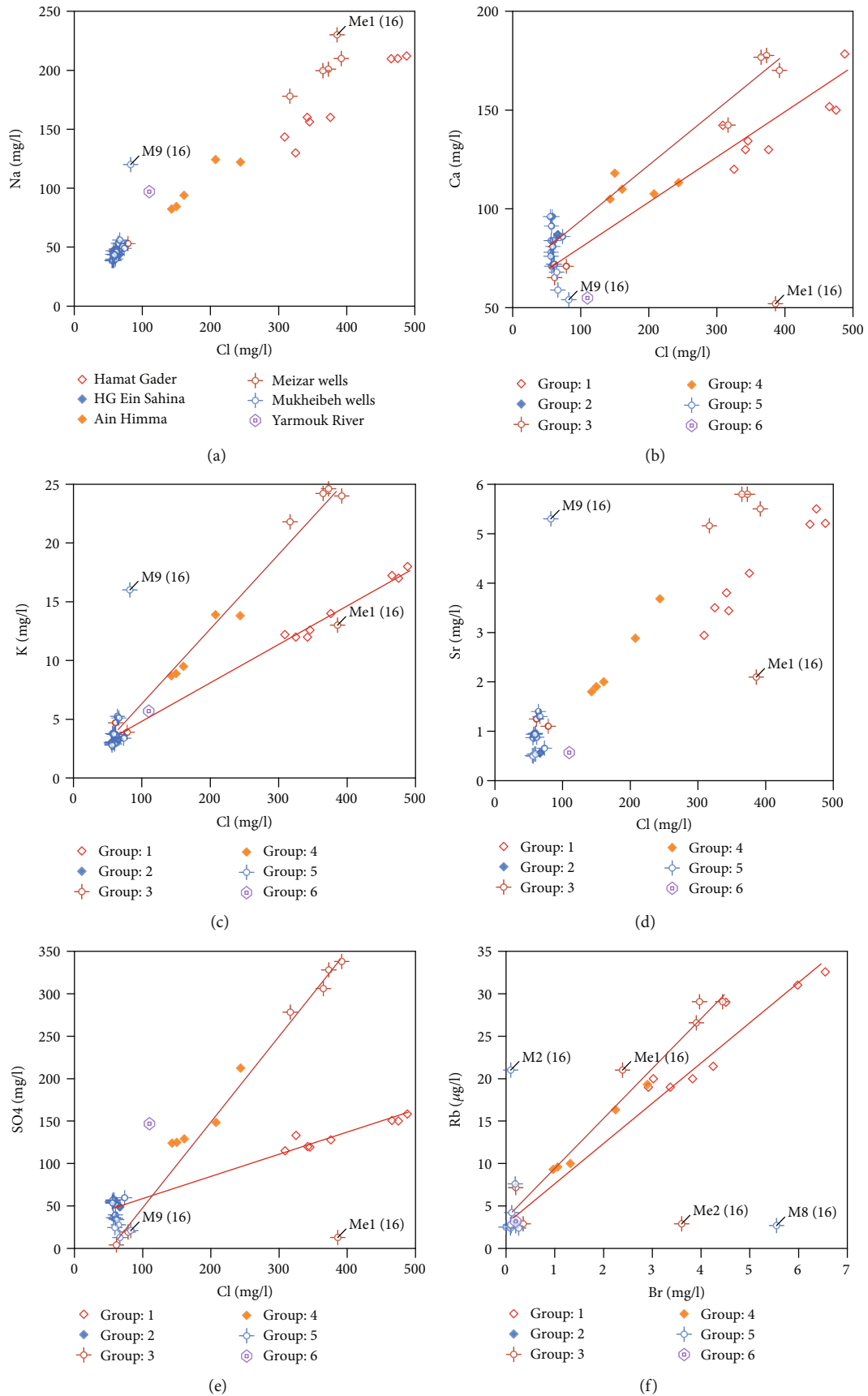


FIGURE 4: Continued.

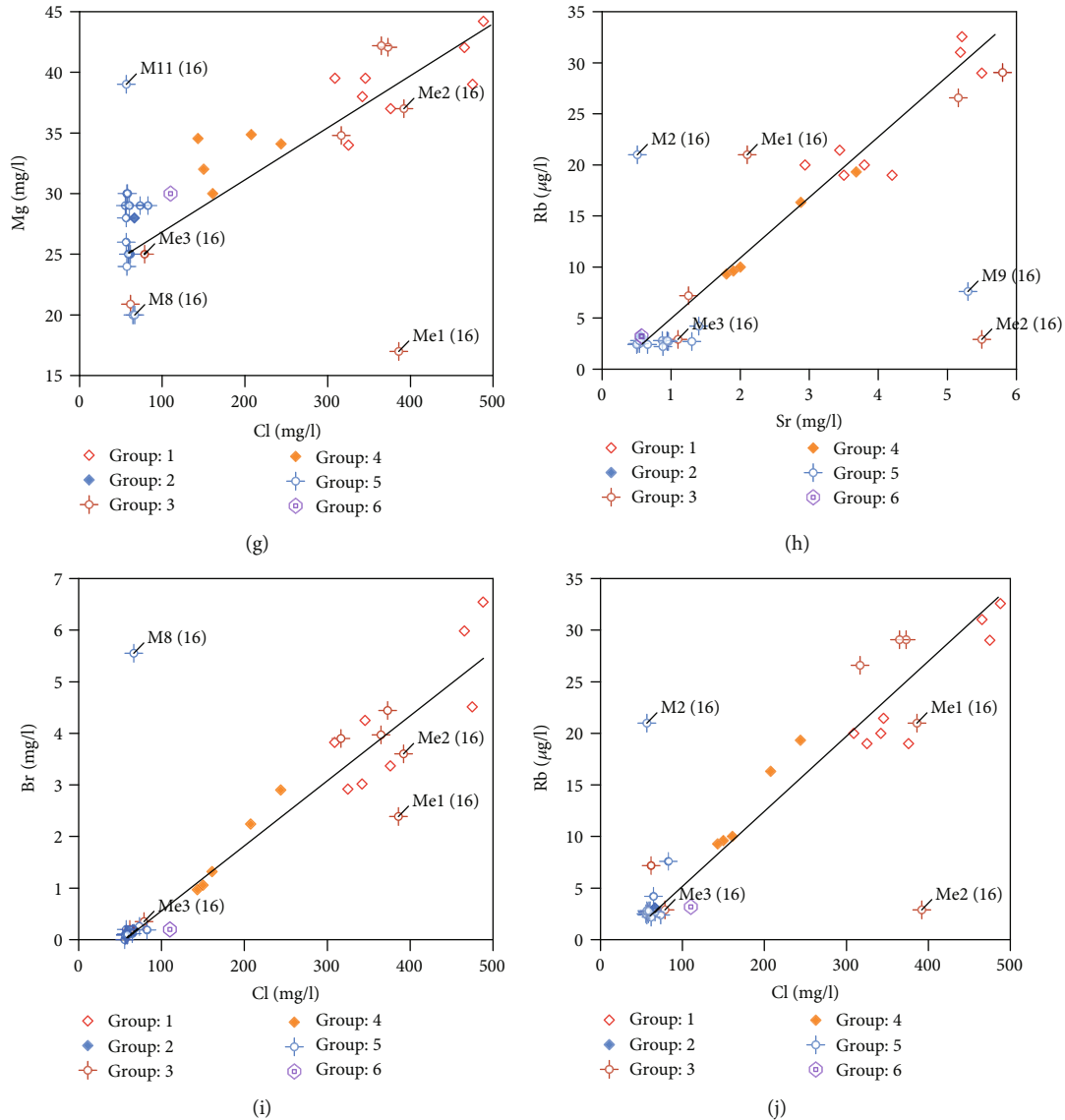


FIGURE 4: Crossplots of elements in the groundwater in the Lower Yarmouk Gorge. For details, refer to text.

cluster, is plotted among the heaviest Mukheibeh waters. Meizar 2 and Meizar 3(08) show the lowest isotope values.

5. Discussion

5.1. Sources of Groundwater. The stable isotopes of water and the element correlations reveal different origins of fresh and saline contributions to the groundwater in the LYG. Distinct groups of stable isotopes suggest regional infiltration areas at different elevations. The Meizar 2 groundwater from 2001 to 2016 with (i) light $\delta^2\text{H}$ and $\delta^{18}\text{O}$ signatures and (ii) REY patterns of nearly limestone water shape and least affected by HFO (t4 in Figure 6(d)) suggests infiltration of precipitation on the outcropping Triassic to Cretaceous limestones of the foothills of the Mt. Hermon Massif. The increase in Cl^- is higher than that in Na^+ probably pointing to mobilization of highly evaporated seawater brines and admix of these brines to the limestone water.

The water of Meizar 2(08) and Meizar 3(08) shows similar chemical and isotopic composition and the same type of REY patterns (t5). Although showing similar U(VI) concentrations, Meizar 2(01) and Meizar 2(16) are dissimilar in REY patterns (t4 and t5). This suggests that these types of groundwater discharge from the same reservoir but the flow path of recharging water differs over the years.

The groundwater with $\delta^{18}\text{O}$ and δD of about -6‰ and -30‰ , respectively, typifies the groundwater from Hamat Gader, Himma, Meizar 3 in 2001 and 2016, and the Mukheibeh field. Most of the Mukheibeh and Hauran groundwater shows a trend of increasingly heavy stable isotopes of water, suggesting evaporation of recharge prior to infiltration (Figure 8). The effect of evaporation on stable isotope enrichment is shown by heaviest δD and $\delta^{18}\text{O}$ signatures in the Yarmouk River.

High molar values of Na^+/Cl^- and $\text{Ca}^{2+}/\text{SO}_4^{2-}$ but low Br^-/Cl^- and low concentrations of Na^+ , Cl^- , Ca^{2+} , Mg^{2+} , K^+ , Sr^{2+} , and Br^- typify the basaltic waters [31]. Pure basaltic

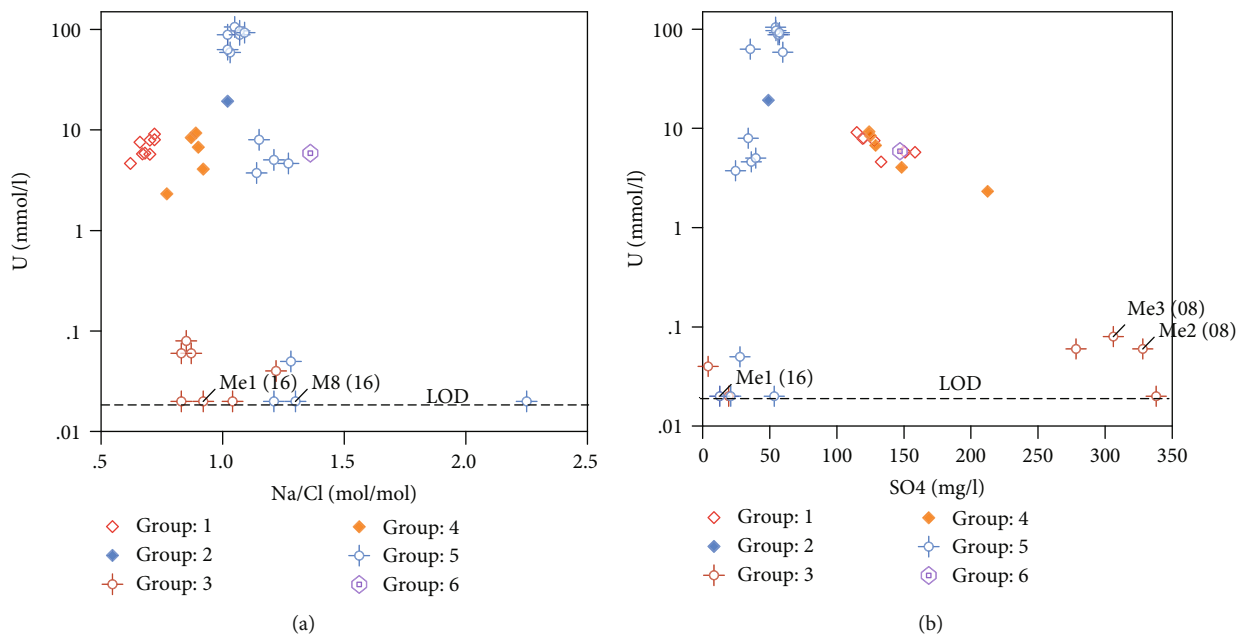


FIGURE 5: Crossplots of U(VI) and Na/Cl values in the groundwater of the Lower Yarmouk Gorge.

water is characterized by $Na^+/Cl^- \gg 1$ (Table 1) and typical REY patterns of type t1 (Figure 6(a)). With increasing leaching of halite from sedimentary rocks, the basaltic waters approach the lowest Na^+/Cl^- value of about 1, whereas mixing with evaporated seawater brines yields $Na^+/Cl^- < 1$ (Figure 9). Comparison of the Mukheibeh waters with those of basaltic composition reveals that the former waters are enriched in all elements (Table 1). The dissolution of anhydrite/gypsum by thermal waters of Meizar and Himma leads to enhanced concentrations of Ca^{2+} and SO_4^{2-} (Figure 4(b)). Ca^{2+} may also increase by dissolution of calcite at enhanced temperatures and albitization of plagioclases in basalts. Mg^{2+} , Rb^+ , Br^- , and K^+ may be gained by ion exchange against Ca^{2+} in marly layers in the aquifers (Figures 3 and 4). A Br^- increase may be gained by contact with the bituminous-rich B2 formation. The correlations of Cl^- with SO_4^{2-} , Ca^{2+} , Mg^{2+} , Sr^{2+} , Rb^+ , and Br^- reveal that, with few exceptions, waters from Hamat Gader, Himma, and Meizar are mixtures of basaltic water and remnants of brines from the Triassic-Cretaceous Arabian carbonate platform. The strong correlation of Rb^+ and Sr^{2+} indicates a common source but not necessarily the same mineral (Figure 4(h)). The two trends in the correlation of Rb^+ and Br^- verify the different sources of both elements (Figure 4(j)).

The molar $1000Br^-/Cl^-$ vs. Na^+/Cl^- values show several trends for groundwater in the Yarmouk basin and the trend of evaporated seawater in salt pans (Figure 9). In this plot, the springs of Hamat Gader, Himma, and well Meizar 2 define vertical trends which are only explainable by leaching of Br^- from the organic-rich B2 formation (Figure 3). Meizar 3 in 2001 and 2016 and all the groundwater with the lowest Br^-/Cl^- values in the vertical groups suggest mixing between Mukheibeh groundwater and seawater brine characterized by Na^+/Cl^- and $1000Br^-/Cl^-$ of about 0.5 and 5.3, respectively. Such ratios resemble those of the Ha'On type of brine, emerg-

ing at SE shoreline of the Lake Tiberias [2, 38, 39]. A second mixing line is indicated by Ein Sahina and Mukheibeh wells 1 and 6; both lines only differ in the Mukheibeh end member.

5.2. *The Impact of HFO Precipitation on U and REY.* U(VI) is highly adsorbed onto the high surface area of HFO [40]. The U content of alkali olivine basalts is in the range of 1 ppb [41]. The infiltrating basaltic groundwater with low U(VI) content passes the growing HFO “filter” within and below the basaltic cover of the Hauran plateau and elsewhere. During the alteration of HFO to goethite, lepidocrocite, or hematite, the adsorbed U(VI) is reduced to U(V) which is more resilient to oxidation than uraninite (UO_2) or adsorbed U(IV) [42, 43]. Adsorption of U(VI) in the pH range of 6.6-7.3 (Table 1) is not affected by additional adsorption of phosphate [44].

The high U(VI) contents of 80 to 105 nmol/l in the groundwater of Mukheibeh artesian wells 1, 2, 4, 6, and 7 are most probably supplied later from the phosphorite-rich B2 aquifer. The phosphorites from the B2 formation in Syria, Jordan, and Israel contain about 100 ppm U [45]. Assuming that U(VI) is mobilized by phosphate as $UO_2(HPO_4)_2^{2-}$ [46], the phosphate concentration should be in the range of 0.2 $\mu\text{mol/l}$ or 6 $\mu\text{g/l}$ which was much below our routine detection limit of phosphate of 1 mg/l.

Meizar 2 water has its source in the flanks of the Mt. Hermon Massif and in the western elevations of the Hauran plateau, which agrees with light stable isotopes of water. Although limestone waters contain 2-20 nmol/l U(IV) from elsewhere in Israel (Siebert unpublished), Meizar 2 and Mukheibeh 8, 9, and 11 waters show less than 0.1 nmol/l U(VI) suggesting that these waters must have had contact with HFO but did not interact with the B2 formation. Though having similar low U, considerably heavier stable isotope signatures in Mukheibeh 8 and 9, the most

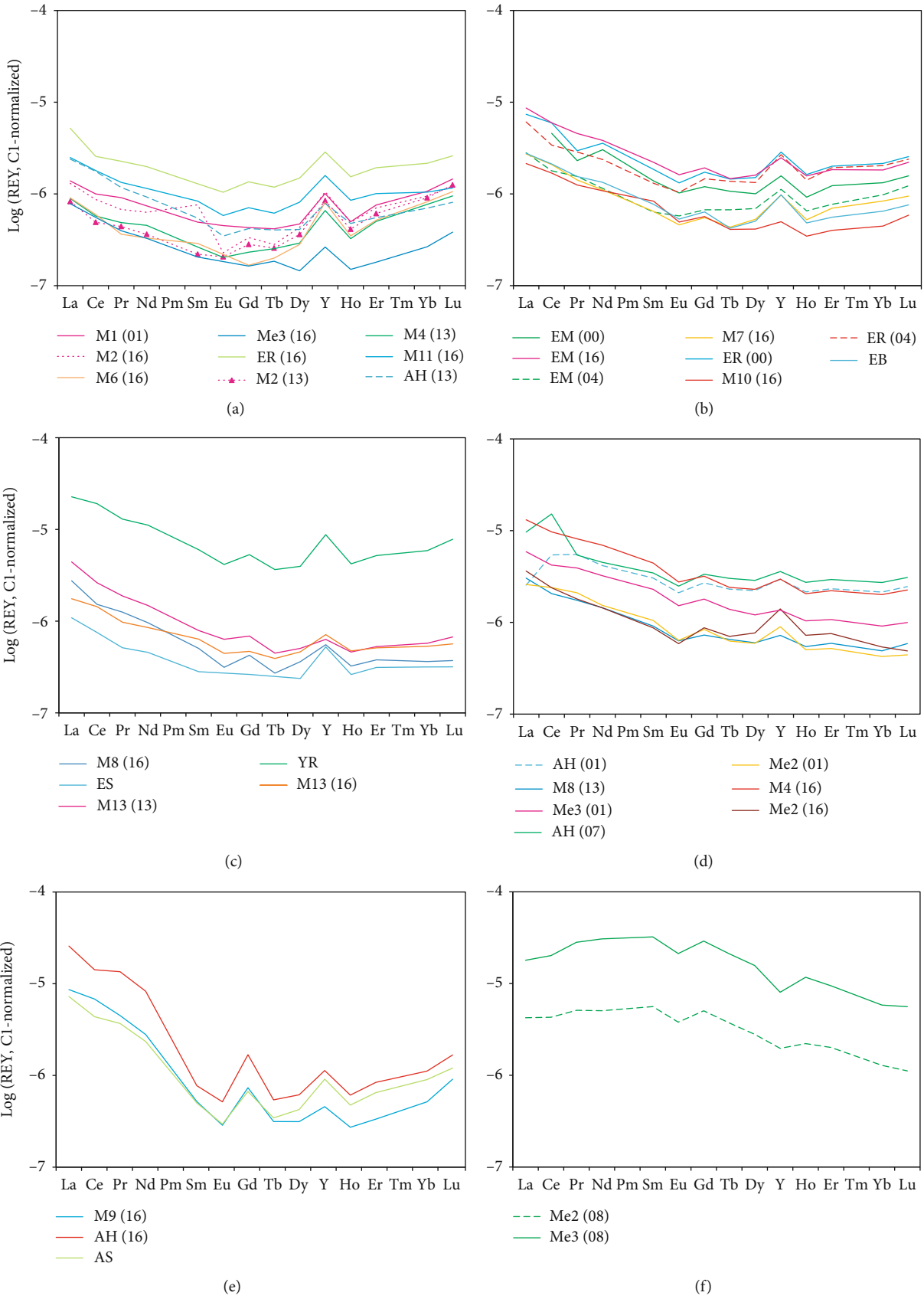


FIGURE 6: Continued.

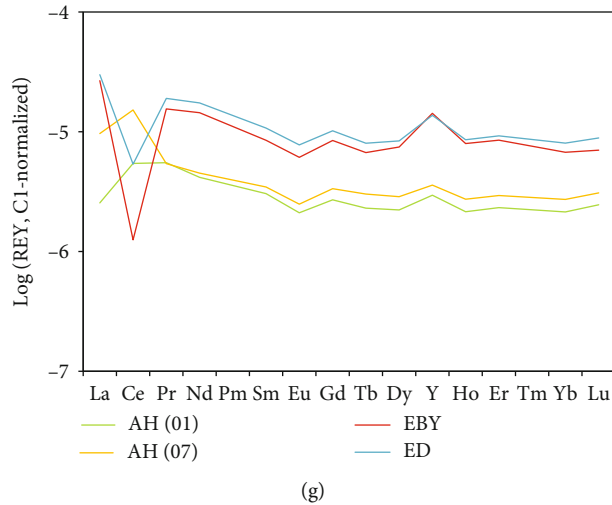


FIGURE 6: REY distribution patterns of groundwater in the Lower Yarmouk Gorge. The visual grouping of patterns shows their high variability.

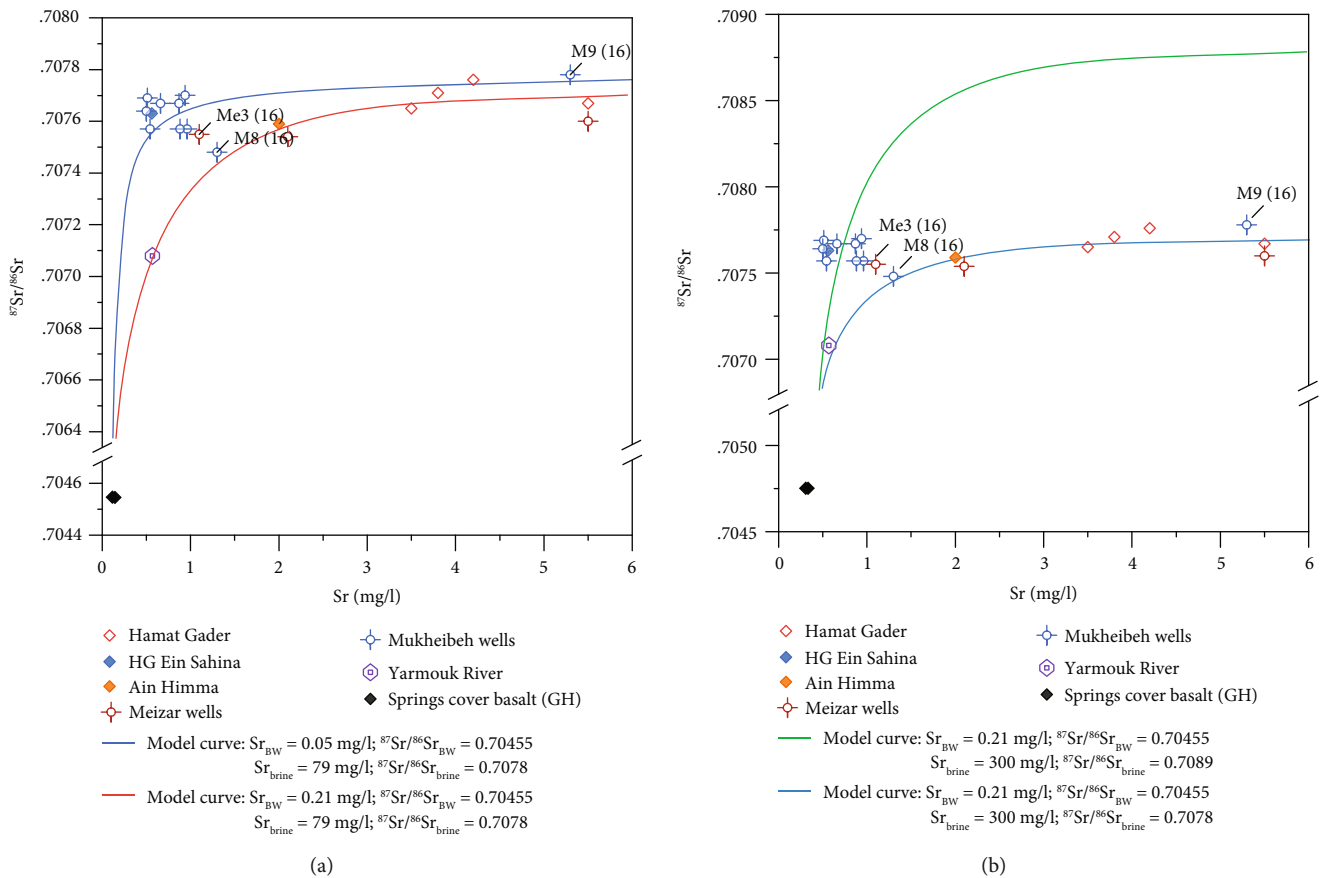


FIGURE 7: Crossplots of Sr isotope ratios and Sr^{2+} in the groundwater from the Lower Yarmouk Gorge.

northeastern samples in the LYG, refer to a recharge area differing from Meizar 2.

HFO scavenges not only U(IV) but also REY and HPO_4^{2-} . There may be some synergetic interaction between

phosphate and REY resulting in type t1 patterns. This seems to be indicated in type t2*, which is possibly due to Y-phosphate precipitation (possibly churchite, Y, and $HREEPO_4$) due to which the light REE are released [47].

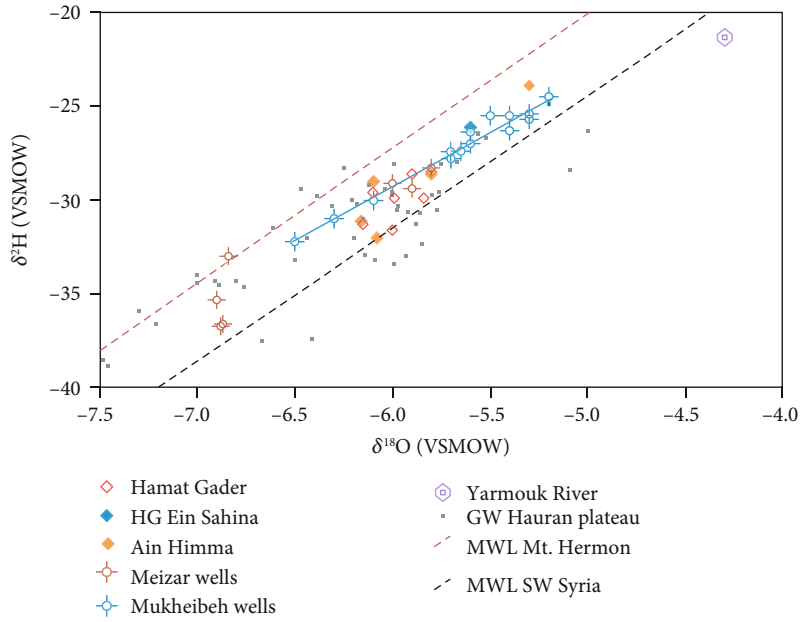


FIGURE 8: δD vs. $\delta^{18}O$ in groundwater of the Lower Yarmouk Gorge ([1]; this study) and the Hauran plateau [18]. MWL for Mt. Hermon and SW Syria are taken from Brielmann [52] and Al Charideh and Zakhem [53], respectively.

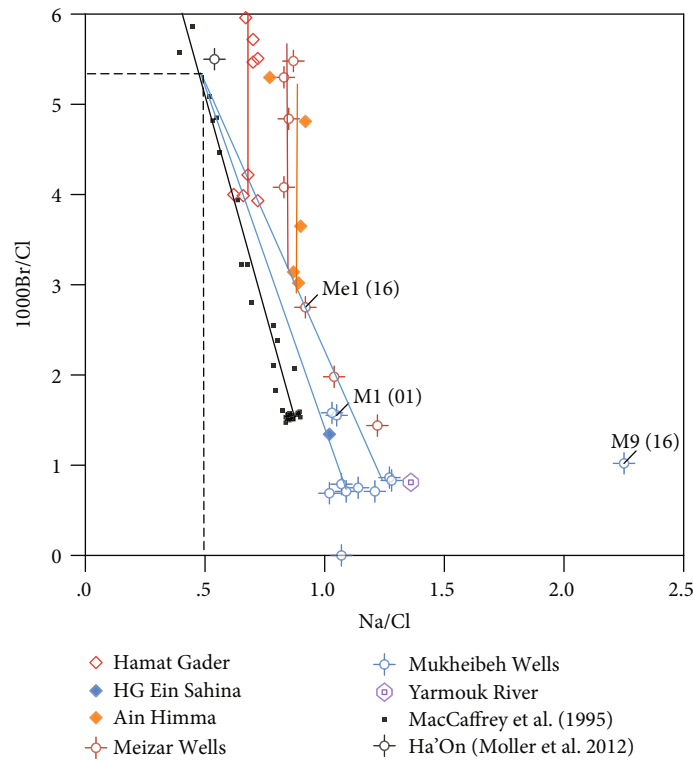


FIGURE 9: Crossplots of 1000Br/Cl and Na/Cl of the groundwater from the Lower Yarmouk Gorge.

All groundwater in the gorge is produced from limestone aquifers. When the REY poor basaltic water passes the limestones at enhanced temperatures, some calcite dissolves and thereby its aliquot of REY is released and mixed with REY

load of the groundwater. More than 99% of the REY is immediately adsorbed onto calcite surfaces [48]. This way, the REY patterns of groundwater change from type t1 to t2, t3, and finally t4 (Figures 6 and 10). At enhanced

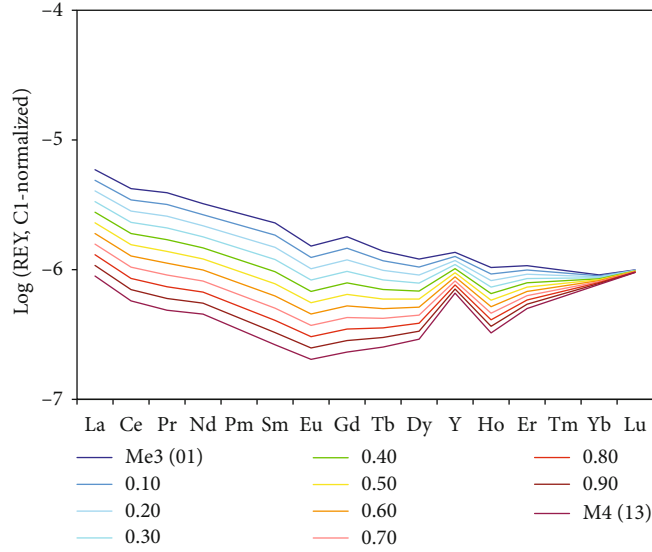


FIGURE 10: Mixing of basaltic and limestone groundwater showing the change in rare earth distribution patterns.

temperatures, release of LREE is faster than that of HREE and Y because their Coulomb binding forces are less for the former bigger than the latter smaller ions. This may qualitatively explain the change in REY patterns of groundwater in the Yarmouk basin.

Although the groundwater of the Yarmouk Gorge is produced from limestone aquifers, their REY patterns still indicate that the groundwater originates from basaltic catchment regions or, more precisely, has passed HFO layers. Although the patterns are similar in shape, the spring waters of Dan and Banyas from limestones of the Mt. Hermon Massif without contact with HFO show higher abundances than the limestone-like waters from the Yarmouk Gorge such as in Himma spring and Mukheibeh well 4(16) (Figure 6(g)). Types t1 to t4 in Figure 5 represent the continuous change of REY patterns due to the interaction of basaltic groundwater after passing the HFO filter t1 and limestones resulting in changes according to t2-t4. These types of patterns result from mixing limestone and basaltic rock waters. It could well be that not the whole volume of water changes due to the interaction but only parts of it and mixing of various types yields the final patterns as shown in Figure 10.

Type t5 (Figure 6(e)) is not showing dissolution of phosphate minerals such as apatite but leachates of altering HFO that loses REY at high levels. The difference between the latter two is that the former should show a positive Eu anomaly [36], whereas the latter is characterized by a negative one.

How does it come that these types of groundwater still show REY patterns typical after infiltration in basaltic catchment areas? The reason is that the REY in calcite surfaces along the pathways in limestones equilibrate with the low REY abundance from the basaltic catchment. Under steady-state conditions, the groundwater from limestones shows patterns achieved by the interaction with groundwater that has passed HFO layers [31].

5.3. *Tracing Mixing by Sr^{2+} and $^{87}Sr/^{86}Sr$.* The above discussed findings, which trace back the genesis of the groundwater in the LYG by variable interactions of basaltic water with late Tertiary brines of Ha'On type and with calcite and limestone of the discharging Cretaceous/Paleogene aquifers, can be fortified by model calculations, which try to resemble the measured $^{87}Sr/^{86}Sr$ values in the groundwater of the LYG by at least interaction of basaltic water and brine (Figure 7).

Using the fraction ϵ_{brine} of brine in the mixture of brine and basaltic water, the mix of Sr^{2+} (Equation (1)) and the mix of the Sr^{2+} isotope ratios (Equation (2)) are estimated.

$$Sr_{mix} = \epsilon_{brine} \times Sr_{brine} + (1 - \epsilon_{brine}) \times Sr_{BW}, \quad (1)$$

$$\begin{aligned} ^{87}Sr/^{86}Sr_{mix} = & ^{87}Sr/^{86}Sr_{brine} \times \epsilon_{brine} \times Sr_{brine}/Sr_{mix} \\ & + ^{87}Sr/^{86}Sr_{BW} \times (1 - \epsilon_{brine}) \times Sr_{BW}/Sr_{mix}, \end{aligned} \quad (2)$$

where index BW is the basaltic water.

Considering the analytical data on Sr^{2+} concentration of groundwater in Table 3, brine, basaltic water, and dissolved calcite and gypsum and their corresponding $^{87}Sr/^{86}Sr$ values and the Sr^{2+} concentration of basaltic water must be below 0.5 mg/l, the lowest value in Mukheibeh water. Indeed, pure basaltic water sampled from 2 springs in the cover basalt of the Golan Heights shows $Sr^{2+} = 0.2$ mg/l. The Sr^{2+} concentration of the brine may be between 79 mg/l as analyzed in Ha'On brine [2] and 300 mg/l, depending on the amount of dissolution of calcite from limestone with assumed average Sr^{2+} concentrations of 100 mg/mol calcite and about 25 mg/mol gypsum from evaporites [49]. The $^{87}Sr/^{86}Sr$ value of basaltic water is 0.70455 to 0.70457, and that of the brine is assumed to be 0.7078, matching the spread of data in Figure 7. The $^{87}Sr/^{86}Sr$ value of 0.7078 may result from mixing of Late Tertiary Tethys

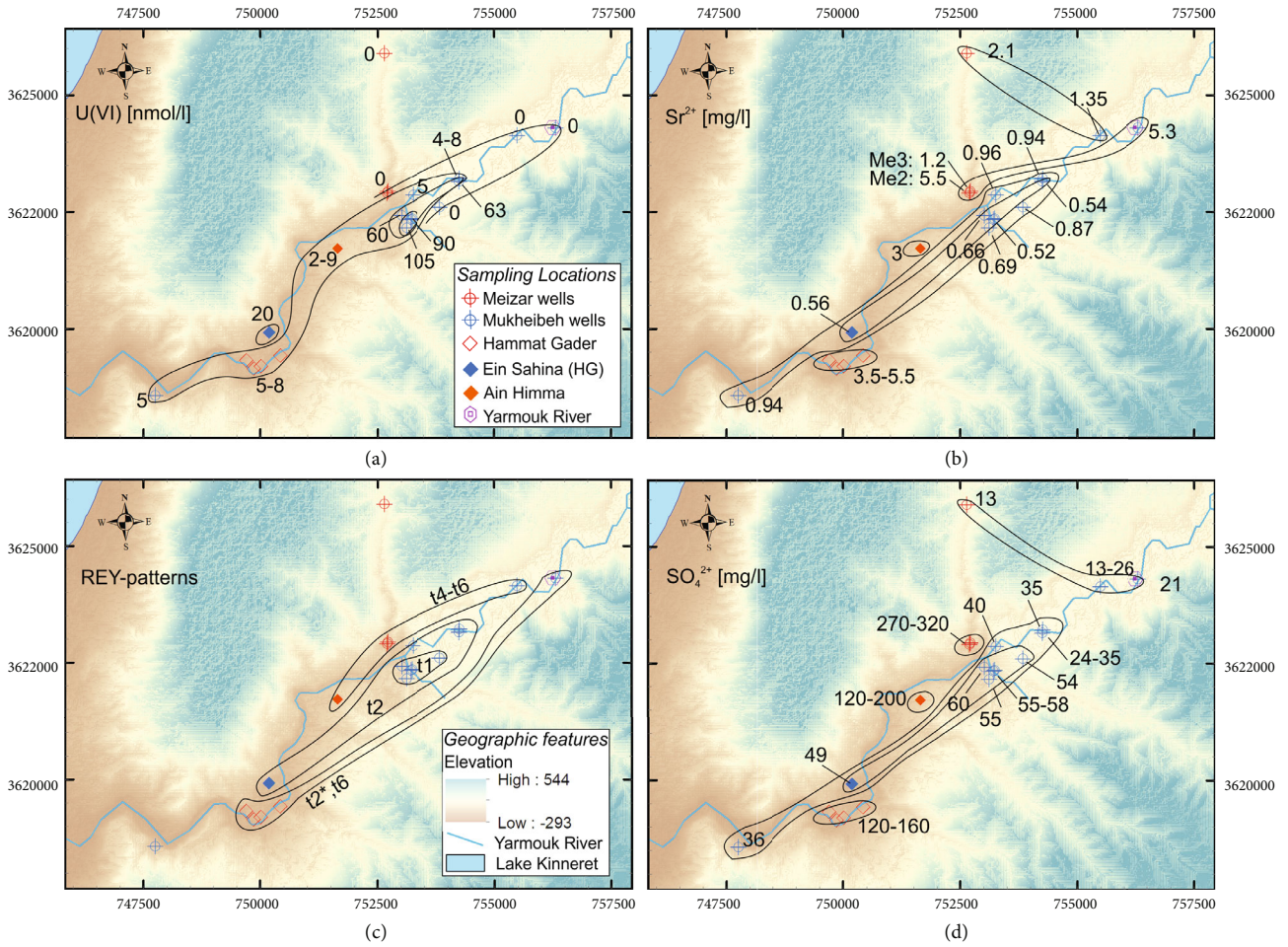


FIGURE 11: Regional distribution of U(VI) (a), Sr²⁺ (b), rare earth distribution patterns (c), and sulfate (d) in the Lower Yarmouk Gorge. Legends given in (a) and (c) are representative for the entire Figure 11.

seawater of 0.7089 [50] and dissolved average Upper Cretaceous limestone in Israel ranging between 0.7076 and 0.7078 (Wilske et al., unpublished data).

The model curves in Figure 6 are fitted by varying Sr²⁺ in basaltic water and in brine as well as the ⁸⁷Sr/⁸⁶Sr value of the brine. Several information can be derived by the following procedure.

- (1) The observed groundwater cannot be fitted by one curve, and the results are sensitive to assumed values of ⁸⁷Sr/⁸⁶Sr and the resulting ϵ_{brine}
- (2) To fit most Mukheibeh groundwater and that of Me3(16), the requested Sr²⁺ concentrations must be 0.05 mg/l, much lower than the observed 0.21 mg/l (Figure 7(a)). Hence, the positive shift of these types of groundwater along the ordinate is assumed to result from the interaction of the proposed fluid mix with calcite and gypsum in the discharging limestone aquifers, which show ⁸⁷Sr/⁸⁶Sr values as high as 0.7078 (Wilske et al., unpublished data)
- (3) The fitting curves are invariant in respect to variations of Sr²⁺ in the brine (compare red curve in Figure 6(a) and blue curve in Figure 7(b))

- (4) If ⁸⁷Sr/⁸⁶Sr values of brine are larger than 0.7078, neither the group of groundwater from Mukheibeh wells and Meizar 3 nor the group of Hamat Gader, Meizar 2, and Ain Himma can be represented (Figure 7(b))

In summary, the ⁸⁷Sr/⁸⁶Sr of the groundwater in the LYG is the result of relic brine, which is diluted by basaltic water and subsequently dissolves calcite and gypsum and experiences some exchange of Ca²⁺ against Mg²⁺, Na⁺, and K⁺ in marly layers of the aquifers (Figure 3). Only Meizar 3 is mainly limestone water.

5.4. Regional Distribution of Dissolved Species. The regional distribution of U(VI), Sr²⁺, and REY shows comparable structures, whereas SO₄²⁻ behaves differently. High and low U(VI) concentrations are present in the NE of the Lower Yarmouk Gorge (Figure 11(a)). The high values of 80-105 nmol/l U mark the area in which Mukheibeh wells 1, 2, 4, 5, 6, and 7 produce artesian water from the phosphorite-rich B2 aquifer. These high U(VI) concentrations decrease to 20 nmol/l SW-ward, downstream the Yarmouk River and to both sides of the gorge. North of and NE-ward in the gorge groundwater contain U(VI) below 1 nmol/l. Such low values can only be established by adsorption of U(VI). In the case of

Mukheibeh 8 and 9, this could be HFO in the Hauran plateau; in the case of Meizar, saline groundwater contact with dissolving HFO is documented in Figure 7(f) in the year 2008. According to Shimron [51], basaltic intrusions are present in the Mt. Hermon anticline, being probably responsible for the low U(VI). Additionally, the long pathway through the limestone aquifers from Mt. Hermon to the LYG altered the REY patterns in groundwater to type t4. In 2016, Meizar 3 shows the REY pattern of type t1. However, in 2001, it resembled type t4 of Meizar 2 in 2001 and 2016.

In the central part of the LYG, Sr^{2+} is about 0.55 mg/l (Figure 11(b)), while it increases to 1 mg/l NE-ward, to 3 mg/l in Himma, to 4 mg/l in Hamat Gader, and to 5 mg/l in both Meizar wells 2 and 3.

A similar shell-like behavior is observable in the REY patterns with t1 patterns in the center followed by t2 SW-ward and t3 type SE-ward and patterns of t4 to t6 in the NW (Figure 11(c)).

The high-uranium water shows SO_4^{2-} concentrations of 30–50 mg/l (Figure 11(d)). Outside that central part, the groundwater shows either much higher SO_4^{2-} concentrations, such as in Hamat Gader (150 mg/l) and Meizar (300 mg/l), or almost no dissolved sulfate as in the NE (0.12 mg/l). The increasing SO_4^{2-} outside the marked center may prove depletion of gypsum in the central region of ascending groundwater. Comparing spatial concentration distribution patterns of Sr^{2+} and SO_4^{2-} results in similar patterns, though the concentration levels differ significantly.

Leaching of brines and/or evaporites alters the chemical composition of the initial basaltic water. The light signatures of water isotopes of Meizar 2 support a catchment area at the Mt. Hermon foothills or at elevated places in the Hauran. Meizar 3 water isotopes correspond with those of Hamat Gader and Himma, which may be taken as an indirect proof for its basaltic water. Their variable REY patterns of types t1, t4, and t5 suggest various flow paths of the groundwater including differing contacts with HFO. The shortest pathway of groundwater flow is indicated by REY patterns of type t1 (Figure 6), while patterns of type t2 and t3 suggest a longer pathway with more intense REY exchange with calcite in limestones. The longest pathways are typified by REY pattern type t4. The REY types and the concentrations of U(VI), Sr^{2+} , and SO_4^{2-} characterize complex flow patterns of groundwater towards the gorge.

The most distinct basaltic water is produced from the B1/B2 limestone aquifers fractured by a complex fault system crossing the LYG [15] (Figure 1(b)). This marks the most important flow path of drainage water from the Hauran into the LYG. The springs of Hamat Gader (including Ein Sahina) and Himma are positioned on an uptilted block, whereby both spring fields are separated from the Meizar field. The deep aquifer which is tapped by Meizar 2 also produced water in the shallow well Meizar 3 in 2008.

Although producing from the same aquifer, the hydrochemical differences in groundwater from Ein Himma and Meizar 3 disprove any transboundary flow below the Yarmouk River. The confined water from basaltic infiltration areas in Syria, however, is present on both sides of the gorge.

6. Conclusions

The conjoint study of major, minor, and trace elements, $\delta^{18}\text{O}$, δD , and $^{87}\text{Sr}/^{86}\text{Sr}$ in the groundwater of the LYG reveals the following:

- (i) Mixtures of water from basaltic rocks and limestones are almost omnipresent in the LYG. A clear exception is Meizar 2 that produces groundwater that was infiltrated at the flanks of Mt. Hermon Massif. The mixtures vary from nearly pure basaltic water to nearly pure limestone water. In addition, leaching of residual brines and evaporites enhances the salinity of the various types of groundwater
- (ii) The sources of salinization in limestone aquifers are given by relic brines, leaching of gypsum, and dissolution of calcite. The origin of high sulfate concentrations could be either the Late Triassic gypsum beds occurring at approximate depths of 2000 m or evaporites of the Late Tertiary rift brine of the inland sea. For instance, groundwater in Meizar 2 and Hamat Gader has leached different amounts of gypsum/anhydrite and calcite. Ion exchange of Ca^{2+} against Mg^{2+} , Na^+ , and K^+ enhanced the concentrations of the latter. Meizar 3 in 2008 resembles Meizar 2 in the same year. Their REY patterns show that this groundwater had dissolved HFO on its altered flow path. The regional distribution of U(VI), Sr^{2+} , and SO_4^{2-} and REY distribution patterns reveal that there is a zone with strongly confined groundwater and the hydrochemical composition changes systematically sideward and downstream along the gorge
- (iii) The regional variation of their chemical composition of groundwater is related to a complex flower-structured fault system crossing the gorge. Groundwater flow in the gorge and the mixing between the different water bodies are controlled by these structural features

Data Availability

All underlying data of the research study are included in the manuscript in the form of Tables 1–3.

Conflicts of Interest

The authors declare that they have no conflicts of interest.

Acknowledgments

The research was partly funded by the German Science Foundation (DFG) (grant MA4450/2) and the DESERVE Virtual Institute (VH-VI-527) funded by the Helmholtz-Association of German Research Centers. The authors thank the Mekorot Co. Ltd. and the IDF and JAF for providing access and security during sampling along the international borders.

References

- [1] C. Siebert, P. Möller, S. Geyer et al., "Thermal waters in the Lower Yarmouk Gorge and their relation to surrounding aquifers," *Geochemistry*, vol. 74, no. 3, pp. 425–441, 2014.
- [2] P. Möller, C. Siebert, S. Geyer et al., "Relationship of brines in the Kinnarot Basin, Jordan-Dead Sea Rift Valley," *Geofluids*, vol. 12, no. 2, 181 pages, 2012.
- [3] P. Möller, E. Rosenthal, N. Inbar, and C. Siebert, "Development of the inland sea and its evaporites in the Jordan-Dead Sea Transform based on hydrogeochemical considerations and the geological consequences," *International Journal of Earth Sciences*, vol. 107, no. 7, pp. 2409–2431, 2018.
- [4] N. Goretzki, N. Inbar, M. Kühn et al., "Inverse problem to constrain hydraulic and thermal parameters inducing anomalous heat flow in the Lower Yarmouk Gorge," *Energy Procedia*, vol. 97, pp. 419–426, 2016.
- [5] F. Magri, N. Inbar, C. Siebert, E. Rosenthal, J. Guttman, and P. Möller, "Transient simulations of large-scale hydrogeological processes causing temperature and salinity anomalies in the Tiberias basin," *Journal of Hydrology*, vol. 520, pp. 342–355, 2015.
- [6] F. Magri, S. Möller, N. Inbar et al., "2D and 3D coexisting modes of thermal convection in fractured hydrothermal systems - Implications for transboundary flow in the Lower Yarmouk Gorge," *Marine and Petroleum Geology*, vol. 78, pp. 750–758, 2016.
- [7] K. Tzoufka, F. Magri, T. Rödiger et al., "The effect of hydraulic anisotropies on intensely exploited groundwater resources: the numerical evaluation of a hydrothermal transboundary aquifer system in the Middle East," *Hydrogeology Journal*, vol. 26, no. 8, pp. 2875–2890, 2018.
- [8] R. Roded, E. Shalev, and D. Katoshevski, "Basal heat-flow and hydrothermal regime at the Golan-Ajloun hydrological basins," *Journal of Hydrology*, vol. 476, pp. 200–211, 2013.
- [9] Mekorot, National Water Co, *Records on wells, water levels water quality and exploitation*, Mekorot Company, Tel Aviv, Israel, 1950-2017.
- [10] WAJ, *Water Information System Database, accessible via the Ministry of Water and Irrigation*, Jordan Ministry of Water and Irrigation, Amman, Jordan, 2016, <http://www.mwi.gov.jo>.
- [11] A. Brunner and E. Dekel, "High resolution seismic reflection survey in Southern Golan," Rep.120/1939/88 IPRG-Israel Institute for Petroleum Research and Geophysics, 1989.
- [12] M. Meiler, M. Reshef, and H. Shulman, "Seismic depth-domain stratigraphic classification of the Golan Heights, central Dead Sea Fault," *Tectonophysics*, vol. 510, no. 3–4, pp. 354–369, 2011.
- [13] J. Sahawneh, "Structural control of hydrology, hydrogeology and hydrochemistry along the eastern escarpment of the Jordan Rift Valley, Jordan," PhD. Thesis, Karlsruhe Inst. für Technologie (KIT), 2011.
- [14] A. Flexer, "Stratigraphy and facies development of Mt. Scopus Group (Senonian-Paleocene) in Israel and adjacent countries," *Israel Journal of Earth Sciences*, vol. 17, pp. 85–114, 1980.
- [15] N. Inbar, E. Rosenthal, F. Magri et al., "Faulting patterns in the Lower Yarmouk Gorge potentially influence groundwater flow paths," *Hydrology and Earth System Sciences*, vol. 23, no. 2, pp. 763–771, 2019.
- [16] E. Rosenthal, "Hydrogeology and hydrogeochemistry of the Bet Shean and Harod Valleys," vol. 2, Geol Surv Israel, 1972, Rep. H/2/1972, in Hebrew.
- [17] E. Rosenthal, G. Weinberger, A. Almogi-Labin, and A. Flexer, "Late cretaceous-early tertiary development of depositional basins in Samaria (Israel) as part of the evolution of regional folding systems," *AAPG Bulletin*, vol. 84, pp. 997–1042, 1999.
- [18] Z. Kattan, "Chemical and environmental isotope study of the fissured basalt aquifer system of the Yarmouk basin," *IAEA Symposium on isotopes in water resources management*, 1995, Vienna, Austria, 1995IAEA-SM/336/28.
- [19] E. Dafny, A. Burg, and H. Gvirtzman, "Deduction of groundwater flow regime in a basaltic aquifer using geochemical and isotopic data: the Golan Heights, Israel case study," *Journal of Hydrology*, vol. 330, no. 3–4, pp. 506–524, 2006.
- [20] T. Rödiger, S. Geyer, U. Mallast et al., "Multi-response calibration of a conceptual hydrological model in the semiarid catchment of Wadi al Arab, Jordan," *Journal of Hydrology*, vol. 509, pp. 193–206, 2014.
- [21] E. Salameh, "Using environmental isotopes in the study of recharge-discharge mechanisms of the Yarmouk catchment area in Jordan," *Hydrogeology Journal*, vol. 12, pp. 451–463, 2004.
- [22] K. Schelkes, *Groundwater balance of the Jordan-Syrian basalt aquifer*, BGR Bundesanstalt für Geowissenschaften und Rohstoffe, Hannover, 1997.
- [23] UN-ESCWA and BGR (United Nations Economic and Social Commission for Western Asia and Bundesanstalt für Geowissenschaften und Rohstoffe), *Inventory of shared water resources in Western Asia. Chapter 21, Yarmouk Basin Basalt Aquifer System*, 2013.
- [24] W. Wagner, *Groundwater in the Arab Middle East*, Springer-Verlag, Berlin, Heidelberg, 2011.
- [25] A. Sneh, Y. Bartov, T. Weissbrod, and M. Rosensaft, *Geological map of Israel 1:2200,000. Israel Geological Survey (4 Sheets)*, Geological Survey of Israel, Jerusalem, Israel, 1998.
- [26] G. Brew, M. Barazangi, A. K. Al-Maleh, and T. Sawaf, "Tectonic and geologic evolution of Syria," *GeoArabia*, vol. 6, no. 4, pp. 573–616, 2001.
- [27] R. Wolfart, "Hydrogeology of the Damascus basin (Southwest-Syria)," *IAHS Red Books*, vol. 64, pp. 402–413, 1964.
- [28] E. Dafny, H. Gvirtzman, A. Burg, and L. Fleischerc, "The hydrogeology of the Golan basalt aquifer, Israel," *Israel Journal of Earth Sciences*, vol. 52, no. 3–4, pp. 139–153, 2003.
- [29] H. Michelson, "The hydrogeology of the southern Golan Heights," Tahal, Tel Aviv. Rep, 1972, HR/72/037.
- [30] H. Michelson, "The geology and paleogeography of the Golan Heights," Tel Aviv University, Tel Aviv. PhD thesis, 1979.
- [31] P. Möller, E. Rosenthal, N. Inbar, and F. Magri, "Hydrochemical considerations for identifying water from basaltic aquifers: the Israeli experience," *Journal of Hydrology: Regional Studies*, vol. 5, pp. 33–47, 2016.
- [32] A. Heimann, "The Dead Sea rift and its margins. Development of Northern Israel in the Pliocene and Pleistocene," PhD Thesis Hebrew Univ, 1990.
- [33] D. Mor, "The volcanism of the Golan Heights," Geol Surv Isr, 1986, Rep.GSI/5/86.
- [34] B. K. Moh'd, *The geology of Irbid and Ash Shuna Ash Shamaliyya (Waqgas) Map Amman, Sheets No. 3154-II and 3154-III*, Natural Resources Authority, Geology Directorate, Amman, Jordan, 2000.

- [35] M. Tichomirowa, C. Heidel, M. Junghans, F. Haubrich, and J. Matschullat, "Sulfate and strontium water source identification by O, S and Sr isotopes and their temporal changes (1997-2008) in the region of Freiberg, central-eastern Germany," *Chemical Geology*, vol. 276, no. 1-2, pp. 104-118, 2010.
- [36] P. Möller, E. Rosenthal, P. Dulski, and S. Geyer, "Characterization of recharge areas by rare earth elements and stable isotopes of H₂O," in *The Water of the Jordan Valley*, H. Hötzl, P. Möller, and E. Rosenthal, Eds., pp. 123-148, Springer Verlag, Berlin, Heidelberg, 2009.
- [37] C. Siebert, E. Rosenthal, P. Möller, T. Rödiger, and M. Meiler, "The hydrochemical identification of groundwater flowing to the Bet She'an- Harod multiaquifer system (Lower Jordan Valley) by rare earth elements, yttrium, stable isotopes (H, O) and Tritium," *Applied Geochemistry*, vol. 27, no. 3, pp. 703-714, 2012.
- [38] G. Bergelson, R. Nativ, and A. Bein, "Salinization and dilution history of ground water discharging into the Sea of Galilee, the Dead Sea Transform, Israel," *Applied Geochemistry*, vol. 14, no. 1, pp. 91-118, 1999.
- [39] O. Klein-BenDavid, E. Sass, and A. Katz, "The evolution of marine evaporitic brines in inland basins: The Jordan-Dead Sea Rift valley," *Geochimica et Cosmochimica Acta*, vol. 68, no. 8, pp. 1763-1775, 2004.
- [40] G. E. Brown Jr., T. P. Trainor, and A. M. Chaka, "Geochemistry of mineral surfaces and factors affecting their chemical reactivity," in *Chemical Bonding at Surfaces and Interfaces*, A. Nilsson, P. LGM, and J. Norskov, Eds., pp. 457-509, Elsevier, New York, 2008.
- [41] E. S. Larsen and D. Gottfried, *Distribution of uranium in rocks and minerals of Mesozoic batholith in Western United States*, vol. 1070-C, US Geol Surv Bull, 1961.
- [42] T. A. Marshall, K. Morris, G. T. W. Law et al., "Incorporation of uranium into hematite during crystallization from ferrihydrite," *Environmental Science & Technology*, vol. 48, no. 7, pp. 3724-3731, 2014.
- [43] H. E. Roberts, K. Morris, G. T. W. Law et al., "Uranium(V) incorporation mechanisms and stability in Fe(II)/Fe(III) (oxyhydr)oxides," *Environmental Science & Technology Letters*, vol. 4, no. 10, pp. 421-426, 2017.
- [44] M. R. Romero-González, T. Cheng, M. O. Barnett, and E. E. Roden, "Surface complexation modeling of the effects of phosphate on uranium(VI) adsorption," *Radiochimica Acta*, vol. 95, no. 5, 2007.
- [45] G. N. Baturin and A. V. Kochenov, "Uranium in Phosphorites," *Lithology and Mineral Resources*, vol. 36, no. 4, pp. 303-321, 2001.
- [46] V. S. Tripathi, "Comments on "Uranium solution-mineral equilibria at low temperatures with applications to sedimentary ore deposits"," *Geochimica et Cosmochimica Acta*, vol. 43, no. 12, pp. 1989-1990, 1979.
- [47] S. Göb, T. Wenzel, M. Bau, D. E. Jacob, A. Loges, and G. Markl, "The redistribution of rare-earth elements in secondary minerals of hydrothermal veins, Schwarzwald, SOUTHWESTERN Germany," *The Canadian Mineralogist*, vol. 49, no. 5, pp. 1305-1333, 2012.
- [48] P. Möller and C. Siebert, "Cycling of calcite and hydrous metal oxides and chemical changes of major element and REE chemistry in monomictic hardwater lake: impact on sedimentation," *Chemie der Erde*, vol. 76, no. 1, pp. 133-148, 2016.
- [49] M. Raab, G. M. Friedman, B. Spiro, A. Starinsky, and I. Zak, "The geological history of Pliocene-Pleistocene evaporites in Mount Sedom (Israel) and how strontium and sulfur isotopes relate to their origin," *Carbonates and Evaporites*, vol. 15, no. 2, pp. 93-114, 2000.
- [50] W. B. F. Ryan, "Modeling the magnitude and timing of evaporative drawdown during the Messinian crisis," *Stratigraphy*, vol. 5, pp. 227-243, 2008.
- [51] A. E. Shimron, "Geochemical exploration and new geological data along the SE flanks of the Hermon Range," Geol Surv Isr, Jerusalem, 1989, Rep GSI/32/89.
- [52] H. Brielmann, "Recharge and discharge mechanism and dynamics in the mountainous northern upper Jordan River catchment, Israel," Ph.D. thesis LMU, Munich, Germany, 2008.
- [53] A. R. Al Charideh and B. A. Zakhem, "Distribution of tritium and stable isotopes in precipitation in Syria," *Hydrological Sciences Journal*, vol. 55, no. 5, pp. 832-843, 2010.

Research Article

Experimental Investigation on Nonlinear Flow Anisotropy Behavior in Fracture Media

Chun Zhu ^{1,2,3} Xiaoding Xu ^{1,2} Xiuting Wang^{3,4} Feng Xiong ^{3,5} Zhigang Tao ²
Yun Lin ^{3,6} and Jing Chen²

¹College of Construction Engineering, Jilin University, Changchun 130026, China

²State Key Laboratory for Geomechanics & Deep Underground Engineering Beijing, China University of Mining & Technology, Beijing 100083, China

³School of Civil, Environmental and Mining Engineering, The University of Adelaide, Adelaide, SA 5005, Australia

⁴School of Civil Engineering and Architecture, Anhui University of Science and Technology, Huainan 232000, China

⁵School of Civil Engineering, Wuhan University, Hubei 430072, China

⁶School of Resource and Safety Engineering, Central South University, Changsha, Hunan 410083, China

Correspondence should be addressed to Feng Xiong; whufengx@163.com and Zhigang Tao; zhigangtao_cumtb@126.com

Received 26 February 2019; Accepted 9 June 2019; Published 24 June 2019

Guest Editor: Frédéric Nguyen

Copyright © 2019 Chun Zhu et al. This is an open access article distributed under the Creative Commons Attribution License, which permits unrestricted use, distribution, and reproduction in any medium, provided the original work is properly cited.

A series of flow experiments were performed on matched fractures to study the problem of non-Darcy flow in fractured media. Five rock fractures of different roughness were generated using indirect tensile tests, and their surface topographies were measured using a stereo topometric scanning system. The fracture was assumed to be a self-affine surface, and its roughness and anisotropy were quantified by the fractal dimension. According to the flow tortuosity effect, the nonlinear flow was characterized by hydraulic tortuosity and surface tortuosity power law relationships based on Forchheimer's law. Fracture seepage experiments conducted with two injection directions (0° and 90°) showed that Forchheimer's law described the nonlinear flow well. Both the proposed model and Chen's double-parameter model gave similar results to the experiment, but the match was closer with the proposed model. On this basis, a new formula for the critical Reynolds number is proposed, which serves to distinguish linear flow and Forchheimer flow.

1. Introduction

A long history of geological and human activities has caused most rock masses to be cut by a large number of faults and fractures [1–5]. These discontinuities form the main channels for groundwater flow, which control the permeability characteristics of the rock mass. In the study of rock mass hydrology, discontinuities are usually generalized into two smooth parallel plates, and the famous cubic law is hence obtained through theory and experiment. A variety of correction models [6–11] has been proposed to account for fracture roughness, contact, or filling.

Some engineering projects involve a high hydraulic gradient, for example, dam construction in the deep weak overburden of a river valley, exploitation of low-permeability oil

and gas wells, and coal mine gas outbursts [12–16]. Under this condition, fluid flow through fractures is not linear, and the use of the cubic law or related modified models would cause large deviations. The well-known Forchheimer law is used to describe this flow behavior:

$$\nabla P = AQ + BQ^2, \quad (1)$$

where ∇P is the pressure gradient between the inlet and outlet of the fracture, Q is the flow rate through the fracture, and A and B are the coefficients of viscosity and inertia, respectively. Zimmerman et al. [17] observed the Forchheimer flow phenomena of rough fractures when the Reynolds number $Re > 20$ through experiments and numerical methods. Zhang and Nemcik [18] discussed the linear and nonlinear flow

characteristics of rough fractures under different confining pressures. Zhou et al. [19] explained the physical significance of the Forchheimer flow coefficients A and B and the internal transition mechanism on the basis of water pressure tests under different confining pressures. However, the effects of fracture roughness on flow were not explained in detail. Jin et al. (2013) pointed out that the influence of a rough geometry on fracture flow is manifested in three aspects: the frictional effect in the fluid, the tortuous effect of the fracture surface, and a local roughness effect. Tsang [20] considered that the roughness of the fracture surface would lead to flow tortuosity, and Xiao et al. [21] introduced a tortuosity factor to describe the tortuosity of flow. Watanabe et al. [22] carried out fluid flow experiments in fractures with shear displacements and found that the nonlinear flow effect decreases as shear increases.

Fractal geometry was first put forward by B.B. Mandelbrot. Xie and Wang [23] introduced it into the description of fracture roughness and then used it to describe fluid flow characteristics at rock fracture surfaces. Murata and Saito [24] studied the influence of fractal parameters on the tortuosity effect, and Wang et al. [25] put forward a flow model using fractal parameters. Ju et al. [26] carried out flow experiments on rough single fractures with different fractal dimensions. These flow tests clarified the influence of a rough structure on seepage flow. Develi and Babadagli [27] carried out saturated seepage tests on seven kinds of artificial tensile fracture surfaces, describing the roughness of the fractures by means of the fractal dimension and discussing the influences of roughness, anisotropy, and normal stress on seepage characteristics.

In this paper, a nonlinear fractal model for rough fractures is deduced based on the tortuous effect and the self-affine fractal characteristics of the fracture surface. The law and anisotropy of Forchheimer flow are analyzed, and the new model is verified by seepage tests.

2. Nonlinear Fractal Model for Rough-Walled Rock Fractures

Forchheimer's law is composed of a linear part AQ and a nonlinear part BQ^2 . When the flow rate is low, a cubic law can be used to describe the relationship of the flow rate and pressure. Hence, A can be expressed as

$$A = \frac{12\mu}{we_h^3}, \quad (2)$$

where μ is the dynamic coefficient of viscosity of the fluid and w is the width of the fracture. e_h is the hydraulic aperture, which can be calculated as $e_h = (12\mu Q/w/\nabla P)^{1/3}$.

The coefficient B represents the degree that the seepage curve deviates from that in the linear stage. Schrauf and Evans [28] put forward a form of B using dimensional analysis:

$$B = b_D \frac{\rho}{e_h^3 w^2}, \quad (3)$$

where ρ is the fluid density and b_D is a parameter related to the roughness of the fracture surface. Chen et al. [6] used the peak asperity height to describe fracture roughness and obtained a two-parameter model for b_D :

$$b_D = a \left(\frac{\xi}{2e_h} \right)^b, \quad (4)$$

where a and b are fitting parameters, respectively. However, the peak asperity height does not account for flow tortuosity and anisotropy. Chen et al. [6] also used numerical simulation to study non-Darcy behavior in fracture flow. The results showed that the rougher the surface was, the more tortuous the flow would be, and eddy currents and recirculation would occur at high velocity, which would increase the inertial resistance. In order to characterize the effect of flow tortuosity, the following power law relations are proposed by Murata and Saito [24] and Ji et al. (2015):

$$b_D = c\tau^a \tau_s^b, \quad (5)$$

where a , b , and c are fitting parameters. τ is the hydrological curvature, which is defined as the ratio of the actual length L_t of the seepage path to the horizontal length L_c along the pressure gradient of the fracture. τ_s is the curvature of the surface, which is defined as the ratio of the surface area to the projection area of the fracture surface.

For fractal fractures, the relationship between measure $F(\delta)$ and measurement scale δ is as follows:

$$F(\delta) = F_0 \delta^\alpha, \quad (6)$$

where α is a parameter related to the fractal dimension D and D is in the range 1-3. F_0 is the apparent measurement. Based on this, the relationship between the fracture surface area A_s and a square mesh with dimension δ_1 is as follows:

$$A_s = F_1 \delta_1^{2-D_s}, \quad (7)$$

where D_s is the fractal dimension of the fracture area. For a square fracture, when δ_1 is equal to L_c and equation (7) is substituted into $A_s(L_c) = A_c$, F_1 can be obtained as follows:

$$F_1 = A_c^{D_s/2}. \quad (8)$$

Hence, τ_s can be obtained:

$$\tau_s = \frac{A_s(\delta_1)}{A_c} = \left(\sqrt{\frac{\delta_1^2}{A_c}} \right)^{2-D_s}. \quad (9)$$

In addition, the fractal relationship of the length of the seepage path L_t and measure δ_2 is as follows:

$$L_t(\delta_2) = F_2 \delta_2^{1-D_r}, \quad (10)$$

where D_T is the fractal dimension of the seepage path. When δ_2 is equal to L_c and equation (10) is substituted into $L_t(L_c) = L_c$, F_2 can be obtained as

$$F_2 = L_c^{D_T}. \quad (11)$$

Hence, τ can be obtained:

$$\tau = \frac{L_t(\delta_2)}{L_c} = \left(\frac{\delta_2}{L_c}\right)^{1-D_T}. \quad (12)$$

Mandelbrot, the founder of fractal theory, suggested that the fractal dimension of the surface could be calculated by adding the dimension of a surface profile to 1. Therefore, the relationship between the fractal dimension of the profile length and the fractal dimension of the area is as follows:

$$D_s = D_l + 1. \quad (13)$$

Jin et al. [29] considered D_l as equal to D_T . Hence, b_D can be obtained by substituting equation (9) and equation (12) into equation (5):

$$b_D = c \left(\frac{\delta_2}{L_c}\right)^{a(1-D_l)} \left(\sqrt{\frac{\delta_1^2}{A_c}}\right)^{b(1-D_l)}. \quad (14)$$

When δ_1 and δ_2 are e_h , equation (1) becomes

$$b_D = c \left(\frac{e_h}{L_c}\right)^{(a+b)(1-D_l)}. \quad (15)$$

Hence, a new model of parameter B in Forchheimer's law can be obtained:

$$B = a \left(\frac{e_h}{L_c}\right)^{b(1-D_l)} \frac{\rho}{e_h^3 w^2}, \quad (16)$$

where a and b are constants that can be determined with fracture permeability tests. Firstly, the fractal dimension is calculated from fracture surface data. The curve relating flow to pressure gradient is then obtained through fracture permeability tests, and this is used to obtain a and b .

3. Fracture Surface Measurement

3.1. Rock Fracture Preparation. The effect of fracture surface roughness on fluid flow was studied by way of saturated seepage tests of rock fracture surfaces of different roughness. A natural fracture surface is difficult to obtain, so artificial tension fracture specimens were used to study the characteristics of fluid flow in fractures. In this study, natural granite selected from a quarry in Sichuan Province was processed into 150 mm × 150 mm × 150 mm square specimens in the laboratory, and then, the specimens were split using the Brazilian splitting test method to obtain artificial tensional

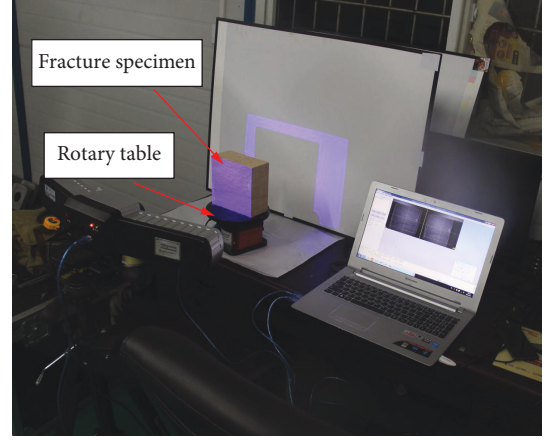


FIGURE 1: Stereo topometric scanning system.

joint specimens. Finally, five groups of fracture surfaces (F1, F2, F3, F4, and F5) with different roughness were prepared.

3.2. Measurement Procedure. A portable 3D optical three-dimensional scanning system was used to measure the three-dimensional morphology of the fracture surface (Figure 1). The system broadly comprises a scanning control unit, scanning lens, turn table, and tripod. The scanning lens is placed on the tripod, which can rotate freely and adjust its position conveniently. The other components are connected via USB. The system acquires a visible grating image projected onto the surface of the object then accurately determines the spatial coordinates (X , Y , Z) of each point using the phase and triangulation methods according to the shape of fringe curvature change, forming a three-dimensional point cloud data. This approach has the benefits of being fast, high precision (measuring accuracy 25 μm), and allowing noncontact measurement.

In the actual measurement process, features of the measurement environment (light, dust, etc.) and the measurement methods will have an impact on the accuracy of the three-dimensional topographic data. Therefore, after acquiring the three-dimensional data for a fracture surface, the point cloud data were processed by using the self-contained software CloudForm to reduce noise, remove irrelevant points, filter data ripples, and patch. Additionally, the original point cloud of the fracture surface is composed of hundreds of thousands of discrete points with an average spacing of 0.025 mm, which amount to a huge amount of disordered data. Data analysis was facilitated by compiling the program with MATLAB software to delete and reorder the measured points. The newly obtained fracture surface has a total of 22801 points at an average spacing of 1 mm. The measured topographic parameters of the fracture surfaces shown in Figure 2 are listed in Table 1.

4. Calculation of Fractal Dimension

There are many methods for calculating the fractal dimension of a rough fracture surface. Clarke [30] first proposed

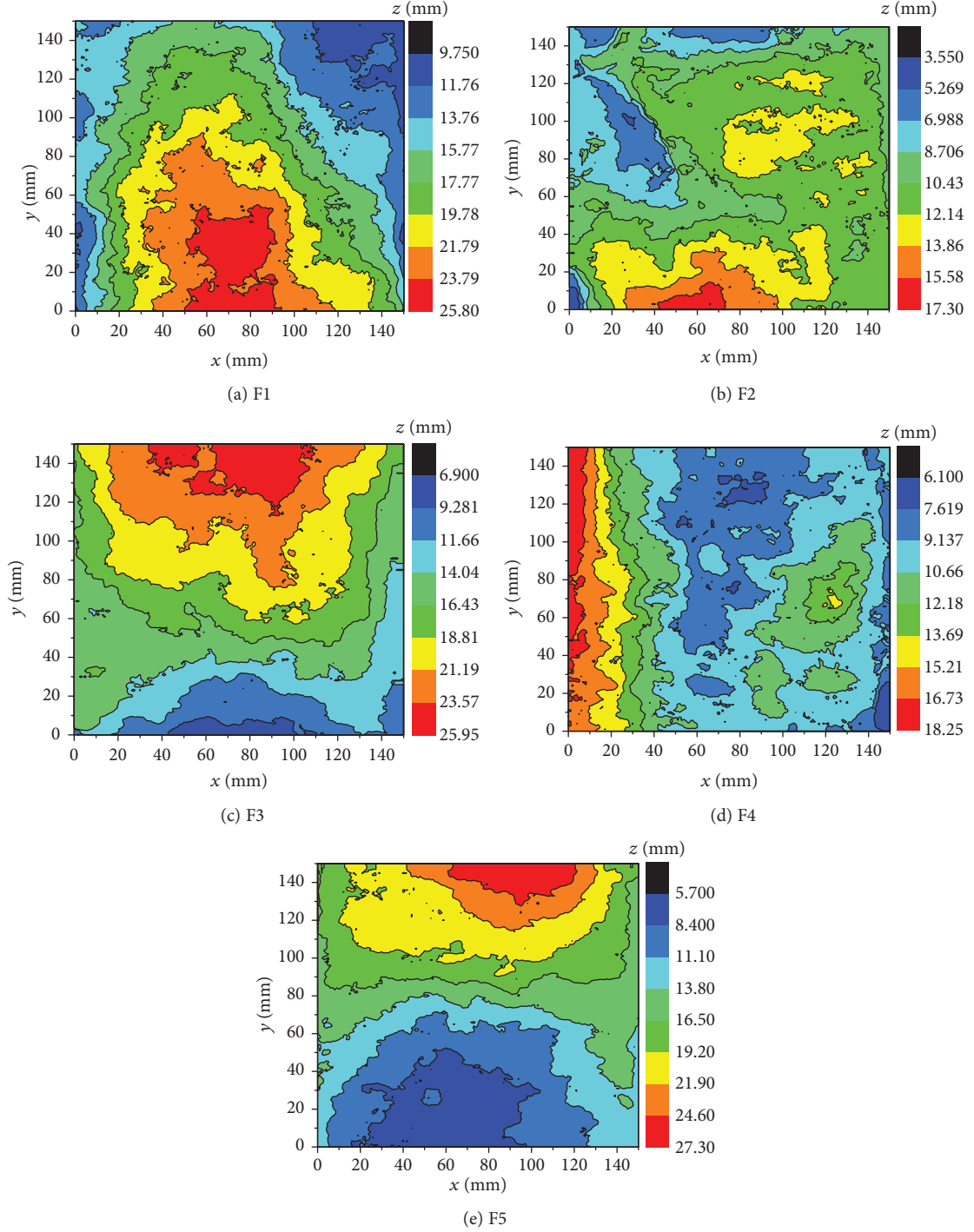


FIGURE 2: Surfaces topographies of fractures (lower surfaces).

TABLE 1: Geometrical details of fractures.

Specimen	Length L (mm)	Width w (mm)	Peak asperity height ξ (mm)	Variance R_{rms} (mm^2)	Average R_m (mm)	JRC
F1	149.9	150.1	3.74	2.06	1.58	11.3
F2	150.1	150.0	3.65	2.07	1.55	11.0
F3	150.1	150.1	3.97	4.14	3.52	12.8
F4	150.2	149.9	4.89	5.16	4.39	16.9
F5	150.1	149.9	3.27	3.87	3.29	13.9

the triangular prism surface area method, which takes the spatial surface area as the variable and a square grid as the measure scale. Later, Xie and Wang [23] proposed a projection coverage method. These two methods can be categorized as driver methods. The dimension calculated by these two methods is a similar fractal dimension, not a geometric fractal dimension. Zhou et al. [19] proposed box-counting methods for calculating the fractal dimension of a three-dimensional surface, including a cube coverage method and an improved cube coverage method. The above computational theories are based on statistical self-similarity. However, Brown [31] and Kulatilake et al. [32, 33] argue that rough rock fracture surfaces conform to the characteristics of a self-affine model.

Kulatilake et al. [32] put forward a variogram method as a self-affine model to determine the fractal dimension. This takes the variogram function $2\gamma(x, h)$ of the profile as a variable and the interval distance h as the measure scale.

The detailed method is as follows:

Step 1. Generation of two-dimensional contour data in different directions. Firstly, the fracture surface data are meshed into $1\text{ mm} \times 1\text{ mm}$ grids. 2D profiles are divided from the fracture surface data in accordance with the directions $\theta = 15 \times k$ ($k = 1, 2, \dots, 11$). The height data $Z(x, y)$ of a directional line is then calculated. The height data Z_Q of the coordinate $Q(x, y)$ is found on the 15-degree directional line P . The height of the coordinate radius within a 1 mm range is calculated according to equation (17). The profile data are then obtained cyclically. The next set of profile data with a distance of 10 mm is obtained by the same method. Finally, the profile data in each direction are obtained by repeated cyclic calculation.

$$Z(x, y) = \frac{\sum_{i=1}^n Z_i / r_i}{\sum_{i=1}^n 1 / r_i}, \quad (17)$$

where Z_i is the height of the point within a radius of 1 mm from point Q and r_i is the distance from point i to point Q .

Step 2. Calculation of the fractal dimension of all of the directional lines. The variogram function is defined as

$$2\gamma(h) = \frac{1}{N} \sum_{i=1}^N [Z_{i+1} - Z_i]^2, \quad (18)$$

where $\gamma(h)$ [L^2] is the semivariogram, Z_i [L] and Z_{i+1} [L] are the heights of the 2D profile from the baseline, and N is the number of pairs of Z at a lag distance (h) between them. $\gamma(h)$ can be simplified as a power-law function in the self-affine profile as $h \rightarrow 0$:

$$2\gamma(h) = K_v h^{2H}, \quad (19)$$

where K_v is a proportionality constant and H is the Hurst exponent, which is related to the fractal dimension by $D_v =$

$2 - H$. However, equation (18) and equation (19) cannot be used to calculate D_v directly. D_v should be written in the logarithmic form

$$\log(2\gamma(h)) = 2(2 - D_v) \log h + \log K_v, \quad (20)$$

so that D_v can be obtained by linear regression analysis. At least seven variance functions at different intervals h are calculated for each profile line, and fractal dimension D is obtained by fitting equation (20). The fractal dimension D of all of the profiles in one direction is averaged, and the fractal dimension D in that direction is obtained.

To make the anisotropic characteristics of fracture surface roughness more intuitive, Table 2 presents rose diagrams of the fractal dimensions of five different fracture surfaces (F1–F5). The fractal dimension is randomly distributed in all directions, and the fracture surfaces are characterized by an irregular anisotropic roughness structure. The fractal dimension of the fracture surface of F4 is larger than that of the others and is the highest, 1.60, in the 90° direction. Therefore, F4 has the greatest roughness of the fracture surfaces.

It is noted that the fractal dimension D does not take the difference between forward and backward on the 2D profile into consideration. For example, the fractal dimension of the 0° profile is the same as that of 180° . Hence, equation (20) is correct when assuming there is the same nonlinear flow in the θ and $\theta + 180^\circ$ directions.

5. Nonlinear Flow Behavior of Rough-Walled Rock Fractures

5.1. Seepage Tests of Rough-Walled Rock Fractures. The five groups of rock fracture surfaces (F1–F5) mentioned in the previous section were prepared for flow testing with a self-designed device. A detailed description of the device is given in Xiong et al. [7]. Two flow directions (0° and 90°) were tested for each group of fractures, as shown in Figure 3. The pressure difference P under different flow rates Q was recorded during the test process; flow rates were in the range 0–100 ml/s during the tests.

5.2. Nonlinear Flow Behavior. Figures 4 and 5 show the relationship between the flow rate Q and the pressure gradient ∇P of each fracture in the 0° and 90° directions. When the flow rate is small ($Q < 10$ ml/s), the pressure gradient increases linearly with the flow rate. When the flow rate increases, the pressure gradient increases nonlinearly, showing an increase in the inertia effect. In order to describe this relationship, the Forchheimer formula was used to fit the test data for the 0° and 90° directions. The fitting results are shown in Table 3. These results indicate that Forchheimer's law (equation (1)) is able to quantitatively describe the nonlinear flow behavior, which is consistent with Zimmerman et al. [17].

In order to analyze the anisotropic characteristics of flow in a rock fracture, a new parameter describing anisotropy is

TABLE 2: The fractal dimensions at different directions.

Directions (°)	F_1	F_2	F_3	F_4	F_5
0	1.422	1.497	1.421	1.418	1.475
30	1.398	1.486	1.391	1.426	1.426
60	1.431	1.477	1.417	1.486	1.435
90	1.542	1.503	1.434	1.600	1.436
120	1.478	1.466	1.471	1.489	1.389
150	1.425	1.459	1.370	1.424	1.407
180	1.422	1.497	1.421	1.418	1.475
210	1.398	1.486	1.391	1.426	1.426
240	1.431	1.477	1.417	1.486	1.435
270	1.542	1.503	1.434	1.600	1.436
300	1.478	1.466	1.471	1.489	1.389
330	1.425	1.459	1.370	1.424	1.407

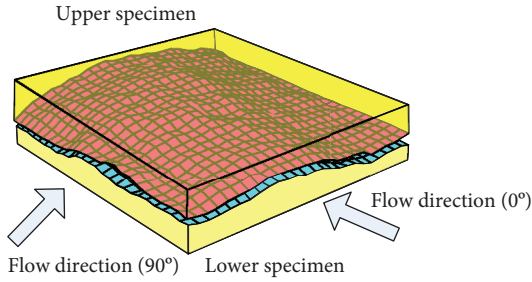


FIGURE 3: Different directions of flow (0° and 90°) in a rock fracture.

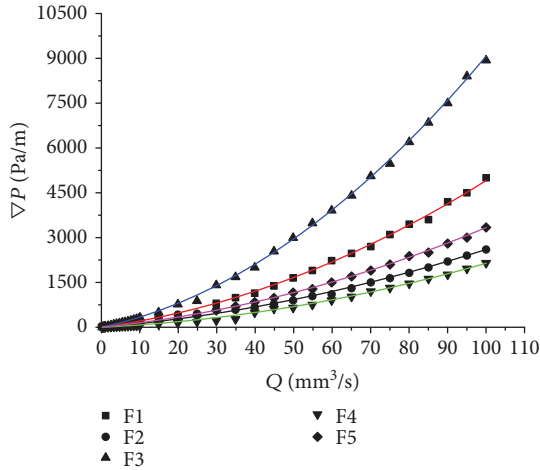


FIGURE 4: Relationship between pressure gradient and flowrate in the 0° direction.

proposed: the ratio of the difference between the 90° and 0° pressure gradients and the 90° pressure gradient.

$$\text{anisotropy} = \frac{\nabla P_{90^\circ} - \nabla P_{0^\circ}}{\nabla P_{90^\circ}}, \quad (21)$$

where ∇P_{90° is the pressure gradient in the 90° direction and ∇P_{0° is the pressure gradient in the 0° direction. Figure 6 shows the variation of anisotropy with flow rate. The anisot-

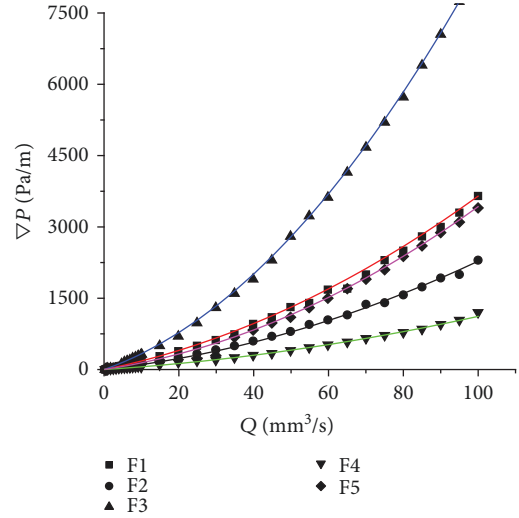


FIGURE 5: Relationship between pressure gradient and flowrate in the 90° direction.

ropy values differ between the different groups, which indicate that the anisotropy of fracture flow exists and is related to the fracture morphology and aperture distribution.

Normalized transmissivity (T_a/T_0) is determined by Zimmerman et al. [17] in the following form:

$$\frac{T_a}{T_0} = \frac{1}{1 + \beta \text{Re}}, \quad (22)$$

where T_a is the apparent transmissivity and T_0 is a special apparent transmissivity in Darcy's flow state and is typically called intrinsic transmissivity. According to experimental data, the values of β are listed in Table 2. The relationship of b_D and β is plotted in Figure 7. It can be seen from the figure that as b_D increases, β linearly increases. And β is about 12 times than b_D , which is consistent with Zimmerman et al. [17].

5.3. Verification of the Nonlinear Flow Model Based on Fractal Theory. In order to solve the undetermined constants a and b , fracture morphology data were first obtained for F1, F2, and F3, and the fractal dimension was then calculated according to the method detailed in Section 4. Then, the seepage test results were fitted according to the Levenberg-Marquardt method, and the parameters a and b were found to be 0.246 and -0.964, respectively.

In order to verify the model, the nonlinear fractal model is compared with the seepage test data and Chen's two-parameter model [6].

For fractures F4 and F5, pressure gradients were calculated according to the proposed model and the Chen model, respectively, and the results were compared with the experimental values, as shown in Figure 8. It can be seen that the results calculated with the nonlinear fractal model are close to the measured values, and the relative errors are mostly within 20%. This shows that the nonlinear fractal model gives a better description of nonlinear seepage in fractured media

TABLE 3: Fractal dimension and fitted parameters of Forchheimer’s law.

Specimen		$A \times 10^6$ (Kg·s ⁻¹ ·m ⁻⁵)	$B \times 10^{10}$ (Kg·m ⁻⁸)	e_h (mm)	Re_c	D	b_D	β
F1	0°	17.62	31.47	1.656	33.90	1.4221	0.00322	0.0027
	90°	15.97	20.50	1.711	56.18	1.542	0.0232	0.002
F2	0°	11.04	15.01	1.935	43.53	1.497	0.0245	0.0021
	90°	8.78	14.21	2.089	42.97	1.503	0.0292	0.0023
F3	0°	27.56	63.18	1.427	35.88	1.421	0.0414	0.0033
	90°	27.47	56.93	1.428	38.03	1.434	0.0374	0.003
F4	0°	6.30	15.10	2.333	28.99	1.418	0.0433	0.0035
	90°	5.09	6.09	2.504	57.82	1.600	0.0216	0.0018
F5	0°	13.07	20.08	1.829	40.84	1.475	0.0277	0.0022
	90°	18.96	2.24	1.890	34.12	1.436	0.0034	0.00026

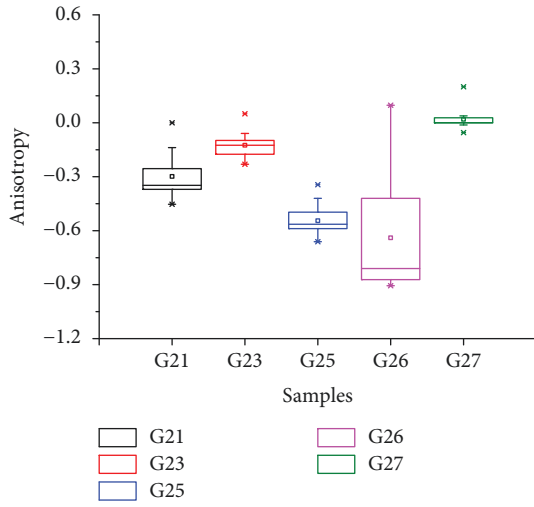


FIGURE 6: Pressure anisotropy of fracture samples F1–F5.

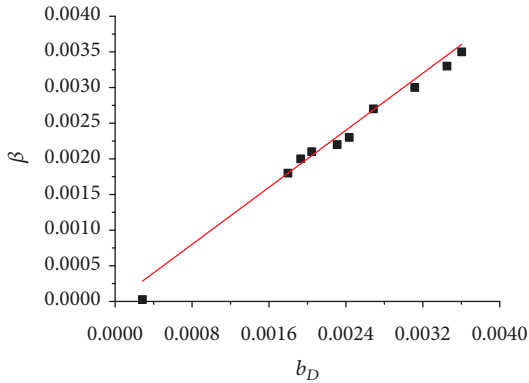


FIGURE 7: The relationships of b_D and β of fracture samples F1–F5.

than does Chen’s model. The error is larger in Chen’s model because absolute roughness is not sufficient to quantify the effect of surface topography on fracture flow.

6. Discussion

Forchheimer’s law has been widely applied for nonlinear seepage flow in fractured media, but the mechanism of the transition from linear flow to nonlinear flow needs to be further discussed.

Zimmerman et al. (2014) considered the linear to nonlinear transition process in fracture fluid flow, distinguishing the two flow regimes by the nonlinear Darcy effect factor α with a value of 0.1:

$$\alpha = \frac{BQ^2}{AQ + BQ^2}. \tag{23}$$

Therefore, many scholars have used the critical Reynolds number to describe the transition mechanism. For fractured media, the Reynolds number can be expressed as follows:

$$Re = \frac{\rho Q}{\mu w}. \tag{24}$$

By substituting equation (16) and equation (23) into equation (24), a new critical Reynolds number can be obtained:

$$Re_c = 5.42 \left(\frac{e_h}{L_c} \right)^{-0.964(D_f-1)}. \tag{25}$$

Equation (25) shows that the critical Reynolds number is closely related to hydraulic aperture, the fractal dimension of the fracture surface, and the flow direction. The smaller the hydraulic aperture and the rougher the fracture surface, the smaller the critical Reynolds number. The critical Reynolds numbers calculated by this method are shown in Table 2. Its value ranges between 30 and 60, much smaller than the 2300 value considered by Wang et al. (2015). The nonuniform distributions of the fracture aperture and the rough surface result in eddy currents and reflux flow, which make the flow tortuous and increase the inertial resistance. This leads to nonlinear flow at a low Reynolds number.

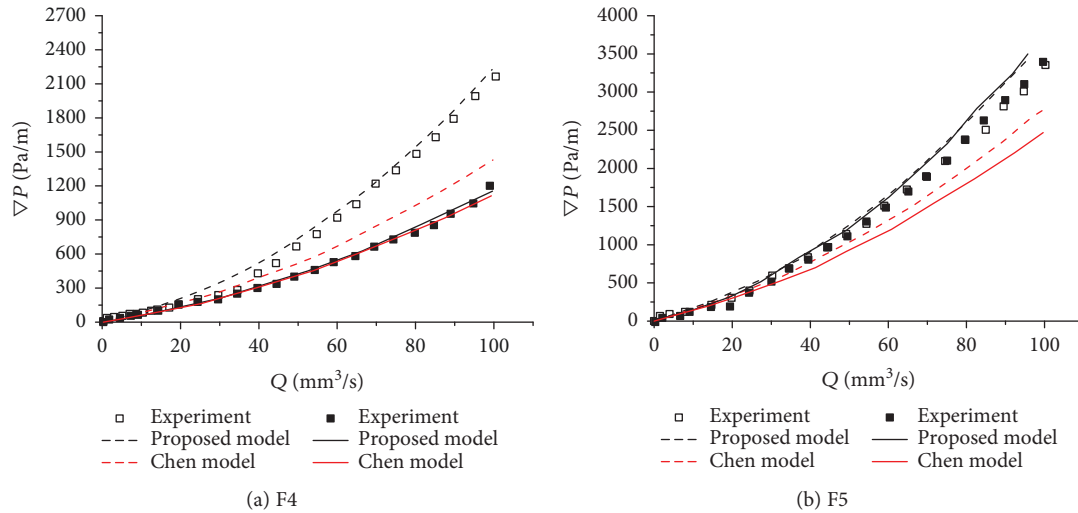


FIGURE 8: Comparison of results from equation (21), equation (22), and experimental measurements (open point is flow test along the 0° direction and solid point is flow test along the 90° direction; dashed line and solid line are proposed and the Chen model in 0° and 90° directions, respectively).

7. Conclusions

This paper discusses the effect of roughness on nonlinear flow in a rock fracture based on previous research and analysis of physical laboratory experiments. The main conclusions are as follows:

- (1) A new nonlinear seepage model for rough fractures, equation (16), is proposed according to flow tortuosity in the fracture and the fractal characteristics of the fracture
- (2) The 3D optical three-dimensional scanning system was used to acquire point cloud data from fracture surfaces. The self-affine fractal dimension calculation method proposed by Kulatilake et al. [32] was used to analyze the anisotropic characteristics of the roughness of the fracture surface
- (3) Five different kinds of rough fractures were tested in seepage experiments in the 0° and 90° directions. The results show that fracture flow conforms to Forchheimer's law and has clear isotropic characteristics. The new model generates results that are closer to those from the experiment than does Chen's two-parameter model
- (4) According to the new model, a new expression of the critical Reynolds number (equation (25)) for distinguishing Darcy flow from Forchheimer flow is proposed. It shows that the critical Reynolds number is closely related to hydraulic aperture, the roughness of the fracture surface, and the flow direction

Data Availability

The data are all available and have been explained in this article; readers can access the data supporting the conclusions of the study.

Conflicts of Interest

The authors declare that they have no conflicts of interest

Authors' Contributions

Chun Zhu and Yun Lin contributed equally to this work.

Acknowledgments

This work was supported by the Key Research and Development Project of Zhejiang Province (Grant No. 2019C03104) and the Special Funds of Fundamental Research Funds for Central Universities (2015QB02). The first author is grateful to the Chinese Scholarship Council and the University of Adelaide for providing an opportunity to conduct this research as a joint Ph.D. student.

References

- [1] W. P. Huang, C. Li, L. W. Zhang, Q. Yuan, Y. S. Zheng, and Y. Liu, "In situ identification of water-permeable fractured zone in overlying composite strata," *International Journal of Rock Mechanics and Mining Sciences*, vol. 105, pp. 85–97, 2018.
- [2] Y. Li, S. Zhang, and X. Zhang, "Classification and fractal characteristics of coal rock fragments under uniaxial cyclic loading conditions," *Arabian Journal of Geosciences*, vol. 11, no. 9, p. 201, 2018.
- [3] X. Wang and L. Tian, "Mechanical and crack evolution characteristics of coal-rock under different fracture-hole conditions: a numerical study based on particle flow code," *Environmental Earth Sciences*, vol. 77, no. 8, p. 297, 2018.
- [4] Z. Wu, H. Sun, and L. N. Y. Wong, "A cohesive element-based numerical manifold method for hydraulic fracturing modeling with voronoi grains," *Rock Mechanics and Rock Engineering*, pp. 1–25, 2019.
- [5] S. C. Zhang, Y. Y. Li, B. T. Shen, X. Sun, and L. Gao, "Effective evaluation of pressure relief drilling for reducing rock bursts

- and its application in underground coal mines,” *International Journal of Rock Mechanics and Mining Sciences*, vol. 114, pp. 7–16, 2019.
- [6] Y. F. Chen, J. Q. Zhou, S. H. Hu, R. Hu, and C. B. Zhou, “Evaluation of Forchheimer equation coefficients for non-Darcy flow in deformable rough-walled fractures,” *Journal of Hydrology*, vol. 529, pp. 993–1006, 2015.
- [7] F. Xiong, Q. Jiang, Z. Ye, and X. Zhang, “Nonlinear flow behavior through rough-walled rock fractures: the effect of contact area,” *Computers and Geotechnics*, vol. 102, pp. 179–195, 2018.
- [8] F. Xiong, Q. Jiang, C. Xu, X. Zhang, and Q. Zhang, “Influences of connectivity and conductivity on nonlinear flow behaviours through three-dimension discrete fracture networks,” *Computers and Geotechnics*, vol. 107, pp. 128–141, 2019.
- [9] C. Yao, C. He, J. Yang, Q. Jiang, J. Huang, and C. Zhou, “A novel numerical model for fluid flow in 3D fractured porous media based on an equivalent matrix-fracture network,” *Geofluids*, vol. 2019, Article ID 9736729, 13 pages, 2019.
- [10] Z. Ye, Q. Jiang, C. Yao et al., “The parabolic variational inequalities for variably saturated water flow in heterogeneous fracture networks,” *Geofluids*, vol. 2018, Article ID 9062569, 16 pages, 2018.
- [11] R. W. Zimmerman and G. S. Bodvarsson, “Hydraulic conductivity of rock fractures,” *Transport in Porous Media*, vol. 23, no. 1, pp. 1–30, 1996.
- [12] S. Gentier, D. Hopkins, and J. Riss, “Role of fracture geometry in the evolution of flow paths under stress,” in *Dynamics of Fluids in the Fractured Rock*, pp. 169–184, American Geophysical Union, 2000.
- [13] T. Ishibashi, N. Watanabe, N. Hirano, A. Okamoto, and N. Tsuchiya, “Beyond-laboratory-scale prediction for channeling flows through subsurface rock fractures with heterogeneous aperture distributions revealed by laboratory evaluation,” *Journal of Geophysical Research: Solid earth*, vol. 120, no. 1, pp. 106–124, 2014.
- [14] Q. Jiang and C. Zhou, “A rigorous solution for the stability of polyhedral rock blocks,” *Computers and Geotechnics*, vol. 90, pp. 190–201, 2017.
- [15] T. Zhigang, Z. Chun, W. Yong, W. Jiamin, H. Manchao, and Z. Bo, “Research on stability of an open-pit mine dump with fiber optic monitoring,” *Geofluids*, vol. 2018, Article ID 9631706, 20 pages, 2018.
- [16] P. A. Witherspoon, “Investigation at Berkeley on fracture flow in rocks: from the parallel plate model to chaotic systems,” in *Dynamics of Fluid in Fractured Rocks*, B. Faybishenko, S. Benson, and P. Witherspoon, Eds., pp. 1–58, American Geophysical Union, Washington, DC, USA, 2000.
- [17] R. W. Zimmerman, A. al-Yaarubi, C. C. Pain, and C. A. Grattoni, “Nonlinear regimes of fluid flow in rock fractures,” *International Journal of Rock Mechanics and Mining Sciences*, vol. 41, no. 3, pp. 163–169, 2004.
- [18] Z. Zhang and J. Nemcik, “Fluid flow regimes and nonlinear flow characteristics in deformable rock fractures,” *Journal of Hydrology*, vol. 477, no. 1, pp. 139–151, 2013.
- [19] J.-Q. Zhou, S.-H. Hu, S. Fang, Y.-F. Chen, and C.-B. Zhou, “Nonlinear flow behavior at low Reynolds numbers through rough-walled fractures subjected to normal compressive loading,” *International Journal of Rock Mechanics and Mining Sciences*, vol. 80, pp. 202–218, 2015.
- [20] Y. W. Tsang, “The effect of tortuosity on fluid flow through a single fracture,” *Water Resources Research*, vol. 20, no. 9, pp. 1209–1215, 1984.
- [21] W. Xiao, C. Xia, W. Wang, and Y. Bian, “Study on calculation of fluid flow through a single rough joint by considering flow tortuosity effect,” *Chinese Journal of Rock Mechanics and Engineering*, vol. 30, no. 9, pp. 2416–2425, 2011.
- [22] N. Watanabe, N. Hirano, and N. Tsuchiya, “Diversity of channeling flow in heterogeneous aperture distribution inferred from integrated experimental-numerical analysis on flow through shear fracture in granite,” *Journal of Geophysical Research*, vol. 114, pp. 115–123, 2009.
- [23] H. Xie and J. Wang, “Direct fractal measurement of fracture surfaces,” *International Journal of Solids and Structures*, vol. 36, no. 20, pp. 3073–3084, 1999.
- [24] S. Murata and T. Saito, “Estimation of tortuosity of fluid flow through a single fracture,” *Journal of Canadian Petroleum Technology*, vol. 42, no. 12, pp. 39–45, 2003.
- [25] G. Wang, N. Huang, Y. Jiang, B. Li, W. Xuezheng, and X. Zhang, “Seepage calculation model for rough joint surface considering fracture characteristics,” *Chinese Journal of Rock Mechanics and Engineering*, vol. 33, pp. 3397–3405, 2014.
- [26] Y. Ju, Q. G. Zhang, Y. M. Yang, H. P. Xie, F. Gao, and H. J. Wang, “An experimental investigation on the mechanism of fluid flow through single rough fracture of rock,” *Science China Technological Sciences*, vol. 56, no. 8, pp. 2070–2080, 2013.
- [27] K. Develi and T. Babadagli, “Experimental and visual analysis of single-phase flow through rough fracture replicas,” *International Journal of Rock Mechanics and Mining Sciences*, vol. 73, pp. 139–155, 2015.
- [28] T. W. Schrauf and D. D. Evans, “Laboratory studies of gas flow through a single natural fracture,” *Water Resources Research*, vol. 22, no. 7, pp. 1038–1050, 1986.
- [29] Y. Jin, J. L. Zheng, J. B. Dong, C. H. Huang, X. Li, and Y. Wu, “Fractal seepage law characterizing fluid flow through a single rough cleat composed of self-affine surfaces,” *Chinese Science Bulletin*, vol. 60, no. 21, pp. 2036–2047, 2015.
- [30] K. C. Clarke, “Computation of the fractal dimension of topographic surfaces using the triangular prism surface area method,” *Computers and Geosciences*, vol. 12, no. 5, pp. 713–722, 1986.
- [31] S. R. Brown, “Fluid flow through rock joints: the effect of surface roughness,” *Journal of Geophysical Research: Solid Earth*, vol. 92, no. B2, pp. 1337–1347, 1987.
- [32] P. H. S. W. Kulatilake, P. Balasingam, J. Park, and R. Morgan, “Natural rock joint roughness quantification through fractal techniques,” *Geotechnical and Geological Engineering*, vol. 24, no. 5, pp. 1181–1202, 2006.
- [33] P. H. S. W. Kulatilake, J. Park, P. Balasingam, and R. Morgan, “Quantification of aperture and relations between aperture, normal stress and fluid flow for natural single rock fractures,” *Geotechnical and Geological Engineering*, vol. 26, no. 3, pp. 269–281, 2008.

Research Article

Evolution Model of Seepage Characteristics in the Process of Water Inrush in Faults

Jianli Shao ^{1,2}, Fei Zhou ^{1,2} and Wenbin Sun ^{1,2}

¹State Key Laboratory of Mining Disaster Prevention and Control, Shandong University of Science and Technology, Shandong 266590, China

²College of Mining and Safety Engineering, Shandong University of Science and Technology, Shandong 266590, China

Correspondence should be addressed to Wenbin Sun; swb@sdust.edu.cn

Received 23 January 2019; Revised 3 April 2019; Accepted 8 April 2019; Published 8 May 2019

Guest Editor: Tanguy Robert

Copyright © 2019 Jianli Shao et al. This is an open access article distributed under the Creative Commons Attribution License, which permits unrestricted use, distribution, and reproduction in any medium, provided the original work is properly cited.

Although the mechanism and influence of fault water inrush have been widely studied, there are still few studies on the migration of filling particles and the evolution process of seepage characteristics within faults. In this work, the coupling effects of water flow, particle migration, and permeability evolution are considered synthetically, and the evolution model of seepage characteristics with multifield coupling is established. This model was used to investigate the evolution process of water inrush within faults and the effects of water pressure, initial effective porosity, and initial permeability on water flow rate. The results show that the evolution of seepage characteristics can be divided into three phases: (i) low velocity seepage, (ii) drastic changes with substantial particle migration, and (iii) steady-state water flow. The multifield coupling causes the effective porosity, permeability, flow velocity, and particle concentration to accelerate each other during the dramatic phase. Moreover, the increases in initial water pressure, initial porosity, and initial permeability have different degrees of promotion on the water flow rate. Finally, the simulation results are approximately the same as the data of water inrush in the mining area, which verifies the correctness of the evolution model established in this work. This work provides new approaches to the evolution process and prevention of water inrush in faults.

1. Introduction

Affected by complex geological and hydrological conditions, water inrush disaster has been a serious challenge in underground engineering such as coal mines in China [1–3]. The existence of the geological structure usually functions as an underground water flow path, thus posing a great threat to the mining production safety [4, 5]. Fault structure is the main factor leading to water inrush in the mine pits. According to statistics, 80% of water inrush accidents are related to faults [6]. For instance, the 9101 working face in the Yangzhuang coal mine of the Feicheng Mining Bureau was between two walking faults, and the fault structures communicated the mining floor with the Xujiazhuang limestone aquifer and Ordovician limestone aquifer, which led to the occurrence of water inrush in the working face two times. Among them, the water pressure of the second water inrush reached 8.5 MPa, with a water flow rate of nearly 600 m³/h. And the

water flow rate sharply increased to 4409 m³/h after 16 hours, which has greatly exceeded the drainage capacity. After 19 hours, the depth of water in the shaft station reached 0.7 m. Finally, the mine was all submerged due to the lack of disaster resistance [7]. Thus, fault structure, as an important water inrush channel, is of great significance to the prevention and control of fault water inrush hazards in coal mines.

Aiming at the mechanism of water inrush caused by geological structures such as faults, the scholars have conducted a large number of experimental investigations. Through laboratory tests, Wu et al. [8] systematically analyzed the deformation and destruction patterns of fault materials under different moisture content, confining pressure, and loading modes. It was pointed out that the intensity of fault materials will be enhanced with the increase in confining pressure, but reduced with the increase in moisture content, and the deformation and destruction characteristics of the fault materials have a close

relation with its materials and loading time. Li et al. [9, 10] developed a large-scale testing system for the measurement of coupled seepage and triaxial stress. The seepage failure model of the filling medium was further revealed. The catastrophe evolution mechanism of water inrush for the filling fault had been researched, and the variation characteristics of fault occurrence, filling ability, and water conductivity have been analyzed. Zhang et al. [11] simulated physically the entire process of crack formation, concealed fault propagation, and evolution of a water inrush channel with high-pressure water directly beneath the mine floor, and the results indicate that water channels are mainly caused by the connection between tectonic rock zones and coal floor cracks, which are the direct cause for water inrush. Miao et al. [12, 13] carried out a series of tests on the permeability characteristics of the fractured rock mass and obtained the variation rules of the permeability of the fractured rock mass under different lithology and stress states. Ma et al. [14–17] carried out a series of seepage experiments on granular rock. The effects of the original particle size distribution (PSD) on the hydraulic properties were investigated, and the evolution of porosity and permeability was calculated and verified in detail.

Many scholars also investigated the theoretical analysis and prediction of fault water inrush. Using digital image processing technology, Zhao et al. [18] developed MATLAB function for threshold segmentation of the section image of broken rock mass and established a three-dimensional digital analysis model. Based on these models, interconnected networks of spatial structures and spatial distribution features of stress, seepage, and speed are identified for cataclastic rock masses. Liu et al. [19] established a coupled thermal-nonlinear-hydraulic-mechanical (THM) model for fault water inrush to study the water-rock-temperature interactions and predict the fault water inrush. Yao et al. [20] presented an inverse velocity theory to predict the water inrush time under different geological and flow conditions. The results showed that the inverse velocity theory was capable of predicting the occurrences of water inrush under different conditions, and the time of water inrush had a power relationship with the rock heterogeneity, water pressure, and initial particle concentration. Song et al. [21] analyzed strata's movement and ground pressure caused by mining's influence on karst water pressure and fault pillar. It was pointed that karst water pressure's increase has an important relationship with overburden strata's movement caused by mining. Especially for the closed karst cave, water pressure will leap under the effect of abutment pressure. In order to investigate the activation failure characteristics of the mining floor fault above a confined aquifer and predict the water inrush from the activated floor fault, Sun and Wang [22] and Jian et al. [23] used microseismic monitoring technique to monitor the mining floor fault.

The above results are of great significance to reveal the mechanism and prediction of fault water inrush. However, the seepage characteristics of faults are the determinants to control the water conductivity of faults and the degree of damage. Permeability is a direct reflection of the water

conductivity of faults. In the process of seepage, the filling particles are constantly migrated and lost due to the erosion of water flow, resulting in changes in porosity and permeability as well as particle concentration. However, the changes in overall permeability will react on the seepage field. It is a process of mutual influence and promotion. Therefore, the coupling effect will be an important reason to reveal the process of fault water inrush. The above correlation analysis rarely involves the influence of the coupling effect between particle migration and seepage characteristics, and the evolutionary process of the interaction has not been systematically studied.

In this work, the author comprehensively considered the coupling effect of water seepage and particle migration in the process of fault seepage and established a multifield coupling model for the evolution of the seepage characteristics. Combined with the geological conditions in the mining area, the governing equations will then be implemented into COMSOL Multiphysics software. The heterogeneity of rocks in faults will be determined using the Weibull distribution, and the evolutionary feature of seepage characteristics, including effective porosity, permeability, particle concentration, and seepage velocity, will be obtained accordingly. The process of seepage characteristics interaction will be analyzed, and the variation of flow rate under different natural conditions will be discussed in detail. The evolution process of the seepage characteristics will be simulated and investigated, and the mechanism of water inrush from the perspective of multiple coupled system movement will be revealed.

2. An Evolution Model of Seepage Characteristics

2.1. Hydrogeological Structural Features of Faults. The hydrogeological structure of the fault is shown in Figure 1, which can be regarded as composed of broken solid medium (skeleton and filling material), liquid medium (fluid) in the pores and fractures, and fine filling particles in the liquid medium. The surrounding rock is relatively hard, and the bottom is confined aquifer. When mining reveals broken geological structures such as water-carrying faults, seepage erodes the filling particles in the framework of broken rock mass and causes migration as well as changes in the permeability characteristics of faults, which may lead to water inrush hazards.

2.2. Governing Equations

2.2.1. Assumptions. In order to establish the evolution model of seepage characteristics and investigate the mechanism of fault water inrush in coal mines, the following assumptions referring Yao et al. [20] have been made:

- (1) The fluid and particles in faults are incompressible
- (2) The suspended particles share the velocity field with the fluid
- (3) The effect of erosion on the permeability change is in proportion to the change of particle concentration in the fluid
- (4) Fault fillings can be regarded as porous materials

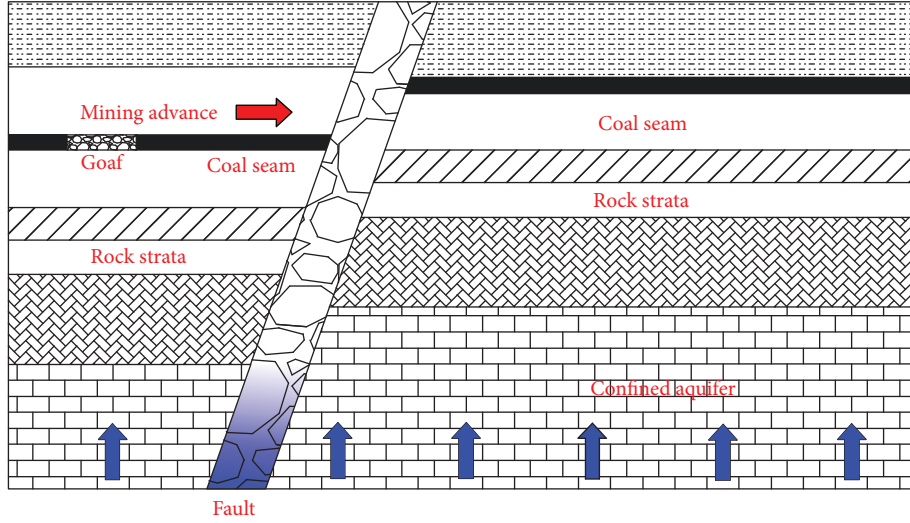


FIGURE 1: Diagram of a fault: different shapes of rock strata represent different types of rocks.

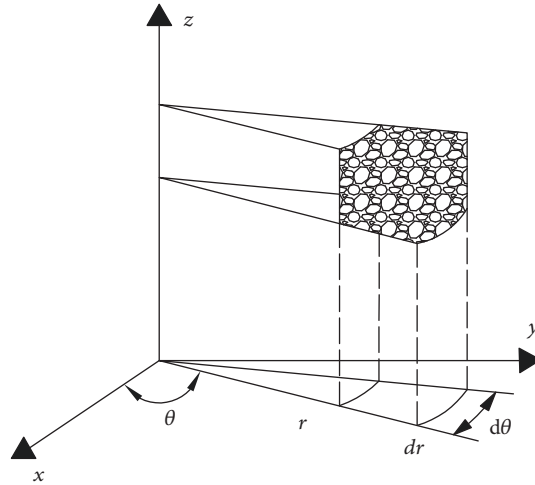


FIGURE 2: The representative element for faults in a cylindrical coordinate.

2.2.2. *Mass Conservation Equations.* A representative element for a typical fault-filling microstructure is shown in Figure 2. Suppose that the coordinate of the element is $P(r, \theta, z)$, then its volume V (m^3) can be expressed as follows:

$$V = drd\theta dz. \tag{1}$$

According to the above analysis, the element is composed of three kinds of media: (1) solid medium with a volume of V_s (m^3), (2) fluid medium with a volume of V_f (m^3), and (3) particles suspended in the fluid with a density of ρ_s (kg/m^3), a volume of V_{fs} (m^3), and a mass of M_{fs} (kg), where the subscripts “s, f, and fs” represent solid medium, fluid medium, and particles in the fluid, respectively. Then, the pore volume V_v (m^3) and porosity φ (%) of the element can be expressed as follows [24]:

$$\begin{aligned} V_v &= V_f + V_{fs}, \\ \varphi &= \frac{V_f + V_{fs}}{V}. \end{aligned} \tag{2}$$

The volume concentration C (%) and mass concentration ρ_{fs} (kg/m^3) of the suspended particles can be expressed as follows:

$$C = \frac{V_{fs}}{V_v}, \tag{3}$$

$$\rho_{fs} = \frac{M_{fs}}{V_v} = C\rho_s. \tag{4}$$

The migration of particles in volumetric elements can be regarded as the result of the combined action of advection-diffusion. As particles with extremely small size

migrate in high-speed flow fields, the tiny diffusion effect can be neglected. Along the z -axis, the average velocity of particles can be defined as q_{pz} (m/s), and the particle mass in the inflow of the element caused by advection in the z -direction per unit time can be expressed as follows:

$$\frac{\partial(\rho_{fs}q_{pz})}{\partial z} r dr d\theta dz. \quad (5)$$

The particle mass in the r direction per unit time can be expressed as follows:

$$\frac{\partial(\rho_{fs}\rho_{pr})}{\partial r} r dr d\theta dz + \rho_{fs}q_{pr} dr d\theta dz. \quad (6)$$

For the unit element, the total particle mass per unit time can be summarized as follows:

$$\left[\frac{\partial(\rho_{fs}q_{pr})}{\partial r} + \frac{\rho_{fs}q_{pr}}{r} + \frac{\partial(\rho_{fs}q_{pz})}{\partial z} \right] r dr d\theta dz. \quad (7)$$

The decrease in element mass per unit time can be expressed as follows:

$$-\frac{\partial}{\partial t}(\varphi\rho_{fs}r dr d\theta dz) + \dot{m}r dr d\theta dz, \quad (8)$$

where \dot{m} (kg/m³/s) is the particle mass that migrates into the fluid from a unit element in a unit time, and \dot{m} is written as follows:

$$\dot{m} = \frac{\partial\varphi}{\partial t}\rho_s. \quad (9)$$

According to the mass conservation law, by combining equations (7) and (8), it can be summarized as follows:

$$\begin{aligned} & -\frac{\partial}{\partial t}(\varphi\rho_{fs}r dr d\theta dz) + \dot{m}r dr d\theta dz \\ & = \left[\frac{\partial(\rho_{fs}q_{pr})}{\partial r} + \frac{\rho_{fs}q_{pr}}{r} + \frac{\partial(\rho_{fs}q_{pz})}{\partial z} \right] r dr d\theta dz. \end{aligned} \quad (10)$$

Assuming that the solid particles are incompressible, and the volume of the element body does not change with time, combining with equations (3) and (4), equation (10) can be summarized as follows:

$$\frac{\partial(C\varphi)}{\partial t} + \frac{\partial}{\partial r}(Cq_{pr}) + \frac{1}{r}(Cq_{pr}) + \frac{\partial}{\partial z}(Cq_{pr}) = \frac{\dot{m}}{\rho_s}. \quad (11)$$

Equation (11) can be expressed as a vector expression as follows:

$$\frac{\partial(C\varphi)}{\partial t} + \nabla \cdot (Cq \rightarrow_p) = \frac{\dot{m}}{\rho_s}, \quad (12)$$

where $\nabla = (\partial/\partial r) + (1/r) + (\partial/\partial z)$.

Substituting equation (9) into equation (12) yields

$$\frac{\partial(C\varphi)}{\partial t} + \nabla \cdot (Cq \rightarrow_p) = \frac{\partial\varphi}{\partial t}. \quad (13)$$

Similarly, the mass conservation equation of the fluid can be obtained as follows:

$$\frac{\partial}{\partial t}[\varphi(1-C)] + \nabla \cdot [(1-C)q \rightarrow] = 0. \quad (14)$$

2.2.3. Water Seepage. Darcy's law describes linear seepage in porous media, and it is derived from balance of momentum for the fluid phase and from a constitutive equation for the fluid-solid interaction force (i.e., the seepage force) [25]. In general, the transient form of Darcy's law can be expressed as follows:

$$\frac{\partial}{\partial t}(\varphi\rho) + \nabla \cdot (\rho q \rightarrow) = Q_m, \quad (15)$$

where ρ (kg/m³) is the density of the fluid, and Q_m (kg/(m³·s)) illustrates the mass sources of the element. The equation for Darcy velocity can be expressed as follows [24]:

$$q \rightarrow = -\frac{k}{\eta}(\nabla p + \rho g \nabla z), \quad (16)$$

where $q \rightarrow$ (m/s) is the Darcy velocity, k (m²) denotes the permeability of the element, η (Pa·s) is the dynamic viscosity of the fluid, p (Pa) denotes the water pressure, and ∇z is the unit vector in the direction of gravity.

2.2.4. Porosity Evolution Equation. Porosity, as an important component of seepage characteristics, affects the evolution of seepage channels and permeability. Sakthivadivel and Irmay [26] investigated the erosion effect for porous media by using both experimental and theoretical methods. Vardoulakis et al. [27] summarized the following: the evolution of permeability was affected by the porosity and particle concentration as well as the seepage velocity. The porosity evolution equation of porous media is given by considering particle migration as follows [27]:

$$\frac{\partial\varphi}{\partial t} = \lambda\rho_s(\varphi_{\max} - \varphi)C|q|, \quad (17)$$

where λ (m⁻¹) denotes the erosion coefficient, φ_{\max} (%) illustrates the maximum value that porosity can reach under fluid erosion, and $|q| = \sqrt{q_x^2 + q_y^2 + q_z^2}$ is the absolute value of the seepage velocity (m/s). q_i represents the velocity component in the direction of i ($i = x, y, z$).

2.2.5. Auxiliary Equation. The velocity of the particles can be expressed as the difference between the velocity of the fluid

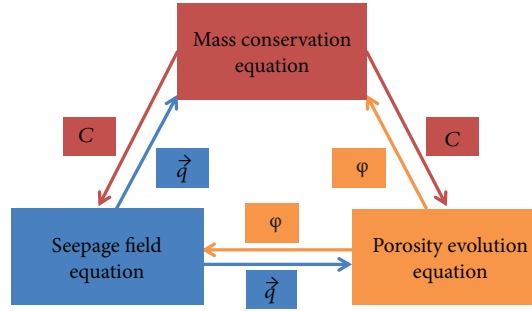


FIGURE 3: The coupling diagram of each equation.

and the velocity of the free subsidence in the static fluid as follows [24]:

$$q_{pr} = \frac{k(\varphi)}{\eta} \frac{\partial p}{\partial r}, \quad (18)$$

$$q_{pz} = \frac{k(\varphi)}{\eta} \left(\frac{\partial p}{\partial z} + \rho g \right) - \varphi \sqrt{\frac{4d_p(\rho_s - \rho)g}{3C_D\rho}}, \quad (19)$$

where d_p (m) denotes the diameter of particles and C_D is the dimensionless drag coefficient, which can be expressed as follows [28]:

$$C_D = \frac{24}{Re} + 0.5, \quad (20)$$

where Re is the Reynolds number of particles, which can be expressed as follows:

$$Re = \frac{d_p |q| \rho}{\eta}. \quad (21)$$

The change of permeability in porous media can be deduced according to the change of porosity, which can be expressed as follows [28]:

$$k = k_0 \left(\frac{\varphi}{\varphi_0} \right)^3 \left(\frac{1 - \varphi_0}{1 - \varphi} \right)^2, \quad (22)$$

where k_0 (m^2) denotes the initial permeability, and φ_0 (%) illustrates the initial porosity.

Equations (13), (14), (16), (17), and (18) together with (22) compose the coupled processes of water transport under erosion effects, as illustrated in Figure 3. To investigate the mechanism of water inrush in faults, the above governing equations will be implemented in COMSOL Multiphysics to further assess the risk of water inrush and predict the time of water inrush under different flow conditions. There are six unknowns with equations, so the set of governing equations can provide a unique solution.

3. Numerical Model Implementation

3.1. Background of the Coal Mine. In this section, a case study was conducted based on the hydrogeological conditions of a

coal mine, which is affiliated with the Jining Mining Industry Group in China. The mining operation is current extracting number 3# coal seam at approximately 900 m depth. To date, a group of faults, most of which are normal faults, were found to cross the working face obliquely. The average thickness of the fault group is 80 m, and the average dip angle is about 60°. The working face and fault group position of this mine are shown in Figure 4. The working face passes through the fault group smoothly in the mining process, and the water flow rate was about 35 m^3/h . However, when the working face was advanced to 560 m, the flow rate increased rapidly from 120 m^3/h . By the time the working face advanced 640 m, the flow rate had increased to 380 m^3/h , and the peak flow rate had reached 432 m^3/h . This process shows obvious lag characteristics, which was considered as a typical coal mine fault water inrush.

3.2. Material Properties of Fault Fillings. Groundwater seepage has a great influence on the mechanical properties of fault zone filling, and it is the key factor that induces rock infiltration and water inrush in the fault zone. In order to obtain the lithological parameters of fault fillings, the conventional mechanical tests were carried out. The test samples were taken from the fault of the working face, collected immediately after underground exposure, and sealed on site and transported to the laboratory. The lithological parameters obtained are shown in Table 1.

In addition, the permeability parameters of the fault filling samples were determined. In this work, the hydraulic conductivity of the specimen is determined by means of a variable head test. The schematic and object of the measuring device are shown in Figure 5. The calculation principle of this measuring device can be expressed as follows [29, 30]:

$$K = \frac{aL}{At} \ln \frac{\Delta h_1}{\Delta h_2}, \quad (23)$$

where K ($cm \cdot s^{-1}$) denotes the hydraulic conductivity, a (cm^2) is the sectional area of the head tube, A (cm^2) illustrates the sectional area of the specimen, t (s) is the measuring period, and Δh_1 and Δh_2 represent the initial and final head differences, respectively.

The seepage properties obtained are shown in Table 2. The relation between hydraulic conductivity (K) and

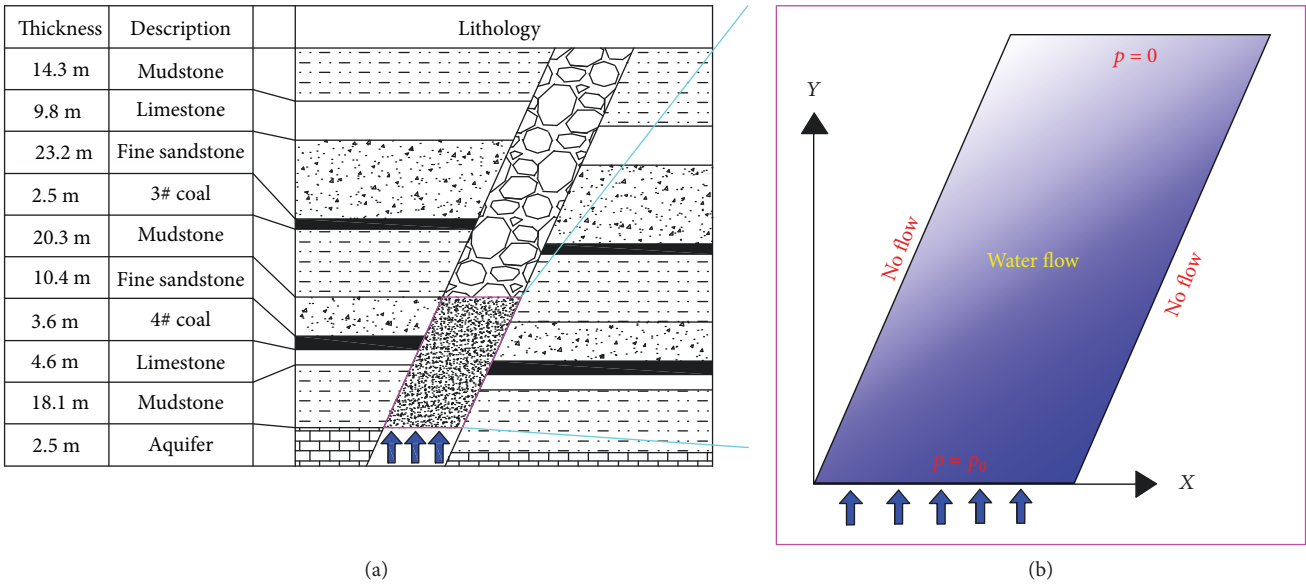


FIGURE 4: Model geometry and setup: (a) illustration of fault and rock strata and (b) 2D simulation model.

TABLE 1: Lithological parameters of the fault fillings.

Test number	Water content (%)	Density (g·cm ⁻³)	Failure stress (MPa)	Deformation modulus (MPa)	Cohesion (MPa)	Internal friction angle (°)
1	3.55	2.33	1.61	206.2	0.37	17.2
2	3.59	2.39	2.09	231.9	0.36	17.5
3	3.64	2.37	3.15	292.6	0.39	16.8
4	3.92	2.35	3.03	346.3	0.36	17.2

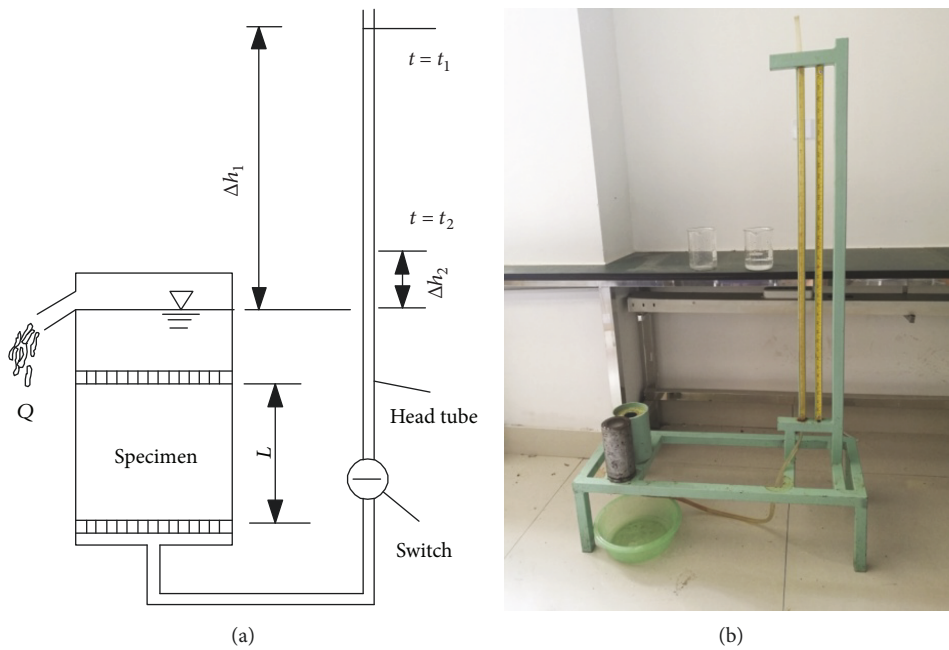


FIGURE 5: Diagram of the measuring device: (a) schematic and (b) object.

TABLE 2: Seepage properties of the fault fillings.

Test number	Hydraulic conductivity ($\text{cm}\cdot\text{s}^{-1}$)	Effective porosity (%)
5	1.62×10^{-4}	15.32
6	8.35×10^{-5}	9.18
7	6.13×10^{-5}	8.79
8	2.56×10^{-4}	18.41
9	9.17×10^{-5}	11.33
10	1.19×10^{-4}	12.56

permeability (k) can be expressed as follows:

$$K = \frac{k\rho g}{\eta}. \quad (24)$$

Digital image technology provides a method for obtaining rock parameters with heterogeneous distribution [18, 31]. The effective porosity of the specimens is determined by digital image processing technology. In particular, the relationship between the pore pixel and the total image pixel is obtained through the threshold value on the slice images of the specimens, and the image processing for specimens is shown in Figure 6. The effective porosity obtained is shown in Table 2.

3.3. Numerical Model Setup. In this paper, the evolution of the seepage characteristics and the water inrush from the bottom to the top are mainly investigated, so the model is simplified into a 2D fault section (i.e., a parallelogram). According to the lithology of the mine, the bottom length and the height are 18 m and 50 m, respectively (as shown in Figure 4). The inlet water pressure p at the bottom of the model was 2.0 MPa, and the outlet pressure at the top of the model was 0.1 MPa; the initial water pressure in the model was 0.1 MPa, the initial particle volume concentration C_0 was 0.01, and the initial effective porosity φ_0 was 10%. Other used parameters are listed in Table 3.

Heterogeneity is a natural feature of rock. There are currently various approaches to obtaining the characteristics of the heterogeneous distribution of rock materials. For example, digital core techniques and mathematical statistics methods have both been utilized. Previous studies have shown that the heterogeneity of rock can be described by the Weibull distribution [31–34]. Thus, the Weibull distribution was selected in this study due to its effectiveness and great simplicity to obtain the heterogeneous distribution of effective porosity in the fault. The distribution probability density equation was as follows:

$$f(\varphi) = \frac{m}{\varphi_0} \left(\frac{\varphi}{\varphi_0}\right)^{m-1} \exp \left[-\left(\frac{\varphi}{\varphi_0}\right)^m \right], \quad (25)$$

where φ indicates the effective porosity, φ_0 denotes the initial effective porosity, and m is the uniformity index. The larger m represents, the higher the level of uniformity. The

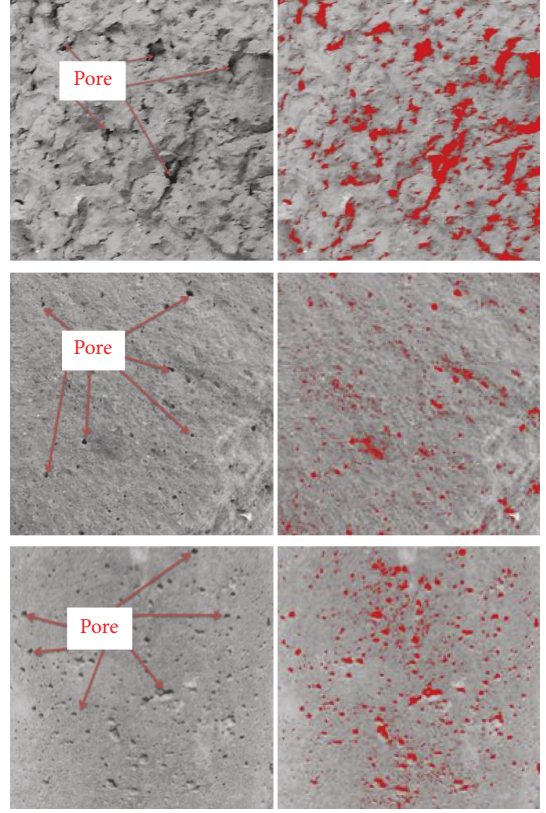


FIGURE 6: Illustration of image processing for specimens.

TABLE 3: Input parameters for the numerical simulation.

$\rho_s/(\text{kg}/\text{m}^3)$	$\eta/(\text{Pa}\cdot\text{s})$	$d_p/(\mu\text{m})$	$k_0/(\text{m}^2)$	C_0	$\lambda/(\text{m}^{-1})$	m
2000	10^{-3}	10	10^{-12}	0.01	0.01	2

initial effective porosity distribution obtained by the numerical generation method is shown in Figure 7.

4. Results and Discussion

In order to analyze the characteristics of seepage at different times, in this study, four different times were selected (i.e., 2, 4, 6, and 8 h). The specific results will be discussed below.

4.1. The Evolution of Seepage Characteristics. Figure 8 illustrates the evolution of effective porosity at different times. Figure 9 illustrates the evolution of permeability at different times. Figure 10 shows the flow velocity at different times at the outlet boundary along the x -axis as marked in Figure 4(b), and the average porosity-time curve and average particle concentration-time curve are plotted in Figure 11. The specific results will be discussed below.

4.1.1. Distribution of the Effective Porosity and Permeability. From equation (22), effective porosity and permeability show a similar evolution process in Figures 8 and 9. At the initial phase, effective porosity and permeability are subject to random distribution with minor difference. As the infiltration continues, the average effective porosity increases by

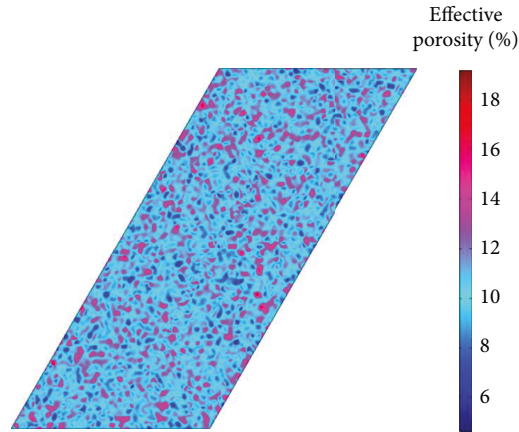


FIGURE 7: Weibull distribution for initial effective porosity.

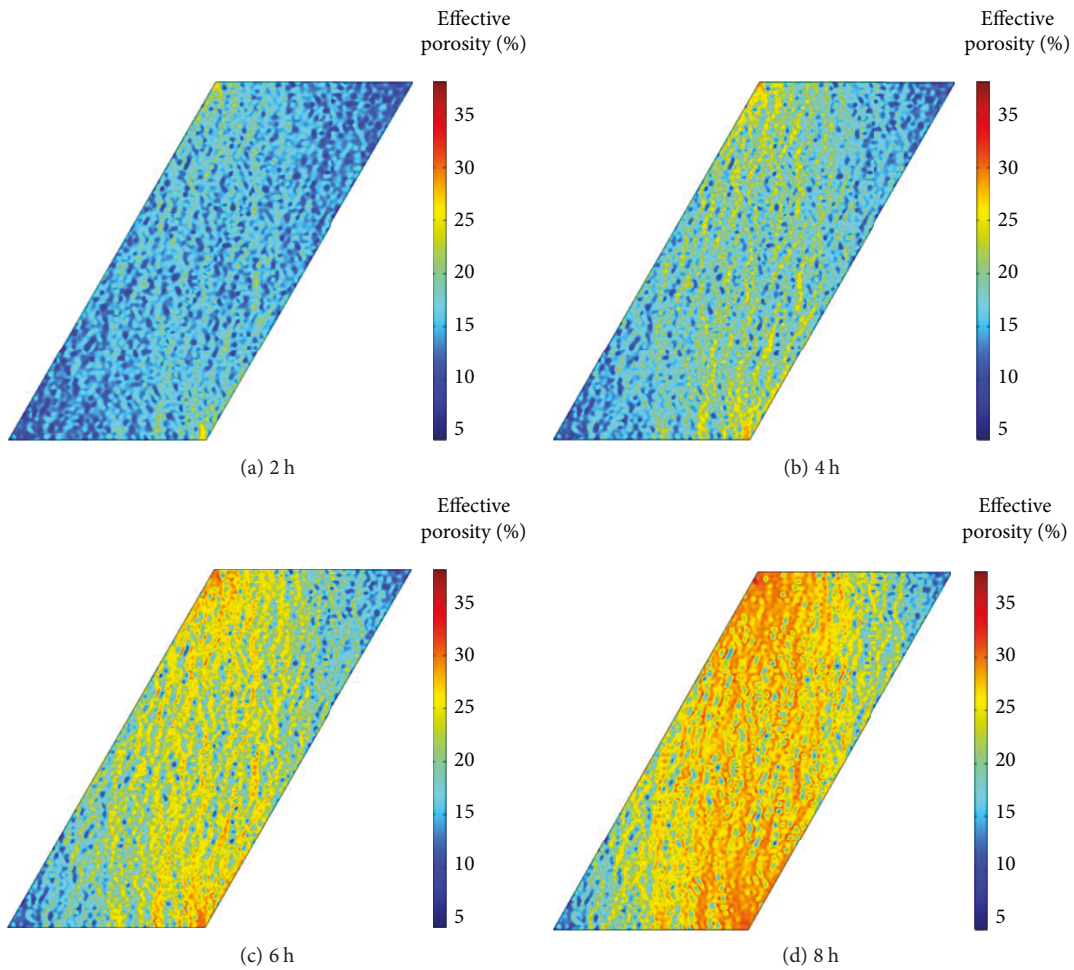


FIGURE 8: The spatial distribution of effective porosity at different times.

approximately 200%, from 10% to nearly 30% (Figure 11). However, this increase is not uniform. The variations of those with larger initial effective porosity and permeability are significant, while those with smaller initial effective porosity and permeability are slightly increased. As the distributions with large initial effective porosity and permeability preferentially increased and interconnect, some major seepage channels are

formed under particle migration effect, as illustrated in Figures 8(d) and 9(d).

4.1.2. Evolution of Flow Velocity at the Outlet Boundary. As shown in Figure 10, the distribution of the flow velocity is significantly related to time. The overall increase in flow velocity is small during the initial phase, with a sharp increase in

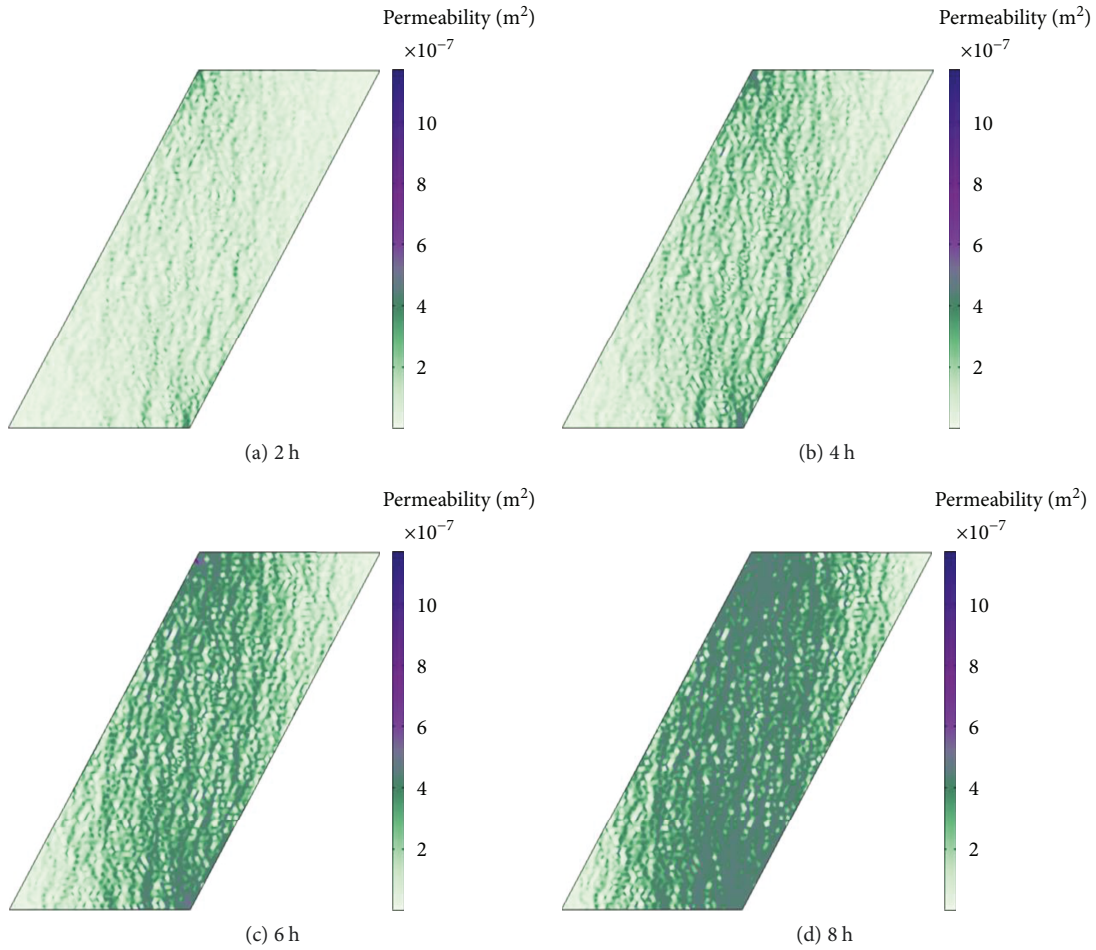


FIGURE 9: The spatial distribution of permeability at different times.

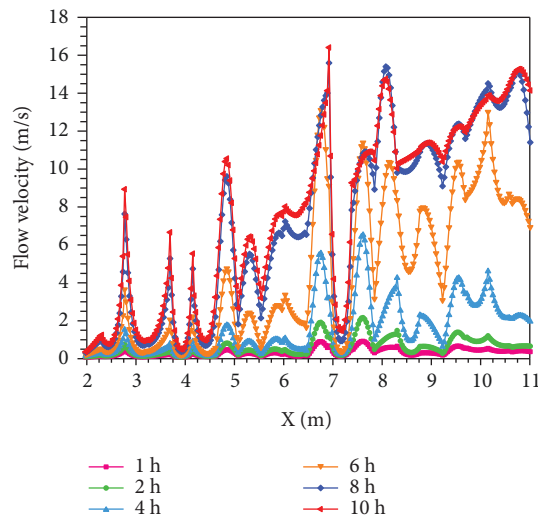


FIGURE 10: The flow velocity curves of the outlet boundary at different times.

subsequent phases and a tiny increase in the final phase. The maximum hourly increase in flow velocity is approximately 1 m/s from 1 h to 2 h, 2 m/s from 2 h to 4 h, 4 m/s from 4 h

to 6 h, 2.5 m/s from 6 h to 8 h, and 0.5 m/s from 8 h to 10 h. The passage of time represents the evolution of the water inrush. Therefore, the evolution process can be roughly

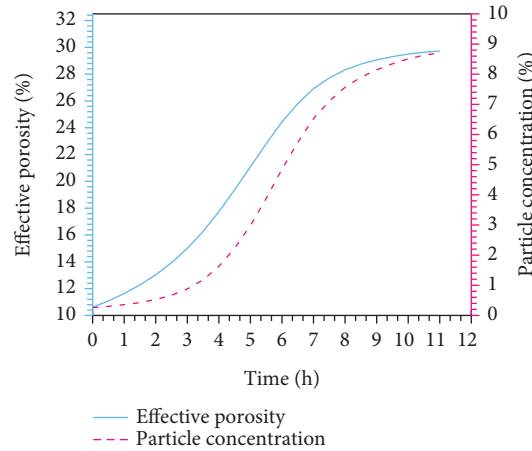


FIGURE 11: The average effective porosity and particle concentration curves with time.

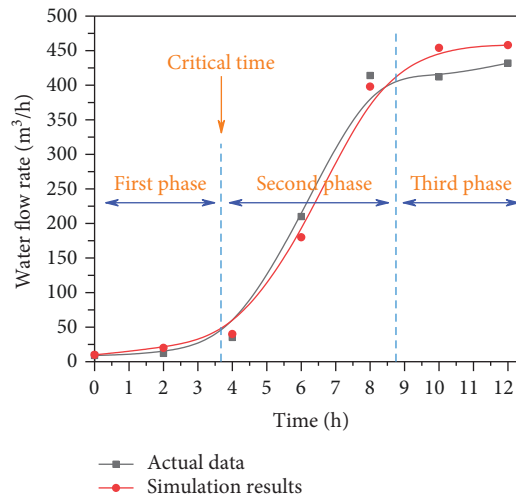


FIGURE 12: The comparison of water inflow between simulation results and actual data.

divided into three phases according to the degree of increase in the flow rate, including (i) low velocity seepage, (ii) drastic increase in flow velocity, and (iii) steady-state water flow. In addition, the figure shows that the increases with high initial flow velocity at the outlet boundary are larger, while those with low initial flow velocity are smaller.

4.1.3. Changes in Average Effective Porosity and Average Particle Concentration. It can be seen from Figure 11 that the process of changing the average particle concentration over time has experienced a slow first phase, a drastic second phase, and a smooth third phase. Combined with the previous analysis, it can be considered that due to the small initial percolation velocity, the erosion of the water flow is weak, resulting in a slow increase in the average particle concentration; then, as the water flow velocity increases, the solid particles migrate into the fluid due to the erosion, resulting in a significant increase in the average particle concentration, and at the same time the effective porosity will also increase significantly. Though the final phase of the seepage channel and water flow rate is stable, the average particle concentration will gradually stabilize.

To sum up, the seepage characteristics have undergone a complete evolution process under the coupling of multiple fields. In the initial phase, this coupling is gradually enhanced although it is weak. As the flow rate gradually increases, the water flow continuously erodes the particles of the granular rock and migrates them. The particle concentration increases rapidly while the effective porosity and permeability also evolve. The change in permeability will in turn increase the seepage velocity and enhance the erosion, and the coupling effect causes drastic changes with substantial particle migration in the second phase. Eventually, as the porosity evolves to its maximum, the percolation channels and flow rates tend to stabilize, and the coupling is no longer significant.

4.2. Comparison between Numerical Simulation Results and Actual Data. Figure 12 plots the curves of simulated fault flow rate and actual data, and it can be seen that the variation trend of the two is basically consistent, which proves the correctness of the seepage characteristic evolution model of fault water inrush established in this paper. In connection with the above discussion, it can be concluded that the process of fault water inrush can be divided into three phases, including (i)

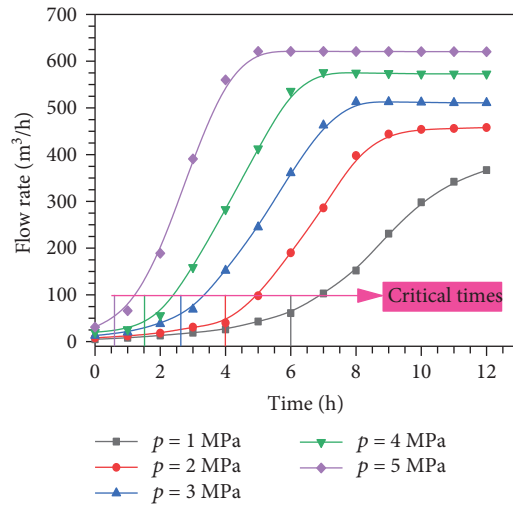


FIGURE 13: Effect of water pressure on flow rate.

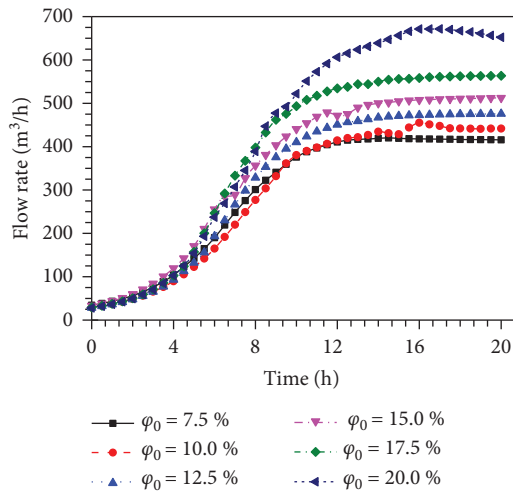


FIGURE 14: Effect of initial effective porosity on flow rate.

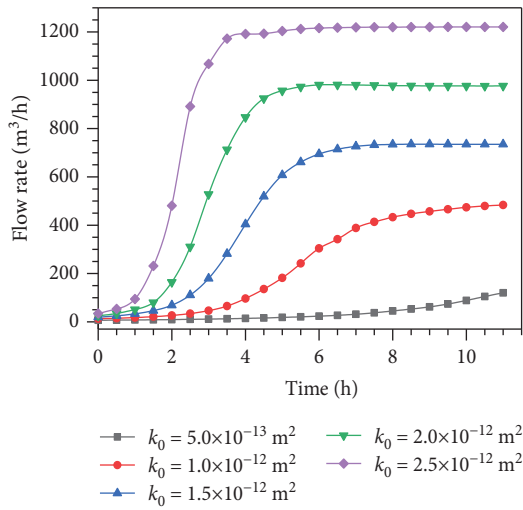


FIGURE 15: Effect of initial permeability on flow rate.

low velocity seepage, (ii) drastic changes with substantial particle migration, and (iii) steady-state water flow. According to the actual situation, after 5 hours, the water flow will increase rapidly and water inrush hazards will occur. This time between the first phase and the second phase is called “the critical time of water inrush.” If measures such as grouting reinforcement are taken on the fault before this time, water inrush hazards can be effectively prevented. Otherwise, once the time is missed, the water flow will increase rapidly. At that point, water flow will be difficult to control and increase the risk of water inrush hazards.

4.3. Analysis of Effect Factors. According to the above analysis, the critical time of water inrush is the key time for taking measures to ensure safety. In order to study the factors affecting the evolution process, the flow conditions of water inrush were discussed. Through numerical simulation of different flow conditions, it is expected to obtain the change rules of flow rate and critical time, so as to provide a theoretical basis for water inrush prediction.

4.3.1. Effect of Water Pressure. Water pressure is the driving force of water inrush, and different water pressures must have an important influence on seepage evolution. Numerical simulation was carried out with 1 MPa, 2 MPa, 3 MPa, 4 MPa, and 5 MPa as inlet pressures. The curve of flow rate changing with time under different water pressure conditions is shown in Figure 13.

As is shown in Figure 13, water flow rate is significantly affected under different water pressure conditions. As the pressure increases, the changes in the flow rates accelerate. For example, for $p = 2$ MPa, the flow rate was only approximately $40 \text{ m}^3/\text{h}$ when $t = 4$ h, and it is increased to $280 \text{ m}^3/\text{h}$ when $p = 4$ MPa. Moreover, the critical time had a noticeable change. It can be seen that the larger the water pressure, the earlier the critical time occurs. As the pressure decreases, the interval between critical times increases. For example, the interval of critical times between $p = 3$ MPa and $p = 2$ MPa was 1.4 hours, and the interval of critical times between $p = 2$ MPa and $p = 1$ MPa increased to 2 hours. In other words, as the pressure decreases, the critical time occurs more slowly, and the risk of water inrush can be better controlled. However, the risk will be difficult to control and prone to water inrush hazards when the water pressure is larger.

4.3.2. Effect of Initial Effective Porosity. Since the formation process of each fault structure is different, the initial effective porosity of fault fillings is also different. By testing the seepage properties of fault fillings, it is possible to predict and prevent water inrush in advance.

Figure 14 plots the effect of different initial effective porosities on water flow rate. The results show that the effect of initial effective porosity on flow rate is obvious, and it is mainly concentrated in the second phase and third phase. The difference in flow rate is small in the initial phase under different initial effective porosity conditions. In the second phase, the difference in the effects of different porosity has become more significant. The main reason for this is that as

the porosity increases, the coupling effect increases and the seepage characteristics evolve more strongly. By the final phase, the difference was significant and stable. However, the effect on the water inrush rate due to the difference in initial effective porosity is not easily noticeable in the initial phase. And it is easy to develop into an uncontrollable water inrush hazard in the fault with high initial effective porosity.

4.3.3. Effect of Initial Permeability. The initial permeability is also an important factor affecting the water flow rate. The initial permeability of the fault fillings can also be obtained by experiments to predict and prevent the water inrush hazards. Numerical simulations were carried out for different initial permeabilities under the same conditions, and the effect of different initial permeability on flow rate is shown in Figure 15.

As shown in Figure 15, for varying initial permeabilities, the evolution of both the water flow rate change and the water inrush critical time shows an obvious gap. As the initial permeability increases, the flow rate evolves more rapidly and intensely, and the critical time of water inrush occurs earlier. The difference in the effect of different initial permeability is significant throughout the process. For larger initial permeability, the evolution of water inrush is accelerated more intensely. Moreover, the larger initial permeability has a higher flow rate upper limit during the steady flow phase.

Initial water pressure, initial effective porosity, and initial permeability are all initial conditions for water inrush. When the values of these initial conditions are larger, the coupling effect tends to be significantly enhanced at the initial phase. At the same time, the evolution of seepage characteristics occurs earlier and more quickly. The result is that the water inrush time is greatly advanced and the upper limit of the flow rate is dramatically increased. However, aquifer water pressure, initial effective porosity, and initial permeability of fault fillings can all be measured in advance. If these conditions are combined with the above analysis and timely measures, it can effectively predict the critical time of water inrush and reduce the risk of water inrush hazards.

5. Conclusions

- (i) In this paper, the coupling effect of seepage and particle migration in the process of water inrush is comprehensively considered, and a multifield coupling model for the evolution of characteristics of fault water inrush is established. The COMSOL software was used to numerically simulate the coupling model, and the simulation results of water inflow change were basically consistent with the field data, indicating the correctness of the evolution model of fault water inrush established in this paper
- (ii) According to the evolution process of seepage characteristics such as effective porosity, permeability, seepage velocity, and particle concentration, the evolution of water inrush process can be divided into three phases, including (i) low velocity seepage, (ii)

drastic changes with substantial particle migration, and (iii) steady-state water flow. The seepage coupling will gradually increase with the evolution of seepage characteristics from the beginning. As the flow rate increases, the erosion of the water flow accelerates particle migration. This makes it easier for areas of large porosity and permeability to expand and connect to form cracks. Then, the overall permeability of the fault is enhanced, which in turn accelerates the evolution of the seepage velocity. This mutually reinforcing process continues to circulate, resulting in a rapid increase in the flow rate of water inrush. By the time the effective porosity has evolved to a maximum, the formation of the seepage channel and the evolution of the seepage characteristics have been stably completed

- (iii) Water flow rate increases with increasing initial water pressure, initial effective porosity, and initial permeability. When the values of these initial conditions are larger, the coupling effect tends to be significantly enhanced at the initial stage. At the same time, the evolution of seepage characteristics occurs earlier and more quickly. The result is that the water inrush time is greatly advanced and the upper limit of the water flow rate is dramatically increased
- (iv) The evolution model of seepage characteristics established in this paper can effectively predict fault water inrush. The critical time of water inrush by conditions such as aquifer water pressure, initial effective porosity, and initial permeability of fault fillings is predicted, so that proper measures can be put in place timely. It is expected to achieve the goal of reducing the risk of water inrush hazards and ensuring safe production

Data Availability

The data used to support the findings of this study are included within the article.

Conflicts of Interest

The authors declare that they have no conflicts of interest.

Acknowledgments

The project is supported by the National Natural Science Foundation of China (51404146), the China Postdoctoral Science Foundation (2015M572067), the Natural Science Foundation of Shandong Province (ZR201807060138), the Postdoctoral Innovation Project of Shandong Province (152799), the Key R&D Projects in Shandong Province (2015GSF120016), the Qingdao Postdoctoral Applied Research Project (2015203), the Anhui Province Key Laboratory of Modern Mining Engineering Foundation

(KLMME12101), the SDUST Research Fund (2018TDJH102), and the Young Teachers' Growth Program of Shandong Province.

References

- [1] Q. Qian, "Challenges faced by underground projects construction safety and countermeasures," *Chinese Journal of Rock Mechanics and Engineering*, vol. 31, no. 10, pp. 1945–1956, 2012.
- [2] Q. Wu, "Progress, problems and prospects of prevention and control technology of mine water and reutilization in China," *Journal of China Coal Society*, vol. 39, no. 5, pp. 795–805, 2014.
- [3] S. Li, Z. Zhou, L. Li, S. Shi, and Z. Xu, "Risk evaluation theory and method of water inrush in karst tunnels and its applications," *Chinese Journal of Rock Mechanics and Engineering*, vol. 32, no. 9, pp. 1858–1867, 2013.
- [4] B. Yao, J. Wei, D. Wang, D. Ma, and Z. Chen, "Numerical study on seepage property of karst collapse columns under particle migration," *Computer Modeling in Engineering & Sciences*, vol. 91, no. 2, pp. 81–100, 2013.
- [5] Y. Chen, M. Yi, C. Chen, and C. Yu, "Bernstein polynomials method for fractional advection-diffusion equation with variable coefficients," *Computer Modeling in Engineering & Sciences*, vol. 83, no. 6, pp. 639–653, 2012.
- [6] C. Huang, T. Feng, W. Wang, and H. Liu, "Research on the failure mechanism of water resisting floor affected by fault," *Journal of Mining & Safety Engineering*, vol. 27, no. 2, pp. 219–222, 2010.
- [7] Z. Song, *Research on Dynamic Information Basis of Prediction and Control of Major Accidents in Coal Mines*, China Coal Industry Publishing House, Beijing, China, 2003.
- [8] Q. Wu, Y. J. Zhou, J. T. Liu et al., "The mechanical experiment study on lag mechanism of water-bursting of fault under coal seam," *Journal of China Coal Society*, vol. 28, no. 6, pp. 561–565, 2003.
- [9] L. Li, S. Liu, S. Li et al., "Development of testing system for coupled seepage and triaxial stress measurements and its application to permeability characteristic test on filling medium," *Rock and Soil Mechanics*, vol. 38, no. 10, pp. 3053–3061, 2017.
- [10] L. Li, S. Li, S. Shi, and Z. Xu, "Water inrush mechanism study of fault activation induced by coupling effect of stress-seepage-damage," *Chinese Journal of Rock Mechanics and Engineering*, vol. 28, no. 2, pp. 290–297, 2009.
- [11] S. Zhang, W. Guo, Y. Li, W. Sun, and D. Yin, "Experimental simulation of fault water inrush channel evolution in a coal mine floor," *Mine Water and the Environment*, vol. 36, no. 3, pp. 443–451, 2017.
- [12] X. Miao, S. Li, Z. Chen, and W. Liu, "Experimental study of seepage properties of broken sandstone under different porosities," *Transport in Porous Media*, vol. 86, no. 3, pp. 805–814, 2011.
- [13] X. Miao, X. Cui, J. Wang, and J. Xu, "The height of fractured water-conducting zone in under-mined rock strata," *Engineering Geology*, vol. 120, no. 1–4, pp. 32–39, 2011.
- [14] D. Ma, H. Duan, J. Liu, X. Li, and Z. Zhou, "The role of gangue on the mitigation of mining-induced hazards and environmental pollution: an experimental investigation," *Science of the Total Environment*, vol. 664, pp. 436–448, 2019.

- [15] D. Ma, M. Rezaia, H. S. Yu, and H. B. Bai, "Variations of hydraulic properties of granular sandstones during water inrush: effect of small particle migration," *Engineering Geology*, vol. 217, pp. 61–70, 2017.
- [16] D. Ma, X. Cai, Z. Zhou, and X. Li, "Experimental investigation on hydraulic properties of granular sandstone and mudstone mixtures," *Geofluids*, vol. 2018, Article ID 9216578, 13 pages, 2018.
- [17] D. Ma, X. Cai, Q. Li, and H. Duan, "In-situ and numerical investigation of groundwater inrush hazard from grouted karst collapse pillar in longwall mining," *Water*, vol. 10, no. 9, pp. 1187–1203, 2018.
- [18] J. Zhao, L. Yin, and W. Guo, "Stress–seepage coupling of cataclastic rock masses based on digital image technologies," *Rock Mechanics and Rock Engineering*, vol. 51, no. 8, pp. 2355–2372, 2018.
- [19] W. Liu, J. Zhao, R. Nie, Y. Liu, and Y. Du, "A coupled thermal-hydraulic-mechanical nonlinear model for fault water inrush," *Processes*, vol. 6, no. 8, p. 120, 2018.
- [20] B. Yao, Z. Chen, J. Wei, T. Bai, and S. Liu, "Predicting erosion-induced water inrush of karst collapse pillars using inverse velocity theory," *Geofluids*, vol. 2018, Article ID 2090584, 18 pages, 2018.
- [21] Z. Song, J. Hao, J. Tang, and Y. Shi, "Study on water inrush from faults prevention and control theory," *Journal of China Coal Society*, vol. 38, no. 9, pp. 1511–1515, 2013.
- [22] J. Sun and L. Wang, "Floor fault water-inrush prediction based on catastrophe analysis of micro-seismic signals," *Journal of China Coal Society*, vol. 38, no. 8, pp. 1404–1410, 2013.
- [23] S. Jian, W. Lianguo, W. Zhansheng, H. Huaqiang, and S. Yifeng, "Determining areas in an inclined coal seam floor prone to water-inrush by micro-seismic monitoring," *Mining Science and Technology (China)*, vol. 21, no. 2, pp. 165–168, 2011.
- [24] B. Yao, X. Mao, J. Wei, and D. Wang, "Study on coupled fluid-solid model for collapse columns considering the effect of particle transport," *Journal of China University of Mining & Technology*, vol. 43, no. 1, pp. 30–35, 2014.
- [25] C. Wang, P. Zhai, Z. Chen, J. Liu, L. Wang, and J. Xie, "Experimental study of coal matrix-cleat interaction under constant volume boundary condition," *International Journal of Coal Geology*, vol. 181, pp. 124–132, 2017.
- [26] R. Sakhthivadivel and S. Irmay, *A Review of Filtration Theories*, Hydraulic Engineering Laboratory, College of Engineering, University of California, Berkeley, CA, USA, 1996.
- [27] I. Vardoulakis, M. Stavropoulou, and P. Papanastasiou, "Hydro-mechanical aspects of the sand production problem," *Transport in Porous Media*, vol. 22, no. 2, pp. 225–244, 1996.
- [28] J. M. Ferreira and R. P. Chhabra, "Accelerating motion of a vertically falling sphere in incompressible Newtonian media: an analytical solution," *Powder Technology*, vol. 97, no. 1, pp. 6–15, 1998.
- [29] W. Sun, S. Zhang, Y. Li, and C. Lu, "Development application of solid-fluid coupling similar material for floor strata and simulation test of water-inrush in deep mining," *Chinese Journal of Rock Mechanics and Engineering*, vol. 34, pp. 2665–2670, 2015.
- [30] W. Sun, H. Du, F. Zhou, and J. Shao, "Experimental study of crack propagation of rock-like specimens containing conjugate fractures," *Geomechanics and Engineering*, vol. 17, no. 4, pp. 323–331, 2019.
- [31] S. Chen, Z. Q. Yue, and L. G. Tham, "Digital image-based numerical modeling method for prediction of inhomogeneous rock failure," *International Journal of Rock Mechanics and Mining Sciences*, vol. 41, no. 6, pp. 939–957, 2004.
- [32] C. A. Tang, L. G. Tham, P. K. K. Lee, T. H. Yang, and L. C. Li, "Coupled analysis of flow, stress and damage (FSD) in rock failure," *International Journal of Rock Mechanics and Mining Sciences*, vol. 39, no. 4, pp. 477–489, 2002.
- [33] W. C. Zhu and C. A. Tang, "Micromechanical model for simulating the fracture process of rock," *Rock Mechanics and Rock Engineering*, vol. 37, no. 1, pp. 25–56, 2004.
- [34] T. H. Yang, L. G. Tham, C. A. Tang, Z. Z. Liang, and Y. Tsui, "Influence of heterogeneity of mechanical properties on hydraulic fracturing in permeable rocks," *Rock Mechanics and Rock Engineering*, vol. 37, no. 4, pp. 251–275, 2004.